

*In situ* measurements of methane cycling in cold seep sediments containing gas hydrates and brines

Laura L. Lapham

A dissertation submitted to the faculty of the University of North Carolina at Chapel Hill in partial fulfillment of the requirements for the degree of Doctor of Philosophy in the Department of Marine Sciences

Chapel Hill  
2007

Approved by

Christopher S. Martens

Jeffrey P. Chanton

Marc Alperin

Dan Albert

Ian R. MacDonald

©2007  
Laura L. Lapham  
ALL RIGHTS RESERVED

## ABSTRACT

Laura L. Lapham: *In situ* measurements of methane cycling in cold seep sediments containing gas hydrates and brines  
(Under the direction of Christopher S. Martens and Jeffrey P. Chanton)

The spatial distributions of dissolved *in situ* methane concentrations and biogeochemical processes were investigated in cold seep sediments containing gas hydrates and brine fluids along the northern continental slope of the Gulf of Mexico and the Northern Cascadia Margin, offshore Vancouver Island. The measured distributions elucidate the role of biogeochemical processes in controlling hydrate stability and provide evidence for a potentially large source of methane directly from brine seeps. To obtain *in situ* methane concentrations, two novel pore-fluid samplers were developed and tested. While both samplers retained gas samples at *in situ* pressures, HYDRA used active suction to collect discreet samples while the Pore-Fluid Array used pumps driven by osmosis to slowly collect a temporal record of pore-fluid chemical composition. Within hydrate-bearing sediments, the successful retrieval of 14 *in situ* methane concentration profiles with HYDRA showed that from immediately adjacent to and as far as 350 cm away from outcropping hydrate, pore-fluids contained less than 15 mM dissolved methane, a factor of four lower than methane saturated fluids. While undersaturated conditions are expected near the sediment-water interface, these results suggest that hydrates in the shallow sediments are not thermodynamically stable and could be dissolving. However, the observed hydrates may be more stable than theory predicts if their dissolution is kinetically controlled by impurities

concentrated on their surfaces. Hydrate stability was not strongly affected by biogeochemical processes occurring adjacent to hydrate. Spatial variability in rates of sulfate reduction and anaerobic methane oxidation were largely controlled by the availability of petroleum and/or chemosynthetically derived carbon, rather than by distance from hydrate deposits. In brine filled sediments, *in situ* dissolved methane concentrations reached 25 mM and steep chloride concentration gradients could be explained by upward advection rates that varied between 3 and 65 cm/year. As there was no indication of methane oxidation in these brine sediments, these sites may be an important direct source of methane to the oceans. The combined results of this study demonstrate the importance of *in situ* quantification of methane concentrations and biogeochemical processes within hydrate and brine sediments.



To My Family

## ACKNOWLEDGMENTS

I'd like to take this opportunity to thank my mentors, colleagues, family and friends for their support, patience, and encouragement over these last few years. The following people have played a large role in the successful completion of my Ph.D., and I thank them all from the bottom of my heart.

First and foremost, I'd like to thank Peter Brewer who originally sparked my interest in gas hydrates. My interest in gas hydrates was then fostered by the support of my dissertation committee. These amazing five scientists have given me advice, support and gentle nudging over the years and I thank them for that. Chris, even though I came to UNC to work in the Amazon rainforest, you recognized my passion for gas hydrates and allowed me to explore them further. You have been an incredible motivator and make me feel like I can do anything. Jeff, your original curiosity of hydrates got me on my first cruise, and we haven't stopped cruisin' since. Thank you so much for your optimism, support and all you have done for me. Ian, your intuitive understanding of gas hydrates has always impressed me. Thanks for sharing that intuition with me. Marc, your inquisitiveness has always amazed and challenged me. I thank you for asking the tough questions. And Dan, thank you for your guidance in the lab.

I have also had the fortunate experience to work with a great group of people in the University of Mississippi Gulf of Mexico Hydrates Research Consortium. While the consortium was initially and continues to be my primary source of funding, over the years, it

has also become more of a home for me to share my ideas and data. Bob, Carol, Paul, Jean, Andy, Matt, and Scott, because of your support, I have gone after things that I may have given up on years ago. Thank-you.

My graduate school experience has truly been enhanced by the support of a wonderful group of fellow students. They have been there to bounce ideas off of, to take leisurely canoe trips with or just to get that afternoon coffee pick-me-up. In particular, I'd like to thank Melissa, my lab partner. I have always been in awe of your wisdom, courage and spirit in the lab. You are a great teacher and I know you will find everything you are looking for in life. Sponges rock! Karen, you will one day be a top gun. I enjoy your inquisitive style and know you will find not only the meaning of life but the organism that started it all. Drew, I hope one day I know as much about bikes as you do. Thanks for keeping such an even keel on life and research. John, you and I were hydrate soul mates from the beginning and I have always enjoyed our hydrate discussions. I know you will take the hydrate world by storm.

I am forever grateful for my wonderful family. Mom, you have always been an inspiration to me. Watching you go to night school since I can remember, listening to you and Jon talk about getting a BS (which I always found amusing) and finally taking the plunge and becoming a full-time student while I was in college really struck a chord with me. I commend you on your achievements and feel like a part of this degree is yours. Thanks for being a great mom and a wonderful friend. Dad, admit it, you are impressed I know what a 316 stainless steel, 1/8 inch tubing with Swagelok compression fitting is. You gave me the confidence to go after things and never give up. These skills have certainly come in handy over the last 7 years. Jon and Renata, you two have been where I am and have given me words of encouragement throughout my journey. Thanks for being my editors, cheerleaders

and SCUBA buddies when I needed it. I think I heard a loud cheer from Brazil when I defended, obrigado. Brian and Donita, you guys have been my close family over the past few years and I have enjoyed every minute of it. Ruby, ever since July 9, 2003, you have been the shining star in many Lapham's eyes but mine especially. You are going to do great things and I can't wait to watch you achieve them. You made me realize what the important things are in life, without even knowing it. Your Auntie La-la loves you. And finally, to my furry family: Lingnoy, KC, Taiden, Cassie, and Abicus. I certainly could not have done any of this without you. You keep me sane, happy and relaxed.

And lastly, to my friends who have supported me through the trials and triumphs of graduate school. Without your encouraging, I could not have done this. Kelly, thanks for being such a great friend over these many years. I wish you the best in life and know one day, you will take your around-the-world trip and enjoy every minute of it. Jeff, not only have you been an incredible scientific support over these past 12 years, but you have also become a wonderful friend. Thanks for everything. Heather, doing laundry that day at FSU changed my life forever. You have truly been an amazing friend for the past 13 years and I hope for many more. Suzi, what can I say, "you alone, you are the everything" (did you really think I would write this book and never quote REM?). You are the best and I am so lucky to have you in my life. And last, but certainly not least, to Patrick. You have been an incredibly patient, loving, and supportive partner over this last year. I thank you for being the wonderful person you are.

## TABLE OF CONTENTS

LIST OF TABLES .....	xii
LIST OF FIGURES .....	xiv
Chapter 1: Introduction .....	1
1. DISSERTATION OBJECTIVES .....	1
2. COLD SEEPS .....	8
3. SULFUR CYCLE .....	10
4. METHANE .....	11
5. MUD VOLCANOES-a significant methane source? .....	17
6. GAS HYDRATES-the largest methane reservoir.....	18
7. BIOGEOCHEMISTRY .....	33
8. REFERENCES .....	42
Chapter 2: Development of a sea-floor probe for <i>in situ</i> sampling of dissolved gases in sediment pore-fluids surrounding gas hydrates .....	50
1. INTRODUCTION .....	51
2. METHODS .....	55
3. RESULTS .....	76
4. DISCUSSION .....	98
5. CONCLUSIONS.....	107
6. REFERENCES .....	109

Chapter 3: A new sampler for measurements of temporal variability in pore-fluid chemistry of Gulf of Mexico hydrate-bearing sediments .....	111
1. INTRODUCTION .....	112
2. METHODS .....	116
3. RESULTS .....	129
4. DISCUSSION .....	138
5. CONCLUSIONS.....	145
6. REFERENCES .....	147
Chapter 4: Utilization of HYDRA for <i>in situ</i> concentrations and $\delta^{13}\text{C}$ values of methane dissolved in pore-fluids surrounding buried gas hydrates: Ramifications for hydrate stability .....	150
1. INTRODUCTION .....	151
2. MATERIALS AND METHODS.....	157
3. RESULTS .....	166
4. DISCUSSION.....	171
5. CONCLUSIONS AND IMPLICATIONS.....	183
6. REFERENCES .....	185
Chapter 5: Utilization of cores and HYDRA to follow biogeochemical processes at three Gulf of Mexico hydrate sites: influence on hydrate stability.....	189
1. INTRODUCTION .....	191
2. METHODS .....	195
3. RESULTS .....	202
4. DISCUSSION .....	218
5. CONCLUSIONS.....	228
6. REFERENCES .....	230

Chapter 6: Biogeochemical processes and advection rates in Gulf of Mexico brine seeps: field and modeling studies .....	234
1. INTRODUCTION .....	235
2. METHODS .....	240
3. RESULTS .....	247
4. DISCUSSION .....	255
5. CONCLUSIONS.....	265
6. REFERENCES .....	266
Chapter 7: Spatial variability in microbial activity associated with acoustic wipe-out zones in the northern Gulf of Mexico .....	269
1. INTRODUCTION .....	270
2. METHODS .....	274
3. RESULTS .....	281
4. DISCUSSION .....	297
5. CONCLUSIONS.....	310
6. REFERENCES .....	311
Appendix 1.....	315
Appendix 2.....	318
Appendix 3.....	326
Appendix 4.....	328
Appendix 5.....	330
Appendix 6.....	354
Appendix 7.....	366

## LIST OF TABLES

Table 1- 1: Atmospheric methane sources and sinks. ....	16
Table 2- 1: Gulf of Mexico (GOM) and Cascadia Margin sites .....	52
Table 2- 2: Dive number, cruise date, and HYDRA collection design. ....	58
Table 2- 3: Gulf of Mexico deployment of HYDRA configuration 2. ....	82
Table 2- 4: Barkley Canyon deployment of HYDRA configuration 3 .....	88
Table 2- 5: Barkley Canyon HYDRA configuration 4 .....	94
Table 2- 6: Measured chloride concentrations of sample chambers for configuration 4 .....	95
Table 3- 1: Configuration of PFA.....	122
Table 3- 2: Predicted and measured smearing spread.....	128
Table 4- 1: Pictures of each HYDRA deployment .....	162
Table 4- 2: Pictures of each HYDRA deployment .....	163
Table 4- 3: Dive, distance to hydrate, measured <i>in situ</i> methane concentrations, and the adjusted methane concentrations. ....	175
Table 4- 4: For equation 8, the listed parameters were used for outcropping hydrate and buried hydrate using assumed methane concentrations. ....	179
Table 5- 1: Locations and water depths of sites visited. ....	196
Table 5- 2: Overview of sampling sites, environments, sample types, and descriptions. .	198
Table 5- 3: Average statistics on %TOC, $\delta^{13}\text{C}$ -TOC, and C:N for down core profiles.....	215
Table 5- 4: DOC concentrations. OLW = overlying water.....	217
Table 5- 5: Model parameters.....	224



Table 6- 1: Site, site description, water depth, sample number, and deployment description .....	241
Table 6- 2: Diagenetic model parameters. ....	258
Table 6- 3: Modeled advection rates for GC 205 and MC 709 cores. ....	259
Table 7- 1: Sulfate gradients calculated from linear fits to sulfate concentration depth profiles. .....	284
Table 7- 2: Carbonate, shell, and DIC carbon isotopic signatures for the moderate and high microbial activity groups. ....	290

## LIST OF FIGURES

Fig. 1- 1: Conceptual model of methane distributions at a cold seep site . . . . .	4
Fig. 1- 2: Three-box model of the sulfur cycle. . . . .	11
Fig. 1- 3: Structure of methane (CH <sub>4</sub> ). . . . .	12
Fig. 1- 4: Key components of the global carbon cycle. . . . .	14
Fig. 1- 5: Worldwide distribution of mud volcanoes. . . . .	17
Fig. 1- 6: General hydrate structures. . . . .	19
Fig. 1- 7: Pressure (or depth in ocean) versus temperature plot. . . . .	22
Fig. 1- 8: Worldwide distribution of gas hydrate deposits. . . . .	23
Fig. 1- 9: Convergent margin gas hydrate cycle. . . . .	25
Fig. 1- 10: Passive margin dominated by salt tectonics. . . . .	25
Fig. 1- 11: Hydrate slope instability leading to geologic hazard . . . . .	27
Fig. 1- 12: Model of how global climate affects hydrate deposits. . . . .	29
Fig. 1- 13: Phase diagram along a marine temperature and pressure profile. . . . .	32
Fig. 1- 14: Diagenetic reactions . . . . .	34
Fig. 1- 15: Concentration profile results of the diagenetic equation. . . . .	41
Fig. 2- 1: Gulf of Mexico sites visited. . . . .	56
Fig. 2- 2: Inset map shows the location of Northern Cascadia Margin. . . . .	57
Fig. 2- 3: Photographs of HYDRA . . . . .	60
Fig. 2- 4: Flush chamber configurations 1, 2, and 3. . . . .	62
Fig. 2- 5: Schematic of HYDRA configuration 4. . . . .	63
Fig. 2- 6: Probe tip configurations . . . . .	65

Fig. 2- 7: HYDRA configuration 1.....	66
Fig. 2- 8: HYDRA configuration 2.....	67
Fig. 2- 9: HYDRA configuration 3.....	68
Fig. 2- 10: HYDRA configuration 4.....	69
Fig. 2- 11: HYDRA configuration 1 methane concentrations and stable isotopes. ....	78
Fig. 2- 12: GC 232 dive 4405. ....	81
Fig. 2- 13: Gulf of Mexico, dive 4553, GC 185. ....	84
Fig. 2- 14: Gulf of Mexico comparisons between HYDRA and core from GC 232-4564....	85
Fig. 2- 15: Barkley Canyon comparison between HYDRA and cores from dive 692.....	89
Fig. 2- 16: Barkley Canyon comparison between HYDRA and cores from dive 696.....	90
Fig. 2- 17: Barkley Canyon comparison between HYDRA and cores from dive 798.....	96
Fig. 2- 18: Barkley Canyon comparison between HYDRA and cores from dive 802.....	97
Fig. 2- 19: Comparison between methane stable carbon isotope values .....	103
Fig. 3- 1: Gulf of Mexico showing sampling site in shaded range.....	115
Fig. 3- 2: Seafloor pictures taken at MC 118.....	116
Fig. 3- 3: Components of the Pore Fluid Array. ....	118
Fig. 3- 4: OsmoSamplers (Jannasch et al., 1994; Jannasch et al., 2004). ....	120
Fig. 3- 5: Pumping rate experiments for OsmoSamplers 1, 2, and 3.....	121
Fig. 3- 6: Conceptual picture of the different materials.....	124
Fig. 3- 7: Fraction collector configuration used to sub-sample OsmoSampler tubing coils.	126
Fig. 3- 8: Temporal resolution due to A) diffusion and B) dispersion. ....	127
Fig. 3- 9: Spreading distances due to both diffusion and dispersion. ....	128

Fig. 3- 10: Deployment of the pore-fluid array at MC-118 in May, 2005.....	130
Fig. 3- 11: Seafloor photos of the PFA retrieval. ....	131
Fig. 3- 12: Chloride concentrations for overlying water (OLW) and 1.2 mbsf.....	135
Fig. 3- 13: Sulfate concentrations for all three coils measured.....	136
Fig. 3- 14: Methane concentrations for all three coils measured.....	136
Fig. 3- 15: Methane isotope composition for 1.2 mbsf.....	137
Fig. 3- 16: For the 1.2 mbsf coil, methane produced and consumed over specific time. ....	142
Fig. 3- 17: Results of thermodynamic model to determine the hydrate stability zone. ....	144
Fig. 4- 1: Barkley Canyon temperature and depth profile. ....	153
Fig. 4- 2: Barkley Canyon site “double mound” .....	156
Fig. 4- 3: Northern Cascadia Margin map. ....	157
Fig. 4- 4: Photographs of HYDRA in action. ....	159
Fig. 4- 5: Conceptual picture of the HYDRA deployments on a hydrate mound.....	161
Fig. 4- 6: Methane concentrations and isotopic ratios for dives 693, 799, and 798. ....	169
Fig. 4- 7: Methane concentrations and isotopic ratios for dives 692, 696, and 802. ....	170
Fig. 4- 8: Age of hydrate outcrop estimates.....	177
Fig. 4- 9: Annual photographs taken of outcropping hydrate at Barkley Canyon.....	181
Fig. 5- 1: Map of northern Gulf of Mexico and hydrate sites.....	196
Fig. 5- 2: Picture of HYDRA on board ship .....	200
Fig. 5- 3: Geochemical results from two transects from a hydrate outcrop.....	204
Fig. 5- 4: Geochemical results from sediments under a thin bacterial mat.....	206

Fig. 5- 5: Geochemical results from sediments under a thin bacterial mat.....	208
Fig. 5- 6: Geochemical results from sediments under a thin bacterial mat.....	210
Fig. 5- 7: Geochemical results from sediments near a tubeworm bed. ....	212
Fig. 5- 8: A) Sulfate and b) $\delta^{13}\text{C}$ -DIC values from three cores collected in background....	214
Fig. 5- 9: Sulfate reduction rates (SRR) from four different environments.....	214
Fig. 5- 10: Total organic carbon (TOC) percentage, $\delta^{13}\text{C}$ -TOC, and C:N ratios.....	216
Fig. 5- 11: Bernard style plot. ....	221
Fig. 5- 12: Synthesis of methane carbon isotopic composition from GC 185 and GC 234.	221
Fig. 5- 13: Measured and modeled results from 4217-core 7.....	224
Fig. 5- 14: Measured and model results for 4217-core 7.....	227
Fig. 6- 1: A) Map of the Texas-Louisiana coast, shelf, and slope. ....	237
Fig. 6- 2: Map of Gulf of Mexico sites visited. ....	242
Fig. 6- 3: Conceptual picture of surrounding environment.....	243
Fig. 6- 4: HYDRA results at GC 233,.....	244
Fig. 6- 5: At GC 233, outside the mussel bed (dive 4222). ....	248
Fig. 6- 6: For GC 205.....	250
Fig. 6- 7: For GB 425-core 2. ....	251
Fig. 6- 8: For GC 205-core 5. ....	254
Fig. 6- 9: Methane $\delta^{13}\text{C}$ values averaged over the depth profiles of cores and HYDRA....	265
Fig. 7- 1: Gulf of Mexico map showing Mississippi Canyon 118.....	275
Fig. 7- 2: Seafloor pictures taken at MC 118.....	276

Fig. 7- 3: Geophysical maps of MC 118.....	277
Fig. 7- 4: Low microbial activity cores. ....	283
Fig. 7- 5: Moderate microbial activity cores collected within the wipe-out zones. ....	286
Fig. 7- 6: High microbial activity cores collected within wipe-out zones. ....	287
Fig. 7- 7: High microbial activity stable isotopic composition.....	291
Fig. 7- 8: Moderate microbial activity stable isotopic composition. ....	291
Fig. 7- 9: Bulk organic matter.....	293
Fig. 7- 10: Bulk organic matter.....	293
Fig. 7- 11: Chloride concentrations for most cores.....	294
Fig. 7- 12: a) Ammonium, b) phosphate, and c) nitrate/nitrite concentrations.....	296
Fig. 7- 13: Stable carbon isotope ratio ranges of organic carbon sources. ....	300
Fig. 7- 14: The observational, geochemical, and geophysical seep evolution model.....	305
Fig. 7- 15: A conceptual cartoon of a north-south cross section through MC 118.....	309

## **Chapter 1: Introduction**

The first chapter of this dissertation introduces the overall objectives, gives a brief introduction to each chapter, and is followed by background information to elucidate the following six chapters. The background information presents a basic introduction to cold seeps and the roles sulfate and methane play at these seeps. It then introduces one of the largest reservoirs of methane in the marine environment, known as methane hydrate, and discusses hydrate occurrence and significance. The introduction ends with a description of biogeochemical processes and techniques used in the dissertation. The subsequent Chapters 2-6 are stand alone chapters including separate introduction, methods, results, discussion, and conclusions. Chapters 3, 5, 6, and 7 are intended for publication following revisions by committee members. At the end of the regular chapters, there is a comprehensive appendix that includes all the data presented in this dissertation plus two data sets not used from Blake Ridge and Cascadia Margin cruise 2002.

### **1. DISSERTATION OBJECTIVES**

The objectives of this dissertation are to measure the horizontal and vertical distributions of interstitial *in situ* dissolved methane concentrations in marine sediments at seeps and to assess the role biogeochemical processes play in hydrate stability. The biogeochemical processes focus on sedimentary microbial reactions such as sulfate reduction, anaerobic methane oxidation, and methanogenesis. These reactions are mediated by microbes that rely on the physical transport of methane and sulfate via advection and diffusion. The central

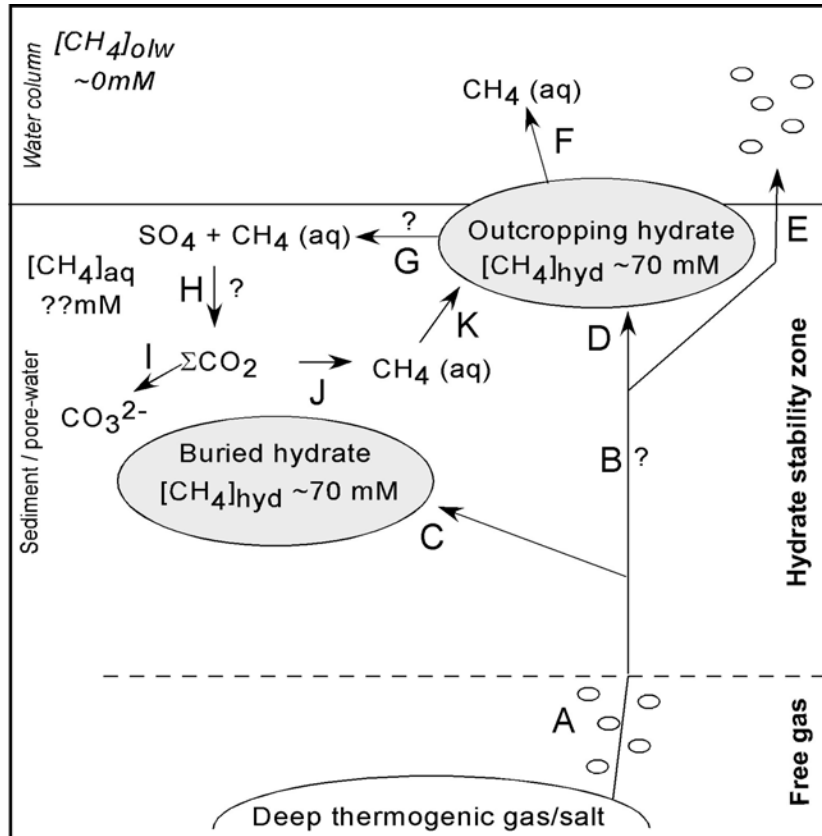
theme of this dissertation can be visualized with a conceptual model shown in Figure 1-1 which describes the interactions between methane fluxes, hydrates, and biogeochemical processes.

In the conceptual model, the primary source of methane is thermal degradation of organic matter in deeply buried sediments (Fig. 1-1A). Below the hydrate stability zone, this thermally generated methane is entrained within fluids that migrate along deep faults to reach pressure and temperature zones that are appropriate for hydrate formation (Fig. 1-1B). Where the pore-fluids are saturated with respect to methane within the hydrate stability zone, hydrates will form within the sediments (Fig. 1-1C) and as outcrops on the seafloor (Fig. 1-1D). If the fluid migration is too rapid to allow hydrate formation, streams of bubbles will emanate from the seafloor (Fig. 1-1E). Hydrate outcrops that are in direct contact with overlying seawater undersaturated with methane should dissolve (Fig. 1-1F). This same equilibration process will proceed in the sediments between dissolved methane and the hydrates (Fig. 1-1G). In the shallow sediments, the physical diffusion of sulfate from ocean waters and the abundance of reduced carbon compounds, including methane, promotes the activity of bacteria and archaea that reduce sulfate and oxidize methane and other hydrocarbons (Fig. 1-1H). As a byproduct of this microbial activity, total carbon dioxide (i.e.,  $\Sigma\text{CO}_2$ ) concentrations increase and either become substrate for methanogens to produce biogenic methane (Fig. 1-1J) or react with surrounding cations to form authigenic carbonates (Fig. 1-1I). If rates of methanogenesis are high enough to sustain saturated methane conditions, this biogenic methane may become entrained within the hydrates (Fig. 1-1K). Also, little is known of the *in situ* aqueous methane concentrations surrounding these shallow



forming hydrates ( $[\text{CH}_4]_{\text{aq}}$  on Fig. 1-1). Major questions stemming from the model remain unanswered and form the foundation on which this dissertation is built, including:

1. Is the concentration of *in situ* pore water methane sufficient (i.e., saturated) to indicate that hydrates are thermodynamically stable? If the hydrates are unstable and decomposing, can dissolved methane concentration gradients be used to determine the rate of dissolution?
2. Is there temporal variability of the dissolved methane pool surrounding hydrate?
3. Does enhanced microbial activity in sediments surrounding gas hydrate contribute to the decomposition of the hydrate?
4. What is the upward flux of methane-rich fluid? And how do these fluids affect biogeochemical cycling of sulfate and methane in the shallow sediments?



**Fig. 1- 1: Conceptual model of methane distributions at a cold seep site with outcropping thermogenic hydrate. A. Source of fluids from deep reservoir gas and salt diapirs. B. Fluid migration along faults. C. Formation of buried hydrates. D. Formation of shallow outcropping hydrate. E. Bubble vents. F. Equilibrium between dissolved methane in ocean water and hydrate. G. Equilibrium between dissolved methane in pore-fluids and hydrate. H. Coupled microbial reactions of sulfate reduction and anaerobic methane oxidation. I. Formation of authigenic carbonates. J. Microbial methanogenesis. K. Formation of biogenic methane hydrate.**

## 1.1. Chapters outline

***Chapter 2: Development of a sea-floor probe for in situ sampling of dissolved gases in sediment pore-fluids surrounding gas hydrates.*** This chapter is focused on approaches towards the quantification of *in situ* dissolved methane concentrations in sediments surrounding gas hydrates. The classic problem with determining dissolved methane in the deep sea has been that where methane concentrations are high, as they are assumed to be in hydrate environments, traditionally collected sediment cores de-gas upon sample recovery. This chapter describes the development and testing of a novel instrument that collects un-decompressed pore-water samples for in situ concentration measurements. Samples collected from this instrument will also be compared to traditionally collected cores.

***Chapter 3: A new sampler for measurements of temporal variability in pore-fluid chemistry of Gulf of Mexico hydrate-bearing sediments.*** This chapter introduces an alternative technology and design to collect pore-fluids and contain them at *in situ* pressures in order to measure *in situ* methane concentrations. This instrument has the advantage that it collects a time-series of samples in order to address temporal variability in methane concentrations.

***Chapter 4: In situ concentrations and  $\delta^{13}C$  values of dissolved methane in pore-fluids surrounding buried gas hydrates: Ramifications for hydrate stability.*** One of the fundamental assumptions within the hydrate literature is that hydrates are stable only if bathed in fluids that are saturated with respect to methane. While this assumption makes thermodynamic sense, it is not consistent with observations that hydrates persist as outcrops protruding into the water column over time. This chapter poses the hypothesis that the

hydrates are more stable than predicted by thermodynamics and presents several mechanisms to explain their observed meta-stability.

***Chapter 5: Biogeochemical processes at three Gulf of Mexico hydrate sites: influence on hydrate stability.*** This chapter addresses the spatial variability of biogeochemical processes such as sulfate reduction, anaerobic methane oxidation, and microbial methane production and the factors controlling such processes across a regional distribution of hydrate outcrops in the Gulf of Mexico. It specifically addresses the question of whether or not microbial activity surrounding hydrates may enhance hydrate dissolution. To conduct this assessment, several core sets were collected as transects across hydrate mounds and analyzed for geochemical indicators of such microbial activity.

***Chapter 6: Biogeochemical processes and advection rates in Gulf of Mexico brine seeps: field and modeling studies.*** In the Gulf of Mexico, the presence of seafloor seeps is due to the migration of brine fluids along faults and fissures created by salt tectonics. The presence of brine gradients generated near the shallow sediment surface by advective flow allows for a rare opportunity to determine the upward fluid flux rate. Furthermore, the presence of brine fluids in these sediments may also affect biogeochemical processes either by inhibiting microbial activity because of the high salt concentrations or through dilution by the physical high flow rates. Finally, the elevated salt concentrations in migrating brine fluids make gas hydrates thermodynamically unstable and thus inhibit their formation.

***Chapter 7: Spatial variability in microbial activity associated with acoustic wipe-out zones in the northern Gulf of Mexico.*** This chapter focuses on the local spatial variability of microbial processes within and outside of areas where geophysical approaches have indicated active venting. At cold seep sites, microbial activity is known to be enhanced due

to the abundance of reduced compounds entrained in upwardly advecting, hydrocarbon-rich fluids. It remains to be determined how this microbial activity influences sedimentary gas fluxes and composition on local and regional scales. An integrated biogeochemical and geophysical approach is used to investigate the local and regional role microbial activity plays at hydrate-bearing cold seeps in the northern Gulf of Mexico.

## 2. COLD SEEPS

Cold seeps, also referred to as methane or hydrocarbon seeps, are areas of the seafloor where fluids rich in reduced compounds seep from deeper sediment depths to the sediment-water interface and typically support extensive biological communities. The terms “cold” and “seep” are used to contrast to the better known hydrothermal vent systems that are also found on the seafloor and support chemosynthetic communities (Kennicutt II et al., 1992; Turnipseed et al., 2003). While seeps are typically found at cold *in situ* ocean temperatures, the term “seep” does not imply a slow fluid venting rate. In fact, seeps are commonly associated with high flow rates that result in bubble vents and mud volcanoes, thought to directly inject methane to the oceans, while in slower flow sites, seeps are associated with gas hydrate deposits (Roberts and Carney, 1997). Understanding the unique connection between the biological communities, the fluids, and the formation of unique seafloor features is therefore imperative.

Cold seep environments typically host extensive biological communities including both chemoautotrophs, such as aerobic sulfur and methane oxidizers and heterotrophs, such as clams, mussels, tube-worms, and heterotrophic bacteria (Kennicutt II et al., 1985; MacDonald et al., 1989; Fisher et al., 1997; Nikolaus et al., 2003). At the base of the cold seep food chain, chemoautotrophs oxidize either sulfide or methane as an energy source, rather than sunlight, to produce organic matter via chemosynthesis. For example, the sulfide oxidizing *Beggiatoa* spp. bacteria lives at the sediment water interface, utilizing the sulfide produced from sulfate reduction and oxygen in the water column and creating extensive white mats on the seafloor (Nikolaus et al., 2003). These communities are typically in symbiotic relationships with heterotrophs. For example, clams and tube-worms are known to

have sulfide-oxidizing symbionts living in their tissues whereas mussels have methane-oxidizing bacteria living in their gills (Childress et al., 1986; Brooks et al., 1987; Cary et al., 1988; Kennicutt II et al., 1992). Heterotrophic bacteria found in the anaerobic portions of the sediment column also take advantage of vent fluids by oxidizing newly available organic carbon and reducing sulfate diffusing in from overlying water (Aharon and Fu, 2000; Arvidson et al., 2004; Joye et al., 2004). This process of sulfate reduction produces large amounts of sulfide and bicarbonate that can then be used by chemoautotrophs.

At cold seeps, enhanced microbial activity and fluid flow allow the development of unique seafloor features, such as carbonate mounds, gas hydrate deposits, and mud volcanoes (Roberts and Carney, 1997). Carbonate mounds form as authigenic carbonate produced from dissolved inorganic carbon, the byproduct of organic matter oxidation (Roberts and Aharon, 1994; Bohrmann et al., 1998; Formolo et al., 2004). Gas hydrate deposits form when the seeping fluids are methane saturated within the hydrate stability zone that is defined by pressure and temperature (Sloan, 1998). When the fluid flow is fast enough, mud volcanoes may emanate from the seafloor and express themselves into the water column (MacDonald et al., 2000). Due to their unique geophysical signatures, these seafloor features can be used to identify cold seeps from a surface ship or satellites (MacDonald et al., 1993; Sassen et al., 2004).

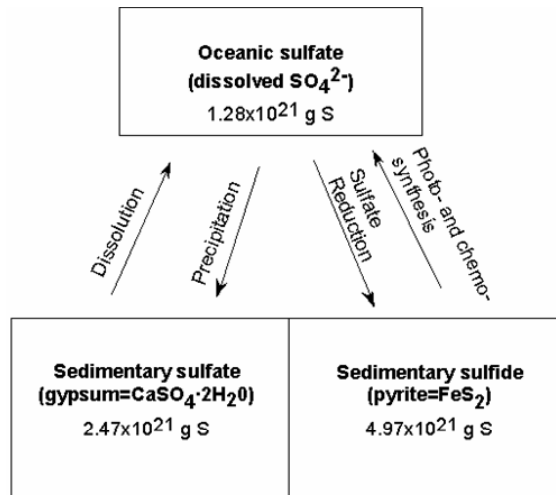
Cold seeps are natural linkages between the sulfur and carbon cycles. They Hydrate deposits that outcrop from the sediments into the water column are ideal environments to find the microbial consortia that both oxidize methane and reduce sulfate (Hoehler et al., 1994; Boetius et al., 2000). While sulfate reduction rates are high within tens of centimeters of the sediment-water interface in hydrate-bearing sediments, (Cragg et al., 1996; Aharon and Fu,

2000; Arvidson et al., 2004; Joye et al., 2004), the elevated rates may not be solely linked to the availability of methane. Other hydrocarbons and petroleum-derived substances also increase the sulfate reducing activity (Joye et al., 2004).

### **3. SULFUR CYCLE**

The sulfur cycle is driven by microbial, physical, and chemical transformations that occur between the major global sulfur pools: oceanic sulfate ( $\text{SO}_4$ ), sedimentary and igneous pyrite ( $\text{FeS}_2$ ), and sedimentary gypsum ( $\text{CaSO}_4$ ) (Fig. 1-2). Oceanic sulfate is produced from the weathering and atmospheric oxidation of igneous pyrite embedded in the crust, by photosynthesis under anoxic conditions, or by aerobic chemosynthesis as occurs in hydrothermal and cold seep environments (Schlesinger, 1997). This sulfate can then be consumed by anaerobic sedimentary sulfate-reducing bacteria to form sulfide. Reacting with available iron in the sediments, bacterially-produced sulfide may then form sedimentary pyrite. Over time, this pyrite pool will become buried and exposed to high temperatures and pressures and form the igneous pyrite pool. Where evaporation rates are high, oceanic sulfate may precipitate as sedimentary gypsum. Exposure of these deposits to water will dissolve them and return liberated sulfate to the oceanic sulfate pool. As the sulfur cycle is naturally linked to the reduced carbon pool via microbial activity, it becomes important to understand the rates of and factors controlling such activity.



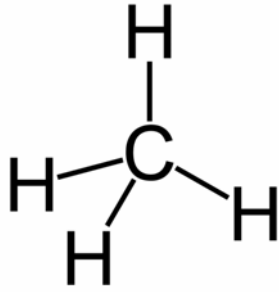


**Fig. 1- 2: Three-box model of the sulfur cycle. Cycle shows the major sulfur pools along with their sulfur content and the processes linking them together (figure redrawn from Schlesinger, 1997).**

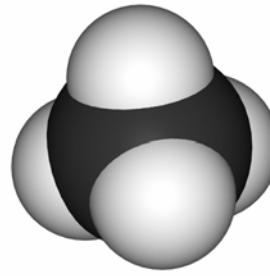
#### 4. METHANE

Methane (CH<sub>4</sub>) is a colorless and odorless hydrocarbon gas (Fig. 1-3). It is an alkane grouped with other straight-chain light hydrocarbons such as ethane (C<sub>2</sub>H<sub>6</sub>), propane (C<sub>3</sub>H<sub>8</sub>), and butane (C<sub>4</sub>H<sub>10</sub>). It is relatively nonpolar, making it relatively insoluble in water. As a reduced form of carbon, methane is an important part of the global carbon cycle. Since methane absorbs infrared radiation 25 times more effectively than CO<sub>2</sub>, on a molecule per molecule basis (Lelieveld et al., 1998; Petit et al., 1999), it is an important greenhouse gas and quantifying methane sources and sinks is important to understanding past and future climate change.

A)



B)



**Fig. 1- 3: Structure of methane (CH<sub>4</sub>). A) 2D representation and B) 3D space filling model. Figures from wikipedia.com.**

#### 4.1. The global carbon cycle

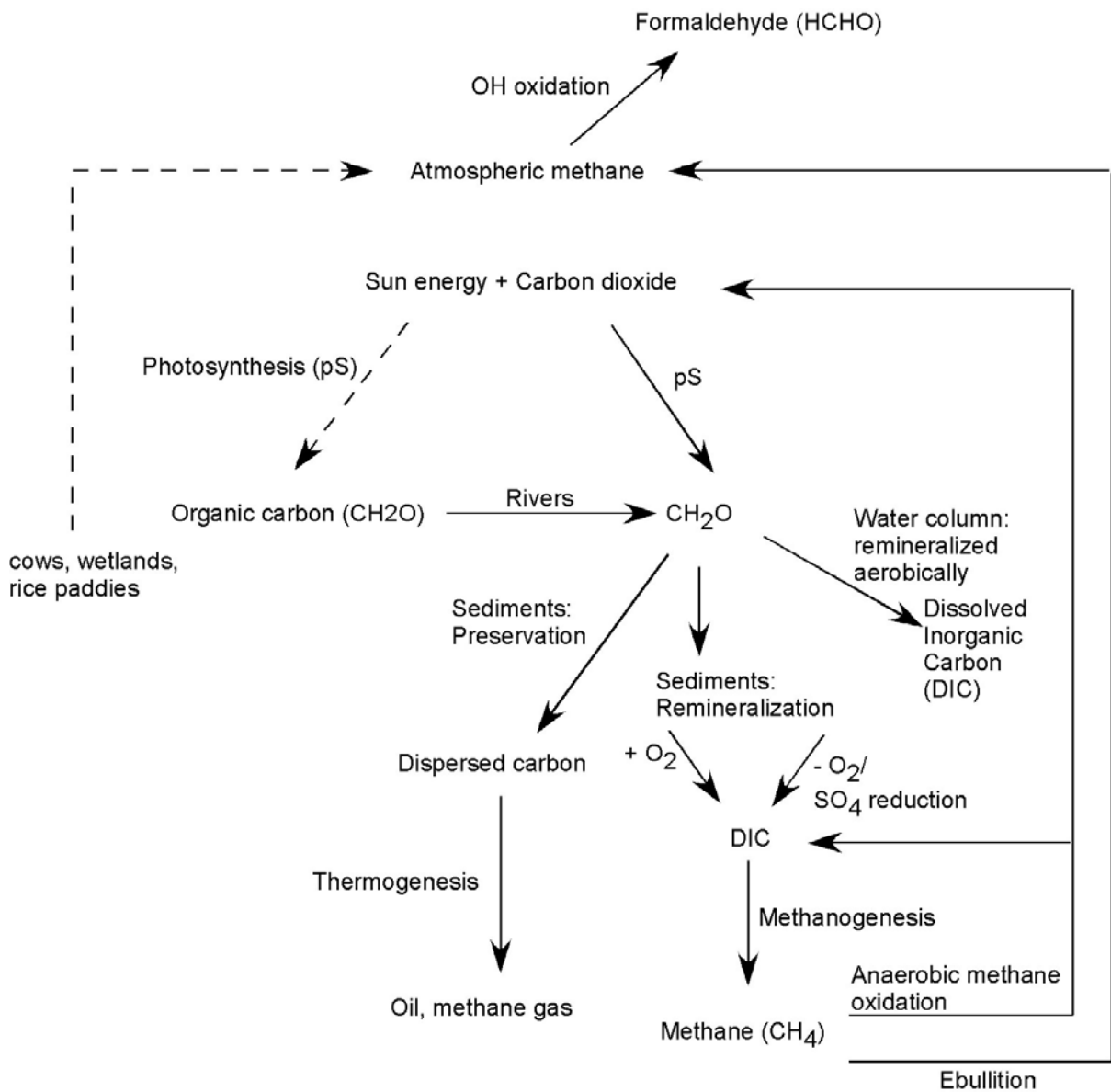
The global carbon cycle accounts for the movement of carbon in its various chemical forms between a variety of different environments (Fig. 1-4). The chemical transformations of compounds between the inorganic and organic carbon pools are accomplished through photosynthesis and respiration (Fig. 1-4). On land, photosynthetic plants harness the sun's energy to transform inorganic carbon into complex organic carbon molecules and oxygen. Living organisms utilize these organic molecules through the process of aerobic respiration where they consume oxygen and organic carbon to produce energy and inorganic carbon. Additionally, since respiration returns bound nitrogen, phosphorus, and carbon to their inorganic forms, it is also referred to as remineralization. Methanogens in anaerobic environments such as cow stomachs, wetlands, and rice paddies also contribute to the atmospheric methane pool.

Similarly, in the oceans, organic carbon is produced in the photic (light-bearing) zone by photosynthetic phytoplankton. This process is also known as primary production as it is the principal method for creating complex carbon compounds. Although most of this carbon is

oxidized by aerobic respiration in the water column, a small percentage of this material will survive oxidation and reach the sediments. Once organic matter is deposited on the seafloor, it can either be further oxidized or remineralized by sedimentary microbes or become preserved in sediments.

Remineralization by microbes in the sediments initially proceeds aerobically, producing dissolved inorganic carbon (DIC). When oxygen is fully consumed, typically within millimeters to centimeters of the sediment surface, the dominant remineralization process switches to anaerobic sulfate reduction (other processes are discussed in ‘biogeochemical processes’ section). Sulfate reduction is carried out by bacteria that oxidize organic matter using sulfate as an electron acceptor to produce sulfide and DIC. Once sulfate is exhausted and no longer available to the microbial population, methanogens will reduce DIC to produce methane. This methane may leave the sediment system by bubble ebullition or diffusion and may contribute to the atmospheric methane pool.

If organic matter survives both aerobic and anaerobic sedimentary remineralization processes, a small portion may become preserved (Berner, 1989; Hedges and Keil, 1995). In marine sediments, preservation typically accounts for ~0.1% of global primary production, although can be greater in areas of high primary production, and allows for an oxygen-rich atmosphere (Berner, 1989). As it becomes buried over time, this organic matter may encounter Earth’s geothermal gradient (~20°C/km) and become thermally altered. Thermal alteration, also known as thermogenesis, breaks down organic matter into oil and light hydrocarbon gases, such as methane, ethane, propane, etc. Although a minor component of the atmospheric methane pool, the thermal and biogenic production of methane may escape the ocean sediments and make it to the atmosphere.



**Fig. 1- 4: Key components of the global carbon cycle with special emphasis on methane. Dashed arrows indicate land processes and solid arrows indicate oceanic processes.**

#### **4.2. Methane sources**

The primary sources of atmospheric methane are wetlands, rice agriculture, ruminant animals, energy production, biomass burning, landfills, termites, ocean and freshwater systems and gas hydrates (Table 1-1). In all these cases, methane is ultimately produced from either the thermogenic or anaerobic biogenic breakdown of organic matter. There are a few other interesting potential sources of methane which are currently under active study. For example, there is some evidence that plants may be involved in an aerobic process of methane formation (Keppler et al., 2006). Also, methane may be produced abiotically in crystalline rocks via a Fischer-Tropsch –type reaction, thought to occur under hydrothermal conditions (Horita and Berndt, 1999). These other sources of methane are usually not included in the methane budget but further study may show that they are important contributors to the global hydrocarbon reservoirs.

#### **4.3. Methane sinks**

The major sinks of atmospheric methane are chemical destruction in the atmosphere, and microbial degradation within sediments, the water column, and soils (Table 1-1). Atmospheric methane has a residence time of about 8 years, twice that of CO<sub>2</sub>, and is subjected to oxidation reactions with hydroxyl radicals to produce formaldehyde (Hobbs, 2000). Microbes within soils consume methane through aerobic oxidation (Mancinelli, 1995).

**Table 1- 1: Atmospheric methane sources and sinks. Terms are ordered by decreasing methane emission amounts.**

<b>Source/sink terms<sup>a</sup></b>	<b>Emissions, Tg CH<sub>4</sub>/yr<sup>a</sup></b>	<b>Consumption, Tg CH<sub>4</sub>/yr<sup>a</sup></b>	<b>Gross production, Tg CH<sub>4</sub>/yr<sup>a</sup></b>
Total wetlands	115	27	142
Swamps	80	12	92
Bogs and tundra	35	15	50
Rice agriculture	100	477	577
Ruminant animals	80	0	80
Biomass burning	55	0	55
Energy	75	18	93
Coal production	35	0	35
Gas production <sup>c</sup>	40	18	58
Landfills	40	22	62
Termites	20	24	44
Ocean, freshwaters	10	75	85
Hydrates	5	5	10
Total sources	500		
Chemical destruction	-450		
Soils	-10	50	40
Total sinks	-460		

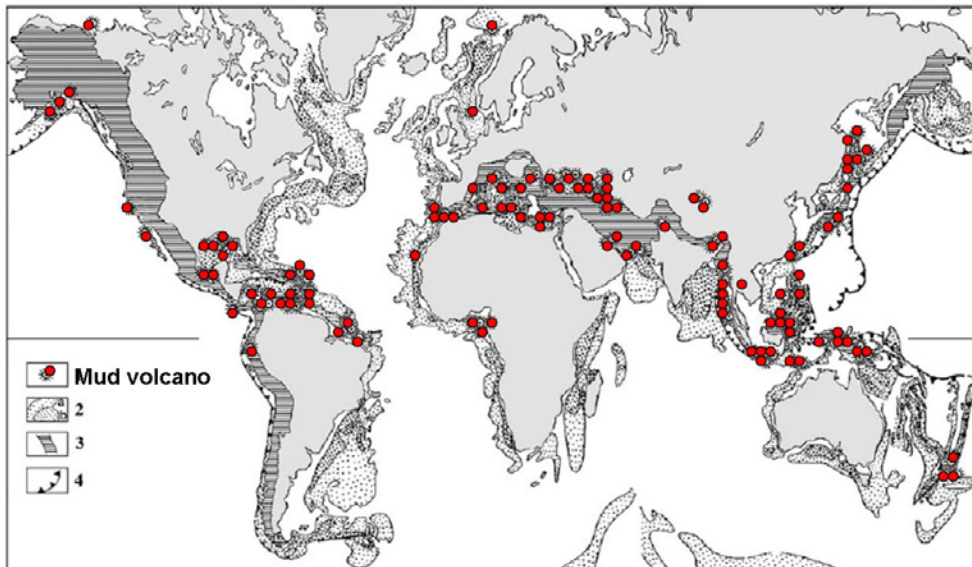
a: after Reeburgh (1996)

b: after Mikaloff Fletcher et al. (2004)

c: Gas production combines venting, flaring, and distribution leaks as introduced in Reeburgh (1996).

## 5. MUD VOLCANOES-a significant methane source?

Mud volcanoes occur where fluidized mud and gases are emitted from Earth's terrestrial surface or its seafloor due to a rapid rate of upward fluid flux (Dimitrov, 2003). The gas entrained within these fluids is mainly methane, although carbon dioxide has also been measured (Dimitrov, 2003). As a direct link from a deep gas source to the atmosphere and oceans, they are thought to be a significant source of atmospheric methane, possibly contributing up to 30 Tg/year (Dimitrov, 2003; Milkov et al., 2003). However, these estimates remain speculative since the flux of methane from mud volcanoes is sporadic and the exact occurrence of mud volcanoes unknown (Fig. 1-5; MacDonald et al., 2000; Dimitrov, 2003; Joye et al., 2005). Of the mud volcanoes studied, they are typically associated with cold seep environments and have a complex association with seep fauna. Because venting rates may be quite high, sedimentary microbial communities may persist in the center of a volcano while other chemosynthetic communities live on the fringes (Roberts and Carney, 1997; de Beer et al., 2006).



**Fig. 1- 5: Worldwide distribution of mud volcanoes. Picture from (Dimitrov, 2003).**

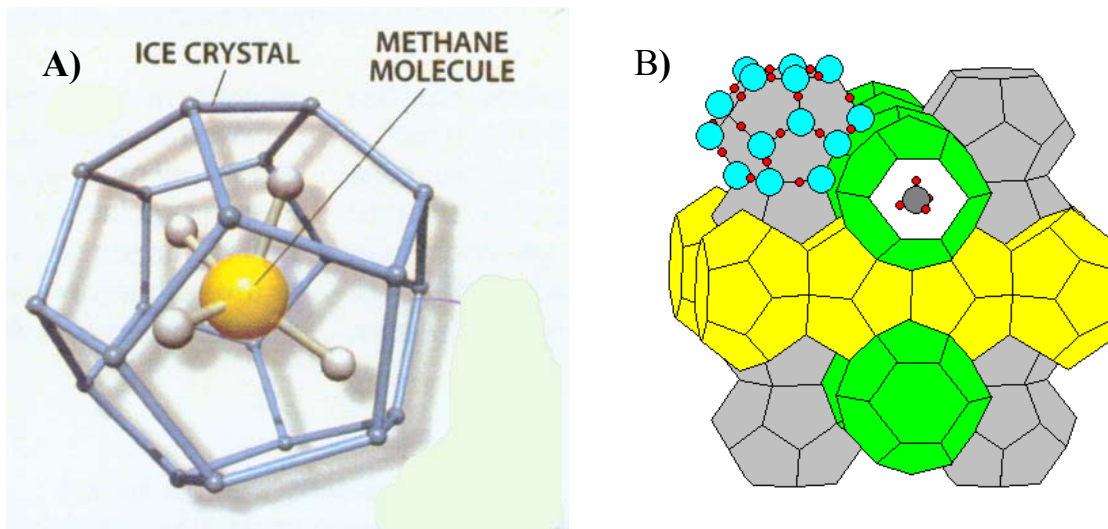
## **6. GAS HYDRATES-the largest methane reservoir**

Natural gas hydrates or clathrates are crystalline ice compounds containing light hydrocarbon gases, primarily methane, CO<sub>2</sub> and H<sub>2</sub>S (Fig. 1-6; Sloan, 1998). Although the term clathrate is more appropriate because it implies a non-stoichiometric gas and water composition, the term hydrate is more common. Hydrates are naturally found worldwide in marine sediments and arctic permafrost. While they are considered a small fraction of the annual atmospheric methane source (Table 1-1), estimates of the amount of methane tied up in hydrate suggest they are the largest reservoir of reduced carbon on Earth. As such, hydrate deposits may be a potential future energy source, geologic hazard, and contributor to climate change.

### **6.1 Global estimates**

Global estimates of the amount of methane contained within worldwide hydrate deposits continue to be revised (Milkov, 2004). In the late 1990s, a consensus estimate of global hydrate-bound methane was accepted to be 10,000 Gt methane carbon ( $2.1 \times 10^{16}$  m<sup>3</sup> methane), with ~95% tied up in marine hydrates and the remainder in arctic permafrost (Kvenvolden, 1988). This is equivalent to a 40-m-thick blanket of methane covering the entire surface of the Earth and twice the amount of carbon contained within the fossil fuel reservoir (Kvenvolden, 1988; Kvenvolden, 1993). More recently, a revised estimate lowered this consensus value to ~500-2500 Gt of methane carbon ( $(1-5) \times 10^{15}$  m<sup>3</sup>) (Milkov, 2004). While these estimates continue to decrease, the abundance of methane within the hydrate reservoir is high.





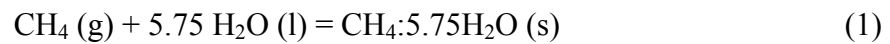
**Fig. 1- 6: General hydrate structures. A) Hydrate structure I (sI) shown with ice crystal lattice enclosing a methane molecule (Suess et al., 1999). B) Detail of hydrate cage sI showing methane and water molecules. Figure from <http://www.uwgb.edu/dutchs/PETROLOGY/Clathrate-0.HTM>**

## 6.2. Structure

Natural gas hydrates are characterized by their crystal structures as either structure I, II, or H (Fig. 1-6). While the hexagonal structure H has only been positively identified in the lab, structures I and II (designated as sI and sII) have been found in many natural environments (Sloan, 1998). sI is a body-centered cubic crystal system that contains 2 small and 6 large cavities within a unit cell. The small cavities are made up of 12 pentagon faces and the large is 12 pentagonal and 2 hexagonal faces. These cavities can be filled with smaller gas molecules such as methane, ethane, carbon dioxide, and hydrogen sulfide. When sI contains pure methane within the cages, its unit cell formula is approximately  $8\text{CH}_4:46\text{H}_2\text{O}$  and has a density of  $0.91\text{g/mL}$ ; these are known as methane hydrates and are typically filled with biogenically produced methane (Matsumoto et al., 2000). Hydrate sII have a diamond cubic crystal system that contains 16 small and 8 large cavities within a unit

cell (not pictured). Although the sII cavities are about the same size as in sI and could contain similar smaller gases, they may be filled with larger gases such as propane and iso-butane. The stoichiometry for sII hydrate is approximately 24gas:136H<sub>2</sub>O. The methane typically enclosed within sII is thermogenic (Sassen et al., 1999; Sassen et al., 2001).

The structural properties of methane hydrate allow the hydrate-bound gas to be much more concentrated than if it were found saturated in water. Considering a full sI hydrate, the equation for hydrate formation is:



where the molecular weight of hydrate is 119.5 g/mol. Pure methane hydrates are thought to have a density of 0.91 g/mL (Sloan, 1998). Therefore, the moles of methane per mL of hydrate is calculated by:

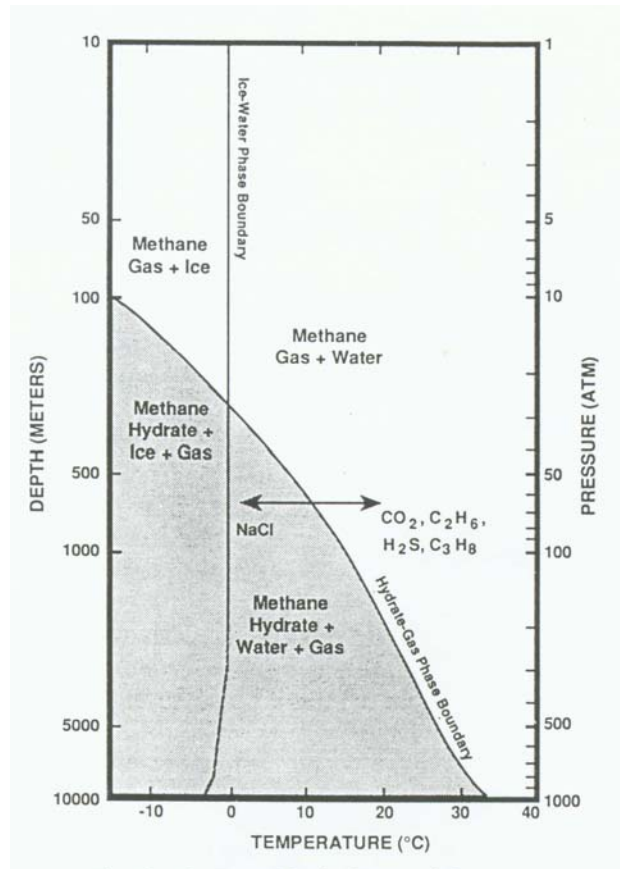
$$\frac{119.5 \text{ g hydrate}}{\text{mol hydrate}} \cdot \frac{\text{mL hydrate}}{0.91 \text{ g hydrate}} \cdot \frac{\text{mol hydrate}}{\text{mol CH}_4} = \frac{131 \text{ mL hydrate}}{\text{mol CH}_4} = \frac{0.008 \text{ mol CH}_4}{\text{mL hydrate}} \quad (2)$$

Using the relationship in equation 2 and PV=nRT at STP, for every mL hydrate, there are 170 mL CH<sub>4</sub> gas (as presented in Kvenvolden, 1993). Likewise, at 1000 meters water depth and 4°C, for every mL hydrate, there are 1.8 mL CH<sub>4</sub> gas or 4470 mM CH<sub>4</sub> gas. In stark contrast to this, saturated dissolved methane at this depth is ~70 mM. This signifies that the trapped methane within the hydrate is 64 times more concentrated than the saturated surroundings alone. This concentrating effect as well as the worldwide occurrence of high pressure and low temperature makes hydrate deposits a significant reservoir of reduced carbon on Earth.

### 6.3. Formation

Hydrates form where methane concentrations exceed the equilibrium concentration between aqueous methane and hydrate (Fig. 1-7). Since the equilibrium concentration

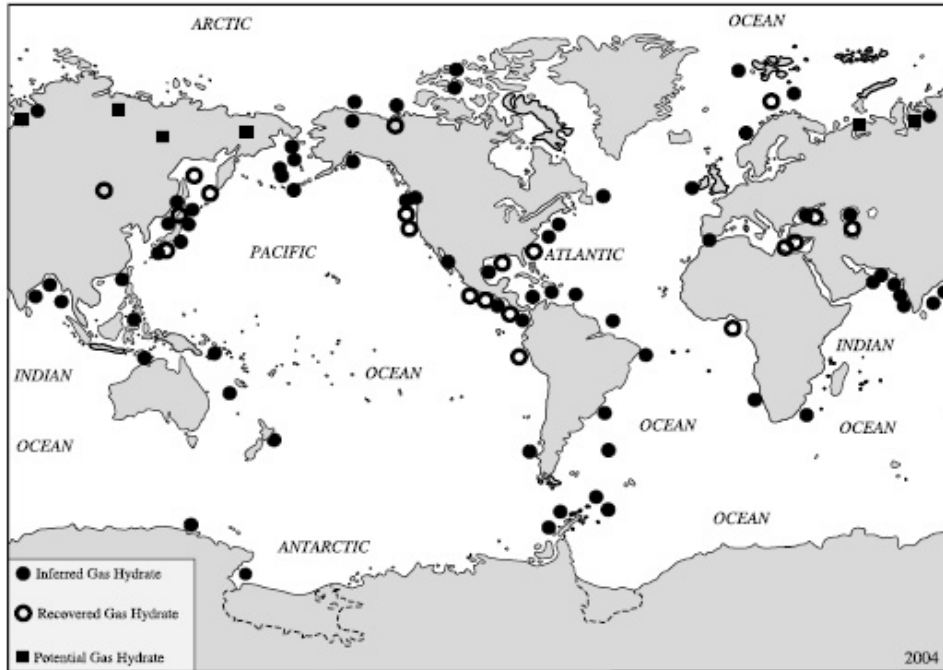
depends on the *in situ* pressure, temperature, and salinity conditions, hydrates typically form where pressures are high, temperatures are low, and moderate salinities are present. In naturally forming oceanic hydrate, pressure is a function of the hydrostatic pressure from the overlying water and sediment column (depending on the location of the hydrate). It can be estimated by multiplying the hydrate depth in meters by 1atm/10m. The temperature of a hydrate is found within a range in which the lower limit is set by the overlying water and sediment temperature and the upper limit is set by the geothermal gradient ( $\sim 20^{\circ}\text{C}/\text{km}$ ). Salt concentrations above seawater values (35psu) will inhibit hydrate formation as salt interacts with water more strongly than the hydrate structure. Hydrates become more stable when in contact with other hydrate forming gases, such as carbon dioxide, ethane, propane, and hydrogen sulfide.



**Fig. 1- 7: Pressure (or depth in ocean) versus temperature plot showing the stability zone for continental shelf oceanic gas hydrates in the shaded region. The addition of salt (NaCl) lowers the stability of hydrate. Whereas, the addition of carbon dioxide (CO<sub>2</sub>), ethane (C<sub>2</sub>H<sub>6</sub>), hydrogen sulfide (H<sub>2</sub>S), and propane (C<sub>3</sub>H<sub>8</sub>) acts to stabilize the hydrate.**

#### 6.4. Worldwide Occurrence

Natural gas hydrates have been found worldwide: in arctic permafrost ~100 meters below the ice and in continental slope sediments where water depths exceed 300 meters (Fig. 1-8). For the majority of natural hydrates, the methane source is biogenic production, but several sites are known to have thermogenically derived gas, such as the Gulf of Mexico, northern Cascadia Margin, and Caspian Sea (Sloan, 1998).

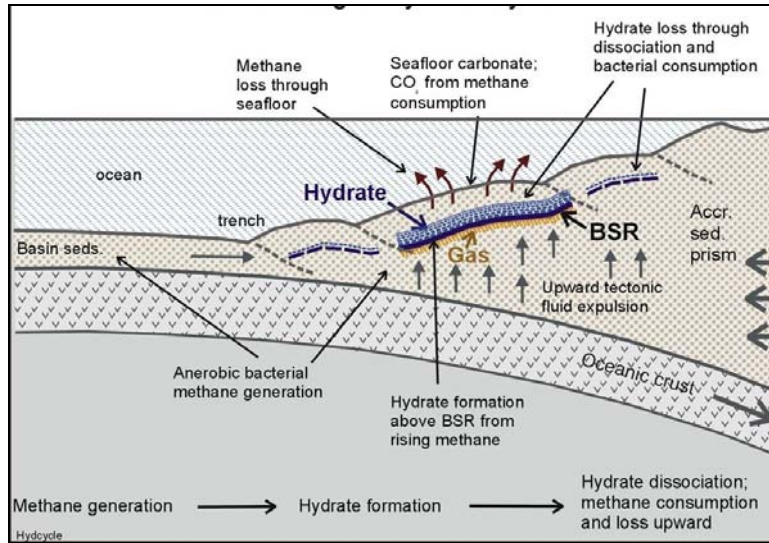


**Fig. 1- 8: Worldwide distribution of gas hydrate deposits. Filled circles are inferred, open circles are recovered and filled squares are potential hydrate deposits. Figure from Kvenvolden and Rogers (2005).**

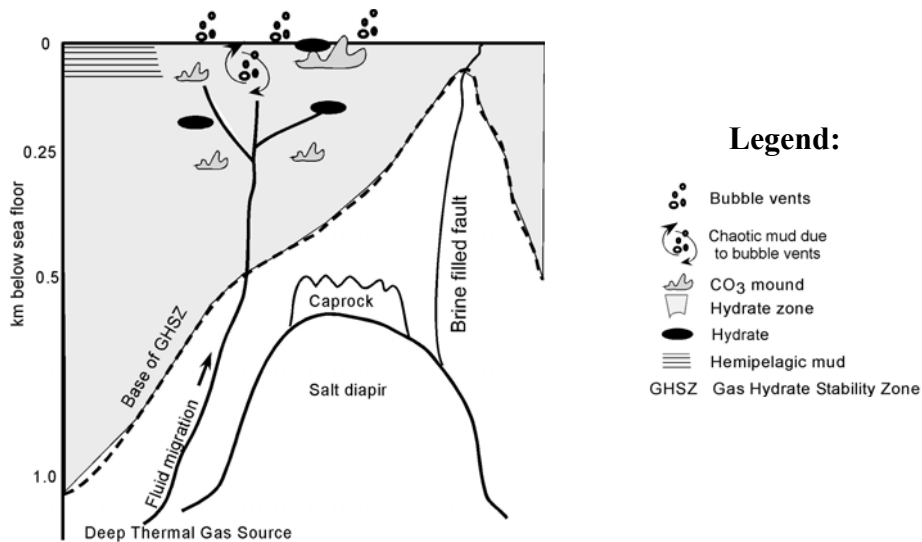
While pressure and temperature are set by natural *in situ* conditions, hydrates formation is limited by the availability of methane. Saturated methane concentrations can be found within the hydrate stability zone (HSZ) by either *in situ* methane production or fluid migration from a deeper source (Paull et al., 1993; Sloan, 1998). Within the HSZ, methanogenesis rates may be high enough at certain sites to form saturated concentrations and precipitate biogenic hydrate (Wellsbury et al., 2000). However, models show that forming hydrate from biogenic methane can only account for a maximum of ~4% hydrate within the sediments (Sloan, 1998). Since biogenic hydrate measured at Hydrate Ridge, southern Cascadia Margin accounts for approximately 15% of sediments, *in situ* production is not the only process occurring (Sloan, 1998). An alternative process could be gas or methane saturated fluid migration from below the HSZ. In this process, fluids that are rich in either thermogenic or

biogenic gases or saturated fluids ascend through the sediment column and exsolve as overlying pressure decreases. Once they reach the base of the HSZ, hydrate will precipitate. These fluids may also ascend through the sediment column via faults that serve as conduits created by sedimentary tectonic activity.

Sedimentary tectonics results from either the movement of plates or salt diapirs. For plates, as one plate subducts under the other, the scraping of sediment builds an accretionary prism that becomes littered with intense faults due to the sediment deformation (Fig. 1-9). An example of such an area is the Cascadia Margin which extends from offshore northern California to British Columbia (Solem et al., 2002; Chapman et al., 2004). For salt diapirs, a density differential is set up between the lower density salt ( $\rho=2.2 \text{ g/cm}^3$ ) that is buried under higher density compacted sediment flows ( $\rho=2.7 \text{ g/cm}^3$ ) and allows the salt to flow upwards through the sediments (Fig. 1-10; Lerche and Petersen, 1995). As these diapirs move upward through the sediment, they cause faults to radiate from them. Salt diapirs may protrude into the shallow sediment regime and form salt-filled sediments or brine pools (Williams and Lerche, 1987; MacDonald et al., 1990b).



**Fig. 1- 9: Convergent margin gas hydrate cycle. BSR is the bottom simulating reflector. Figure courtesy of Ken Grabowski, Naval Research Laboratory.**



**Fig. 1- 10: Passive margin dominated by salt tectonics, example shown in Gulf of Mexico. This conceptual model was conceived by Roger Sassen as unpublished work.**

## **6.5. Significance**

### *6.5.1. Energy resource*

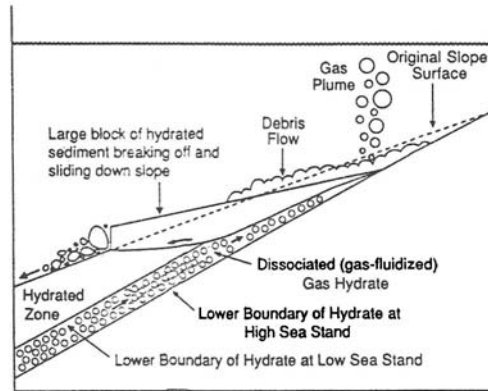
Regardless of variable estimates of methane contained within hydrate, hydrates are a large source of methane gas that is widely distributed around the globe (Kvenvolden, 1988). For this reason, many countries are interested in tapping into the hydrate reservoirs to obtain the methane as an energy resource. Although new technologies are being developed (OTC conference 2006, personal communication), the three principal methods to recover hydrate are thermal stimulation, depressurization, and inhibitor injection (Kvenvolden, 1993). Western Siberia was the first permafrost region to recover methane from hydrate but the operations were very costly and did not proceed (Kvenvolden, 1993 and references therein). Alaska's North Slope oil fields were found to contain hydrates and the first attempt by the United States to tap into these hydrates was reported in April 2003 (NETL, 2003). Operations continue to be costly and environmental repercussions from hydrate recovery unknown.

### *6.5.2. Geologic hazard*

Hydrate deposits are also significant as possible geologic hazards (Kvenvolden, 1993; Lerche and Bagirov, 1998). As either a pressure or temperature change occurs, seafloor deposits may become unstable and dissociate. At the base of the hydrate stability zone, dissociation may form a fluidized layer that can then quickly break off and release a large gas plume and debris flows (Fig. 1-11). For the oil and gas industry whose platform foundations are anchored into the seafloor, the loss of the stable sediment may result in damage to structures and possibly loss of human life (Lerche and Bagirov, 1998). Furthermore,



pipelines resting on the sediments may also be damaged by hydrate instability. Due to hydrates as a significant geologic hazard, the oil and gas industry has devoted research dollars to identifying hydrate occurrence in the seafloor and understand their stability.



**Fig. 1- 11: Hydrate slope instability leading to geologic hazard. Figure from Katz et al. (1999).**

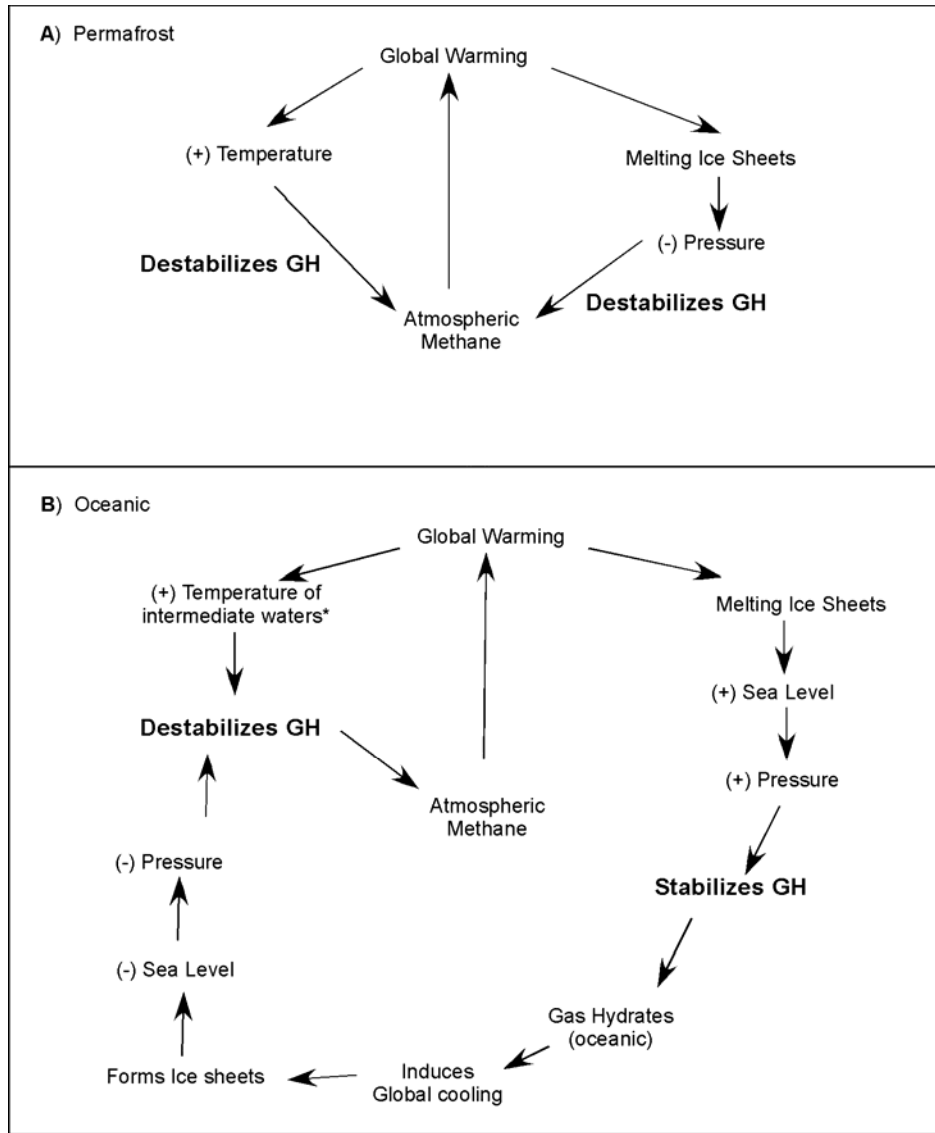
### 6.5.3. Contributor to climate change

If hydrates are destabilized, they could release an enormous amount of the greenhouse gas directly to the atmosphere and contribute to climate change. Although current concentrations of methane have been increasing to the atmosphere, methane is a small contributor to current climate change, as its oceanic emissions are regulated by microbial consumption (Reeburgh, 1996). However, a large release in hydrate-bound methane may bypass oxidation altogether and reach the atmosphere (Kvenvolden, 1993). Studies show that the methane only needs to reach the surface mixed zone (~200m below sea level) to become equilibrated with the atmosphere and negatively affect climate (Brewer et al., 2002). Furthermore, since methane hydrate is buoyant in seawater, it may rise faster than it can dissociate during ascent, reach the surface and directly dissociate to the atmosphere. This was the case when a fishing boat dredged up a ton of hydrate that fizzed on the surface

(Spence et al., 2001). Dissociation during ascent may also be inhibited by hydrates naturally coated in oil and allow oil-coated hydrates and gas bubbles to reach the atmosphere (MacDonald et al., 2002). Additionally, the dissociation of permafrost hydrate may directly inject methane to the atmosphere. Therefore, it is conceivable that hydrate dissociation could be a contributor to climate change.

The mechanism for hydrates role in climate change is complicated by several feedbacks depending on whether permafrost or oceanic hydrates are decomposed (Fig. 1-12). The release of methane from dissociating permafrost hydrate from global warming events may act as a positive feedback to climate change (Fig. 1-12a; Nisbet, 1990). Rising temperatures and resultant melting of the ice sheets will destabilize these hydrates, directly inject methane to the atmosphere, and induce further global warming. The exact magnitude of this positive feedback is unknown.

The oceans contain ~95% of the global hydrate reservoir and their response to changing climate conditions may be more important than the permafrost region (Paull et al., 1991). Since the majority of oceanic hydrates are found in continental shelf and slope water depths, a temperature increase will destabilize hydrate and release methane to the atmosphere (Fig. 1-12b). At the same time, warming will also induce the melting of ice sheets. This water influx to the oceans will increase sea level resulting in an increase in overlying water pressure, stabilizing the oceanic hydrate. Since methane will no longer be released to the atmosphere, this stabilization will induce global cooling that will act as a negative feedback, destabilizing the hydrates, increasing methane concentrations in the atmosphere, and inducing global warming.



**Fig. 1- 12: Model of how global climate affects hydrate deposits in A) Permafrost, as introduced in Nisbet (1990) and B) Oceanic regions as introduced in Paull et al. (1991).**

*Clathrate Gun Hypothesis.* A mechanism for how hydrates affect climate change has been posed as the clathrate gun hypothesis (Kennett et al., 2003). It suggests that an outside climate forcing increased ocean temperatures and destabilized continental shelf hydrates which released an enormous amount of methane directly to the atmosphere and created a

positive feedback to climate warming (Nisbet, 1990; Kennett et al., 2000; Kennett et al., 2003). This warming caused sea levels to rise and retard oceanic hydrate dissociation, which allowed mild interstadial temperatures to resume and the hydrate reservoir to re-establish. The reformation of the hydrates then decreased atmospheric methane concentrations to further induce a cooling trend. This cooling trend then formed so much ice that sea level dropped, released overlying water pressures to oceanic hydrates and triggered a release of methane from the hydrate reservoir yet again initiating a global warming trend.

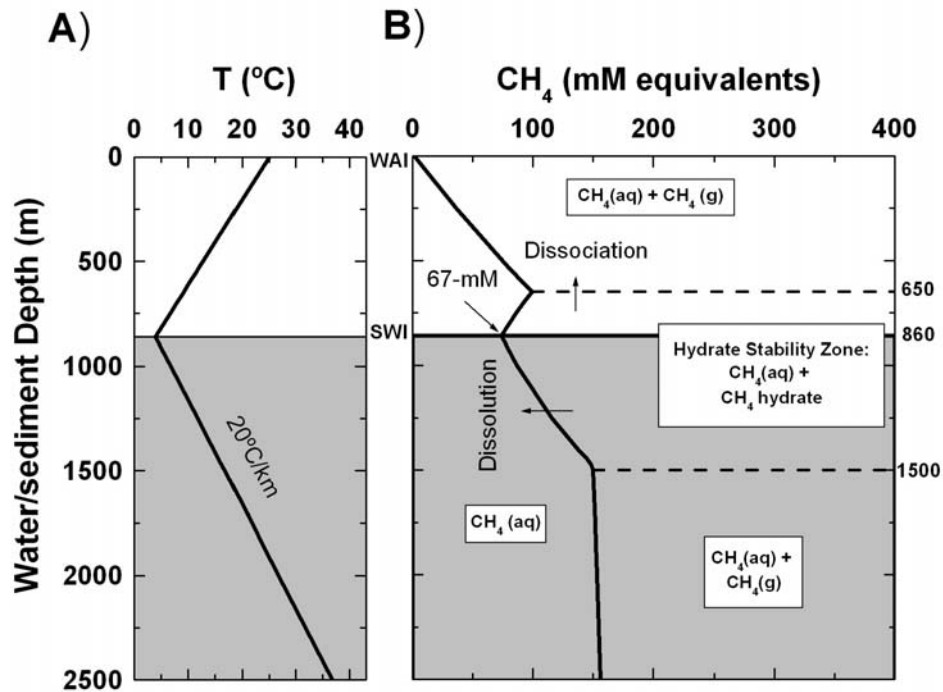
This hypothesis is compelling because several major methane spikes and isotope shifts have occurred in Earth's history. During the late Quarternary (~420,000 years ago), four spikes in atmospheric methane concentrations were measured and found to coincide with the global maxima in atmospheric temperatures and carbon dioxide concentrations (Kennett et al., 2003). At the Paleocene-Eocene thermal maximum, 55 million years ago (Mya), an abrupt carbon isotope excursion exists with one of the largest deep-sea benthic extinctions known (Kennett and Stott, 1991). The carbon isotopic composition of marine carbonates decreased by ~3‰ along with a benthic and planktonic foraminifera isotope change of 2.5-4.5‰ (Kennett and Stott, 1991). The benthic extinction has been attributed to sudden change in ocean circulation, possibly injecting warm waters to deep-sea (Kennett and Stott, 1991). Furthermore, seafloor blow-outs found near the Cretaceous-Tertiary (K-T, 65 Mya) meteorite impact suggest disruption of sea-floor hydrate deposits and subsequent release of this methane to further perturb the ocean-atmosphere system (Max et al., 1999). And finally, detailed isotopic evidence of organic carbon show three negative excursion events of 5-7‰ in the early Jurassic (~180Mya), possibly due to hydrate dissociation (Hesselbo et al., 2000; Kemp et al., 2005). Although several other explanations for these shifts exist, the timing,

rate and magnitude of the carbon isotope excursion are consistent with the release of hydrate (Dickens et al., 1995; Dickens et al., 1997b; Thomas et al., 2002).

#### **6.6. Calculations for the zone of hydrate stability**

In the modern ocean, the hydrate stability zone (HSZ) can be estimated by using thermodynamic models. Using in situ pressure and temperature gradients within such a model, the methane solubility curve was calculated for Barkley Canyon on the Cascadia Margin off the coast of Vancouver Island, British Columbia (Fig. 1-13; Duan and Mao, 2006). At the ocean-atmosphere interface, the resultant solubility curve shows that methane is saturated at dissolved concentrations of 1.2 mM; consistent with other methods of calculating methane solubility (Yamamoto et al., 1976). At greater ocean depths, the solubility concentrations increase due to increasing pressures and decreasing temperatures and the curve shows that methane is only stable in the dissolved and gas phases. At a certain depth, typically around 600 meters below sea level, gaseous methane is no longer thermodynamically favorable and gas hydrate becomes the stable form of methane. This depth defines the upper limit of the hydrate stability zone (dashed line in Fig. 1-13 at 650m). Below this depth, the solubility concentration decreases due to hydrate formation associated with decreasing temperature and increasing pressure. At the sediment-water interface, dissolved methane and hydrate are the only stable forms of methane and are in thermodynamic equilibrium when dissolved concentrations are 67 mM. Below the sediment-water interface, the solubility concentration increases with depth; primarily due to the hydrostatic pressure increase. Concentrations continue to increase until the temperatures associated with the geothermal gradient exceed favorable conditions for hydrate formation. At this depth, hydrate will no longer be stable and gas bubbles form. The depth where this

occurs is the base of the hydrate stability zone. It is important to emphasize that within the hydrate stability zone, gas bubbles and hydrate should not co-exist. If they do, the system is out of thermodynamic equilibrium.



**Fig. 1- 13: Phase diagram along a marine temperature and pressure profile from Barkley Canyon. A) Temperature profile through ocean water/sediment column. Geothermal gradient at this site was assumed to be 20°C/km. B) Phase diagram of methane showing three phases: aqueous CH<sub>4</sub>, gaseous CH<sub>4</sub>, and solid CH<sub>4</sub> hydrate. Methane concentrations are given in mM equivalents. The solid black line represents the maximum methane concentration possible in dissolved phase at thermodynamic equilibrium, estimated using model of Duan and Mao, 2006. The black horizontal dashed lines show the upper and lower depth boundary of the hydrate stability zone (depths in meters given to right of graph). WAI = water atmosphere interface; SWI = sediment water interface.**

Two processes for hydrate decomposition are dissociation and dissolution (Fig. 1-13).

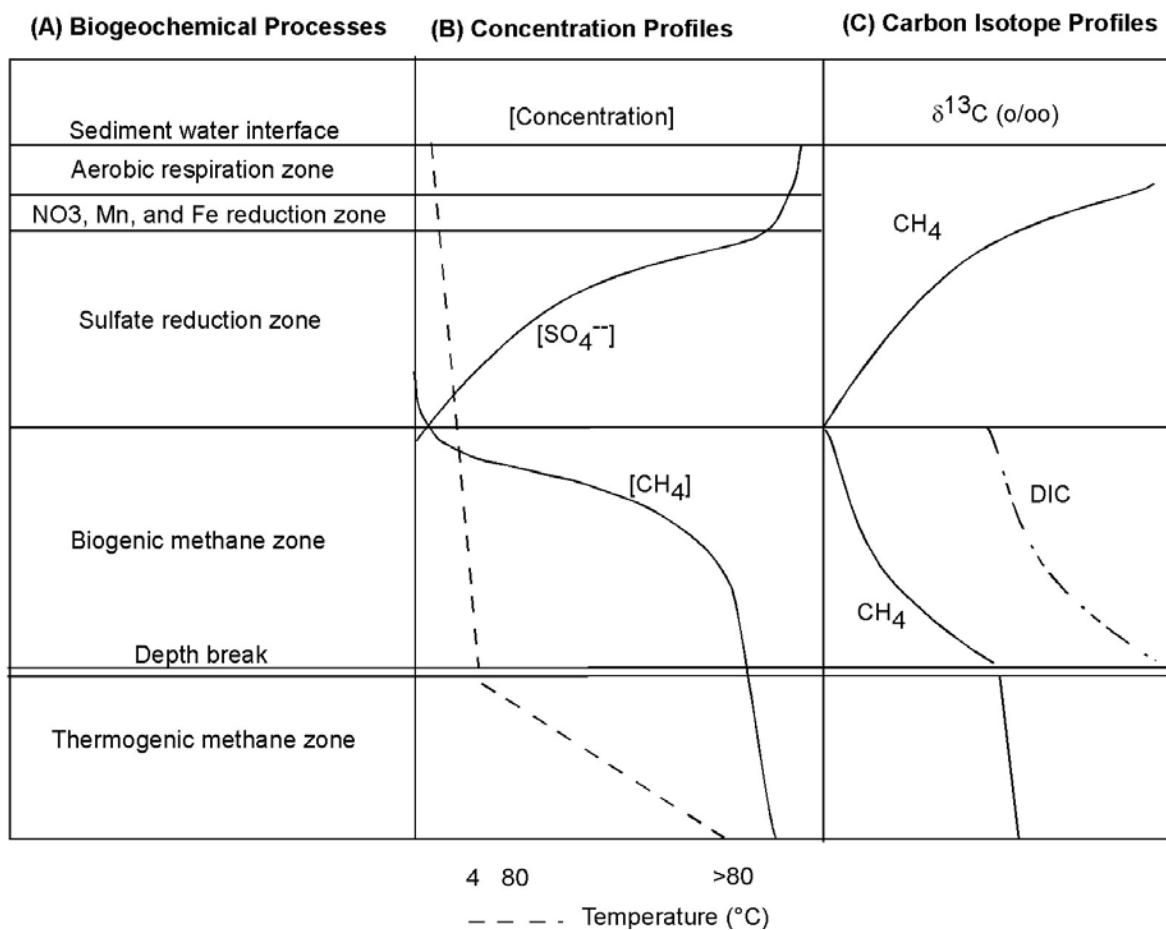
Hydrates dissociate into gas and water when the pressure or temperature change. It is

equivalent to crossing either the lower or upper limit of the hydrate stability zone in Figure 13. This processes was illustrated in oceanic experiments when hydrate was brought from the seafloor to water depths shallower than the upper limit to the HSZ and shown to rapidly bubble (Brewer et al., 2002). Alternatively, hydrate dissolution occurs when surrounding dissolved methane concentrations fall below their solubility. This is equivalent to crossing the vertical solubility concentration line on Figure 13. Although many studies have addressed hydrate decomposition via dissociation, few studies have focused on understanding hydrate dissolution.

## **7. BIOGEOCHEMISTRY**

The study of sedimentary biogeochemistry intimately ties together the interactions between biology, geology, and chemistry. It can be as broad as understanding the interactions between the biosphere, atmosphere, and lithosphere or as focused as understanding the microbial processes that link the carbon and sulfur cycles at a specific location. For the context of this paper, we shall focus on the biogeochemical processes that link the carbon and sulfur cycles in shallow marine sediments.

Marine sediments are an active environment for the remineralization of organic matter via biogeochemical processes. Processes such as microbial respiration oxidize organic matter through a series of energetically favorable diagenetic reactions that alter particles after deposition to the sediment-water interface (Froelich et al., 1979). These reactions can be characterized into five microbial zones and illustrated with depth dependent concentration and stable carbon isotope ratio profiles (Fig. 1-14).



**Fig. 1- 14: Diagenetic reactions: A) zones of biogeochemical processes (discussed in section 7.1.), B) generic concentration profiles for sulfate and methane (discussed in section 7.2.1.), and C) generic carbon stable isotope compositions of both methane and dissolved inorganic carbon (DIC) associated with biogeochemical processes (discussed in section 7.2.2.).**



## 7.1. Zones of biogeochemical processes

### 7.1.1. Aerobic respiration zone

Near the sediment water interface where oxygen is readily available, aerobic respiration is the dominant process:



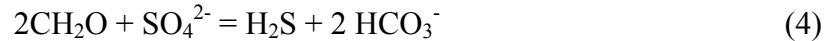
Where  $\text{CH}_2\text{O}$  is the stoichiometric representation of general organic matter and  $\text{CO}_2$  is predominantly found in the bicarbonate form at *in situ* pH. The sediment section where this process occurs is known as the aerobic respiration (AR) zone (Fig. 1-14a). The depth of this zone is typically a few mm to cm, depending on the oxygen demand.

### 7.1.2. Nitrate, manganese, and iron reduction zone

Below the AR zone where oxygen is exhausted, organic carbon remineralization proceeds through the reduction of nitrate ( $\text{NO}_3^-$ ), manganese (as  $\text{MnO}_2$ ), and iron (as  $\text{Fe}(\text{OH})_3$ ). Where these molecules are present is known as the  $\text{NO}_3$ ,  $\text{MnO}_2$ , and  $\text{Fe}(\text{OH})_3$  (NMI) zone (Fig. 1-14a). The depth of this zone is shallow.

### 7.1.3. Sulfate reduction zone

Below the NMI zone, sulfate reduction takes over as the dominate process for organic carbon remineralization (Fig. 1-14a). Sulfate reduction is bacterially mediated and quantitatively converts sulfate to sulfide through the oxidation of organic matter by the following net equation:



Where  $\text{SO}_4^{2-}$  is dissolved sulfate,  $\text{H}_2\text{S}$  is hydrogen sulfide, and  $\text{HCO}_3^-$  is bicarbonate. Although this net equation is written with the general representation for organic matter, sulfate reducers do not break down such complex molecules. Instead, they rely on

fermentative organisms to break down complex molecules into smaller competitive substrates, such as acetate and hydrogen. In turn, sulfate reducers consume hydrogen, keeping the concentrations low enough not to inhibit fermentors. This area in the sediment where sulfate reduction is occurring is known as the sulfate reduction (SR) zone (Fig. 1-14a). The depth of this zone depends greatly on the rate of sulfate reduction. In highly productive coastal zones, the depth can be 5-10cm. In deep ocean sediments with little to no organic carbon input, these depths may be as great as hundreds of meters and may never reach sulfate depletion.

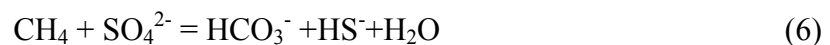
#### 7.1.4. Biogenic methane production zone

Below the SR zone, where sulfate concentrations reach zero, organic matter remineralization proceeds via methane production (Fig. 1-14a). This process is carried out by methanogens who reduce carbon dioxide following this equation:



where CH<sub>4</sub> is methane. The generation of biogenic methane occurs within the biogenic methane production (MP) zone and results in increasing methane concentrations at greater depths within this zone. The depth of this zone is dependent upon a continued source of organic carbon and ideal temperatures for biogenic methane production.

At the interface depth between the SR and MP zones, where sulfate and methane concentrations are low, anaerobic methane oxidation (AMO) may occur via the following net equation:



Geochemical evidence suggested that this AMO zone is a major control on methane release to the atmosphere, preventing ~80% of the methane from reaching the sediment-water

interface (Reeburgh et al., 1993; Reeburgh, 1996). However, the organisms and mechanisms for this process remained elusive. It was hypothesized that a consortium of sulfate reducers and methanogens, working in reverse, carried out the above process (Hoehler et al., 1994). In close proximity, the methanogen community would oxidize methane and produce hydrogen while the sulfate reducer community would keep the hydrogen concentrations to low levels. Microscopic evidence now suggests a close spatial association between methanogen-like archaea and sulfate reducing bacteria in methane-rich sediments and corroborates the consortium hypothesis (Boetius et al., 2000).

#### *7.1.5. Thermogenic methane production zone*

Below the zone of biogenic methane production, buried organic matter in contact with Earth's geothermal gradient will decompose into methane, other light hydrocarbon gases and possibly oil. This zone is known as the thermogenic methane (TM) zone (Fig. 1-14a). Although this methane is termed thermogenic, it still has an original biogenic source and should not be confused with abiogenic methane. Abiogenic methane is methane that has been produced by any process that does not involve organic precursors (Sherwood Lollar et al., 1993) such as when magma cools or in hydrothermal systems (Sherwood Lollar et al., 2002).

## **7.2. Methods used in biogeochemistry**

### *7.2.1. Concentration depth gradients*

The microbial processes described above can be assessed by following the down-core trend in products or reactants of specific reactions (Fig. 1-14b). For example, sulfate concentrations will decrease with depth during sulfate reduction. Likewise, methane concentrations will be low until sulfate reduction has ceased and methanogenesis begins.

Although this is a qualitative assessment of sulfate reduction and methanogenesis, modeling techniques can help determine rates of processes (described in diagenetic model section below).

### 7.2.2. Stable carbon isotope trends

The stable carbon isotope composition ( $\delta^{13}\text{C}$ ) of certain compounds can be used to elucidate the source of the compound or processes that have occurred. Stable isotopes are powerful tools due to the kinetic isotope effect that results when biogenic processes produce a compound. Carbon exists in two principal isotopic forms,  $^{12}\text{C}$  and  $^{13}\text{C}$ , where the lighter isotope is 100 times more abundant and slightly more kinetically reactive than  $^{13}\text{C}$  due to its smaller mass. When biogenic processes take up a compound the kinetic isotope effect causes a mass dependent isotopic fractionation that results in the preferential uptake of  $^{12}\text{C}$ , causing the products to be more depleted in  $^{13}\text{C}$  than the reactants. The ratios are compared between a sample and standard by expressing the relative change in  $^{13}\text{C}$  using the conventional  $\delta$  notation with units of per mil, ‰:

$$\delta^{13}\text{C}(\text{‰}) = \left( \frac{R_{\text{sample}} - R_{\text{standard}}}{R_{\text{standard}}} \right) \times 1000 \quad (7)$$

where  $R = ^{13}\text{C}/^{12}\text{C}$  for both the sample and the Peedee Belemnite standard.

These isotope trends can be used to distinguish between biogenic and thermogenic methane. For the case of biogenic methane, the resultant methane is depleted in  $^{13}\text{C}$  relative to the original organic matter. Alternatively, thermogenic methane or methane produced by the thermal decomposition of organic carbon, has little or no isotope fractionation associated with it and so the resulting carbon isotopic signature of methane is similar to that of the parent organic carbon. Therefore, biogenic methane can be distinguished from thermogenic methane because it is more depleted in  $^{13}\text{C}$  (Bernard et al., 1978)

Methanogenesis and anaerobic methane oxidation can be further understood by measuring the down-core variation in the stable carbon isotope composition of both the dissolved CH<sub>4</sub> and the dissolved inorganic carbon (DIC). Within the methane production zone and assuming methanogenesis proceeds via the reduction of DIC, the DIC pool will become progressively more enriched in <sup>13</sup>C down-core. The produced methane will be depleted in <sup>13</sup>C as much as 95‰, as determined by the fractionation factor for methanogenesis (Whiticar, 1999). As the reactant pool becomes more enriched in <sup>13</sup>C down-core, the methane also becomes more enriched in <sup>13</sup>C (Fig. 1-14c). Anaerobic methane oxidation will result in the methane pool becoming more enriched in <sup>13</sup>C, as the microbes preferentially uptake <sup>12</sup>C, as you move up through the AMO zone (Fig. 1-14c).

### 7.2.3. Diagenetic model

Diagenesis refers to the sum total of processes (physical, chemical, and biological) that alter particles after deposition to the sediment-water interface (Berner, 1980). For our purposes, the “particles” are chemical constituents dissolved in the sedimentary pore-fluids, such as sulfate and methane. The only processes altering the chemical constituents are chemical diffusion, advection, and microbial consumption or production. These processes can therefore be followed using a diffusion-advection-reaction diagenetic model as illustrated in the following equation:

$$\frac{dC}{dt} = D_s \cdot \frac{d^2C}{dx^2} - \omega \cdot \frac{dC}{dx} \pm R \quad (8)$$

where C is the concentration of a chemical constituent, t is time, D<sub>s</sub> is the molecular diffusion coefficient for the constituent at appropriate pressures, temperatures, and salinity, x is the vertical sediment depth where the constituent was measured, ω is the sediment advection rate defined by the sedimentation rate, and R is any reaction that may produce (+R) or consume (-

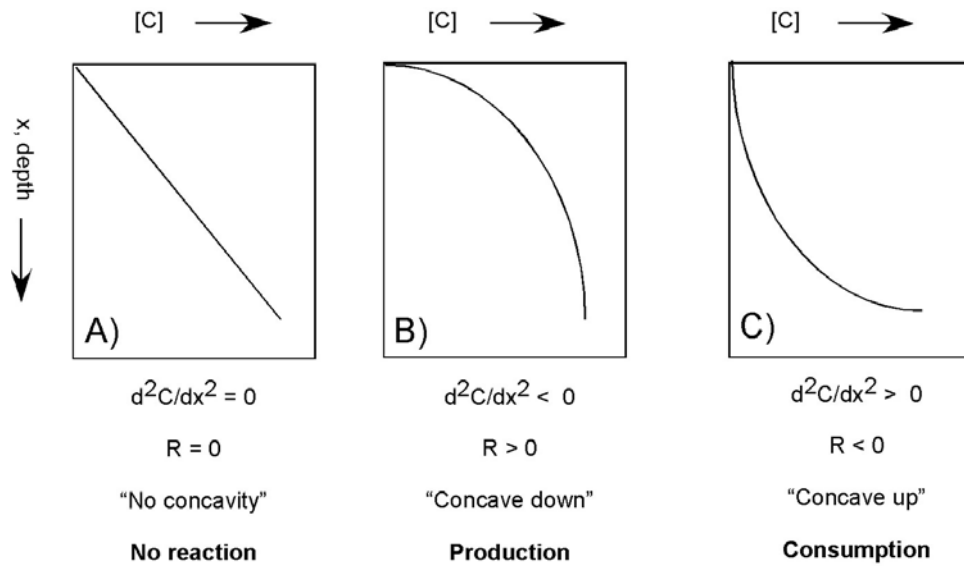
R) the constituent. By stating several assumptions and knowing the diffusion coefficient and sedimentation rate for a particular constituent, this equation will allow the qualitative determination of processes affecting the constituent from the down-core concentration and isotope profiles. This equation can further be solved to calculate the reactions rates. Assumption implicit in equation 8 are as follows: steady state ( $dC/dt = 0$ ), no compaction during sedimentation, no change in diffusion coefficient with depth, all concentration gradients are vertical and not horizontal, and sediment deposition and molecular diffusion are the only significant transport processes (i.e., ignoring bioturbation, bioirrigation, bubble transport, sediment mixing by wind or currents, and no forced advection due to groundwater intrusion).

In practice, the diagenetic model can be used to determine the processes affecting the chemical constituents by looking at the shape of the concentration distribution down-core. Consider the diagenetic equation (equation 8) for an ion dissolved in pore fluids. Assuming steady state, the equation shows that diffusion plus advection equal the reaction. Since diffusion dominates the transport of ions in pore fluids, the advection term can be eliminated. The simplified diagenetic equation then becomes:

$$-D_s \cdot \frac{d^2C}{dx^2} = R \quad (9)$$

Therefore, by knowing the change in concentration with depth, you can determine if R is 0, positive, or negative; which respectively means it is controlled by diffusion, production, or consumption (Fig. 1-15). If there is no reaction ( $R=0$ ), the shape of the down-core concentration profile would be linear. If the reaction term is dominated by production, the shape would be concave-down. Likewise, if the reaction is due to consumption, the profile would be concave-up (Fig. 1-15c). Therefore, the concavity of the profiles of sulfate and

methane concentrations can be used to illustrate biogeochemical processes such as sulfate reduction, methanogenesis, or anaerobic methane oxidation.



**Fig. 1- 15: Concentration profile results of the diagenetic equation for A) no reaction, B) production, and C) consumption.**

## 8. REFERENCES

- Aharon P. and Fu B. (2000) Microbial sulfate reduction rates and sulfur and oxygen isotope fractionations at oil and gas seeps in deepwater Gulf of Mexico. *Geochimica et Cosmochimica Acta* **64** (2), 233-246.
- Arvidson R. S., Morse J. W., and Joye S. B. (2004) The sulfur biogeochemistry of chemosynthetic cold seep communities, Gulf of Mexico, USA. *Marine Chemistry* **87**, 97-119.
- Bernard B. B., Brooks J. M., and Sackett W. M. (1978) Light hydrocarbons in recent Texas Continental Shelf and Slope sediments. *Journal of Geophysical Research* **83** (C8), 4053-4061.
- Berner R. A. H. D. Holland (1980) *Early Diagenesis: A theoretical approach*. Princeton University Press, Princeton.
- Berner R. A. (1989) Biogeochemical cycles of carbon and sulfur and their effect on atmospheric oxygen over Phanerozoic time. *Palaeogeography. Palaeoclimatology. Palaeoecology*. **73**, 97-122.
- Boetius A., Ravensschlag K., Schubert C. J., Rickert D., Widdel F., Gieseke A., Amann R., Jorgensen B. B., Witte U., and Pfannkuche O. (2000) A marine microbial consortium apparently mediating anaerobic oxidation of methane. *Nature* **407**, 623-626.
- Bohrmann G., Greinert J., Suess E., and Torres M. E. (1998) Authigenic carbonates from the Cascadia subduction zone and their relation to gas hydrate stability. *Geology* **26** (7), 647-650.
- Brewer P. G., Paull C. K., Peltzer E. T., Ussler III W., Rehder G., and Friederich G. (2002) Measurements of the fate of gas hydrates during transit through the ocean water column. *Geophysical Research Letters* **29** (22), 38-1 to 38-4.
- Brooks J. M., Kennicutt II M. C., Fisher C. R., Macko S. A., Cole K., Childress J. J., Bidigare R. R., and Vetter R. D. (1987) Deep sea hydrocarbon seep communities: evidence for energy and nutritional carbon sources. *Science* **238**, 1138-1142.



- Cary C. S., Fisher C. R., and Felbeck H. (1988) Mussel growth supported by methane as sole carbon and energy source. *Science* **240**, 78-80.
- Chapman N. R., Pohlman J., Coffin R., Chanton J. P., and Lapham L. L. (2004) Thermogenic Gas Hydrates in the Northern Cascadia Margin. *EOS, Transactions, American Geophysical Union* **85** (38), 361.
- Childress J. J., Fisher C. R., Brooks J. M., Kennicutt II M. C., Bidigare R. R., and Anderson A. E. (1986) A methanotrophic marine molluscan (bivalvia, mytilidae) symbiosis: mussels fueled by gas. *Science* **233**, 1306-1308.
- Cragg B. A., Parkes R. J., Fry J. C., Weightman A. J., Rochelle P. A., and Maxwell J. R. (1996) Bacterial populations and process in sediments containing gas hydrates (ODP Leg 146: Cascadia Margin). *Earth and Planetary Science Letters* **139**, 497-507.
- de Beer D., Sauter E. J., Niemann H., Kaul N., Foucher J. P., Witte U., Schluter M., and Boetius A. (2006) In situ fluxes and zonation of microbial activity in surface sediments of the Hakon Mosby Mud Volcano. *Limnology and Oceanography* **51** (3), 1315-1331.
- Dickens G. R., O'Neil J. R., Rea D. K., and Owen R. M. (1995) Dissociation of oceanic hydrate as a cause of the carbon-isotope excursion at the end of the Paleocene. *Paleoceanography* **10**, 965-971.
- Dickens J. R., Castillo M. M., and Walker J. C. G. (1997) A blast of gas in the latest Paleocene: Simulating first-order effects of massive dissociation of oceanic methane hydrate. *Geology* **25** (3), 259-262.
- Dimitrov L. I. (2003) Mud volcanoes- a significant source of atmospheric methane. *Geo-Marine Letters* **23**, 155-161.
- Duan Z. and Mao S. (2006) A thermodynamic model for calculating methane solubility, density, and gas phase composition of methane-bearing aqueous fluids from 273 to 523 K and from 1 to 2000 bar. *Geochimica et Cosmochimica Acta* **70**, 3369-3386.
- Fisher C. R., Urcuyo I. A., Simpkins M. A., and Nix E. (1997) Life in the slow lane: Growth and longevity of cold-seep Vestimentiferans. *Marine Ecology* **18** (1), 83-94.

- Formolo M. J., Lyons T. W., Zhang C., Kelley C. A., Sassen R., Horita J., and Cole D. R. (2004) Quantifying carbon sources in the formation of authigenic carbonates at gas hydrate sites in the Gulf of Mexico. *Chemical Geology* **205**, 253-264.
- Froelich P. N., Klinkhammer G. P., Bender M. L., Luedtke N. A., Heath G. R., Cullen D., Dauphin P., Hammond D., Hartman B., and Maynard V. (1979) Early oxidation of organic matter in pelagic sediments of the eastern equatorial Atlantic: suboxic diagenesis. *Geochimica et Cosmochimica Acta* **43**, 1075-1090.
- Hedges J. I. and Keil R. G. (1995) Sedimentary organic matter preservation: an assessment and speculative synthesis. *Marine Chemistry* **49**, 81-115.
- Hesselbo S. P., Grocke D. R., Jenkyns H. C., Bjerrum C. J., Farrimond P., Morgans Bell H. S., and Green O. R. (2000) Massive dissociation of gas hydrate during a Jurassic oceanic anoxic event. *Nature* **406**, 392-395.
- Hobbs P. V. (2000) *Introduction to atmospheric chemistry*. Cambridge University Press, Cambridge.
- Hoehler T. M., Alperin M. J., Albert D. B., and Martens C. S. (1994) Field and laboratory studies of methane oxidation in an anoxic marine sediment: Evidence for a methanogen-sulfate reducer consortium. *Global Biogeochemical Cycles* **8** (4), 451-463.
- Horita J. and Berndt M. E. (1999) Abiogenic methane formation and isotopic fractionation under hydrothermal conditions. *Science* **285**, 1055-1057.
- Joye S. B., Boetius A., Orcutt B. N., Montoya J. P., Schulz H. N., Erickson M. J., and Lugo S. K. (2004) The anaerobic oxidation of methane and sulfate reduction in sediments from Gulf of Mexico cold seeps. *Chemical Geology* **205**, 219-238.
- Joye S. B., MacDonald I. R., Montoya J. P., and Peccini M. (2005) Geophysical and geochemical signatures of Gulf of Mexico seafloor brines. *Biogeosciences* **2**, 295-309.
- Katz M. E., Pak D. K., Dickens G. R., and Miller K. G. (1999) The source and fate of massive carbon input during the Latest Paleocene Thermal Maximum. *Science* **286**, 1531-1533.

- Kemp D. B., Coe A. L., Cohen A. S., and Schwark L. (2005) Astronomical pacing of methane release in the Early Jurassic period. *Nature* **437**, 396-399.
- Kennett J. P., Cannariato K. G., Hendy I. L., and Behl R. J. (2000) Carbon isotopic evidence for methane hydrate instability during quaternary interstadials. *Science* **288**, 128-133.
- Kennett J. P., Cannariato K. G., Hendy I. L., and Behl R. J. (2003) *Methane hydrates in Quaternary climate change: The clathrate gun hypothesis*. American Geophysical Union, Washington, DC.
- Kennett J. P. and Stott L. D. (1991) Abrupt deep-sea warming, palaeoceanographic changes and benthic extinctions at the end of the Palaeocene. *Nature* **353**, 225-229.
- Kennicutt II M. C., Brooks J. M., Bidigare R. R., Fay R. R., Wade T. L., and McDonald T. J. (1985) Vent-type taxa in a hydrocarbon seep region on the Louisiana slope. *Nature* **317**, 351-353.
- Kennicutt II M. C., Burke Jr. R. A., MacDonald I. R., Brooks J. M., Denoux G. J., and Macko S. A. (1992) Stable isotope partitioning in seep and vent organisms: chemical and ecological significance. *Chemical Geology* **101**, 293-310.
- Keppler F., Hamilton J. T. G., Brab M., and Rockmann T. (2006) Methane emissions from terrestrial plants under aerobic conditions. *Nature* **439** (12 January), 187-191.
- Kvenvolden K. A. (1988) Methane hydrate-a major reservoir of carbon in the shallow geosphere? *Chemical Geology* **71**, 41-51.
- Kvenvolden K. A. (1993) Gas hydrates-geological perspective and global change. *Reviews of Geophysics* **31**, 173-187.
- Kvenvolden K. A. and Rogers B. W. (2005) Gaia's breath-global methane exhalations. *Marine and Petroleum Geology* **22**, 579-590.
- Lelieveld J., Crutzen P. J., and Dentener F. J. (1998) Changing concentration, lifetime and climate forcing of atmospheric methane. *Tellus* **50B**, 128-150.
- Lerche I. and Bagirov E. (1998) Guide to gas hydrate stability in various geological settings. *Marine and Petroleum Geology* **15** (5), 427-437.

- Lerche I. and Petersen K. (1995) *Salt and sediment dynamics*. CRC Press, Boca Raton.
- MacDonald I. R., Boland G. S., Baker J. S., Brooks J. M., Kennicutt II M. C., and Bidigare R. R. (1989) Gulf of Mexico hydrocarbon seep communities. *Marine Biology* **101**, 235-247.
- MacDonald I. R., Buthman D. B., Sagar W. W., Peccini M. B., and Guinasso Jr N. L. (2000) Pulsed oil discharge from a mud volcano. *Geology* **28** (10), 907-910.
- MacDonald I. R., Guinasso Jr N. L., Ackleson S. G., Amos J. F., Duckworth R., Sassen R., and Brooks J. M. (1993) Natural oil slicks in the Gulf of Mexico visible from space. *Journal of geophysical research* **98** (C9), 16351-16364.
- MacDonald I. R., Leifer I., Sassen R., Stine P., Mitchell R., and Guinasso Jr N. L. (2002) Transfer of hydrocarbons from natural seeps to the water column and atmosphere. *Geofluids* **2** (95-107).
- MacDonald I. R., Reilly II J. F., Guinasso Jr N. L., Brooks J. M., Carney R. S., Bryant W. A., and Bright T. J. (1990) Chemosynthetic mussels at a brine-filled pockmark in the northern Gulf of Mexico. *Science* **248**, 1096-1099.
- Mancinelli R. L. (1995) The regulation of methane oxidation in soil. *Annual Review of Microbiology* **49**, 581-605.
- Matsumoto R., Uchida T., Waseda A., Uchida T., Takeya S., Hirano T., Yamada K., Maeda Y., and Okui T. (2000) 2. Occurrence, structure, and composition of natural gas hydrate recovered from the Blake Ridge, Northwest Atlantic. In *Proceedings of the Ocean Drilling Program, Scientific Results*, Vol. 164 (ed. C. K. Paull, R. Matsumoto, P. J. Wallace, and W. P. Dillon).
- Max M. D., Dillon W. P., Nishimura C., and Hurdle B. G. (1999) Sea-floor methane blow-out and global firestorm at the K-T boundary. *Geo-Marine Letters* **18**, 285-291.
- Milkaloff Fletcher S. E., Tans P. P., Bruhwiler L. M., Miller J. B., and Heimann M. (2004) CH<sub>4</sub> sources estimated from atmospheric observations of CH<sub>4</sub> and its <sup>13</sup>C/<sup>12</sup>C isotopic ratios: 1. Inverse modeling of source processes. *Global Biogeochemical Cycles* **18** (GB4004, doi.1029/2004GB002223).

- Milkov A. V. (2004) Global estimates of hydrate-bound gas in marine sediments: how much is really out there? *Earth-Science Reviews* **66**, 183-197.
- Milkov A. V., Sassen R., Apanasovich T. V., and Dadashev F. G. (2003) Global gas flux from mud volcanoes: A significant source of fossil methane in the atmosphere and the ocean. *Geophysical Research Letters* **30** (2), doi: 10.1029/2002GL016358.
- National Energy Technology Laboratory. (2003) Drilling of U.S.'s First Hydrate Well Underway on North Slope Using Anadarko Petroleum's Innovative "Arctic Platform". [http://www.netl.doe.gov/publications/press/2003/tl\\_arcticplatform.html](http://www.netl.doe.gov/publications/press/2003/tl_arcticplatform.html).
- Nikolaus R., Ammerman J. W., and MacDonald I. R. (2003) Distinct pigmentation and trophic modes in *Beggiatoa* from hydrocarbon seeps in the Gulf of Mexico. *Aquatic Microbial Ecology* **32**, 85-93.
- Nisbet E. G. (1990) The end of the ice age. *Canadian Journal of Earth Sciences* **27**, 148-157.
- Paull C. K., Ussler III W., and Borowski W. S. (1993) Sources of biogenic methane to form marine gas hydrates: In situ production or upward migration? *Department of Energy's Office of Scientific and Technical Information*  
[http://www.osti.gov/energycitations/product.biblio.jsp?osti\\_id=10185837](http://www.osti.gov/energycitations/product.biblio.jsp?osti_id=10185837).
- Paull C. K., Ussler W., and Dillon W. P. (1991) Is the extent of glaciation limited by marine gas-hydrates? *Geophys. Res. Lett.* **18**, 432-434.
- Petit J. R., Jouzel J., Raynaud D., Barkov N. I., Barnola J. M., Basile I., Bender M. L., Chappellaz J., Davis M., Delaygue G., Delmotte M., Kotlyakov V. M., Legrand M., Lipenkov V. Y., Lorius C., Pepin L., Ritz C., Saltzman E., and Stievenard M. (1999) Climate and atmospheric history of the past 420,000 years from the Vostok ice core, Antarctica. *Nature* **399**, 429-436.
- Reeburgh W. S. M. E. Lidstrom and F. R. Tabita (1996) *"Soft spots" in the global methane budget*. Kluwer Academic Publishers, Intercept, Andover, UK.
- Reeburgh W. S., Whalen S. C., and Alperin M. J. (1993) The role of methylotrophy in the global methane budget. In *Microbial growth on C1 compounds* (ed. J. C. Murrell and D. P. Kelly), pp. 1-14. Intercept Ltd.

- Roberts H. H. and Aharon P. (1994) Hydrocarbon-derived carbonate buildups of the northern Gulf of Mexico continental slope: A review of submersible investigations. *Geo-Marine Letters* **14**, 135-148.
- Roberts H. H. and Carney R. S. (1997) Evidence of episodic fluid, gas and sediment venting on the Northern Gulf of Mexico Continental Slope. *Economic Geology* **92**, 863-879.
- Sassen R., Joye S., Sweet S. T., DeFreitas D. A., Milkov A. V., and MacDonald I. R. (1999) Thermogenic gas hydrates and hydrocarbon gases in complex chemosynthetic communities, Gulf of Mexico continental slope. *Organic Geochemistry* **30**, 485-497.
- Sassen R., Roberts H. H., Carney R., Milkov A. V., DeFreitas D. A., Lanoil B., and Zhang C. (2004) Free hydrocarbon gas, gas hydrate, and authigenic minerals in chemosynthetic communities of the northern Gulf of Mexico continental slope: relation to microbial processes. *Chemical Geology* **205**, 195-217.
- Sassen R., Sweet S. T., Milkov A. V., DeFreitas D. A., and Kennicutt II M. C. (2001) Thermogenic vent gas and gas hydrate in the Gulf of Mexico slope: Is gas hydrate decomposition significant? *Geology* **29** (2), 107-110.
- Schlesinger W. H. (1997) *Biogeochemistry: An analysis of global change*. Academic Press, San Diego.
- Sherwood Lollar B., Frapre S. K., Weise S. M., Fritz P., Macko S. A., and Welhan J. A. (1993) Abiogenic methanogenesis in crystalline rocks. *Geochimica et Cosmochimica Acta* **57**, 5087-5097.
- Sherwood Lollar B., Westgate T. D., Ward J. A., Slater G. F., and Lacrampe-Couloume G. (2002) Abiogenic formation of alkanes in the Earth's crust as a minor source for global hydrocarbon reservoirs. *Nature* **416** (4 April 2002), 522-524.
- Sloan E. D. E. D. Sloan (1998) *Clathrate hydrates of natural gases, second edition*. Marcel Dekker, Inc., New York.
- Solem R. C., Spence G. D., Vukajlovich D., Hyndman R. D., Riedel M., Novosel I., and Kastner K. A. (2002) Methane advection and gas hydrate formation within an active vent field offshore Vancouver Island. *Yokohama Hydrate Conference*.

- Spence G. D., Chapman N. R., Hyndman R. D., and Cleary C. (2001) Fishing trawler nets massive "catch" of methane hydrates. *EOS, Transactions, American Geophysical Union* **82** (50).
- Suess E., Bohrmann G., Greinert J., and Lausch E. (1999) Flammable Ice. *Scientific American* **281** (5), 76-83.
- Thomas D. J., Zachos J. C., Bralower T. J., Thomas E., and Bohaty S. (2002) Warming the fuel for the fire: Evidence for the thermal dissociation of methane hydrate during the Paleocene-Eocene thermal maximum. *Geology* **30** (12), 1067-1070.
- Turnipseed M., Knick K. E., Lipcius R. N., Dreyer J., and Van Dover C. L. (2003) Diversity in mussel beds at deep-sea hydrothermal vents and cold seeps. *Ecology Letters* **6**, 518-523.
- Wellsbury P., Goodman K., Cragg B. A., and Parkes R. J. (2000) 36. The geomicrobiology of deep marine sediments from Blake Ridge containing methane hydrate (sites 994, 995, and 997). In *Proceedings of the Ocean Drilling Program, Scientific Results*, Vol. 164 (ed. C. K. Paull, R. Matsumoto, P. J. Wallace, and W. P. Dillon).
- Whiticar M. J. (1999) Carbon and hydrogen isotope systematics of bacterial formation and oxidation of methane. *Chemical Geology* **161**, 291-314.
- Williams D. F. and Lerche I. (1987) Salt domes, organic-rich source beds and reservoirs in intraslope basins of the gulf coast region. In *Dynamical geology of salt and related structures* (ed. I. Lerche and J. J. O'Brien), pp. 751-786. Academic Press, Inc.
- Yamamoto S., Alcauskas J. B., and Crozier T. E. (1976) Solubility of methane in distilled water and seawater. *Journal of Chemical and Engineering Data* **21** (1), 78-80.

## **Chapter 2: Development of a sea-floor probe for *in situ* sampling of dissolved gases in sediment pore-fluids surrounding gas**

### **hydrates**

**Abstract-** A sea-floor probe (HYDRA, capitalized to differentiate from “hydrate”) was developed to collect and recover pore-fluid samples at *in situ* pressures for determination of dissolved hydrocarbon gas concentrations and carbon stable isotopic composition in gas hydrate environments. This paper presents proof-of-concept results from deployments in representative deep-sea settings. HYDRA collects pore-fluids at discrete depth intervals from 0 to 50 cm below the sediment surface. Its stainless steel sample chambers are pressure rated to 270 bar, allowing it to collect samples from water depths up to ~2700 meters. HYDRA was deployed at two gas hydrate sites and obtained a total of fourteen profiles. Six profiles were collected from Barkley Canyon, off Vancouver Island, BC, on the Cascadia Margin (950 m water depth) from the remotely operated vehicle ROPOS and eight profiles were collected from three gas hydrate sites in the northern Gulf of Mexico (~550 m water depth) from the Johnson-Sea Link submersible. Methane concentrations and stable carbon isotope ratios from HYDRA were compared with pore-fluid samples obtained with conventional push cores from adjacent sediments. When methane concentrations in the core were below saturation at atmospheric pressure ( $<1200 \mu\text{M}$ ), concentrations in HYDRA were similar. Alternatively, when *in situ* methane concentrations exceeded this saturation concentration, concentrations were generally higher in HYDRA than adjacent cores unless



disseminated gas hydrates were present in core samples. While two corrections had to be made to the methane concentrations for HYDRA, maximum corrected *in situ* dissolved methane concentrations reached as high as 12 mM at Barkley Canyon and 14 mM in the GOM hydrate sites. Although high, these concentrations were still below the saturation concentration for equilibrium between dissolved methane and hydrate which is ~67 mM. In the cores, the dissolved methane stable carbon isotope compositions were typically depleted in  $^{13}\text{C}$  compared to HYDRA pore-fluids. In HYDRA, the pore-fluids were isotopically similar to the hydrate-bound methane. This study indicates that pore-fluid collections from push cores in gas hydrate bearing sediments give inaccurate dissolved methane concentrations due to degassing or hydrate decomposition during sample recovery. The HYDRA sampler can alleviate these issues.

## 1. INTRODUCTION

Gas hydrates are composed of rigid cages of water molecules that enclose low-molecular-weight hydrocarbons, principally methane, and other gases such as carbon dioxide and hydrogen sulfide. They naturally occur in deep ocean sediments, particularly those on the continental slope, or on land in the arctic permafrost. The global hydrate reservoir is estimated to contain around ~500 to 2,500 Gt methane carbon or  $1$  to  $5 \times 10^{15}$  m<sup>3</sup> methane at STP (Milkov, 2004) and could be the largest known methane reservoir on Earth (Kvenvolden, 1988). If changes in pressure or temperature destabilize hydrate, the released methane could reach the atmosphere and contribute to climate change. Furthermore, hydrate destabilization could also create hazards for seafloor petroleum operations. Therefore, it is critical to understand factors that control hydrate formation, decomposition, and stability.

In deep ocean sediments, hydrate formation and stability are controlled by the local conditions of *in situ* pressure, temperature, and surrounding pore-fluid gas concentrations (Sloan, 1998). The optimal conditions necessary for hydrate formation are defined by the hydrate stability zone (HSZ) which can be calculated by thermodynamic models (i.e., models found in Sloan, 1998 and Duan and Mao, 2006). These models show that the HSZ in the continental shelf is between 500 and 1000 m thick and is confined to ocean depths of 300-1000 m. They also determine the *in situ* methane concentration needed for hydrate to form and remain stable. A thermodynamic model developed by Duan and Mao (2006) predicts that the saturated methane concentrations for Barkley Canyon and Gulf of Mexico sites at the sediment water interface will be between 67 and 79 mM (Table 2-1). This model also shows that the three phases of methane (aqueous, hydrate, and gas) can only co-exist at the upper and lower hydrate stability depths, approximately 600 and 1500 m. While these theoretical models are important in determining the HSZ and saturation methane concentrations, *in situ* methane concentrations should be directly measured for verification and improved accuracy.

**Table 2- 1: Gulf of Mexico (GOM) and Cascadia Margin sites, locations, maximum water depths, bottom water temperatures, salinities, and predicted saturated methane concentrations. The saturated methane concentrations were calculated from a thermodynamic model (Duan and Mao, 2006). GC=Green Canyon and BC=Barkley Canyon.**

Basin	Site	Location	Water depth (m)	Bottom Water Temp (°C)	Salinity (psu)	[CH <sub>4</sub> ] <sub>saturated</sub> (mM)
GOM	GC 185	27°46.9'N, 91°30.4'W	565	7	35	79
	GC 234	27°44.7'N, 91°13.3'W	540	7	35	77
	GC 232	27°44.5'N, 91°19.9'W	620	5	35	72
Cascadia Margin	BC	48°18.84'N, 126°03.26'W	860	4	35	67

Within hydrate bearing sediments, quantifying the *in situ* dissolved methane concentration is difficult. Methane is highly insoluble in seawater and therefore, comes out of solution readily during sample recovery from the deep sea. This results in the need for specialized instruments that either directly measure methane concentrations *in situ* (i.e., underwater mass spectrometry) or collect a sediment sample and bring it to the surface under *in situ* pressures for a surface-based measurement (i.e., pressurized core barrels). Currently, the technology does not exist to measure pore-fluid chemistry with an underwater mass spectrometer. Additionally, technology to collect pore-fluids and retain them at *in situ* pressures does not exist.

Several technologies exist to collect pore-fluids in shallow water systems. Peepers use dialysis membranes that equilibrate with surrounding pore-fluid solutes and dissolved gases (Hesslein, 1976; Mayer, 1976). Harpoon samplers use active suction to collect pore-fluids across a filtered probe tip (Sayles et al., 1973; Sayles et al., 1976). And a sampler that combines “passive” harpoon sampling along with solute diffusion takes advantages of both the peepers and harpoon sampler technologies but decreases sample smearing and sample deployment time (Carmouze et al., 1997). While these instruments are appropriate for shallow water sample collection, they do not maintain samples at *in situ* pressures or temperatures. Therefore, they are not ideal for use in deep water sediments where methane may be near saturation concentrations.

More frequently at hydrate sites, short sediment push cores are collected using submersibles. But these too, allow the pore-fluids to degas upon sample recovery. Resultant methane concentrations are therefore minimums, typically near the saturated concentration at atmospheric pressure, or 1200  $\mu\text{M}$ . Coring is further complicated by the possible

entrainment of disseminated hydrate within the sediments and therefore, the cores will also contain a signature from dissociating hydrate and give an inaccurate representation of the dissolved methane pool.

To combat the issues with degassing, a pressurized sampler was developed to collect whole sediments in deep sea hydrate environments. The Pressure Core Sampler (PCS) was deployed in gas hydrate-rich sediments in Blake Ridge, western Atlantic Ocean (Dickens et al., 1997a). It collected a 1,320 cm<sup>3</sup> (1 m long and 4.1 cm diameter) sediment core and retained it at *in situ* pressures by sealing the ends with ball valves. Once recovered from the seafloor, it was sampled for *in situ* concentrations through manual valves. Although this sampler gave an estimate of the total methane concentrations within the sediments, the estimate included bubbles, hydrate, and dissolved gas and did not isolate the dissolved phase. To understand the dissolved gas content, the pore-fluids must be separated from the sediment and hydrate fractions and held at *in situ* pressures.

The purpose of this study was to develop and test an *in situ* pore-fluid collection device, known as HYDRA. This instrument is similar to the harpoon-type instruments developed by Sayles (1976) in that it uses suction to collect pore-fluid samples from sediments as a vertical profile. Unlike the harpoon, HYDRA has high pressure values that retain the samples at *in situ* pressure until analysis onboard ship. It was designed to be deployed from either a submersible or a remotely operated vehicle (ROV). The intent is to improve the accuracy of measurements for methane concentrations beyond that of traditionally collected sediment push cores.

In this chapter, I will describe HYDRA and compare measured methane concentrations and stable carbon isotope ratios from HYDRA to sediment push cores. I expect

concentrations in HYDRA will exceed those within the cores. Stable carbon isotope ratios of the dissolved methane will also be measured. Stable isotopes are important because they assess the source of the methane and whether microbial processes have altered it. Studies have shown that the isotopic fractionation at atmospheric pressures during air-water transfer for methane is negligible (on the order of 1‰, Fuex, 1980; Knox et al., 1992). On this basis, methane carbon isotope ratios should be similar between HYDRA and sediment cores.

## 2. METHODS

### 2.1. Study sites

#### 2.1.1. Gulf of Mexico Hydrate sites

In the summers of 2000, 2002, and 2003, HYDRA was deployed at three sites within the Green Canyon (GC) lease block in the Gulf of Mexico on the Northern Texas-Louisiana continental shelf, about 120 km offshore Louisiana (Fig. 2-1, Table 2-1). GC 185 and GC 234 contained exposed hydrates along with chemosynthetic communities (*Beggiatoa* mats, tube worms, methanotrophic mussels, and clams), venting gas streams of low molecular weight hydrocarbons (such as methane, ethane, and propane), and oil associated with the surrounding sediments. At GC 232, a small deposit of hydrate, orange in color, was observed in close proximity to tubeworms and bacterial mats. Oil droplets were also observed seeping out of sediments adjacent to the exposed hydrate. HYDRA was deployed eight times on eight different dives (Table 2-2)<sup>1</sup>.

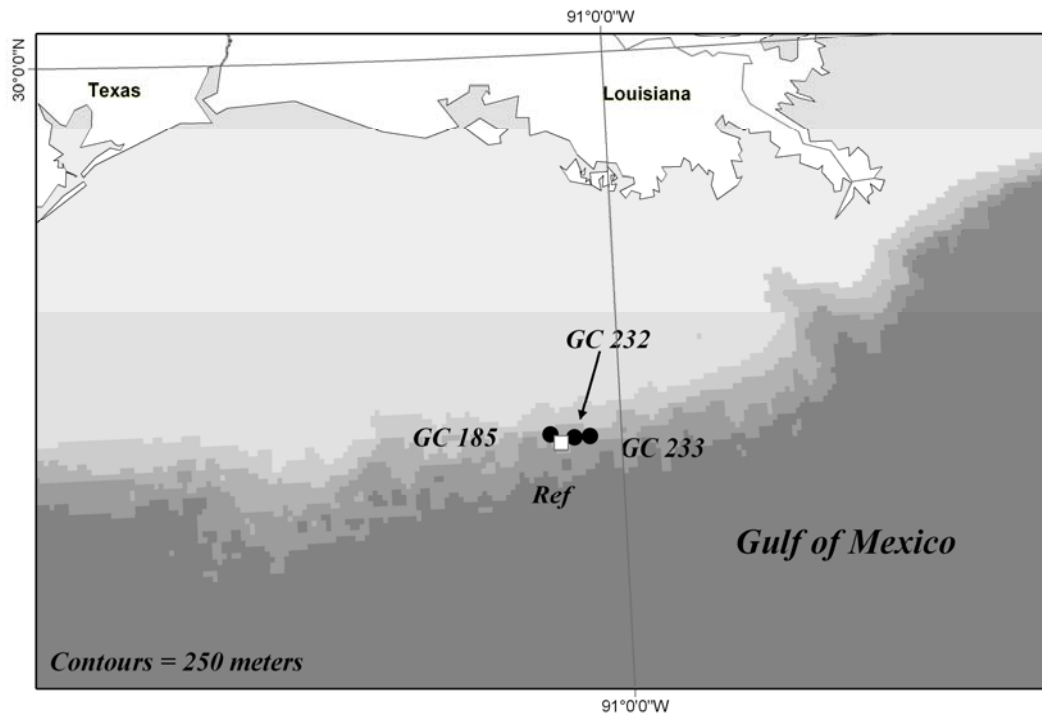
#### 2.1.1. Cascadia Margin Hydrate site

In the summers of 2003 and 2004, HYDRA was deployed six times at Barkley Canyon, northern Cascadia Margin, about 80 km off the west coast of Vancouver Island, British

---

<sup>1</sup> HYDRA was also deployed at four other sites but, since these sites contained elevated concentrations of chloride, they are treated separately in Chapter 6.

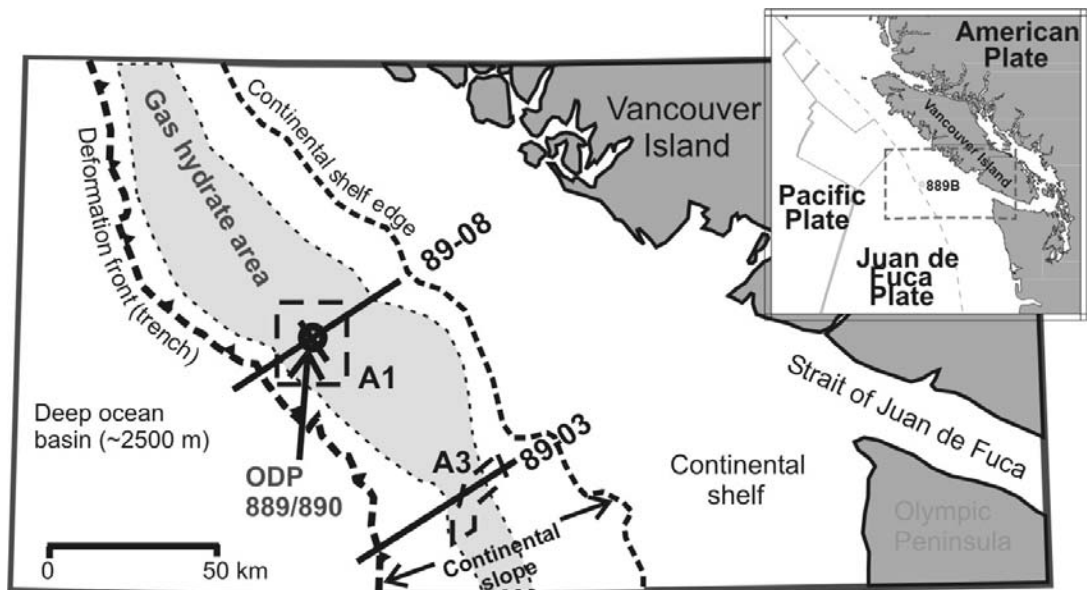
Columbia (Fig. 2-2, Table 2-1; Spence et al., 2001) aboard the Canadian Coast Guard Ship J.P. Tully with the ROV ROPOS (Remotely Operated Platform for Ocean Science). This site



**Fig. 2- 1: Gulf of Mexico sites visited. Black circles are Green Canyon (GC) 185, 232, and 234. Open square is the reference site. Figure created in ArcGIS.**

contains exposed hydrates, as tall as 3 m, which were in close association with thick, white bacterial mats and both living and dead clams (Chapman et al., 2004; Pohlman et al., 2005). No other chemosynthetic communities were found in this area. Natural gas vents were found near outcropping hydrate. Also, bubbles and oil droplets were released from sediment upon submersible disturbance. HYDRA was deployed six times (Table 2-2)<sup>2</sup>.

<sup>2</sup> Pictures of Barkley Canyon dives are shown in Chapter 4.



**Fig. 2- 2: Inset map shows the location of Northern Cascadia Margin. The main map shows the Barkley Canyon site as A3 (Spence et al., 2001).**

**Table 2- 2: Gulf of Mexico, Green Canyon (GC) and Cascadia Margin, Barkley Canyon (BC) sites with individual dive number, cruise date, and HYDRA collection design. See text for description of HYDRA configurations. Also shown are core numbers collected adjacent to HYDRA, corrections made, description of the local environment, and distance between HYDRA and cores. NA means no core was collected along side HYDRA.**

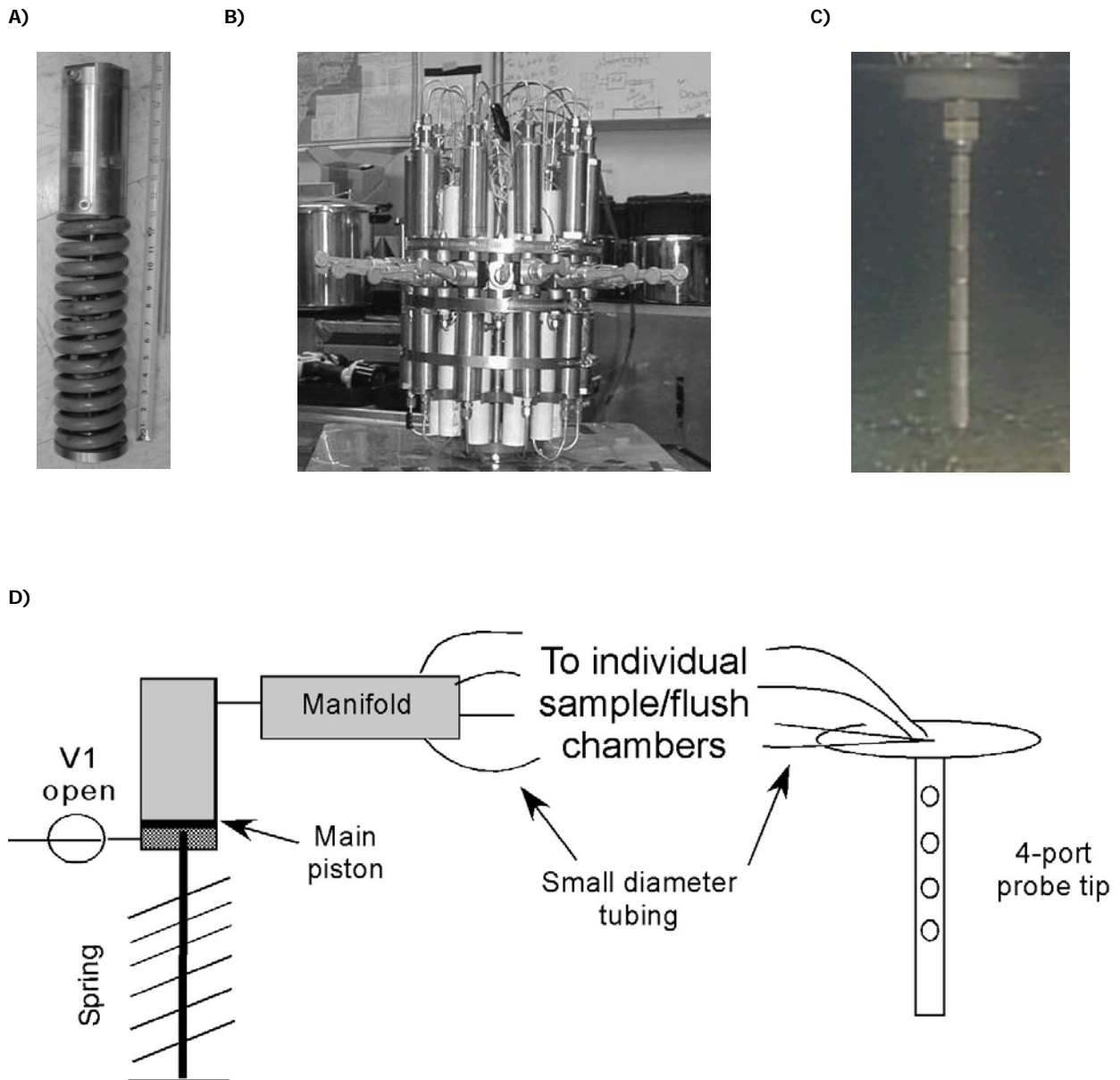
Site	Dive #	Cruise date	HYDRA Configuration	Sample tip array	Use of High Pressure Valves?	Use of flush chamber?	Core #	Corrections made	Descriptions of local environments	Distance between HYDRA and push cores (cm)
GC 185	4210	2000	1	Vertical	N	Y	NA	None	In tubeworm cluster, next to bubble stream	NA
GC 185	4213	2000		Vertical	N	Y	NA	None	Soft sediments near mound	NA
GC 234	4217	2000		Vertical	N	Y	NA	None	Near mussel bed	NA
GC 234	4218	2000		Vertical	N	Y	NA	None	Soft sediments	NA
GC 232	4405	2002	2	Vertical	Y	Y	NA	None	Soft sediments	NA
GC 185	4553	2003		Vertical	Y	Y	NA	DI water	In shelly region	NA
GC 234	4557	2003		Vertical	Y	Y	11	DI water	Placed in orange bacterial mat, next to sparse tubeworms	200
GC 232	4564	2003		Vertical	Y	Y	11	DI water	At base of mound??	50
BC	692	2003	3	3D	Y	Y	2	DI water; channeling	Soft sediments with clam shells	20
BC	693	2003		3D	Y	Y	2	DI water; channeling	Soft sediments	50
BC	696	2003		3D	Y	Y	1	DI water; channeling	Next to hydrate, bacterial mats around	50
BC	798	2004	4	3D	Y	N	1	DI water; channeling	White bacterial mats around	50
BC	799	2004		3D	Y	N	2	DI water; channeling	Soft sediments, not much around	50
BC	802	2004		3D	Y	N	1	DI water; channeling	On top of hydrate, tips resting on hydrate	30



## 2.2. HYDRA description

HYDRA is a modified version of the Harpoon sampler (Sayles et al., 1973; Sayles et al., 1976). It is made up of three main parts: a master cylinder, sample and flush chambers, and probe tip (Fig. 2-3). The master cylinder creates the suction needed to collect the pore-fluids through the filtered probe tip and into the sample and/or flush chambers. This master cylinder is connected to a multi-port stainless steel manifold that evenly disperses suction to the chambers (Fig. 2-3b). The chambers contain the sample or flush pore-fluids which are sucked through filtered ports and retain the fluids at *in situ* pressures because of high pressure valves and o-ringed pistons. Each part is described below.

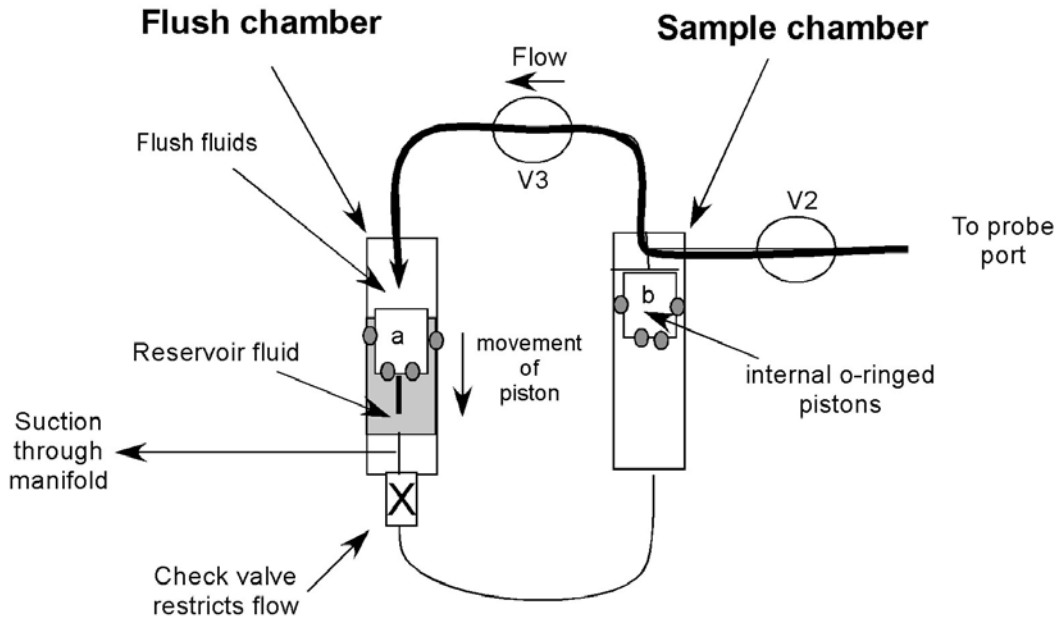
The master cylinder is a 250 mL stainless steel cylinder with an internal piston that controls the expansion and compression of a coupled car spring (Fig. 2-3a). The backside of the piston is plumbed to the master valve and a hand pump (Fig. 2-3b). The front-side of the piston is plumbed to a manifold which equally distributes the suction to the sample chambers created by the expansion of the spring. Between the front-side of the piston and the chambers, reservoir water was contained within the space (Fig. 2-3b). To load the cylinder on the boat, hydraulic fluid (water) is pumped into the backside of the piston which displaces the piston deeper into the master cylinder until it no longer moves (Fig. 2-3b). The valve is then closed and the cylinder is ready for deployment (Fig. 2-3c). When the samples are ready to be taken, the master valve is opened and the spring expands creating a vacuum that collects the pore-fluids through the probe tips and into the sample and flush chambers.



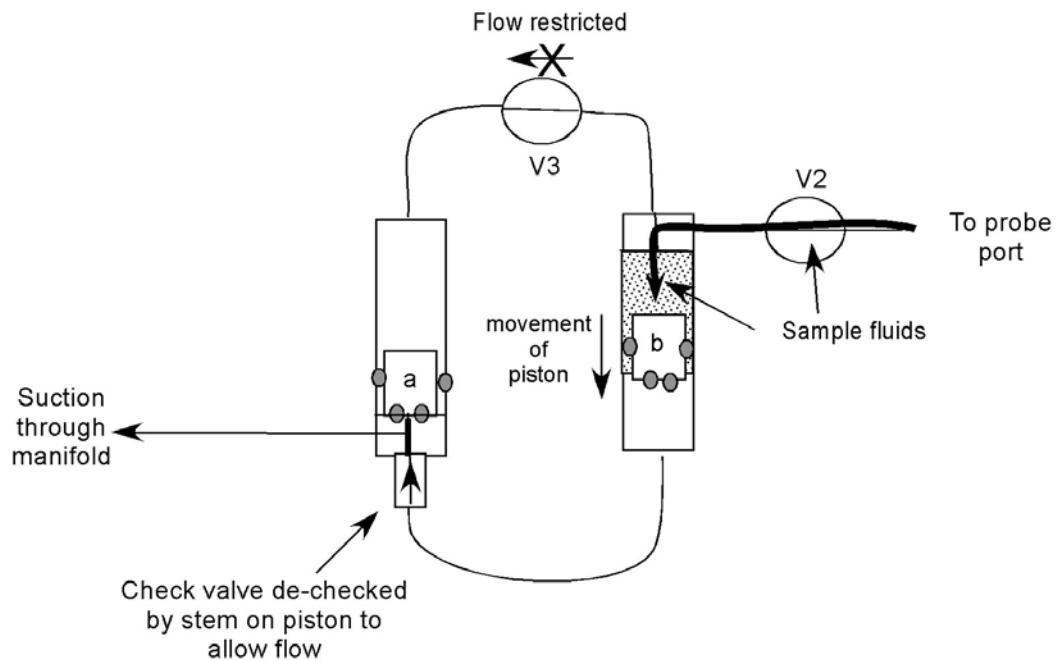
**Fig. 2- 3: Photographs of A) the master cylinder shown with spring and the large volume chamber (measuring tape is in inches), B) Sample and flush chambers in rosette configuration, and C) 50 cm long vertical probe tip. D) Cartoon of HYDRA system prior to loading the spring. To load, the main valve (v1) is opened and hydraulic fluid (water) is pumped into the backside of the main piston. V1 is then closed for travel to the seafloor. Once on the seafloor, the probe tip is inserted into the sediments and V1 is opened to collect pore-fluids.**

The manifold was connected to individual sample and flush chambers with thin tubing (Figs. 2-4 and 2-5). The chambers were configured in one of two ways. The first way has two chambers per depth; a flush chamber that clears the sample lines filled with DI water prior to the deployment and a sample chamber that retains the sample (Fig. 2-4). The flush chambers were either 20 mL PVC or 7 mL stainless steel chambers and the sample chambers were always 7 mL stainless steel chambers. The second configuration of the sample chambers contained only one 7 mL stainless steel sample chamber (shown in Fig. 2-5). The chambers contain internal pistons which isolate the DI water or sample pore-fluids from the reservoir fluid. The pistons have o-rings on both the sides and bottom to seal during sample collection and after collection, respectively. The chambers were also outfitted with high pressure valves to maintain *in situ* pressures within the chambers (V2 and V3 in Figs. 2-4 and 2-5).

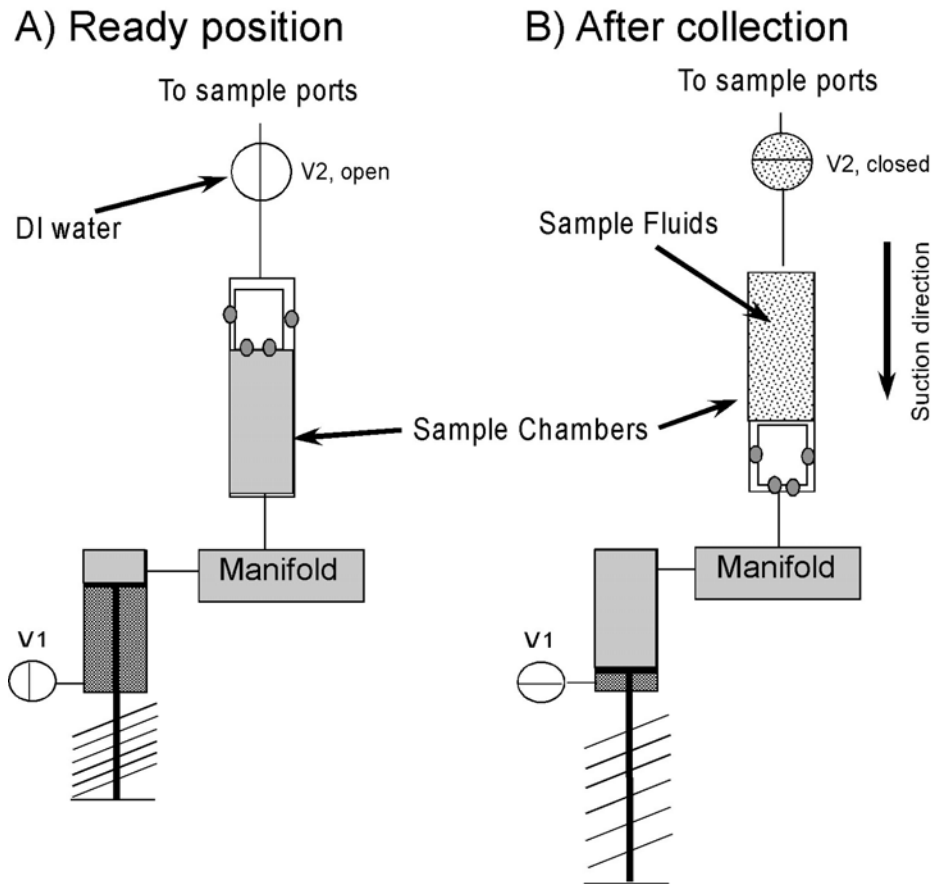
### A) Collecting flush fluids



### B) Collecting sample fluids

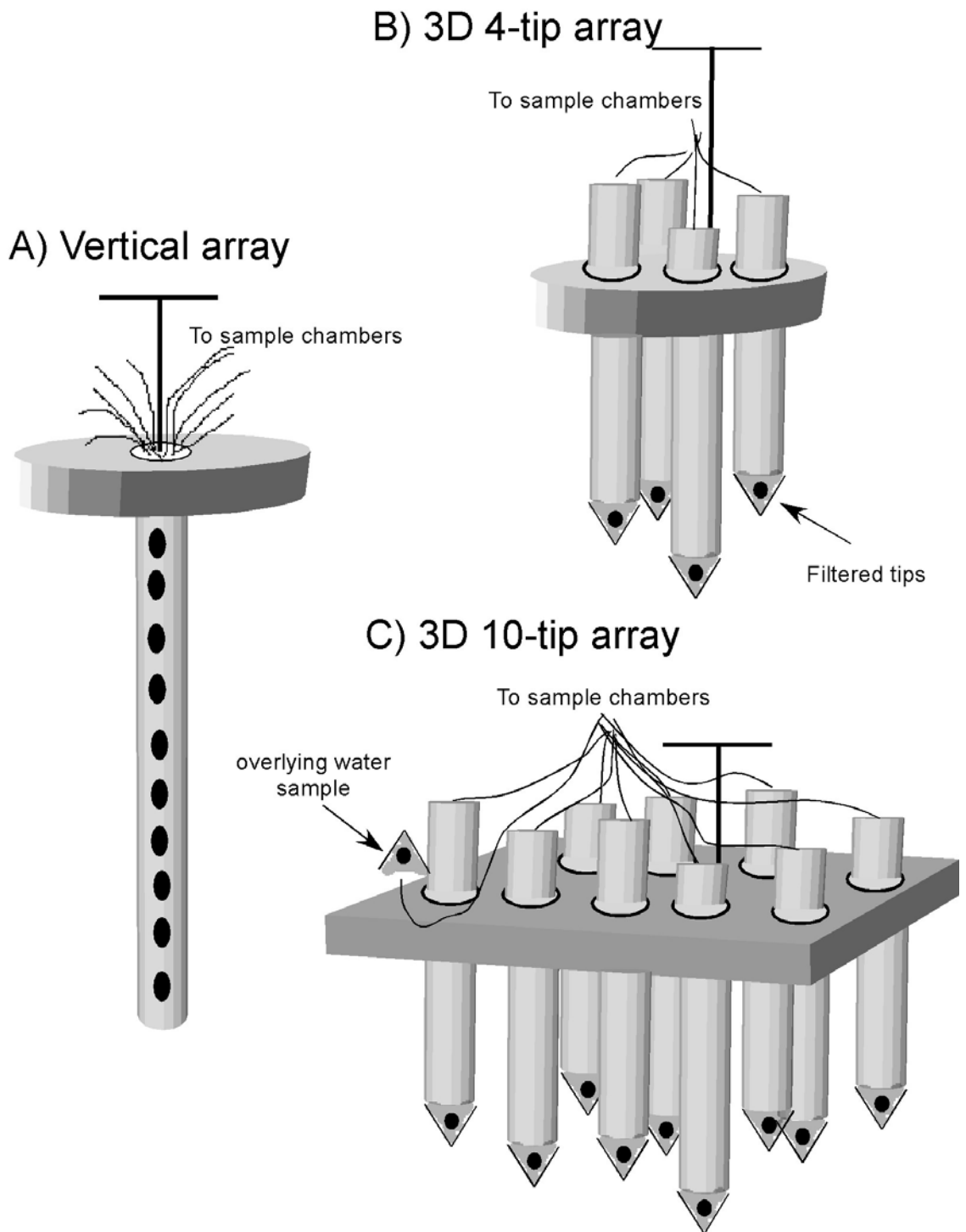


**Fig. 2- 4: Flush chamber configurations 1, 2, and 3. A) To collect flush fluids, suction is first applied from manifold, moving the stemmed piston (a) along the flush chamber and sucking flush fluids through valves 2 (V2) and V3 and into the flush chamber. B) To collect sample fluids, once the stemmed piston reaches the end of the flush chamber, it de-checks the check valve. Now, the suction pulls the sample chamber piston (b) down the chamber which pulls sample fluids through V2.**



**Fig. 2- 5: A) Schematic of HYDRA configuration 4 in the ready position, as it would be on the seafloor. An example sample chamber is shown, even though there are typically either 4 or 10 such chambers that make up the rosette. B) Schematic of HYDRA after the sample has been collected on the seafloor. The colors within each of the HYDRA parts refer to different fluids: the dark gray contained within the master cylinder is hydraulic fluid, the light gray between the master cylinder piston and the sample chamber pistons is reservoir fluid (shown in A), and the stippled gray within the sample chambers is the sample pore-fluid (shown in B).**

Each chamber is plumbed to a filtered sampling port that is housed within either a vertical or 3D-horizontal probe tip array (Fig. 2-6). The vertical array consists of a 50 cm stainless steel tip with ten sampling ports spaced every 5 cm (Fig. 2-6a). Small diameter (1/16 inch outer diameter) stainless steel tubing connects each sample chamber to its sample port. Stainless steel filters (Dynapore, #405745, 25-40  $\mu\text{m}$  mesh) cover each port to provide *in situ* filtration. The 3D-horizontal array contains either 4 or 10 individual 30 cm long PVC tips that have a polycarbonate filters on the ends (Figs. 2-6b and 2-6c). The depths for each tip on the 3D arrays can be varied according to the environment sampled. Accordingly, the 3D array was used to sample within the thin veneer of sediments which frequently covered hydrates found in Cascadia. In the Gulf of Mexico, the sediments are deeper and so the vertical array was used.

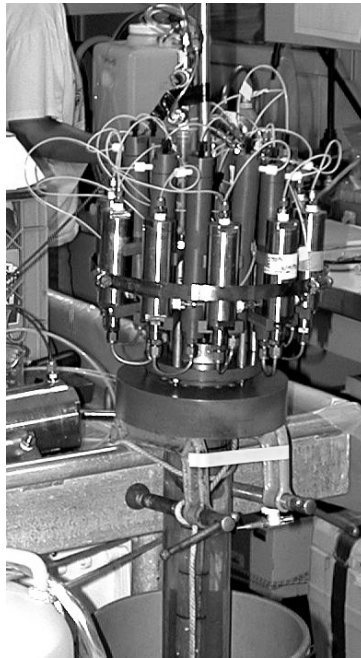


**Fig. 2- 6: Probe tip configurations. A) Vertical array, b) 3D 4-tip array, and c) 3D 10-tip array.**

### 2.2.1. HYDRA configurations

Although the three main parts of HYDRA remained the same for each deployment, they were configured in four different ways. Configurations were based on the presence/absence of high pressure valves, the use of a flush chamber, and the design of the probe tip array (Table 2-2).

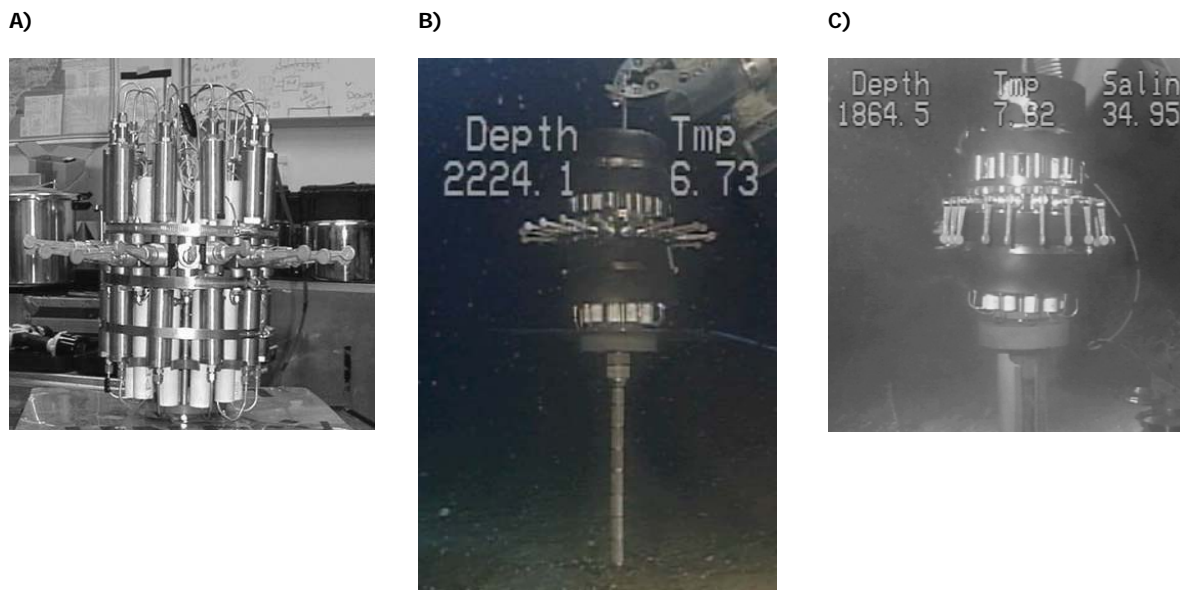
2.2.1.1. *Configuration 1.* Although the overall purpose of this study was to design an instrument to retain pore-fluids for *in situ* methane concentration measurements, the first configuration did not have high pressure valves and so the methane concentrations are still considered minimums (Fig. 2-7 and Table 2-2). Also, this configuration used a flush chamber and the vertical sample tip array design (Fig. 2-7). Adjacent cores were not collected for this configuration.



**Fig. 2- 7: HYDRA configuration 1. Sample chambers are stainless steel and flush chambers are PVC. The vertical probe tip array is submerged in water within an acrylic tube.**



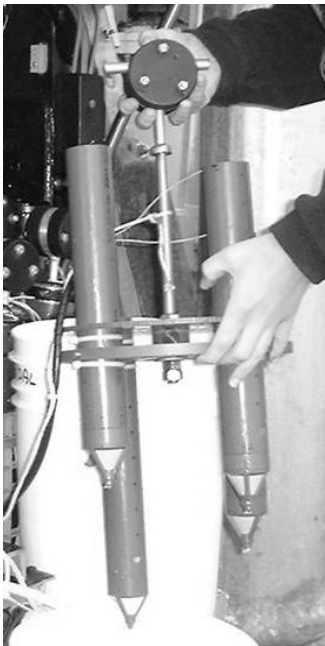
2.2.1.2 *Configuration 2*. For the second configuration, and all subsequent configurations, HYDRA was outfitted with high pressure valves (Fig. 2-8 and Table 2-2). Circle Seal T900 on/off toggle valves were used because they were pressure rated to 6,000 psi and could be easily manipulated by the submersible arm. However, the use of these valves considerably increased the dead volume within the whole system which was not directly measured for this set up. Similar to the first configuration, configuration 2 also used the flush chamber and the vertical tip array. There were four deployments of HYDRA configuration 2; two of which were accompanied by the collection of a sediment core.



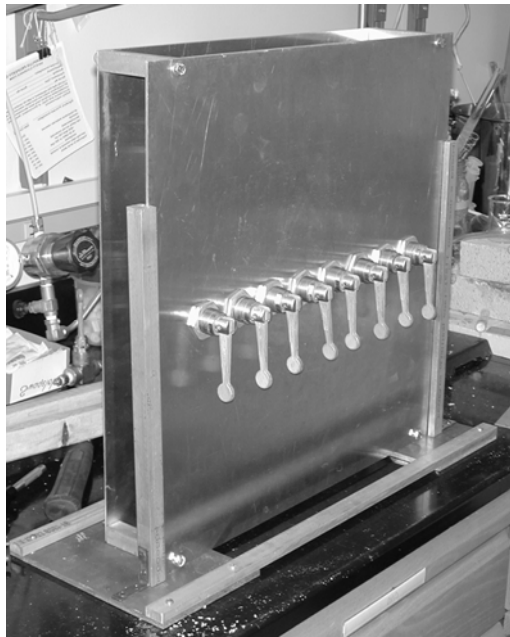
**Fig. 2- 8: HYDRA configuration 2. A) Sample and flush chambers shown with high pressure valves in between the chambers in the open position. B) HYDRA deployed by JSL (notice manipulator jaw in upper portion of picture). The vertical tip is visible, valves are open and a black sheath is covering the chambers. C) After HYDRA deployment, valves are closed, as shown in this photo.**

2.2.1.3. *Configuration 3.* A third configuration of HYDRA was needed in order to sample the thin veneer of sediment overlying gas hydrate at Cascadia. This veneer was typically 10-15 cm thick, much too thin to accommodate the 50 cm vertical probe tip. Therefore, this configuration implemented the use of the 3D probe tip array (Fig. 2-9 and Table 2-2). This array had 4 sample ports whose depth could be changed to accommodate the local environment (Fig. 2-9a). In order to fit on the front of the ROV ROPOS, the sample and flush chambers were modified to no longer be in a rosette but mounted in a flat plate (Fig. 2-9b). This modification did not affect the way HYDRA sampled. However, the sampling tubings connecting all parts of HYDRA were modified by shortening their length. Although this would have decreased the dead volume within the system, the dead volume was not measured.

A)

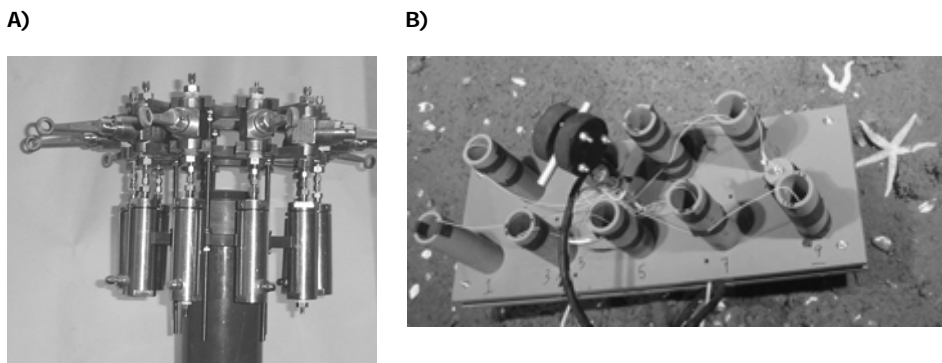


B)



**Fig. 2- 9: HYDRA configuration 3. A) The 3D 4-port probe tip with white filters shown on each end. B) Sample and flush chambers hidden behind steel plates with high pressure valves visible.**

2.2.1.4. *Configuration 4.* For the fourth configuration, HYDRA did not use the flush chambers (Fig. 2-5) and the 3D probe tip array was modified to accommodate 6 more ports (Fig. 2-10). Furthermore, the pistons within the sample chambers were cut in half in order to increase the volume from 7 mL to ~11 mL. This also eliminated the need for the second high pressure valve and reduced the dead volume within the system. However, the dead volume for this set-up was not measured.



**Fig. 2- 10: HYDRA configuration 4. A) Sample chambers only. High pressure valves are also shown on top of chambers. B) The 3D 10-port probe tip shown deployed in sediments.**

### 2.2.2. HYDRA sampling procedure

1. Prior to each cruise, Hydra was pressure tested by introducing 270 bar of gas pressure to the collection chambers over a 24 hour period. Since HYDRA deployments never exceeded 5 hours, this time period was sufficient. No pressure losses were noted during these test intervals.
2. Prior to deployment, the master cylinder was loaded by pumping it with hydraulic water, driving the piston up the cylinder and compressing the car spring into the 'ready' position. This action then pushed reservoir water through the manifold to push each sample and flush chamber's internal pistons into the ready position (Figs. 2-3 and 2-5). This action forced DI water to be retained within all tubing of HYDRA so no air was left.
3. The main valve, v1 (Fig. 2-3c and 5a), was then closed for water column descent.
4. Once on the sea-floor, the submersible placed the appropriate probe tip array into the desired sediment.
5. The master valve, v1, was opened by the manipulator arm which expanded the compression spring and introduced suction to the backsides of the internal pistons. The pistons then moved up the chambers which pulled pore-fluids through the filtered ports and into the sample and flush chambers.
6. HYDRA was allowed to sit and collect samples for 30 minutes. After collection, the high pressure valves on each sample and flush chambers were closed by the submersible arm, isolating the pore-water samples at *in situ* pressure for subsequent geochemical analysis (Figs. 2-4 and 2-5b). HYDRA tips were then placed back onto the submersible front deck.

7. A sediment push core was then collected next to the footprint of HYDRA.
8. Once HYDRA and cores were on board ship, HYDRA pore-fluid samples were sub-sampled as described in the section 2.4.1. The cores were also sub-sampled as described in section 2.3.

### **2.3. Sediment push cores**

Sediment push cores were collected adjacent to most HYDRA deployments as described above. Once on board ship, cores were sectioned into 3 cm intervals. In each section, sediment plugs, using 3 mL cut-off plastic syringes, were collected and placed into 20 mL serum vials. The vials were sealed with butyl rubber stoppers and capped with aluminum seals. To each vial, 3 mL degassed de-ionized water added. From these vials, 3 mL headspace aliquots were collected and analyzed for gas concentrations on board ship. For land based stable isotope analysis, the vials were then preserved by freezing them inverted to create a water ice seal on the rubber stopper and eliminate gas diffusion. From the remaining whole sediment of each section, pore-fluids were expressed with a Reeburgh-type squeezer (Reeburgh, 1967) and analyzed for sulfate and chloride concentrations. Ammonium concentrations were also measured but are not reported here.

### **2.4. Analytical methods**

#### *2.4.1. Methane concentrations*

HYDRA pore-fluids (volumes given in Tables 2-3, 2-4, and 2-5) were collected into evacuated ~30 mL vials. The vials were pressurized by addition of ~20 mL of helium so that when the 6 mL headspace sub-sample was removed for analysis, the remaining sample was at atmospheric pressure. The vials were shaken for 2 minutes and a 6 mL headspace gas aliquot was collected to inject into the gas chromatograph (GC). Core sub-section samples

were measured for methane concentrations by shaking vials for 2 minutes to release the dissolved methane into the gas phase and injecting a 3 mL gas aliquot into the GC. All gas samples were injected into a Shimadzu Mini-II gas chromatograph equipped with a poroplot-Q column set at 50°C. Scott specialty gas standards were used for calibration. Sample integrated areas were converted to concentrations (in part per million, ppm) by:

$$CH_4(ppm) = \frac{std\ ppm \times sample\ area}{std\ area} \quad (1)$$

where ‘std ppm’ is the known concentration of the gas standards, ‘sample area’ is the integrated area of each sample, and ‘std area’ is the integrated area of the gas standards.

HYDRA concentrations were then calculated by:

$$CH_4(\mu M) = \frac{CH_4(ppm)}{R \times T} \times \frac{helium\ volume\ (mL)}{sample\ volume\ (mL)} \times \frac{1}{0.95} \times \frac{1}{correction\ factor} \quad (2)$$

where R is the gas constant (0.08205 L·atm/mol·K), T is temperature in K, ‘helium volume’ is the volume of helium (mL) added to each evacuated vial to slightly over-pressurize it, ‘sample volume’ is the volume (mL) of pore fluid extracted from HYDRA, 1/0.95 is the known methane extraction efficiency, and the correction factor term is discussed below. For the cores, methane concentrations were calculated using the following equation:

$$CH_4(\mu M) = \frac{CH_4(ppm)}{R \times T} \times \frac{(vial\ volume - sed\ volume)\ (mL)}{pore\ fluid\ volume\ (mL)} \times \frac{1}{0.95} \quad (3)$$

where ‘vial volume’ is the volume of the serum vial (mL) prior to filling with sample, ‘sed volume’ is the volume (mL) of sediment sub-core placed in vial, and ‘pore fluid volume’ was measured by weight difference between wet and dry sediments corrected for sediment density for each sample.

2.4.1.2. *Methane concentration correction factors.* HYDRA methane concentrations had to be corrected for two effects: (1) dilution of sample with DI water, which was used to flush the small diameter tubing prior to deployment (see section 2.2.2. step 2) and (2) channeling of overlying seawater down the sampling tips due to a poor seal with the sediment during deployment. The calculations for these factors are presented here.

The first correction factor,  $f$ , was applied to correct samples for DI water present in the small diameter tubing prior to deployment. It was calculated from a simple mixing model of the *in situ* sample and DI water using chloride concentrations following the equation:

$$[Cl]_{measured} = [Cl]_{in\ situ} (f) + [Cl]_{DI\ water} (1 - f) \quad (4)$$

where  $[Cl]_{measured}$ ,  $[Cl]_{in\ situ}$ , and  $[Cl]_{DI\ water}$  are the chloride concentrations measured within probe samples, *in situ* pore water, and DI water.  $f$  is the fraction of pore fluid collected that is sample. At Barkley Canyon,  $[Cl]_{in\ situ}$  is  $545 \pm 7$  mM ( $n=15$ ) (Pohlman, 2006). Since the chloride concentration for DI water is zero, the last term of equation 4 drops out and the correction factor becomes:

$$f = \frac{[Cl]_{measured}}{545} \quad (5)$$

The correction,  $f$ , in equation 5 was then applied to equation 2 to calculate the *in situ* methane concentrations corrected for DI-water dilution (hereafter referred to as  $CH_4$ - $f$ ). Chloride concentrations were only measured on HYDRA deployments in 2003 to the Gulf of Mexico and all Barkley Canyon dives.

Since equation 5 assumes that the chloride concentration of the pore-fluid sample should be similar to sea-water, the correction factor,  $f$ , was also verified using a second chloride-independent dye method for a limited number of samples. This method relied on dyeing the original DI water flushed through the HYDRA tubings with a color of known absorbance

(A= 2.5385). Upon collection of the pore-fluids, their absorbance was then measured at the same wavelength ( $\lambda=498$  nm) and the correction factor,  $f_{color}$ , calculated from the following equation and compared to the values calculated for f:

$$f_{color} = \frac{(2.5385 - \text{sample absorbance})}{2.5385} \quad (6)$$

The second correction factor was made for channeling of overlying seawater down the sampling tips due to a poor seal with the sediment during deployment. Channeling effects were corrected by correcting HYDRA pore-fluid sulfate concentrations with core sulfate concentrations, assuming that only 30 mM sulfate overlying water was channeled in. A correction factor, x, was calculated from a simple mixing model between the in situ concentration estimated from the cores and the overlying water sulfate concentration:

$$\frac{[SO_4]_{measured}}{f} = [SO_4]_{core} (x) + [SO_4]_{OLW} (1 - x) \quad (7)$$

Where  $[SO_4]_{measured}$ ,  $[SO_4]_{core}$ , and  $[SO_4]_{OLW}$  are the sulfate concentrations measured within probe samples, measured in adjacent cores and overlying water; respectively. f is the correction factor for the DI water dilution, calculated from equation 5 and x is the fraction of sample collected that is pore-fluid. The measured probe sample sulfate concentration was corrected for the DI water dilution described above. The *in situ* pore water sulfate concentration was estimated by extrapolating the measured core sulfate concentrations for the appropriate depth. Unfortunately, the cores did not penetrate as deeply as the probe samples and therefore, this correction could not be made for all depths. The overlying water sulfate concentration was taken as 30 mM. The correction factor, x, was then applied to equation 2 to calculate the *in situ* methane concentration corrected for channeling (hereafter referred to as CH<sub>4</sub>-x).



#### 2.4.2. Methane carbon stable isotope analysis

Isotope samples were analyzed at the UNC stable isotope facility for carbon isotope ratios using a Finnigan Mat 252 isotope ratio mass spectrometer coupled via a combustion interface to a Hewlett-Packard 5890 GC (GC-C-IRMS). The GC was equipped with a 25m Poropak Q column set at 30°C. Gas aliquots were injected into the GC-C-IRMS by two different methods, depending on the methane concentration. Low concentration samples (<0.08 mM) were analyzed by pre-concentrating a ~1-30mL sample on a 25cm long, 1/8 inch outer diameter stainless steel column packed with poropak Q and immersed in a liquid nitrogen/ethanol slush (-130°C). The trap was then warmed with an air gun and the sample was introduced into the GC where a second concentration step froze the gas onto the capillary tubing. This was then warmed and injected into the IRMS. High concentration samples (>0.08 mM) were injected directly onto the GC column using the septa. The difference between duplicates was ~0.3‰ (n=3). The ratios are compared between a sample and standard by expressing the relative change in <sup>13</sup>C using the conventional δ notation with units of per mil, ‰ or ppt:

$$\delta^{13}\text{C}(\text{‰ or ppt}) = \left( \frac{R_{\text{sample}} - R_{\text{standard}}}{R_{\text{standard}}} \right) \times 1000 \quad (8)$$

where  $R = {}^{13}\text{C}/{}^{12}\text{C}$  for both the sample and the Peedee Belemnite standard.

#### 2.4.3. Sulfate and chloride concentrations

Dissolved sulfate and chloride concentrations were also measured in both HYDRA and core samples. They were measured on a Dionex Ion Chromatograph (IC) equipped with a conductivity detector (Crill and Martens, 1983). 100uL of original sample was diluted to

10mL with buffering eluent, injected into IC, and compared to standards for determination of sulfate and chloride concentrations.

### 3. RESULTS

HYDRA, a newly developed *in situ* pore-fluid sampler, was successfully tested in 2 different ocean basins, the northern Cascadia Margin and the northern Gulf of Mexico, with 14 deployments at 4 hydrate sites over 5 years. For the four configurations tested, the chloride, sulfate, and methane concentrations and methane and dissolved inorganic carbon (DIC) stable carbon isotope compositions are given and compared to adjacently collected cores.

#### 3.1. Configuration 1- Decompressed methane in Gulf of Mexico

The first configuration of HYDRA, used in the Gulf of Mexico, was not pressure tight and samples were allowed to decompress upon ascent to the surface. Therefore, methane concentrations are still considered minimums. Pore-fluids from the flush chambers were not measured. Furthermore, chloride concentrations were not measured on the fluids from the sample chambers so no corrections were made for these measurements.

Methane concentrations were low on dives 4210 and 4218 (Figs. 2-11a and 2-11b). On dive 4210, GC 185, methane concentrations were ~5 uM from the surface to 37 cmbsf where concentrations sharply increased to 40 uM by 48 cmbsf (Fig. 2-11a). The  $\delta^{13}\text{C-CH}_4$  values showed no down core trend, averaging  $-46.1 \pm 0.4\%$  (Fig. 2-11b). Dive 4218, GC 234, showed similar results. Methane concentrations reached a maximum of 80 uM at 27.5-cmbsf (Fig. 2-11a) and the average  $\delta^{13}\text{C-CH}_4$  value was  $-47.2 \pm 2.3\%$  (Fig. 2-11b).

On dive 4213, GC 185, dissolved methane concentrations were low at the surface, increased to a sub-surface maximum methane peak of 1900 uM at 27.5 cmbsf, and decreased

to 750 uM at 43 cmbsf (Fig. 2-11c). This sub-surface maximum trend is a result of samples that are above methane saturation at 1 atm degassing upon ascent through the water column and was expected since this configuration of HYDRA did not contain the samples at *in situ* pressures. The methane isotopic composition was consistent down core and averaged -46.9±2.2‰ (Fig. 2-11d).

On dive 4217, GC 234, although the methane concentration profile is noisy, the concentration increased from near zero values at the surface to 2200 uM at 22.5 cmbsf (Fig. 2-11c). The isotopic composition of this methane exhibited little variation with depth and the average  $\delta^{13}\text{C-CH}_4$  value was -50.4±1.7‰ (Fig. 2-11d).

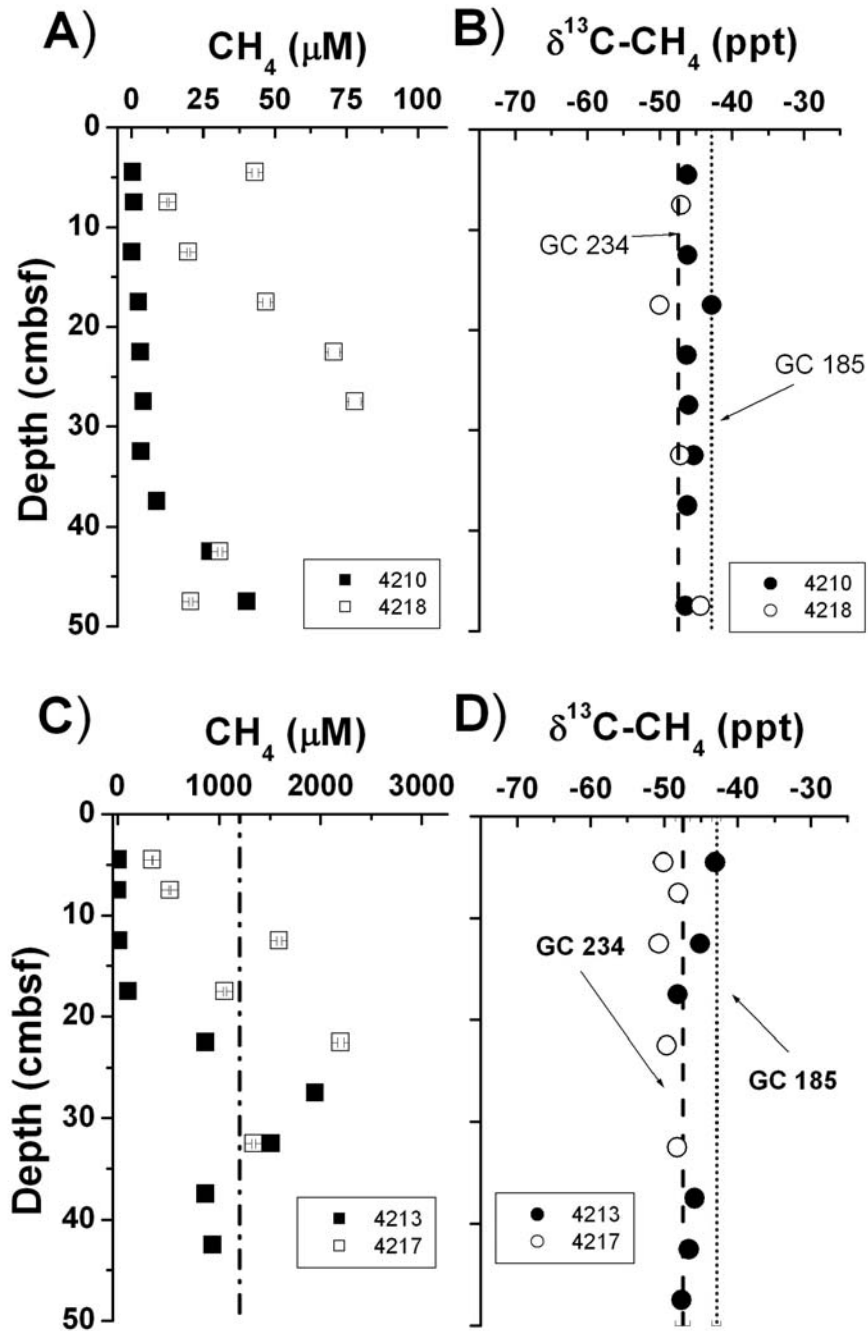


Fig. 2- 11: HYDRA configuration 1 methane concentrations and stable isotopes. Dives 4210 and 4218 A) methane concentrations and B)  $\delta^{13}\text{C}-\text{CH}_4$ . Dives 4213 and 4217 C) methane concentrations and D)  $\delta^{13}\text{C}-\text{CH}_4$ . In panel C, dotted-dashed line is saturation concentration at atmospheric pressure (1200  $\mu\text{M}$ ). In panels B and D, the dashed line is the isotopic composition for hydrate-bound methane at GC 234 and the short dot line is for GC 185 (Sassen et al., 2004). The concentrations were not corrected for any dilutions and display error bars (standard deviation of measurement).

### **3.2. Configuration 2- *In situ* methane concentrations without and with DI water correction in Gulf of Mexico**

The second configuration of HYDRA had high pressure valves which resulted in measurements of higher methane concentrations and smoother profiles for four separate dives. Although both flush and sample chambers were part of this configuration, analyses were only conducted on the sample chamber pore-fluids.

For dive 4405, at GC 232, DI water corrections could not be applied because HYDRA pore-fluids were not measured for chloride concentrations. However, methane concentrations reached 15,000  $\mu\text{M}$  at 50 cmbsf and the profile exhibited a smooth concave-up curvature (Fig. 2-12a). The isotopic signature of this methane was  $-41\text{‰}$  near the sediment water interface and became depleted in  $^{13}\text{C}$  at 20 cmbsf to  $-57\text{‰}$  (Fig. 2-12b). Below 20 cmbsf, the isotopic signature became more enriched in  $^{13}\text{C}$  until it leveled out at about  $-46\text{‰}$ .

For the other three profiles obtained with configuration 2 of HYDRA, chloride concentrations were measured which allowed an assessment for how well the flush chamber flushed the lines. With the exception of 3 depths, chloride concentrations in the flush chambers were lower than the sample chambers (Table 2-3). Applying these chloride concentrations to equation 4, the DI water correction factor  $f$  was calculated. The results showed that between 7-79% of the fluids in the flush chambers was seawater (Table 2-3). In the sample chambers, seawater made up between 31-90% which is still below full seawater strength. The DI water correction factor,  $f$ , was then applied to the measured methane concentrations to give corrected methane concentrations.

In dive 4553, GC 185, corrected methane concentrations averaged  $3.1 \pm 0.9$   $\mu\text{M}$  from the surface to 50 cmbsf and were similar between the flush and sample cylinders (Fig. 2-13a and Table 2-3). The isotopic composition of this methane between the flush and sample cylinders was very similar and overall, showed little depth change, averaging  $-37.9 \pm 2.7\text{‰}$  (Fig. 2-13b). This value is more enriched in  $^{13}\text{C}$  than the hydrate-bound methane of  $-42.9 \pm 0.6\text{‰}$  (Sassen et al., 2004).

On dive 4564, at GC 232, corrected methane concentrations between the core and HYDRA are similar, although HYDRA penetrated deeper than the core (Figs. 2-14a and 2-14b). At the sediment water interface (SWI), methane concentrations in HYDRA were around 11  $\mu\text{M}$  and increased to 2000  $\mu\text{M}$  at 47.5 cmbsf (Fig. 2-14a). Similarly, the core was also low at the SWI and increased steadily to 130  $\mu\text{M}$  by 16.5 cmbsf (Fig. 2-14a). At the next depth, however, concentrations reached 3700  $\mu\text{M}$ , much higher than the HYDRA values at this depth. Along with the concentrations measured, the carbon isotopic ratios were similar between the core and HYDRA pore-fluids. HYDRA flush samples averaged  $-46.3 \pm 3.7\text{‰}$ , sample cylinders averaged  $-46.0 \pm 4.5\text{‰}$ , and the core averaged  $-48.4 \pm 4.4\text{‰}$  (Fig. 2-14b). These values bracket around the hydrate-bound methane isotopic signature,  $-47.5 \pm 1.0\text{‰}$  (Sassen et al., 2004).

Methane concentrations between HYDRA and the core were very different when *in situ* concentrations exceeded saturation values with respect to methane at atmospheric pressure. On dive 4557, at GC 234, core methane concentrations reached a maximum of 2-6  $\mu\text{M}$  at 20 cmbsf but methane concentrations in HYDRA reached as high as 13,000  $\mu\text{M}$  methane at the deepest depth (47 cmbsf; Fig. 2-14c). The isotopic values of HYDRA pore-fluids are enriched in  $^{13}\text{C}$  compared to the core (Fig. 2-14d). HYDRA flush samples averaged -

50.7±3.2‰, sample cylinders averaged -51.6±2.2‰ and the core averaged -55.9±4.0‰. All of these isotope values were more depleted in <sup>13</sup>C compared to the hydrate-bound methane (Fig. 2-14d; Sassen et al., 2004). The down-core profile between HYDRA and the core are similar in shape; the values become depleted in <sup>13</sup>C down-core, exhibit a minima around 8 cmbsf, and then become more enriched in <sup>13</sup>C (Fig. 2-14d).

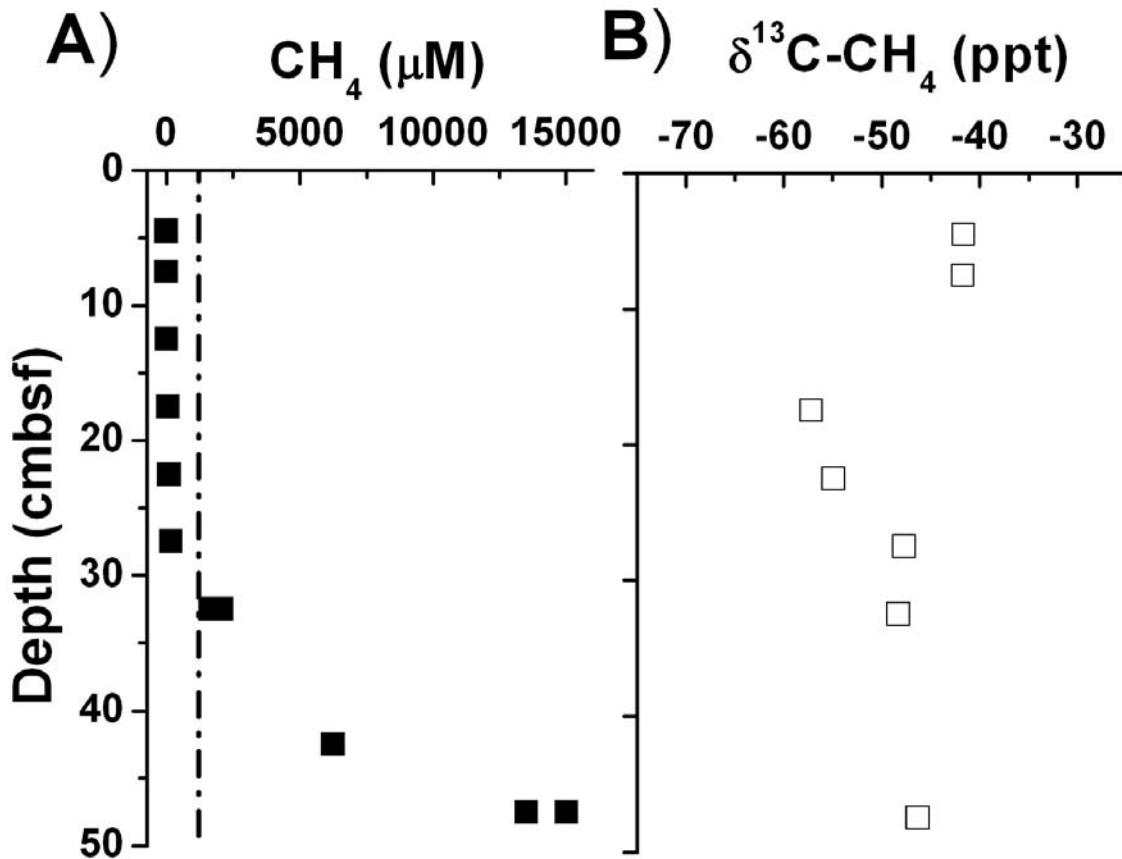


Fig. 2- 12: GC 232 dive 4405 A) methane concentrations and B) δ<sup>13</sup>C-CH<sub>4</sub>. Dotted-dashed line is saturation concentration at 1-atm (1200 uM). No corrections were made to methane concentrations. Concentrations include standard error of measurement.

**Table 2- 3: For the 2003 Gulf of Mexico deployment of HYDRA configuration 2, chloride and methane concentrations between flush and sample chambers. Methane concentrations in ppm were directly measured while methane concentrations corrected for DI water dilution (CH4-f) were calculated using equation 2. Shaded cells indicate depths where the flush chamber chloride concentrations are higher than in sample chambers.**

Dive	Depth (cm)	FLUSH chambers									
		Cl (mM)	stdev	f	stdev	sample volume (mL)	helium volume (mL)	CH4 (ppm)	stdev	CH4-f (uM)	stdev
4553	4.5	252.75	7.6	0.46	0.01	7	30	6.12	0.03	2.43	0.41
	7.5	267.83	8.0	0.49	0.01	7	30	8.80	0.04	3.30	0.56
	12.5	229.82	6.9	0.42	0.01	7	30	3.37	0.02	1.48	0.25
	17.5	215.36	6.5	0.40	0.01	5	30	3.11	0.02	2.03	0.34
	22.5	91.16	2.7	0.17	0.01	5	30	2.84	0.01	4.38	0.74
	27.5	140.83	4.2	0.26	0.01	5	30	3.09	0.02	3.09	0.52
	32.5	362.53	10.9	0.67	0.02	7	30	12.98	0.07	3.60	0.61
	37.5	236.82	7.1	0.43	0.01	7	30	10.31	0.05	4.38	0.74
	42.5	174.23	5.2	0.32	0.01	7	30	4.25	0.02	2.45	0.41
	47.5	313.88	9.4	0.58	0.02	7	30	12.97	0.07	4.16	0.70
4557	4.5	294.52	8.8	0.54	0.02	7	30	295.19	1.49	100.78	16.99
	7.5	241.24	7.2	0.44	0.01	7	30	6673.37	33.74	2781.62	468.80
	12.5	253.7	7.6	0.47	0.01	7	30	3006.43	15.20	1191.60	200.83
	17.5	233.69	7.0	0.43	0.01	7	30	6154.57	31.12	2648.25	446.32
	22.5	252.08	7.6	0.46	0.01	7	30	3246.68	16.42	1295.10	218.27
	27.5	224.8	6.7	0.41	0.01	7	30	3562.80	18.01	1593.66	268.59
	32.5	152.05	4.6	0.28	0.01	7	30	2262.47	11.44	1496.23	252.16
	37.5	269.57	8.1	0.49	0.01	7	30	15278.93	77.25	5699.31	960.53
	42.5	156.95	4.7	0.29	0.01	7	30	3324.37	16.81	2129.85	358.95
	47.5	256.87	7.7	0.47	0.01	7	30	35118.16	177.56	13747.37	2316.89
4564	4.5	408.65	12.3	0.75	0.02	7	30		0.00		
	7.5	373.59	11.2	0.69	0.02	7	30	100.13	0.51	26.95	4.54
	17.5	335.7	10.1	0.62	0.02	7	30	683.49	3.46	204.73	34.50
	27.5	151.28	4.5	0.28	0.01	5	30	104.20	0.53	96.96	16.34
	32.5	131.78	4.0	0.24	0.01	3	30		0.00		
	37.5	80.39	2.4	0.15	0.00	3	30	83.71	0.42	244.31	41.17
	42.5	39.38	1.2	0.07	0.00	2	30	12.47	0.06	111.45	18.78
	47.5	433.35	13.0	0.80	0.02	7	30	9105.93	46.04	2112.94	356.10



**Table 2-3 (continued): For the 2003 Gulf of Mexico deployment of HYDRA configuration 2, chloride and methane concentrations between flush and sample chambers. Methane concentrations in ppm were directly measured while methane concentrations corrected for DI water dilution (CH4-f) were calculated using equation 2. Shaded cells indicate depths where the flush chamber chloride concentrations are higher than in sample chambers. Na means samples were not collected from chamber.**

Dive	Depth (cm)	SAMPLE chambers									
		Cl (mM)	stdev	f	stdev	sample volume (mL)	helium volume (mL)	CH4 (ppm)	stdev	CH4-f (uM)	stdev
4553	4.5	352.61	10.58	0.65	0.02	7	30	8.99	0.05	2.56	0.43
	7.5	334.32	10.03	0.61	0.02	7	30	8.95	0.05	2.69	0.45
	12.5	273.14	8.19	0.50	0.02	6	30	7.00	0.04	3.01	0.51
	17.5	242.47	7.27	0.44	0.01	7	30	8.21	0.04	3.41	0.57
	22.5	172.16	5.16	0.32	0.01	7	30	2.57	0.01	1.50	0.25
	27.5	204.13	6.12	0.37	0.01	4	30	3.24	0.02	2.80	0.47
	32.5	456.11	13.68	0.84	0.03	7	30	16.54	0.08	3.65	0.61
	37.5	342.93	10.29	0.63	0.02	7	30	152.22	0.77	44.63	7.52
	42.5	279.56	8.39	0.51	0.02	7	30	11.31	0.06	4.07	0.69
	47.5	402.06	12.06	0.74	0.02	7	30	11.38	0.06	2.85	0.48
4557	4.5	422.92	12.69	0.78	0.02	7	30	348.75	1.76	82.92	13.97
	7.5	357.93	10.74	0.66	0.02	7	30	14046.58	71.02	3946.15	665.06
	12.5	315.72	9.47	0.58	0.02	7	30	2001.12	10.12	637.34	107.41
	17.5	387.81	11.63	0.71	0.02	7	30	7653.15	38.69	1984.37	334.43
	22.5	271.88	8.16	0.50	0.01	7	30	2202.12	11.13	814.45	137.26
	27.5	169.34	5.08	0.31	0.01	7	30		0.00		0.00
	32.5	180.46	5.41	0.33	0.01	7	30	3445.88	17.42	1920.09	323.60
	37.5	291.45	8.74	0.53	0.02	7	30	14289.20	72.25	4929.98	830.87
	42.5	131.82	3.95	0.24	0.01	7	30	1857.93	9.39	1417.26	238.86
	47.5	425.24	12.76	0.78	0.02	7	30	30293.66	153.16	7163.39	1207.27
4564	4.5	496.56	14.90	0.91	0.03	7	30	54.46	0.28	11.03	1.86
	7.5	463.17	13.90	0.85	0.03	7	30	122.60	0.62	26.62	4.49
	17.5	376.86	11.31	0.69	0.02	2	30	233.40	1.18	217.97	36.74
	27.5	Na									
	32.5	Na									
	37.5	Na									
	42.5	Na									
47.5	420.22	12.61	0.77	0.02	7	30	7781.42	39.34	1862.02	313.81	

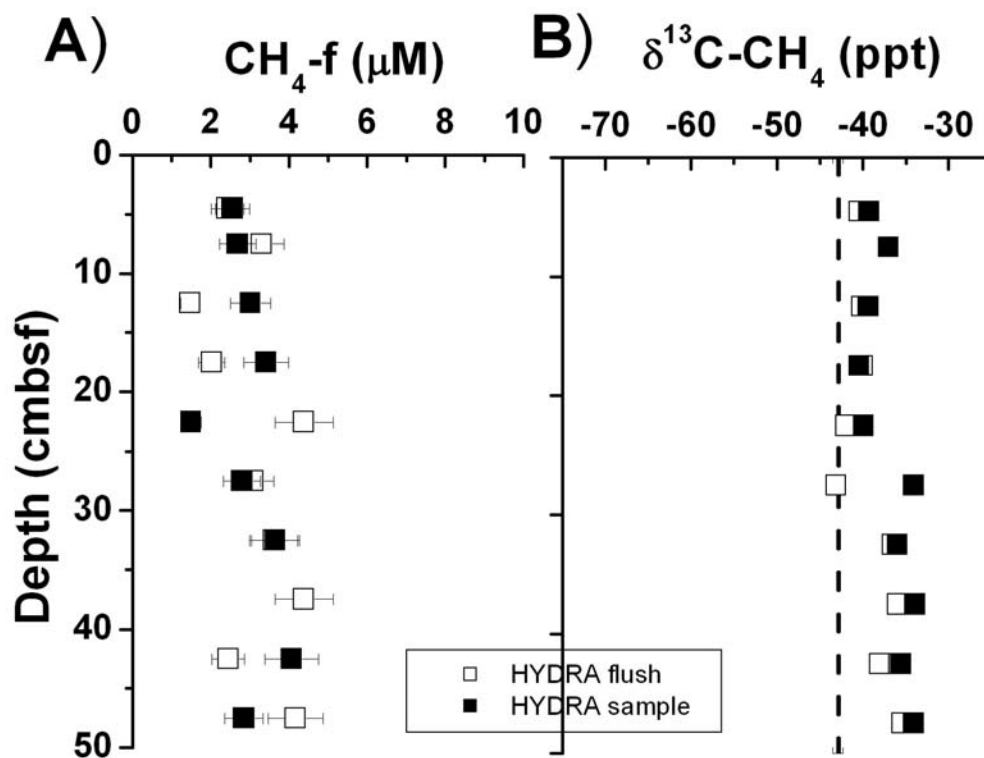


Fig. 2- 13: Gulf of Mexico, dive 4553, GC 185 methane a) concentrations corrected for “DI water” dilution and b) isotopic composition where the dot-dashed line indicates the isotopic value of hydrate-bound methane (Sassen et al., 2004). Concentration error bars represent analytical error.

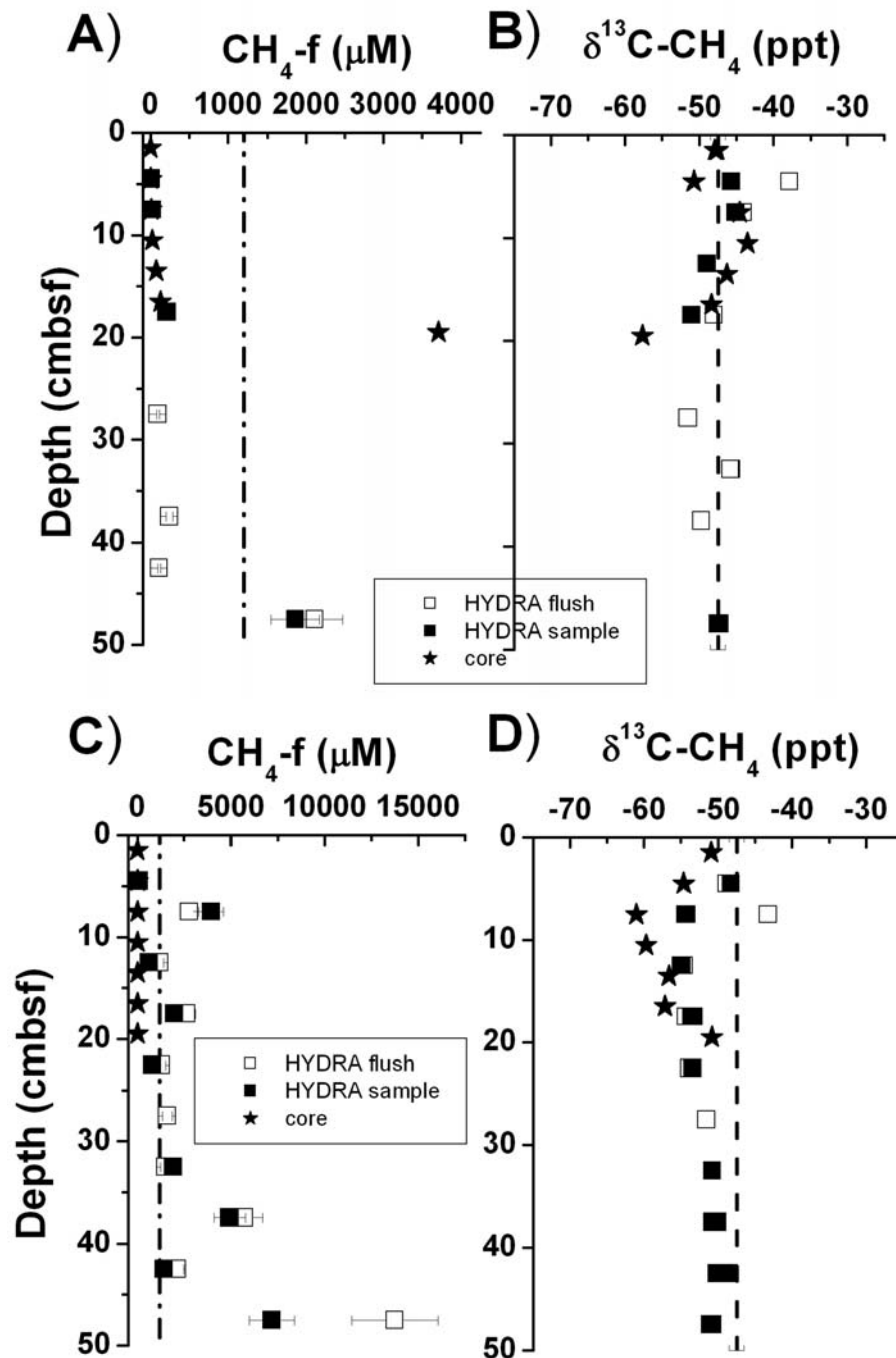


Fig. 2- 14: Gulf of Mexico comparisons between HYDRA and core from GC 232-4564 for a) methane concentrations corrected for DI water dilution and b) methane stable carbon isotopes. At GC 234-4557 c) methane concentrations corrected for DI water dilution and d) methane stable carbon isotopes. Dotted-dashed line in A) and C) is the saturation concentration at atmospheric pressure (1200  $\mu\text{M}$ ). Dashed line in C) and D) is the isotopic value of hydrate-bound methane (Sassen et al., 2004). Concentration error bars represent analytical error.

### **3.3. Configuration 3- *In situ* methane with DI water and channeling corrections at Barkley Canyon**

At the Cascadia Margin Barkley Canyon site, sediments overlie hydrate as thin veneers. In order to sample these sedimentary pore-fluids, HYDRA was configured for the third time. This configuration used the 3-D 4-port horizontal probe tip array which gave versatility in sample port depth. The large cone-shaped tips were also used to seal around the tips and reduce the possibility of overlying water channeling down the tips. Only four sample ports were on this configuration (see picture in Fig. 2-9). Although the footprint of this tip array was about 50 cm in diameter, the profiles were still assumed to result in vertical resolution. The methane profiles were corrected for both the DI water dilution and channeling of overlying water (Table 2-4). However, since the cores did not always penetrate as deeply as HYDRA, some of the overlying water channeling corrections could not be made.

For chloride concentrations, the flush chambers were always lower than the sample chambers (DI water correction, f; Table 2-4). For dive 692, the chambers collected between 67-86% seawater. For dive 693, the chambers exhibited a larger variation in the amount of seawater collected, between 13-61%. For dive 696, the chambers collected between 53-87% seawater.

On dive 692, HYDRA flush and sample chamber pore-fluids exhibited very similar methane concentrations and isotopic signatures (Figs. 2-15a and 2-15b). HYDRA methane concentrations reached as high as 3540  $\mu\text{M}$  at 17 cmbsf (Fig. 2-15a). In contrast, the core (which only penetrated to 13 cmbsf) exhibited maximum methane concentrations of only 120  $\mu\text{M}$  at 13 cmbsf (Fig. 2-15a). The isotopic signature of HYDRA averaged  $-40.1 \pm 0.9\text{‰}$  ( $n=7$ ) whereas the core was more enriched in  $^{13}\text{C}$ ,  $-26.9 \pm 3.3\text{‰}$  (Fig. 2-15b).

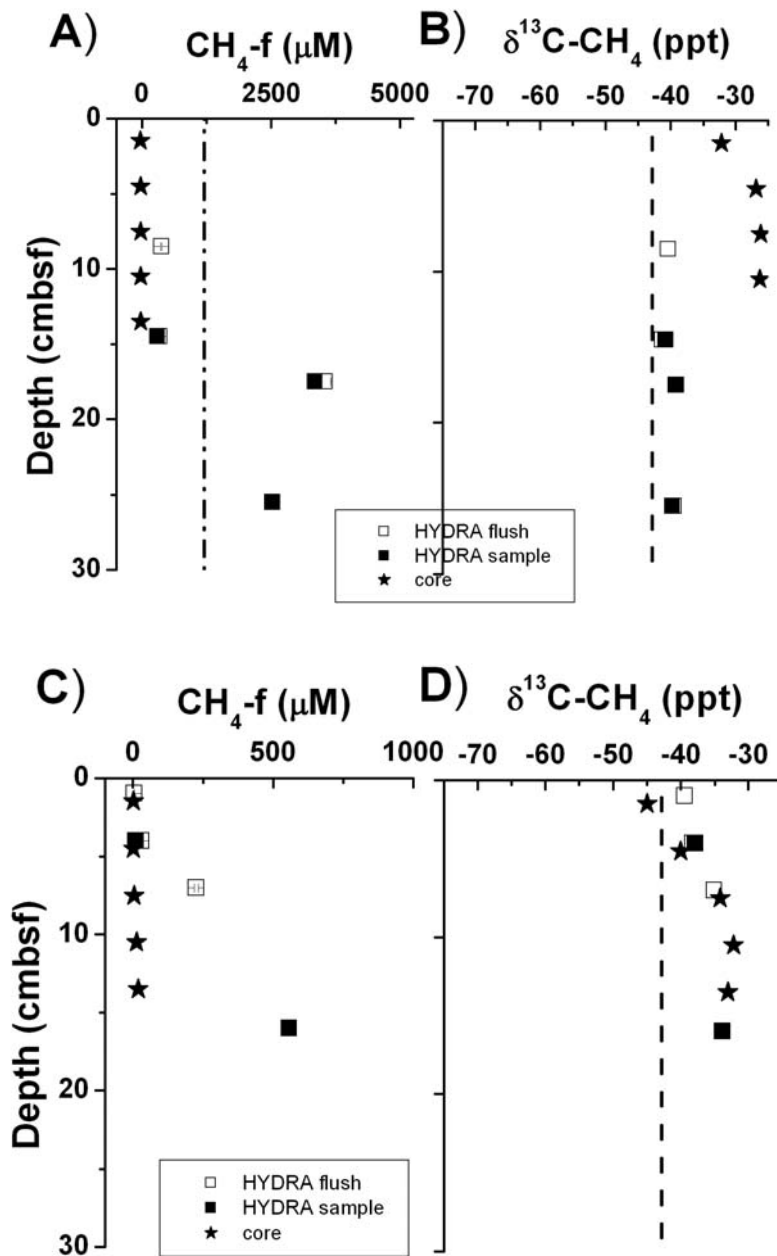
On dive 693, HYDRA methane concentrations reached a maximum of 560 uM at 16 cmbsf while the cores concentrations only reached 19 uM at 13.5 cmbsf (Fig. 2-15c).

Although the concentrations were different, the isotopic signature of HYDRA was similar to the core values and averaged  $-36.9 \pm 2.3\%$  and  $-36.9 \pm 5.5\%$ , respectively (Fig. 2-15d).

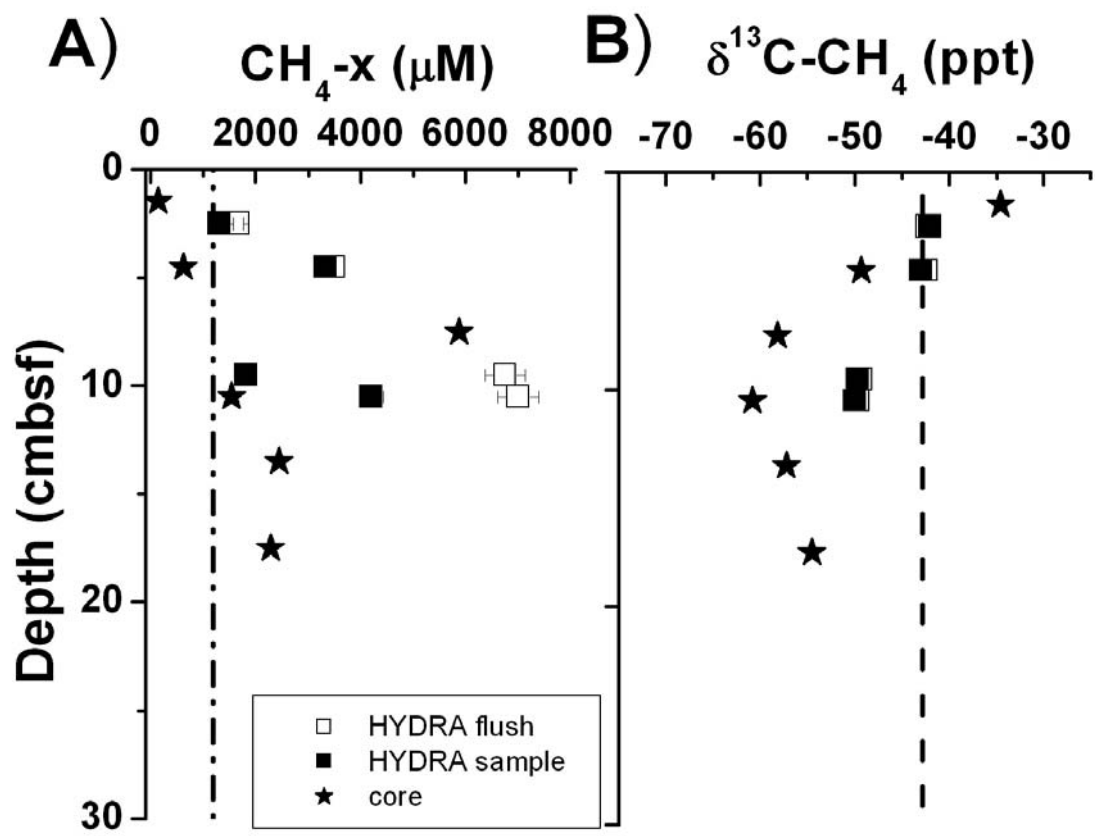
On dive 696, the methane concentrations from HYDRA (corrected for both DI water and channeling) and the core both reached  $\sim 5000$  uM by 10 cmbsf (Fig. 2-16a). Below this depth, the concentrations in the HYDRA increased to 7000uM while in the core, concentrations decreased, presumably due to dissolution during sampling. Also, there was a greater difference between the flush and sample cylinders at the deeper depths. Isotopically, the core and HYDRA methane were distinct from each other (Fig. 2-16b). While the core exhibited a sub-surface minimum of  $-60.8\%$ , HYDRA pore-fluids showed little down-core variation and averaged  $-46.1 \pm 3.8\%$  (Fig. 2-16b). This average isotopic value is slightly depleted in  $^{13}\text{C}$  compared to the hydrate-bound methane of  $-42.9 \pm 0.4\%$  (Pohlman et al., 2005).

**Table 2- 4: For the 2003 Barkley Canyon deployment of HYDRA configuration 3, values of measured sulfate, chloride, and methane concentrations. CH4-f are methane concentrations corrected for the DI water dilution and CH4-x are methane concentrations corrected for channeling. F= flush chamber and S= sample chamber. Shaded cells represent concentrations reported in Figs. 2-15 and 2-16.**

Dive	Sample or flush	Depth (cm)	Cl (mM)	stdev	f	stdev	Sample volume (mL)	Helium volume (mL)	CH4 (ppm)	stdev	CH4-f (uM)	stdev	SO4 (mM)	stdev	Core SO4 (mM)	stdev	x	stdev	CH4-x (uM)	stdev
692	F	8.5	387.06	11.61	0.71	0.02	7	20	2167.19	36.84	375.34	13.81	18.58	0.56	28.58	0.86				
	F	14.5	374.94	11.25	0.69	0.02	7	20	1908.28	28.88	341.18	12.27	19.55	0.59	28.45	0.85				
	S	14.5	466.92	14.01	0.86	0.03	7	20	2077.61	31.44	298.29	10.73	23.99	0.72	28.45	0.85				
	F	17.5	365.95	10.98	0.67	0.02	7	20	19331.34	292.56	3541.20	127.39	10.49	0.31						
	S	17.5	410.35	12.31	0.75	0.02	7	20	20491.72	310.12	3347.60	120.42	10.43	0.31						
	S	25.5	447.64	13.43	0.82	0.03	7	20	16860.79	255.17	2524.99	90.83	12.59	0.38						
693	F	1	330.38	9.91	0.61	0.02	7	20	26.82	0.46	5.44	0.20	17.06	0.51	28.69	0.86				
	F	4	121.65	3.65	0.22	0.01	3	20	19.89	0.34	30.69	1.13	6.62	0.20	28.39	0.85				
	S	4	224.65	6.74	0.41	0.01	4	20	20.15	0.34	10.52	0.39	10.64	0.32	28.39	0.85				
	F	7	163.88	4.92	0.30	0.01	3	20	235.76	4.01	225.03	8.28	8.42	0.25	28.09	0.84				
	S	16	72.40	2.17	0.13	0.00	2	20	128.86	2.19	556.78	20.49	4.84	0.15						
696	F	2.5	368.00	11.04	0.68	0.02	7	20	4552.51	68.90	829.30	29.83	17.74	0.53	22.44	0.67	0.49	0.03	1682.71	93.60
	S	2.5	451.32	13.54	0.83	0.03	7	20	5148.44	77.92	764.72	27.51	21.20	0.64	22.44	0.67	0.58	0.03	1314.63	73.12
	F	4.5	400.93	12.03	0.74	0.02	7	20	12366.89	187.16	2067.77	74.38	16.37	0.49	16.92	0.51	0.59	0.03	3491.64	194.22
	S	4.5	475.32	14.26	0.87	0.03	7	20	13809.50	208.99	1947.61	70.06	19.48	0.58	16.92	0.51	0.59	0.03	3324.49	184.92
	F	9.5	322.10	9.66	0.59	0.02	7	20	24535.14	371.32	5106.32	183.69	5.72	0.17	3.12	0.09	0.76	0.04	6754.56	375.71
	S	9.5	362.91	10.89	0.67	0.02	7	20	8129.60	65.21	1501.69	50.46	5.22	0.16	3.12	0.09	0.82	0.04	1821.55	98.59
	F	10.5	290.41	8.71	0.53	0.02	7	20	23097.96	349.57	5331.78	191.80	3.96	0.12	0.36	0.01	0.76	0.04	7002.63	389.51
	S	10.5	466.56	14.00	0.86	0.03	7	20	23198.40	186.08	3333.19	112.01	5.54	0.17	0.36	0.01	0.79	0.04	4199.09	227.27



**Fig. 2- 15: Barkley Canyon comparison between HYDRA and cores from dive 692 a) methane concentrations corrected for DI water dilution and b) stable carbon isotopes. And from dive 693 c) methane concentrations corrected for DI water dilution and d) stable carbon isotopes. Dotted-dashed line in a) is the saturation concentration at atmospheric pressure (1200  $\mu\text{M}$ ). Dashed line in c) and d) is the isotopic value of hydrate-bound methane (Pohlman et al., 2005). Concentration error bars represent analytical error.**



**Fig. 2- 16: Barkley Canyon comparison between HYDRA and cores from dive 696 a) methane concentrations corrected for channeling and b) stable carbon isotopes. Dotted-dashed line in a) is the saturation concentration at atmospheric pressure (1200  $\mu\text{M}$ ). Dashed line in b) is the isotopic value of hydrate-bound methane (Sassen et al., 2004). Concentration error bars represent analytical error.**



### **3.4. Configuration 4- *In situ* methane with channeling overlying water correction at Barkley Canyon**

Changes to the fourth configuration of HYDRA included modifying the previous 3-D probe tip array to contain 10 sample ports (instead of 4) and eliminating the flush cylinder so only one sample cylinder was used (see Fig. 2-10). These changes were made to increase sample resolution and to decrease sample volume. Cores were also collected adjacent to HYDRA so the methane concentrations could be corrected for both the DI-water dilution and channeling of overlying water. For dive 798, the chambers collected between 10-72% seawater within the fluids (correction  $f$ , Table 2-5). For dive 799, the chambers exhibited a larger variation in the amount of seawater collected, between 10-71%. For dive 802, the chambers collected between 8-67% seawater within the fluids.

Prior to the dives, the sample chamber DI water fluids were prepared with green dye to check the assumption that the pore-fluids were seawater concentrations of chloride. The results of the dye calculated DI water dilution were similar to the seawater assumed DI water dilution, exhibiting at most a 7% difference (Table 2-6).

For dive 798, methane concentrations in HYDRA were only corrected for DI-water dilution (Table 2-5). These concentrations were similar to the core until about 15 cmbsf where the core concentrations exceeded HYDRA (Fig. 2-17a). Below this depth, the maximum methane concentration measured in the core was 3000  $\mu\text{M}$  whereas in HYDRA, concentrations only reached 890  $\mu\text{M}$  (Fig. 2-17a). Isotopically, the core exhibited a subsurface minimum  $\delta^{13}\text{C-CH}_4$  value of -62.2‰ at 10 cmbsf (Fig. 2-17b). For HYDRA, the  $\delta^{13}\text{C-CH}_4$  value was -45.3‰ at the surface, reached -47‰ at depth, and the average value was  $-43.7 \pm 3.4$ ‰ (Fig. 2-17b).

For dives 799 and 802, methane concentrations were corrected for both the DI-water dilution and the channeling of overlying water (Table 2-5). On dive 799, maximum core methane concentrations reached ~2,500 uM at 11.5 cmbsf and did not exceed this value down-core (Fig. 2-17c). Methane concentrations measured in HYDRA were similar to the core concentrations until 18 cmbsf (Fig. 2-17c). At 18 cmbsf, the two samples collected with HYDRA were 3300 and 17780 uM (Fig. 2-17c). This large variation could have been due to the horizontal variability in methane concentrations. The  $\delta^{13}\text{C-CH}_4$  values from HYDRA were -47.3‰ at the surface, reached -43.3‰ at depth, and the average value was  $-42.8 \pm 2.0\%$  (Fig. 2-17d). Core  $\delta^{13}\text{C-CH}_4$  values resulted in more down-core variability. Values from the SWI to 20 cmbsf were around -47‰, below this depth, values become depleted in  $^{13}\text{C}$  until the minima was reached of -61‰ and then became more enriched in  $^{13}\text{C}$  (Fig. 2-17d).

On dive 802, the importance of having a pore-fluid sampler in hydrate sites was illustrated. When the core was collected, it contained disseminated hydrate chips. As the core was brought from the seafloor to the ocean surface and sub-sampled for geochemical analysis, these hydrate chips were visibly decomposing and releasing methane. As a result, methane concentrations were higher in the core than in HYDRA (Fig. 2-18a). It is interesting to note, however, that even with dissociating hydrate contained within the core, methane concentrations only reached as high as 24,000 uM, about 3 times less than saturated methane concentrations at Barkley Canyon (67,000 uM). Yet, the  $\delta^{13}\text{C-CH}_4$  of the core samples averaged  $-46.1 \pm 6.4\%$  for the whole core profile and  $-48.4 \pm 1.8\%$  from 4-15 cmbsf (Fig. 2-18b). For HYDRA, methane concentrations were less than 2500 uM (Fig. 2-18a) and had an average stable carbon isotopic composition of  $-43.1 \pm 2.0\%$  (Fig. 2-18b), similar to the

hydrate-bound methane value of  $-42.9 \pm 0.4\%$  observed at the same site (Pohlman et al., 2005).

**Table 2- 5: For 2004 Barkley Canyon HYDRA configuration 4, measured sulfate, chloride, and methane concentrations and correction factors as discussed in section 2.4.1.2. Shaded cells are concentrations reported in Figs. 2-17 and 2-18.**

Site	Depth (cm)	Cl (mM)	stdev	f	stdev	Sample volume (mL)	Helium volume (mL)	CH4 (ppm)	stdev	CH4-f (uM)	stdev	SO4 (mM)	stdev	Core SO4 (mM)	stdev	x	stdev	CH4-x (uM)	stdev
798	0.0	346.09	10.38	0.64	0.02	11	19	15.45	0.09	1.81	0.06	16.98	0.51	28.00	0.84				
	0.0	346.09	10.38	0.64	0.02	11	22	14.48	0.09	1.96	0.07	16.98	0.51	28.00	0.84				
	0.0	54.06	1.62	0.10	0.00	11	19	7.01	0.04	5.26	0.17	2.72	0.08	28.00	0.84				
	7.0	108.14	3.24	0.20	0.01	11	19	5.33	0.03	2.00	0.07	5.02	0.15	19.48	0.58				
	16.0	389.86	11.70	0.72	0.02	11	19	2019.22	12.12	209.90	6.96	19.10	0.57	*	0.00				
	19.0	284.75	8.54	0.52	0.02	10	20	2214.53	13.29	364.94	12.11	13.67	0.41	*	0.00				
	19.0	108.30	3.25	0.20	0.01	11	19	442.51	2.66	165.59	5.49	4.41	0.13	*	0.00				
	22.0	244.12	7.32	0.45	0.01	11	19	5357.06	32.14	889.33	29.51	8.44	0.25	*	0.00				
799	0.0	342.96	10.29	0.63	0.02	11	19	85.08	0.51	10.05	0.33	17.72	0.53	28.70	0.86	1.42	0.08	7.10	0.45
	9.0	257.64	7.73	0.47	0.01	11	19	1282.24	7.69	201.70	6.69	12.74	0.38	14.67	0.44	0.20	0.01	1013.86	63.85
	9.0	387.27	11.62	0.71	0.02	11	19	4529.76	27.18	474.02	15.73	19.60	0.59	14.67	0.44	0.16	0.01	3006.96	189.37
	9.0	251.35	7.54	0.46	0.01	11	19	707.80	4.25	114.12	3.79	13.56	0.41	14.67	0.44	0.04	0.00	2926.36	184.29
	12.0	44.21	1.33	0.08	0.00	6	24	278.93	1.67	592.12	19.65	3.71	0.11	8.38	0.25	^			
	12.0	54.34	1.63	0.10	0.00	6	24	34.54	0.21	59.65	1.98	3.30	0.10	8.38	0.25	^			
	12.0	94.32	2.83	0.17	0.01	5	25	8.17	0.05	10.16	0.34	4.49	0.13	8.38	0.25	0.19	0.01	54.14	3.41
	18.0	55.20	1.66	0.10	0.00	11	19	48757.13	292.54	35796.29	1187.75	3.27	0.10	1.00	0.03	^			
802	18.0	220.64	6.62	0.40	0.01	12	18	6805.94	40.84	1085.61	36.02	8.28	0.25	1.00	0.03	0.33	0.02	3297.41	207.66
	18.0	360.24	10.81	0.66	0.02	11	19	22759.06	136.55	2560.36	84.95	17.07	0.51	1.00	0.03	0.14	0.01	17783.98	1119.96
	0.0	365.89	10.98	0.67	0.02	11	22	2.00	0.01	0.26	0.01	19.45	0.58	28.18	0.85	0.57	0.03	0.45	0.03
	0.0	365.89	10.98	0.67	0.02	11	22	2.08	0.01	0.27	0.01	19.45	0.58	28.18	0.85	0.57	0.03	0.47	0.03
	5.5	360.74	10.82	0.66	0.02	11	22	142.00	0.85	18.47	0.61	18.30	0.55	13.12	0.39	0.14	0.01	132.52	8.35
	5.5	41.24	1.24	0.08	0.00	10	23	77.62	0.47	101.56	3.37	2.65	0.08	13.12	0.39	^			
	5.5	224.78	6.74	0.41	0.01	9	24	101.86	0.61	28.35	0.94	11.79	0.35	13.12	0.39	0.08	0.00	338.43	21.31
	8.0	321.54	9.65	0.59	0.02	12	22	5345.52	32.07	729.24	24.20	14.15	0.42	9.27	0.28	0.29	0.02	2512.78	158.24
802	11.0	197.81	5.93	0.36	0.01	10	18	500.98	3.01	106.96	3.55	8.15	0.24	6.11	0.18	0.32	0.02	338.67	21.33
	13.0	159.25	4.78	0.29	0.01	11	19	924.82	5.55	235.35	7.81	6.95	0.21	4.63	0.14	0.24	0.01	960.83	60.51

^ samples where the DI-water dilution correction resulted in sulfate concentrations greater than the 30 mM which artificially exaggerated corrected methane concentrations and gave negative values for the x correction factor.

\* cores that did not penetrate as deeply as HYDRA

**Table 2- 6: Measured chloride concentrations of sample chambers for configuration 4, Cascadia Margin. The correction factor, f, was estimated with both assuming the values were seawater and using an independent color dye method.**

<b>Dive</b>	<b>Depth (cm)</b>	<b>Cl (mM)</b>	<b>f<sub>seawater</sub></b>	<b>f<sub>color dye</sub></b>
798	0	346.09	64	62
	0	54.06	10	17
	7	108.14	20	24
	16	389.86	72	68
	19	284.75	52	56
	19	108.30	20	25
	22	244.12	45	47
799	0	342.96	63	60
	9	257.64	47	45
	9	251.35	46	45
	9	387.27	71	67
	12	44.21	8	9
	12	54.34	10	13
	12	94.32	17	18
	18	360.24	67	62
	18	220.64	40	36
	18	55.20	10	14
802	0	365.89	67	61
	5.5	41.24	8	7
	5.5	224.78	41	39
	5.5	360.74	66	62
	8	321.54	59	53
	11	197.81	36	32
	13	159.25	29	27

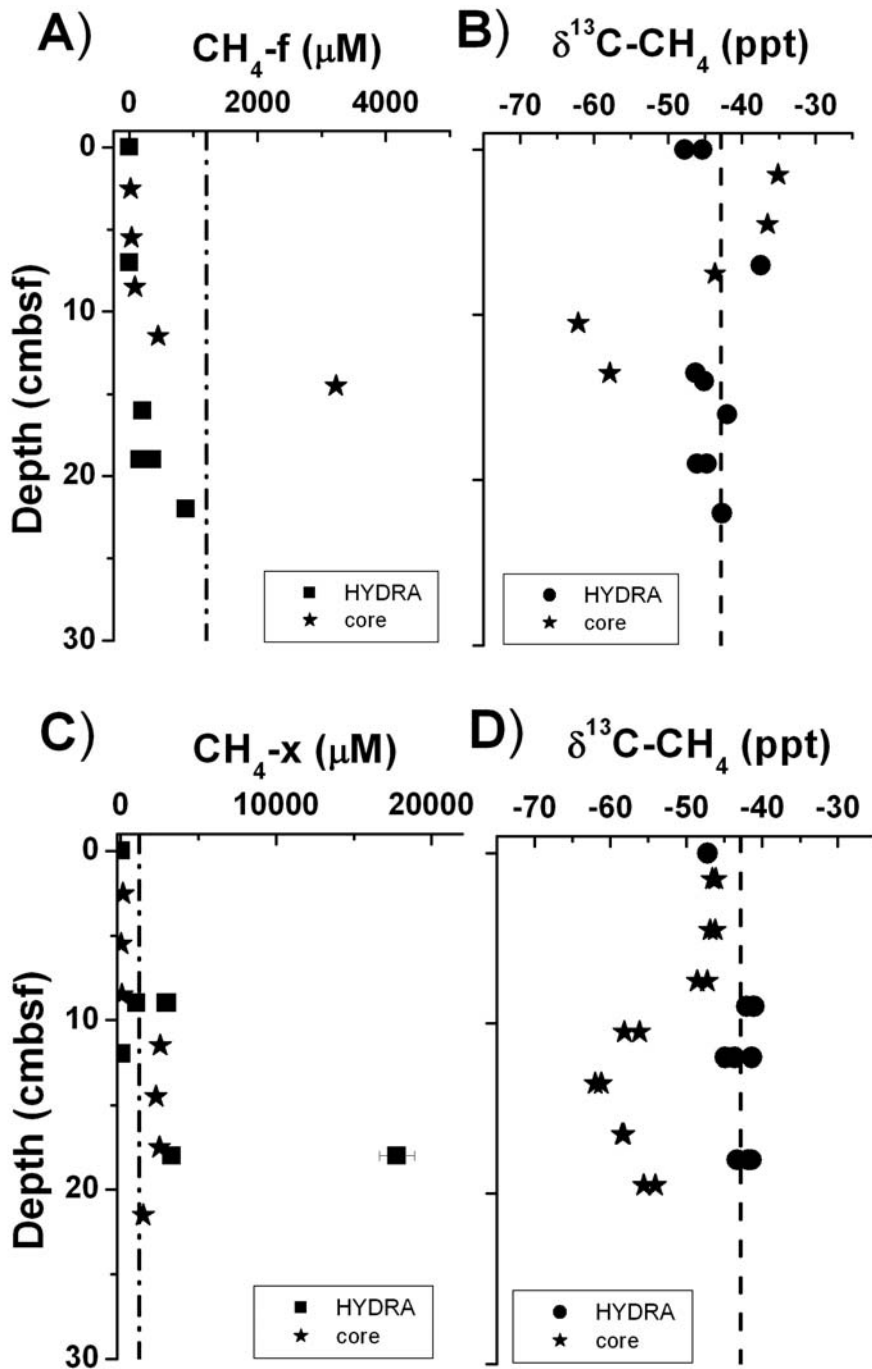


Fig. 2- 17: Barkley Canyon comparison between HYDRA and cores from dive 798 a) methane concentrations corrected for DI water dilution and b) stable carbon isotopes. And from dive 799 c) methane concentrations corrected for channeling and d) stable carbon isotopes. Dotted-dashed line in a) and c) is the saturation concentration at atmospheric pressure (1200  $\mu\text{M}$ ). Dashed line in b) and d) is the isotopic value of hydrate-bound methane (Pohlman et al., 2005). Concentration error bars represent analytical error.

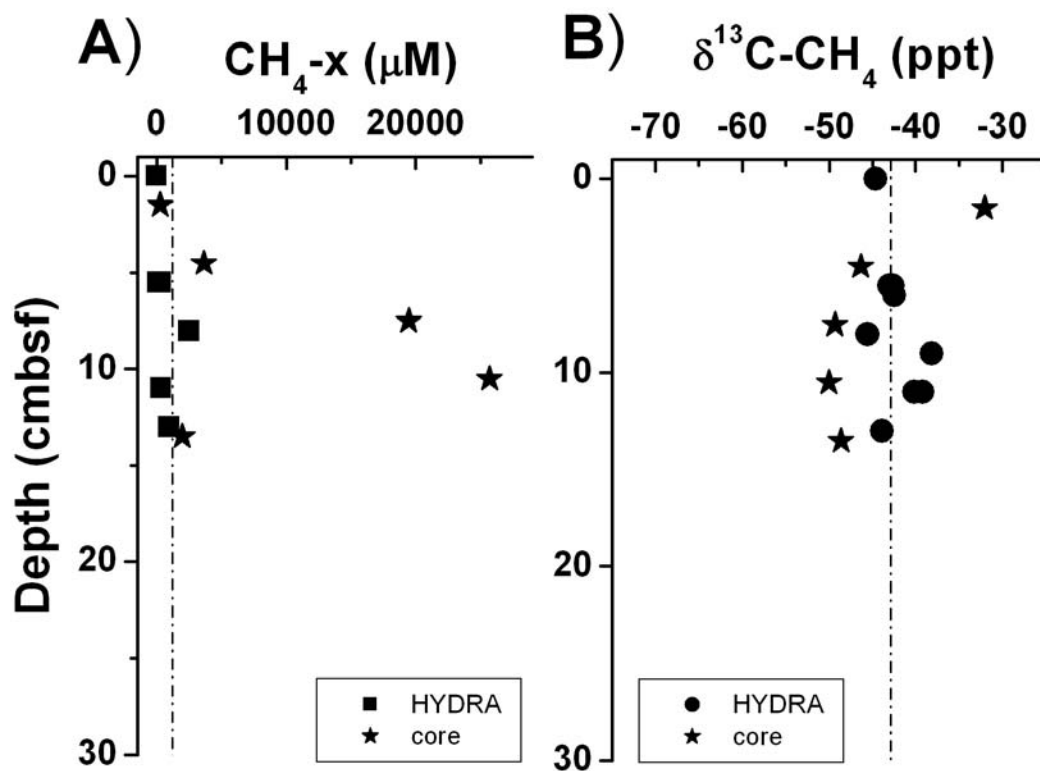


Fig. 2- 18: Barkley Canyon comparison between HYDRA and cores from dive 802 a) methane concentrations corrected for channeling and b) stable carbon isotopes. Concentration error bars represent analytical error.

## 4. DISCUSSION

In order to fully understand hydrate stability, the *in situ* dissolved methane concentrations and stable isotopic composition surrounding such hydrates are needed. Since dissolved methane de-gasses during the ascent through the water column, traditional coring techniques may not be suitable for obtaining *in situ* methane concentrations. Therefore, HYDRA was developed and tested in hydrate-bearing sediments. Different configurations were needed to address specific issues with the design. It was successfully deployed fourteen times and of those, eight were compared to concentration and stable isotope profiles from adjacently collected cores to test whether the former method is a more accurate way to determine *in situ* methane concentrations in hydrate-bearing sediments.

### 4.1. Overall HYDRA considerations

#### 4.1.1. HYDRA design for gas concentrations

The main goal of this chapter was to modify an existing instrument to collect pore-fluid samples for the measurement of *in situ* methane concentrations. This instrument actively collects sample through small ports along a probe tip. One of the fundamental problems with this design is that it creates such a large pressure drop at the sample port, it may essentially degas the solution and result in higher methane concentrations than are found *in situ*. Tests to determine if this was a problem were not conducted for these deployments and should be considered for future use.

#### 4.1.2. HYDRA configurations

The development of HYDRA over the 14 deployments resulted in four different configurations. In the first and earliest configuration, the pore-fluid samples were not retained at *in situ* pressures. The concentrations resulted in classic degassing profiles where



concentrations reached saturation at atmospheric pressure and then tailed off (i.e., Fig. 2-11c). Therefore, the addition of high pressure valves was critical and all subsequent configurations had these valves. With the valve addition, there was no evidence of a tailing off when concentrations exceeded saturation at atmospheric pressure (i.e., Fig. 2-12a). The difference between profiles without and with valves shows that the valves were successful in retaining the samples and giving more accurate concentrations.

Assessment of the flush and sample chambers led to some changes in the HYDRA configuration. While the  $\delta^{13}\text{C-CH}_4$  values between the flush and sample chambers exhibited exceptional agreement, the flush chamber was not efficient at flushing the lines. Furthermore, the flush chamber setup collected a large volume of pore-fluid, ~15 mL. For a sediment porosity of 0.9, this pore-fluid volume corresponds to a sediment volume of 17 mL which means sampling occurred at a minimum radius of 2 cm from the sample ports (assuming sampling is constant as a semi-sphere from port intake). In the vertical tip array, since the sample ports are spaced at 5 cm increments, there is a possibility that the pore-fluids will be sampled from overlapping depths. Therefore, to reduce the possibility of collecting large volumes of samples at one depth, the flush chamber was eliminated in the fourth configuration which decreased the total volume from 14 mL to 11 mL. From the fourth configuration, chloride concentrations results showed that the sample chambers still only collected ~7% seawater at some depths (Table 2-5). It is possible that the dead-volume within the high pressure valves is too large. For future configurations, alternative valves that are low dead volume should be considered.

#### 4.1.3. Correction factors

While HYDRA concentration profiles more accurately depicted *in situ* conditions, there was evidence of sample dilution that resulted in lower measured concentrations. One such dilution was caused by the inefficient flushing of the lines during deployment and was referred to as the “DI water” dilution. This was corrected by measuring the sample fluids for chloride concentrations and assuming they should be seawater values. This correction was made for most of the concentration profiles. The DI water correction factor was also made by adding colored water to the system prior to deployment, measuring the initial absorbance of this water and then measuring the resulting absorbance after sample collection (Table 2-6). The correction factors from the color dye were comparable to the correction factors assuming a seawater chloride value.

The variability of the dilution factors was remarkable between and within all configurations of HYDRA. For configuration 2, the dilution factors ranged from 17-67% in flush chambers and 31-91% in sample chambers. The dilution factors were improved in configuration 3, due to the shortening of the tubing and subsequent decrease of the dead volume. In this configuration, the dilution factors ranged from 22-74% in flush chambers and 13-87% in sample chambers. What was surprising was that in configuration 4, the dilution factors were actually lower, suggesting that the sample volume increase and use of only one valve did not improve the dead volume issue.

At times, application of the DI water correction resulted in sulfate concentrations that were higher in HYDRA than typical seawater. This tended to occur when the sample was between 8-10% pore-fluid. Since seawater is typically ~30 mM, values from samples

containing small amounts of pore-fluids (where sample was mostly overlying water) should be considered suspect.

The need for a second correction factor was evident when sulfate concentrations were compared between HYDRA pore-fluids and adjacent cores. After applying the “DI water” correction to the measured HYDRA sulfate concentrations, sulfate concentrations were higher in HYDRA than in cores at similar depths. A possible explanation for this was channeling of overlying seawater down the probe tips during sampling. Therefore, this channeling correction was estimated by comparing sulfate concentrations between the core and HYDRA sample waters. After applying the “DI water” correction to sulfate concentrations of HYDRA waters, these concentrations were compared to those measured in the cores and the correction factor  $x$  was calculated (Table 2-4).

The channeling water dilution correction was made for the Barkley Canyon deployments with mixed success. For some of the cores, the sulfate concentrations did not change with depth so the correction was not effective and possibly not necessary. However, for the remaining cores, the correction was made and showed that between 4 and 82% of the fluids collected were pore-fluids and not overlying seawater.

There are three issues with the channeling correction factor. First, it assumes that the water channeling down the probe tips is pure seawater and no mixing between other pore-fluids takes place. Since we have no independent method to determine the source of the channeling fluids, this was the best assumption to make. This assumption may overestimate the correction factor and result in an underestimate of the methane concentrations. The second issue was that the channeling correction factor assumes that the sulfate profiles in the cores will be the same in the large spatial scale covered by the 3D probe tip arrays.

However, other researches have reported on the high spatial variability of biogeochemical processes at seep sites (Arvidson et al., 2004; Joye et al., 2004; Orcutt et al., 2005).

Therefore, future deployments of HYDRA should collect more than one core surrounding the probe tip. The third issue for the channeling correction was in using sulfate itself. In areas where sulfate does not change with depth, this correction could not be made. Yet, the fluids may still be channeling. Therefore, sulfate may not be the best tracer for channeling fluids and future experiments should consider ammonium as a more sensitive tracer.

#### **4.2. HYDRA versus cores: methane concentrations**

With the corrections made, the concentrations in HYDRA were typically higher than in the cores. The exception to this was when HYDRA concentrations were below saturation at atmospheric pressure. Then, the concentrations were comparable. What was unexpected was that even with issues and large corrections that had to be made, maximum methane concentrations in HYDRA still only reached 17,780  $\mu\text{M}$  (i.e. Figs. 2-12a and 2-14c). Since these are below the saturation concentration of  $\sim 67,000$   $\mu\text{M}$ , the fluids around hydrates are undersaturated with respect to methane. However, the high methane concentrations were not corrected for any dilution effects and may still be minimums.

There were two exceptions to the overall result that methane concentrations in HYDRA were higher than in the cores. First, on dives 4564 and 798, at two depths, methane concentrations in the core were higher than HYDRA. This could be explained by a bubble entrained within the core. And secondly, methane concentrations were higher in the core than in HYDRA pore-fluids on dive 802. However, this was due to the decomposition of disseminated hydrate pieces contained within the lower parts of the core. These results show that it is critical to collect pure pore-water samples at *in situ* pressures at hydrate sites.

### 4.3. HYDRA versus cores: $\delta^{13}\text{C-CH}_4$ values

We expected the  $\delta^{13}\text{C-CH}_4$  values to be similar between HYDRA and sediment cores. When the isotope results were analyzed overall, of the 8 deployments, 2 showed that HYDRA and cores were similar (dives 4564 and 693), 5 showed that the cores were slightly depleted in  $^{13}\text{C}$  than in HYDRA (dives 4557, 696, 792, 793, 802), and 1 showed that the cores were enriched in  $^{13}\text{C}$  compared to HYDRA (dive 692). However, when the  $\delta^{13}\text{C-CH}_4$  values were compared at the same depth, a different pattern emerged (Fig. 2-19). Sixty percent of the data was explained by the core data being enriched in  $^{13}\text{C}$  compared to HYDRA data. Four explanations are offered for the pattern.

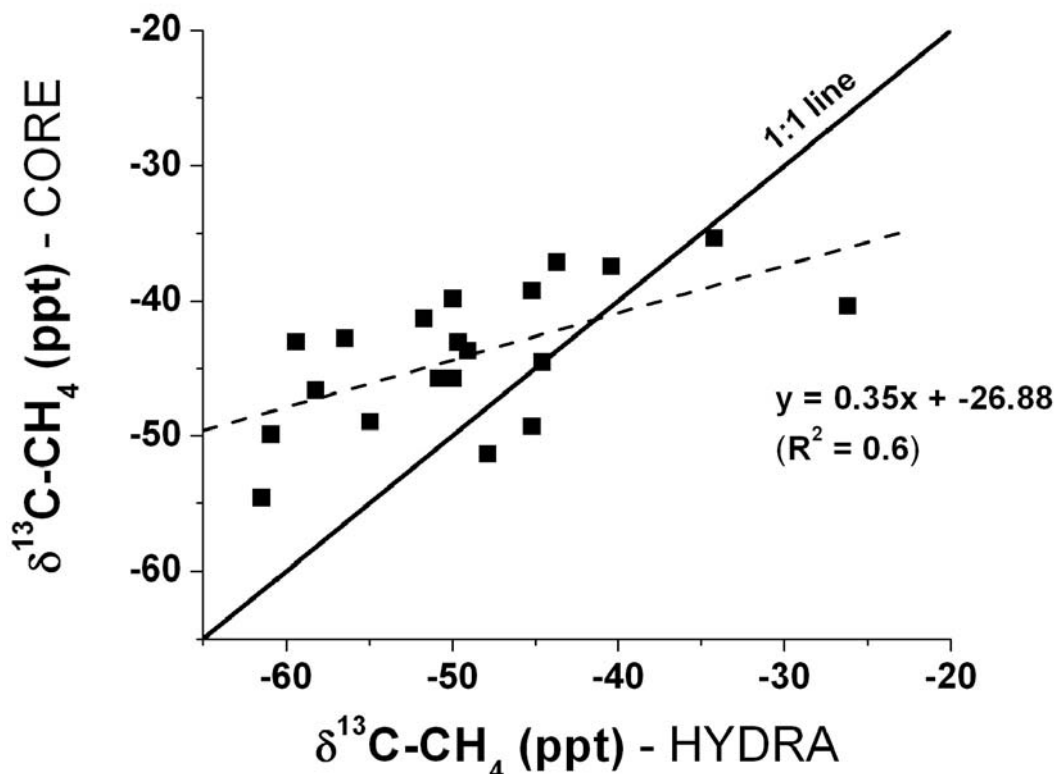


Fig. 2- 19: Comparison between methane stable carbon isotope values of cores and HYDRA. The solid line is the 1:1 line for reference and the dotted line is the linear regression of all data with the resultant equation on the plot.

*HYDRA leak.* One potential explanation for the isotopic difference is a leak in HYDRA itself. Even though the instrument was pressure tested prior to dives and no bubbles were seen during ascent, a small leak may fractionate the isotopes, allowing the  $^{12}\text{C}$  to escape first and leaving the remaining pore-waters enriched in  $^{13}\text{C}$  compared to the core values. However, this explanation should result in a consistent difference between HYDRA and core comparisons. Since the isotope results were scattered (Fig. 2-19), this explanation is not supported with the current data set. Furthermore, this explanation is probably not valid because the flush and sample chambers had very similar  $\delta^{13}\text{C-CH}_4$  values for every deployment of HYDRA. If there was a leak in HYDRA, you might expect inconsistent results between these two chambers.

*Isotope fractionation.* A second possible explanation is that the methane isotopes fractionate during ascent in the cores. As the cores ascend and degas, the light isotope is lost from the dissolved methane pool, leaving the residual methane isotopically enriched in  $^{13}\text{C}$ . However, as in the first explanation, fractionation during ascent would also result in a consistent difference between the HYDRA and core isotope values and this was not observed. Furthermore, experiments have shown that cores do not fractionate during degassing (Wallace et al., 2000).

*HYDRA not collecting dissolved methane pool.* The third possible explanation for the isotopic differences between HYDRA and cores is that the HYDRA isotope values were not reflective of the dissolved methane pool. Throughout the HYDRA profiles, the isotope values of HYDRA pore-fluids were similar to the isotope values of the hydrate-bound methane. Since HYDRA collects a sample by actively sucking the pore-fluid over a short period of time, there is a possibility that it dissociates tiny pieces of hydrate upon collection.

Although this possibility makes sense for dive 802 where disseminated hydrate was visually observed during sampling, there was no direct evidence of disseminated hydrate on the other dives. However, an acoustic survey conducted over the sampling sites at Barkley Canyon suggested that disseminated hydrate is widely dispersed and quite abundant (Ross Chapman, personal communication, 2005). Therefore, the resulting isotopic difference between HYDRA and the cores could be due to the two methods collecting different methane pools.

*HYDRA fractionates during collection.* Although the later explanation can't be discounted, a final explanation could be a result of a fundamental problem with the way HYDRA works. As presented in section 4.1.1., the HYDRA design could create such a large pressure drop at the sample port that it may essentially degas the solution. This degassing could then affect the isotope values by collecting the lighter isotope preferentially over the heavier isotope. This preferential uptake would then explain the isotope distribution seen in Figure 19. However, because HYDRA is left for over 15 minutes, the isotopes should re-equilibrate over this time. This possibility was not directly tested with in lab experiments and needs to be considered for future understanding of HYDRA.

#### **4.4. Overall assessment of HYDRA**

HYDRA has several advantages. It was shown to measure higher methane concentrations compared to traditionally collected cores and therefore, is possibly more accurate for assessing the *in situ* methane concentrations. It can sample deeper sediments as well as thin layers covering hydrate and therefore sample micro environments not sampled by cores. Its large footprint samples both vertical and horizontal gradients. The disadvantages of this instrument are that it has a large footprint and is therefore hard to determine simple vertical gradients, like a core. Right now, the design leaves too many

questions as to the corrections that need to be made. Although the DI water issue was resolved, we can not constrain the overlying water channeling issue. Another problem is that HYDRA samples such large volumes that the actual depth which was sampled is still in question. And finally, HYDRA may be artificially dissolving disseminating hydrate.

With these advantages and disadvantages, the fact remains that even with 14 deployments to collect *in situ* concentrations, from several different local environments, and different distances from hydrate, nearly saturated fluids were never measured. This leaves us to suppose that the pore-fluids around hydrates may therefore play a role in hydrate stability.

#### **4.5. Hydrate stability and *in situ* methane concentrations**

This chapter is mainly concerned with the development of HYDRA, the interpretation of the data presented is discussed in chapter 4. However, it is worth briefly mentioning what the data presented means for hydrate stability. Although several HYDRA methane concentration profiles could not be corrected for dilution issues, three profiles (dives 696, 799, and 802) were corrected for both dilution issues and represent the best *in situ* concentrations obtained. Of these profiles, one was collected on top of hydrate, within 3-15 cm of the hydrate surface. So, to address hydrate stability, within the context of methane concentrations, the data collected from dive 802 will be used.

As discussed in the introduction, hydrates remain stable when they are surrounded by fluids that are saturated with methane, ~67,000 uM at Barkley Canyon. This concentration was not found at any of the dives sites presented in this paper, not even for dive 802 that was within 3 cm of the hydrate surface. According to theory, this suggests that the hydrates are currently dissolving. In chapter 4, I show how these concentrations can be used to calculate dissolution rates and how the data suggest that shallow hydrates may be more stable than



theory predicts. Therefore, quantifying the dissolved methane concentrations surrounding hydrate is critical to understanding hydrate stability.

## 5. CONCLUSIONS

The first ever *in situ* pore-fluid samples were collected from hydrate-rich sediments in the northern Gulf of Mexico and northern Cascadia Margin using a novel instrument HYDRA. HYDRA was successfully deployed at hydrate sites on 14 dives over 5 years. Samples were measured for methane concentrations and isotopic compositions and compared to adjacent cores to determine the importance of *in situ* versus core sampling at hydrate sites. Methane concentrations and isotopic compositions were different in HYDRA than in cores. When disseminated hydrate was not present, methane concentrations were, on average, higher in HYDRA than the core. The fact that tiny disseminated chips of hydrate were present in cores suggests that coring in hydrate-rich sediments is not ideal to obtain dissolved methane concentrations. Different configurations of HYDRA were also tested and compared. High pressure valves are needed to retain *in situ* pressure. Also, the 3D tip array is more ideal for hydrate environments since concentration gradients in shallow sediments draping hydrate can be sampled yet, can cause more questions with the large footprint and possible introduction of horizontal gradients. While much effort was put into HYDRA, it is concluded that it is not an ideal way to sample pore-fluids at hydrate sites. Future work needs to concentrate on another technology that collects fluids slowly and can completely flush out DI-water within the instrument to eliminate dilution effects. However, it is apparent from this study that the *in situ* concentration data is necessary to fully understand hydrate stability.

*Acknowledgements.* I would like to thank the Link Foundation for their generous financial support through the Ocean and Engineering Fellowship. Financial support was also

provided by the P.E.O. Scholars Award and the University of Mississippi. This work would not have been possible without the engineering guidance from Howard Mendlovitz and manufacturing expertise provided by the UNC Chemistry machine shop. Drs. Ian MacDonald, Ross Chapman, Rick Coffin and Miriam Kastner gave me the opportunity to test HYDRA at sea. John Pohlman provided sulfate and methane data for the cores. I thank the crews of the Johnson Sea-Link, ROPOS, R/V Seward Johnson, and CCGS John P. Tully for all their help.

## 6. REFERENCES

- Arvidson R. S., Morse J. W., and Joye S. B. (2004) The sulfur biogeochemistry of chemosynthetic cold seep communities, Gulf of Mexico, USA. *Marine Chemistry* **87**, 97-119.
- Carmouze J.-P., Bellotto V., Maddock J., and Romanazzi A. (1997) A versatile in situ sediment pore water sampler. *Mangroves and salt marshes* **1**, 73-78.
- Chapman N. R., Pohlman J., Coffin R., Chanton J. P., and Lapham L. L. (2004) Thermogenic Gas Hydrates in the Northern Cascadia Margin. *EOS, Transactions, American Geophysical Union* **85** (38), 361.
- Crill P. M. and Martens C. S. (1983) Spatial and temporal fluctuations of methane production in anoxic coastal marine sediments. *Limnology and Oceanography* **28** (6), 1117-1130.
- Dickens G. R., Paull C. K., Wallace P., and Party O. L. S. (1997) Direct measurement of in situ methane quantities in a large gas-hydrate reservoir. *Nature* **385**, 426-428.
- Duan Z. and Mao S. (2006) A thermodynamic model for calculating methane solubility, density, and gas phase composition of methane-bearing aqueous fluids from 273 to 523 K and from 1 to 2000 bar. *Geochimica et Cosmochimica Acta* **70**, 3369-3386.
- Fuex A. N. (1980) Experimental evidence against an appreciable isotopic fractionation of methane during migration. *Physical, chemical and earth sciences* **12**, 725-732.
- Hesslein R. H. (1976) An in situ sampler for close interval pore water studies. *Limnology and Oceanography* **21**, 912-914.
- Joye S. B., Boetius A., Orcutt B. N., Montoya J. P., Schulz H. N., Erickson M. J., and Lugo S. K. (2004) The anaerobic oxidation of methane and sulfate reduction in sediments from Gulf of Mexico cold seeps. *Chemical Geology* **205**, 219-238.
- Knox M., Quay P. D., and Wilbur D. (1992) Kinetic isotopic fractionation during air-water gas transfer of O<sub>2</sub>, N<sub>2</sub>, CH<sub>4</sub>, and H<sub>2</sub>. *Journal of Geophysical Research* **97** (C12), 20,335-20,343.
- Kvenvolden K. A. (1988) Methane hydrate-a major reservoir of carbon in the shallow geosphere? *Chemical Geology* **71**, 41-51.
- Mayer L. (1976) Chemical water sampling in lakes and sediments with dialysis bags. *Limnology and Oceanography* **21** (6), 909-912.

- Milkov A. V. (2004) Global estimates of hydrate-bound gas in marine sediments: how much is really out there? *Earth-Science Reviews* **66**, 183-197.
- Orcutt B. N., Boetius A., Elvert M., Samarkin V. A., and Joye S. B. (2005) Molecular biogeochemistry of sulfate reduction, methanogenesis, and the anaerobic oxidation of methane at Gulf of Mexico cold seeps. *Geochimica et Cosmochimica Acta* **69** (17), 4267-4281.
- Pohlman J. W. (2006) Sediment biogeochemistry of Northern Cascadia Margin shallow gas hydrate systems. Ph. D. Thesis, College of William and Mary.
- Pohlman J. W., Canuel E. A., Chapman N. R., Spence G. D., Whiticar M. J., and Coffin R. B. (2005) The origin of thermogenic gas hydrates on the northern Cascadia Margin inferred from isotopic ( $^{13}\text{C}/^{12}\text{C}$  and D/H) and molecular composition of hydrate and vent gas. *Organic Geochemistry* **36**, 703-716.
- Reeburgh W. S. (1967) An improved interstitial water sampler. *Limnology and Oceanography* **12**, 163-165.
- Sassen R., Roberts H. H., Carney R., Milkov A. V., DeFreitas D. A., Lanoil B., and Zhang C. (2004) Free hydrocarbon gas, gas hydrate, and authigenic minerals in chemosynthetic communities of the northern Gulf of Mexico continental slope: relation to microbial processes. *Chemical Geology* **205**, 195-217.
- Sayles F. L., Mangelsdorf J., P. C., Wilson T. R. S., and Hume D. N. (1976) A sampler for the in situ collection of marine sedimentary pore waters. *Deep-Sea Research* **23**, 259-264.
- Sayles F. L., Wilson T. R. S., Hume D. N., and Mangelsdorf J., P. C. (1973) In situ sampler for marine sedimentary pore waters: evidence for potassium depletion and calcium enrichment. *Science* **181** (4095), 154-156.
- Sloan E. D. E. D. Sloan (1998) *Clathrate hydrates of natural gases, second edition*. Marcel Dekker, Inc., New York.
- Spence G. D., Chapman N. R., Hyndman R. D., and Cleary C. (2001) Fishing trawler nets massive "catch" of methane hydrates. *EOS, Transactions, American Geophysical Union* **82** (50).
- Wallace P. J., Dickens G. R., Paull C. K., and Ussler III W. (2000) 10. Effects of core retrieval and degassing on the carbon isotope composition of methane in gas hydrate- and free-gas bearing sediments from the Blake Ridge. *Proc. ODP Sci. Results* **164**, 101-112.

## **Chapter 3: A new sampler for measurements of temporal variability in pore-fluid chemistry of Gulf of Mexico hydrate-bearing sediments**

**Abstract-** Hydrate formation and decomposition events may result in temporal changes of methane, chloride, and sulfate concentrations dissolved within pore-fluids. To follow such changes and collect pore-fluids over time, we designed a specialized Pore-Fluid Array (PFA) made up of an interchangeable instrument package that houses four individual OsmoSamplers (Jannasch et al., 2004), a connector that allows the instrument package to be changed out while minimizing sample disruption, and a 10-meter long probe tip along which 8-filtered ports are evenly spaced. At each port, pore-fluids are slowly pumped up the probe tip, across the connector, and into long length of small-diameter tubing coil using OsmoSampler technology to collect ~4 months data with week resolution. Two of the four samplers were plumbed into a high-pressure valve that, when closed on the seafloor, kept the sample from degassing upon ascent through the water column. In May 2005, the PFA was deployed at a cold seep site in Mississippi Canyon lease block 118 (MC 118), Gulf of Mexico, on the northern edge of a bright acoustic seafloor anomaly known to have outcropping hydrate. After 1.5 years, the PFA's instrument package was successfully recovered and the individual OsmoSamplers were found to be collecting from the overlying water, 1.2 m, 3.2 m, and 8.5 m below the seafloor. From the sampler coils, pore-fluids were extracted and measured for chloride, sulfate, and methane concentrations and methane

isotope ratios. The overall results showed normal seawater conditions in the bottom waters, averaging 549 mM chloride and 30 mM sulfate. At deeper depths, there was evidence for brine fluids, averaging 4561 mM chloride and 0.7 mM sulfate. Since brine inhibits hydrate formation, the discovery of brine radically changes the hydrate stability zone. At deeper depths, high methane concentrations were also measured, averaging 4.2 mM with a maximum of 14 mM, whose  $\delta^{13}\text{C-CH}_4$  averaged  $-32.35 \pm 3.4\%$ , suggesting a mixed biogenic and thermogenic source. Over the 4 month collection, temporal variations in methane concentrations and isotopic ratios suggest this mixed source methane is accompanied by spikes of purely thermogenic fluid. Although hydrate formation and decomposition events were not evident in this deployment due to the presence of the brine, the PFA is a valuable instrument needed to follow hydrate formation and decomposition over time.

## 1. INTRODUCTION

Gas hydrates are crystallized mixtures of hydrocarbon gas (mainly methane) and water that occur naturally where saturated methane conditions exist within high pressure and/or low temperature environments, as found in continental shelves and permafrost (Sloan, 1998). Based upon interpretations of seismic data and estimates from thermodynamic models, gas hydrate deposits are thought to represent one of the largest carbon reservoirs on Earth, containing  $\sim (1-5) \times 10^{15} \text{ m}^3$  or 500-2,500 Gt of methane carbon (Milkov, 2004). In spite of their magnitude, hydrates are considered a small source of atmospheric methane in current global methane budgets (Lelieveld et al., 1998). However, these budgets fail to consider the potentially dynamic nature of hydrate deposits. If changes occur in overlying water and sedimentary pressure and temperature, salinity, and methane concentrations, hydrates can become unstable and decompose; possibly releasing enormous amounts methane into the

water column and potentially the atmosphere. It is important to learn more about the stability of hydrate deposits if we hope to better understand their hypothesized role (e.g. Kennett et al., 2003) in abrupt climate change.

Hydrates form and are stable within a unique depth zone where saturated methane and moderate salinities are present under the appropriate pressures and temperatures (Sloan, 1998). This hydrate stability zone (HSZ) is typically defined by thermodynamic models that use the depths and temperatures from ocean water and sediments to define pressure and temperature while assuming saturated gas and moderate salinity conditions. However, saturated gases may not always be present and, especially in the Gulf of Mexico, brine fields may exist. Since brine fluids and saturated methane cannot be accurately determined by remote methods, their direct measurement is required to fully identify the hydrate stability zone.

Along with defining the HSZ, *in situ* gas and ion concentrations can also be used to trace hydrate formation and decomposition events because of changes occurring during hydrate formation and decomposition. Upon formation, hydrates exclude salts from the enclosed molecular cages while taking up surrounding dissolved methane (Ussler and Paull, 2001). Therefore, when hydrates form, an increase in chloride concentrations and a decrease in the dissolved methane concentrations are expected. Likewise, when hydrates dissociate, they release large amounts of methane and freshwater.

Hydrate stability may also be affected by increased microbial methane oxidation in the shallow sediments (Bidle et al., 1999; Lanoil et al., 2001; Marchesi et al., 2001; Mills et al., 2003). Carbon isotopic studies indicate biological oxidation of hydrate-bound methane gas compared to vent gas (Sassen et al., 1998). Related studies have also shown elevated

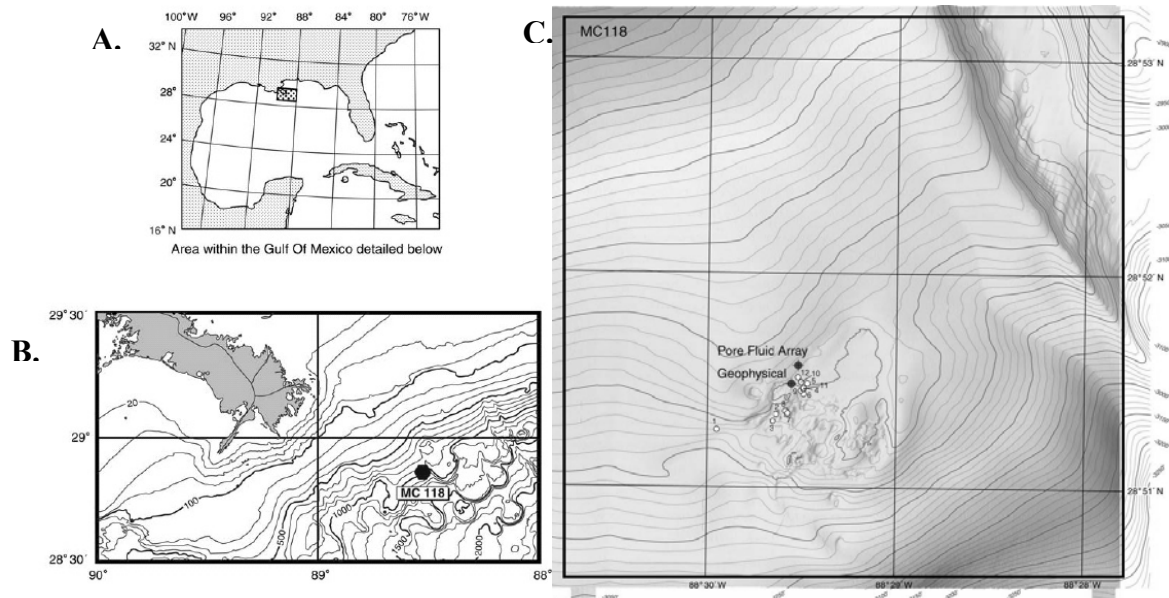
anaerobic methane oxidation rates in sediments surrounding hydrate compared to background oceanic sediments (Joye et al., 2004; Orcutt et al., 2004). The affect of microbial activity can be assessed by following the isotopic composition of the dissolved methane near the hydrate. *In situ* dissolved gas concentrations and methane carbon isotopic compositions are needed to understand the current stability of hydrate and the relative importance of biological oxidation of methane.

Understanding and monitoring the long term stability of gas hydrates found in the Gulf of Mexico has been the focus of multi-institution research program led by the University of Mississippi. The goal of this Gulf of Mexico Hydrates Research Consortium (GOMHRC) has been to establish a seafloor hydrate monitoring observatory to understand temporal and spatial variability in the processes controlling hydrate growth and decomposition in a well characterized sedimentary environment. Using novel water column and sediment arrays, seismic, chemical, and microbial processes are being monitored at Mississippi Canyon Lease Block 118 where several acoustic anomalies have been found and outcropping hydrate have been directly visited.

As part of the monitoring station, the purpose of this study was to develop, deploy, and recover a novel Pore-Fluid Array (PFA) sampler that collects samples over time for later determination of chloride, sulfate, and dissolved methane concentrations. Although the PFA was designed specifically for our hydrate site, it was modeled after similar instrumented approaches utilized in convergent margin settings (Jannasch et al., 2003; Fisher et al., 2005a; Fisher et al., 2005b). Using OsmoSampler technology, we collected pore-fluids near a hydrate mound and determined temporal changes in salt and gas concentrations over a four month period to not only determine microbial activity and the hydrate stability parameters



but also to monitor hydrate formation and/or decomposition events. Samples were also measured for changes in the carbon isotopic ratio of methane in order to differentiate between thermogenic and biogenic sources. Temporal changes in these constituents may tell us something about the relative importance of local hydrate formation and decomposition as well as control of microbial processes. This is the first study to approach hydrate stability by monitoring geochemical changes over time in pore-fluids at MC 118 and lays the foundation for the hydrate seafloor monitoring station where hydrate stability is assessed through long term monitoring of both geophysics and geochemistry.

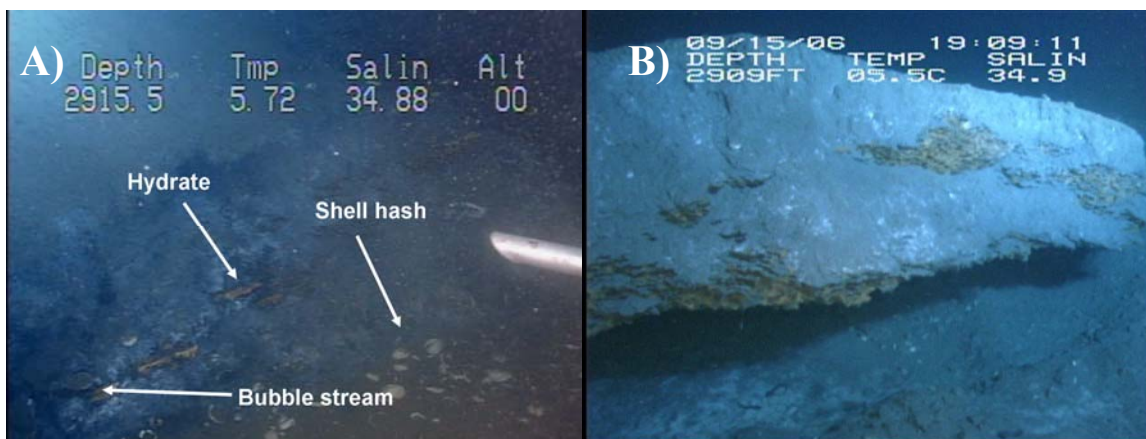


**Fig. 3- 1: A. Gulf of Mexico showing sampling site in shaded range. B. Contour map showing MC 118 offshore Mississippi River birdfoot delta. C. Mississippi Canyon 3 mile x 3 mile lease block 118 showing site of pore fluid array and geophysical array. White dots show cores collected in 2005.**

## 2. METHODS

### 2.1. Site characteristics

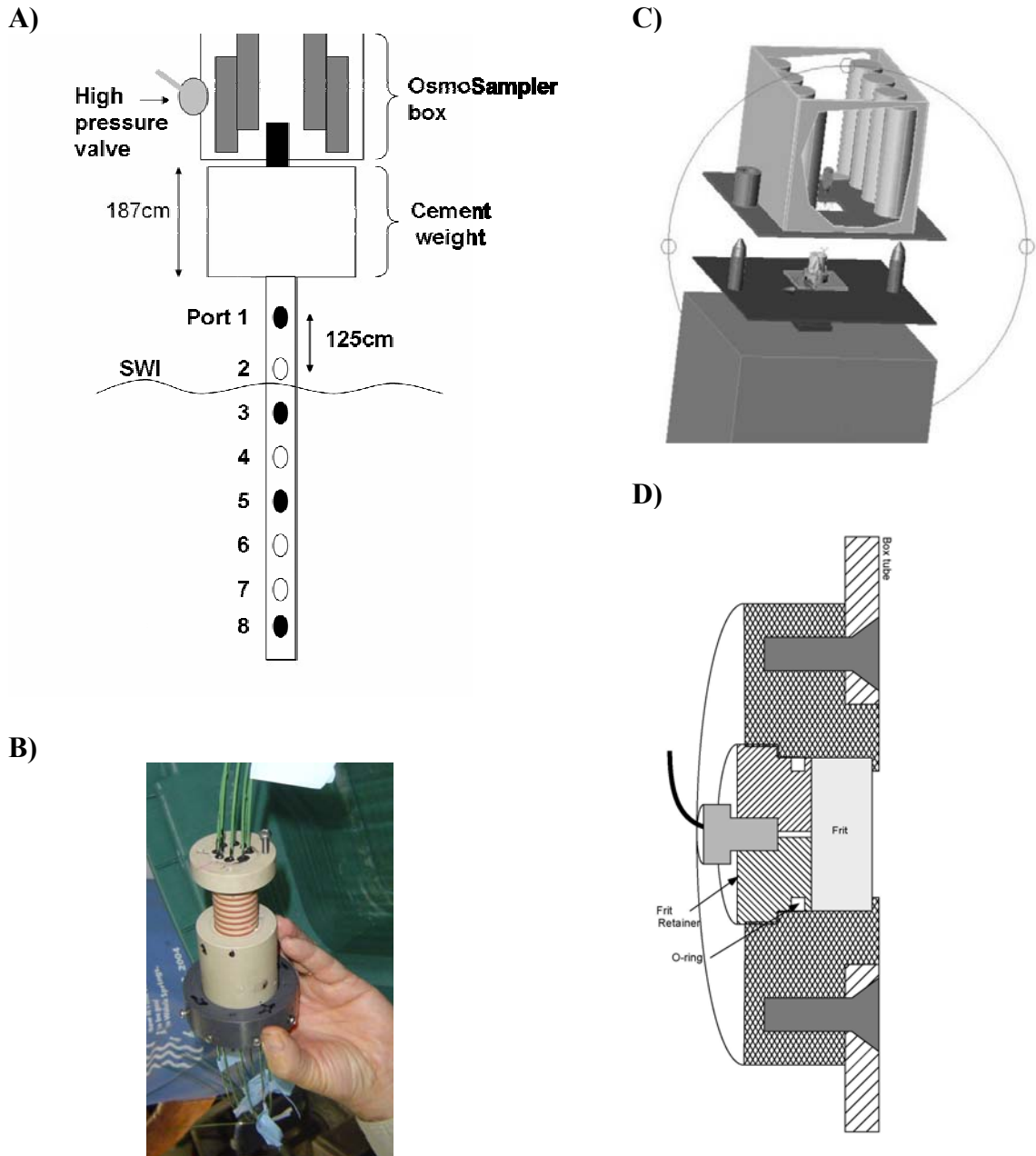
Mississippi Canyon 118 (MC 118) is located offshore from Louisiana and is the easternmost discovery of gas hydrate in the Gulf of Mexico to date (28°51.47', 88°29.52', 970m water depth; Fig. 3-1, Sassen and Roberts, 2004). The regional bathymetry is dominated by the Mississippi Canyon to the west and a smaller, fault controlled, canyon to the east (Fig. 3-1c; Woolsey et al., 2005). Geophysical anomalies near the seafloor indicate hydrate occurrence (Sassen and Roberts, 2004). The manned submersible, Johnson Sea-Link visited the site in 2002 and found hydrate mounds and outcropping veins that formed in a circular pattern ~25 meters in diameter (Fig. 3-2; Sassen and Roberts, 2004). The host sediment is hemiplagic clay with no sand. The source rock and petroleum system may be different than more well studied hydrates found in Green Canyon lease blocks (Sassen and Roberts, 2004). Oil, bacterial mats and clams were present in the sediments.



**Fig. 3- 2: Seafloor pictures taken at MC 118. A) JSL dive 4414 in 2002. Bottom right hand shows clam shells, diagonally in the middle shows yellow outcropping hydrate with white bacterial mat surrounding it and the top left of the picture is sediment. B) JSL dive 3573 in 2006. Large hydrate outcrop with sediment drape and ice worms.**

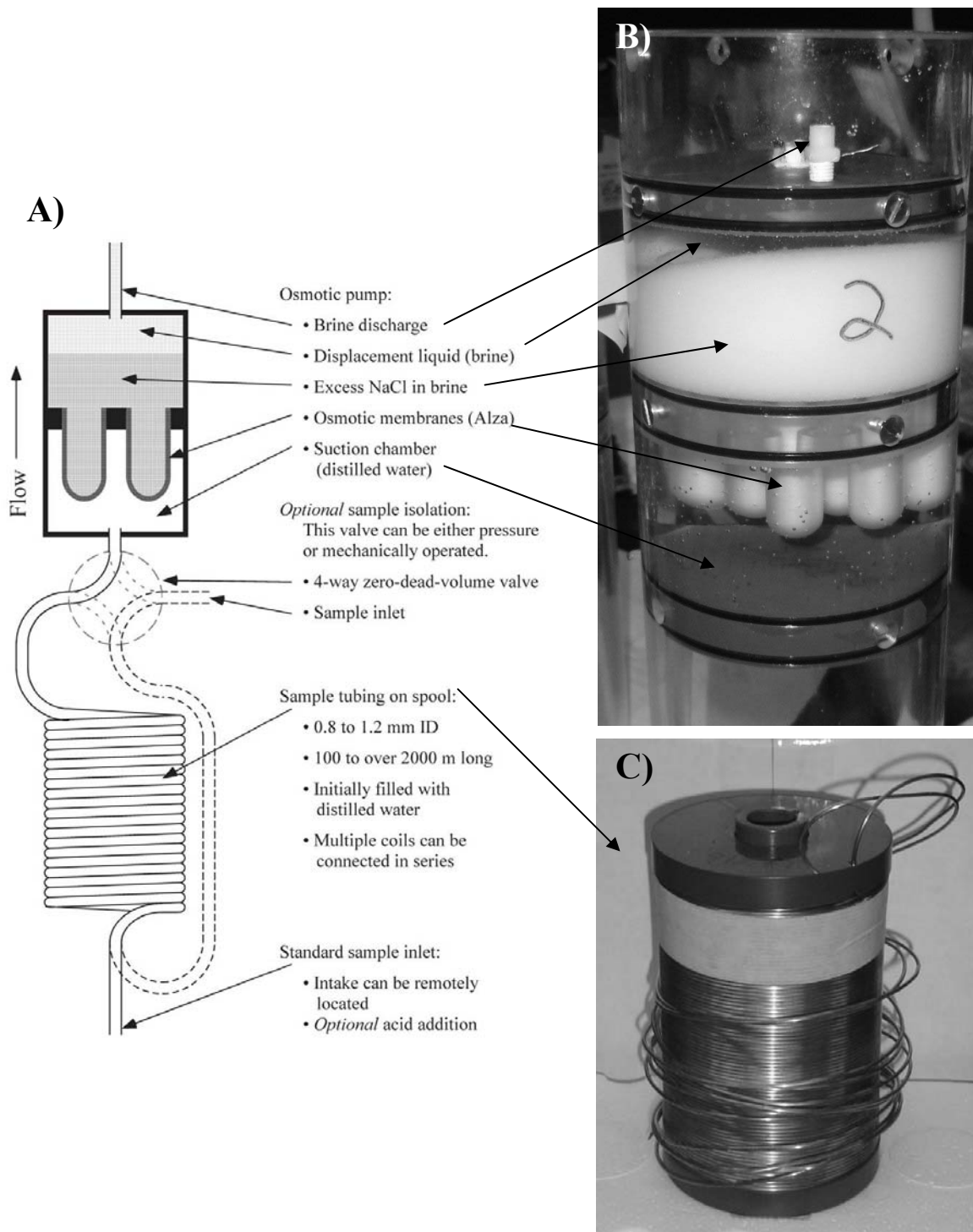
## **2.2. Pore-Fluid Array design**

The Pore-Fluid Array (PFA) is a weighted seafloor sediment probe that contains a filtered probe ports along a shaft which are interfaced to a pore fluid sampling instrument package via a low dead-volume connector (Fig. 3-3). Deployed from a surface ship, the PFA probe tip is inserted into the sediment under its own weight. The hollow steel probe shaft (10m long x 7.6cm square) contains eight evenly spaced filtered sampling ports (Figs. 3-3a and 3-3d). Small diameter tubing from each port runs the inside length of the shaft to a customized connector (Fig. 3-3b; developed by Paul Higley, Specialty Devices, Inc.). This zero dead-volume connector is keyed to interface each sampling port to an individual pore-fluid sampler housed within the instrument package. It allows a remotely operated vehicle to replace the instrument package periodically without removing the probe shaft from the sediments, thus minimizing disruption of sample collection between each visit. The pore-fluid instrument package (Figs. 3-3a and 3-3c) is made up of four OsmoSamplers (Fig. 3-4; Jannasch et al., 2004) and a high pressure valve.

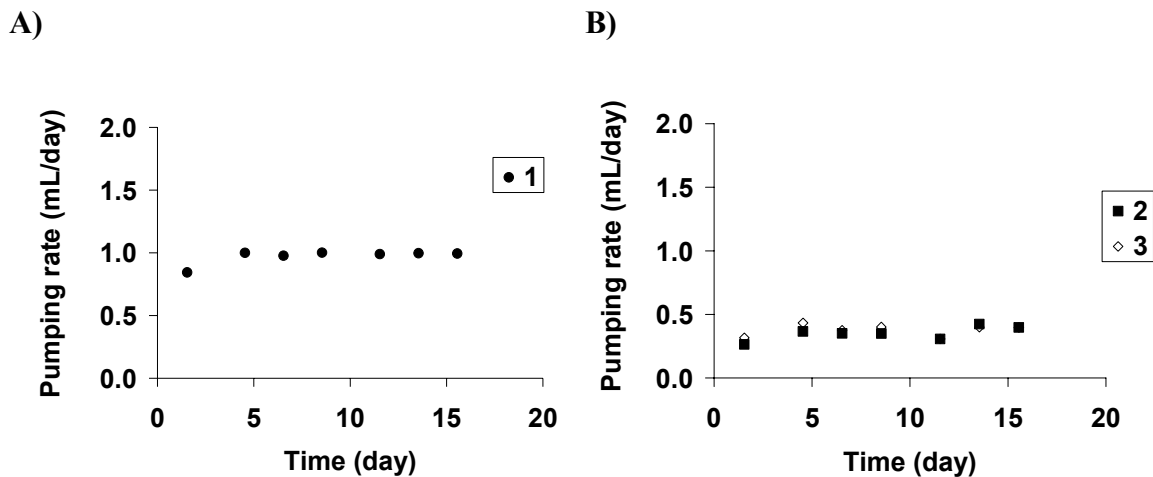


**Fig. 3- 3: Components of the Pore Fluid Array. A) Conceptual picture of the PFA with instrument package containing OsmoSamplers (gray) with valve on left side of box (light gray), connected to cement weight with the keyed connector (black), and the 10m probe tip. White circles signify sampling ports used, black circles were not used. Sediment depths were determined by the circumstances of deployment. B) Actual picture of the keyed connector. C) Osmosampler basket mated to the cement weight via the connector. D) Cross-section of sampling port in side of probe.**

Four identical OsmoSamplers were built. They use osmotic pumps (Fig. 3-4a) to pull pore-fluids into the coils of small diameter gas-tight tubing (Fig. 3-4b). They require no power and have no moving parts. Each sampler fits into a 4 inch outer diameter acrylic housing (Fig. 3-4a). Within the housing, four individual compartments are separated with a 1 inch thick PVC or acrylic disk. The bottom compartment houses the long length tubing coil, above that is the DI-water reservoir, then the saturated salt solution, and finally, the top compartment is the outflow solution (Fig. 3-4a and 3-4b). The DI-reservoir and the salt solution compartments are separated by eight osmotic membranes (2ML1, Durect Co, Cupertino, CA; Fig. 3-4a). Although the nominal pumping rate of these membranes is 0.8 mL/day @ 20°C, pumping rates for each sampler were directly determined in the lab (Fig. 3-5). Since pumping rates are dependent upon temperature, rate experiments were conducted at 22°C and then 4°C, the latter to correspond to the bottom water temperature at MC 118. Pump #1 remained at 22°C for the duration of the 15 day rate experiment and averaged a pumping rate of 0.99±0.01 mL/day (Fig. 3-5a). For pumps #2 and 3, rate experiments were conducted at 4°C for 16 days. Average pumping rates were 0.35±0.05 mL/day for pump #2 and 0.38±0.05 mL/day for pump #3 (Fig. 3-5b). Pump #4 was visibly leaking prior to deployment and so after fixing the leak, pumping rate was not determined. Rates correspond to ~90 cm of tubing per day. During the deployment period, the pumps overpumped their coils and contained higher salinity water in the DI reservoir. So, after the deployment, the OsmoSampler pumping rates were re-determined for the elevated salinity DI reservoir. Rates are still being determined in the lab.



**Fig. 3- 4: OsmoSamplers (Jannasch et al., 1994; Jannasch et al., 2004). A) Schematic of flow pathway picture taken from Jannasch et al., 2004. B) An example of the OsmoSamplers built for this study. The main housing contains the deionized water and brine reservoir separated by the osmotic membranes contained within an acrylic tube. C) Sample tubing coil (copper is shown).**



**Fig. 3- 5: Pumping rate experiments for OsmoSamplers 1, 2, and 3 at different temperatures. A) For OsmoSampler 1, the rate experiment was conducted at 22°C and b) For OsmoSamplers 2 and 3, the rate experiments were conducted at 4°C.**

The osmotic differential between the DI and salt reservoirs pumps pore-fluids through the filtered sampling ports along the probe shaft and into the sample tubing coil where it is preserved as a time series record. The tubing coils are made out of either copper or PEEK (polyetheretherketone) (0.159 cm outer diameter, 0.076 cm inner diameter) and are both rated up to high pressures of 13.8MPa (~200atm, Fig. 3-5c). The high pressure rating is needed in order to contain the samples at *in situ* pressures and allow for an *in situ* methane concentration to be measured. Within the narrow diameter tubing, sample smearing is minimized due to the slow pumping rates and slow diffusion (Jannasch et al., 2004). The two different coil materials were tested to determine which one was best for combined measurements of chloride, sulfate, and methane. Although both materials can withstand high pressures, the ideal tubing will also have low gas permeability, be unreactive to dissolved ions, and be easy to sub-sample. Approximately 128-227 m of tubing was coiled for each sampler which, at the pumping rates of these instruments, corresponds to ~5 months of

sampling time (Table 3-1). To maintain these samples at *in situ* pressure during recovery, along with a high pressure tubing material, two of the OsmoSamplers were plumbed to a high pressure valve housed within the instrument package (Valco 12-port valve). Because this valve is made of stainless steel, we also tested different union materials to avoid contact of dissimilar metals between the copper coils and the valve. Therefore, PEEK (Valco Co, #ZU1PK) or gold-plated stainless steel (Swagelok) unions were used between copper tubing coils and the high pressure valve (see Table 3-1).

Coils were all filled with methane-free degassed deionized (DI) water prior to deployment. The DI water was first bubbled with nitrogen gas to eliminate methane and then degassed by boiling for 5 minutes. Each coil was then filled slowly by allowing DI water to fill coils by gravity. Since the coils were not attached to the samplers until they were ready for deployment on the ship, they were then transported submerged in a degassed water reservoir.

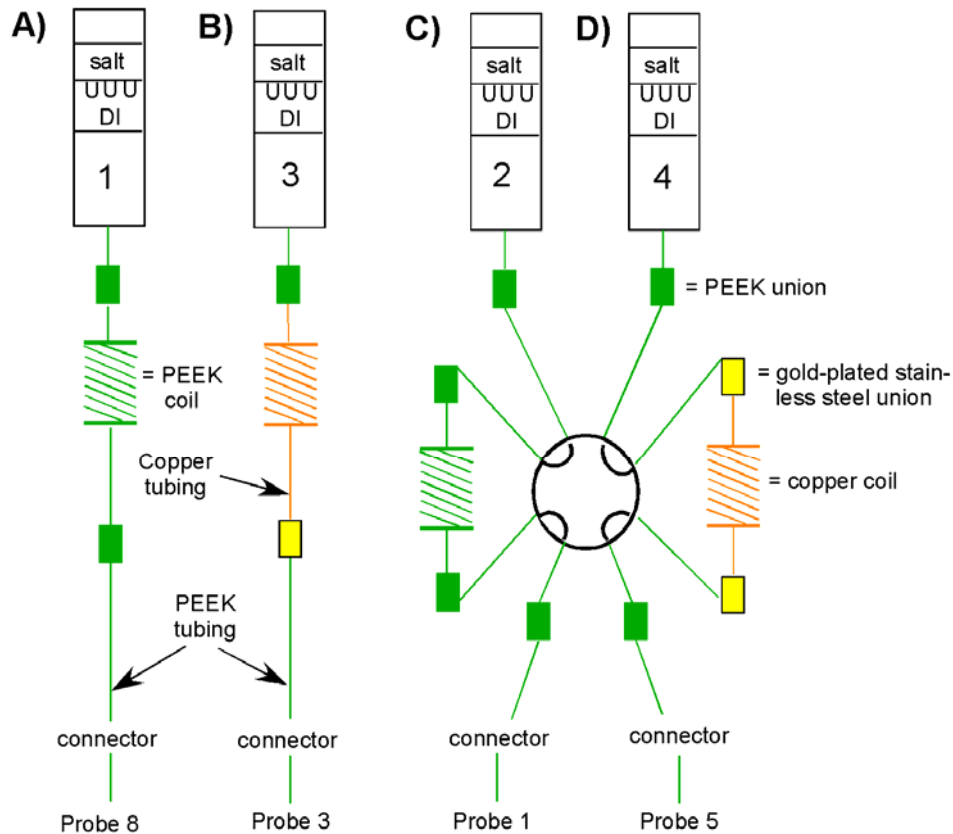
**Table 3- 1: Configuration of PFA.**

Probe Port	Depth (mbsf)	OsmoSampler #	Coil material	Coil length (m)	Plumbed to Valve?	Unions used
1	OLW	2	PEEK	77	Y	PEEK
2		Open				
3	1.2	3	Copper	117	N	Gold
4		Open				
5	3.7	4	Copper	120	Y	Gold
6		Open				
7		Open				
8	8.5	1	PEEK	66	N	PEEK



### **2.3. PFA construction**

On the May 2005 GOMHRC cruise, the PFA was constructed with its three main parts (instrument package, connector, and shaft) using different tubing and union material configurations (Fig. 3-6 and Table 3-1). Four OsmoSamplers were built into the instrument package; two were connected to the copper tubing coils and two were connected to the PEEK. Two of these samplers were also plumbed to the high pressure valve and two were not (Fig. 3-6 and Table 3-1). From each OsmoSampler, PEEK tubing was plumbed to a PEEK union and either directly into a tubing coil or into the stainless steel high pressure valve (Fig. 3-6). For sampler 1, the tubing coil was made out of PEEK tubing coil which was connected to a PEEK union and finally the connector (Fig. 3-6a). For sampler 3, the tubing coil was made out of copper which was connected to a gold-plated stainless steel union and finally the connector (Fig. 3-6b). However, for samplers 2 and 4, the coils were plumbed to a high pressure valve. For sampler 2, all PEEK fittings and tubing was used (Fig. 3-6c). For sampler 4, PEEK tubing connected the sampler to the valve (Fig. 3-6d). Then, the copper coil was connected to the valve with PEEK unions on either side. From the valve to the connector, a PEEK union was used. From the connector to each probe port, PEEK tubing was used with a PEEK union. Once the connections were made, the valve and gold plated unions were liberally coated in lithium grease to protect them from seawater corrosion.



**Fig. 3- 6: Conceptual picture of the different materials used to connect each OmoSampler to the tubing coil, the high pressure valve, the connector, and the probe ports.**

#### 2.4. Processing tubing coils after retrieval

Upon retrieval of the instrument package from the PFA left in the seafloor, the OmoSamplers and tubing coils were taken out. The coils not connected to the high pressure valve were immediately disconnected from the OmoSampler pumps, outfitted with on/off valves (Swagelok, zero dead-volume) turned in the ‘off’ position, and frozen. The coils connected to the high pressure valve were dealt with separately. For the copper coil, because the gold unions failed, it was detached from the valve and on/off valves connected to each coil end. The valves were turned in the ‘off’ position and coils frozen. Further inspection of

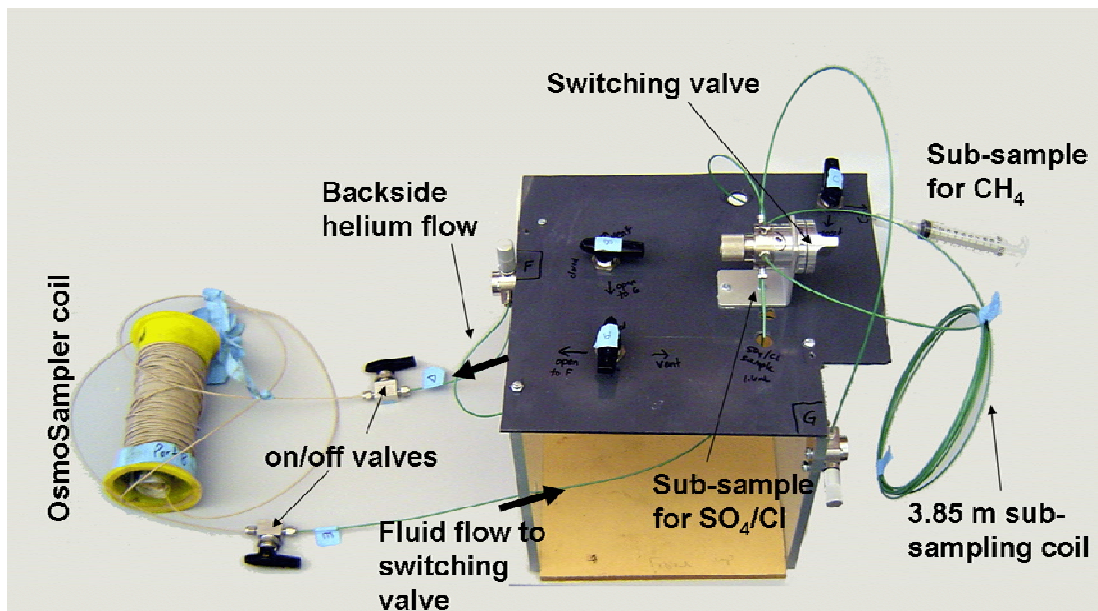
the high pressure valve showed that it may have corroded during the 1.5 years on the seafloor and did not allow the valve handle to actually close it on the seafloor. So, the final PEEK coil connected to the high pressure valve was also disconnected from the valve, outfitted with on/off valves on each coil end, valves placed in ‘off’ position, and immediately frozen.

#### *2.4.1. Sub-sampling tubing coils*

Typically, the tubing coils are sub-sampled by cutting along certain lengths of tubing to avoid additional sample smearing during fluid extraction (Jannasch et al., 2004). However, this technique is typically used for samples that are not under high pressures. For high pressures, two additional techniques were considered. The first was to crimp the tubing at various distances down the coil. This was not used because laboratory tests could not maintain pressures of 50 psi. The second technique was to sub-sample the coil pore-fluids by forcing the fluid out one end and into a custom made fraction collector (Fig. 3-7). Each sub-sample was then time-stamped based on the original *in situ* flow rates and tube volume and then analyzed for *in situ* methane and ion concentrations. Since this sub-sampling method increases sample smearing and therefore the temporal record, we calculated and determined the affect of smearing on our samples (see section 2.4.2.).

The tubing coils were sub-sampled by connecting each end of the coil to the fraction collector (Fig. 3-7). Once connected, helium (20 psi, ~1.25mL/min) was introduced on the backside of the coils to force the fluid out the other end and through a high pressure switching valve. In the valve, the sample goes through a 3.85-meter long coil to collect a 2 mL sample. In the ‘load’ position, the sample comes out a port to collect ~1.5 mL in a micro-centrifuge tube. This sub-sample was collected for sulfate and chloride concentrations. Once this sub-sample is collected, the switching valve is turned to ‘inject’

position and the fluid is directed into a 10 mL gas tight syringe. Since only 2 mL of sub-sample is collected, the syringe is also filled with ~8 mL of helium. This sub-sample is then injected into an evacuated 10 mL gas serum vial and measured for methane concentrations and isotopes. Sub-sampling then continued for the length of the tubing and for all coils. However, the copper sample coil collected at the 3.2 mbsf depth had several corroded spots along the coil. Therefore, when helium pressure was applied to the backside, it leaked in numerous spots and no sub-samples were collected. This coil was about 8 years old, which may have contributed to its demise. The other copper coil was new and did not corrode.



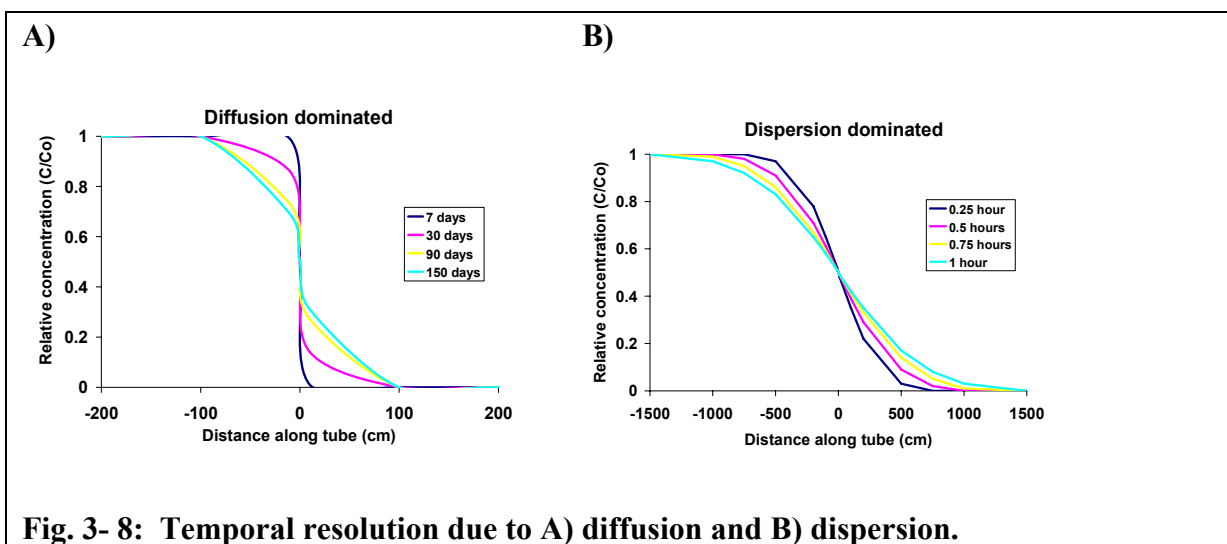
**Fig. 3- 7: Fraction collector configuration used to sub-sample OsmoSampler tubing coils.**

#### 2.4.2. Temporal resolution considerations

“Temporal changes in the chemical composition of samples that are pulled through the sample tubing are prone to smearing by molecular diffusion, gradient dispersion due to shear in flow stream, and chemical interaction with tubing walls” (Jannasch et al., 2004). These broadening effects all result in decreased temporal resolution. Diffusion was the dominate

process during sample collection out in the field, while dispersion was the dominate process during sub-sampling in the lab. We considered chemical interactions to be negligible in our system. Therefore, diffusion and dispersion were both calculated and measured to determine the temporal resolution for our samplers.

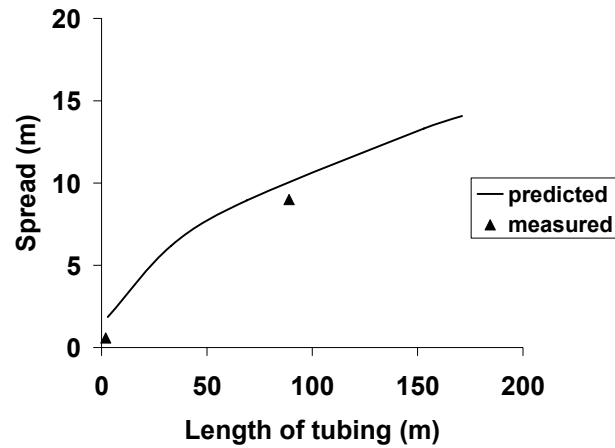
*Predicted temporal resolution.* As described in Jannasch et al. (2004), temporal resolution was calculated using the error function to be, at most, 3 days (or 2 meters along tube) for diffusion and 45 days (or 30 meters along tube) for dispersion (Fig. 3-8).



**Fig. 3- 8: Temporal resolution due to A) diffusion and B) dispersion.**

*Laboratory measured temporal resolution.* Since smearing could have been introduced by specific fittings and pathways within the fraction collector, the temporal resolution was also directly measured in the laboratory. This was done by connecting the fraction collector with 2, 4, and 91 meter PEEK sampling coils to an HPLC system. The HPLC was equipped with a photo diode array to detect the sample of green tinted water at 435 nm wavelength. For the experiment, the green water sample was run through the fraction collector at our sub-sampling flow rate (ie 1.25 mL/min) for both the 2 meter and then the 4 meter coil lengths. Since the peak width distance is equal to 4 standard deviations (or 99.99% confidence

interval), which was the SD used to calculate the predicted smearing (equation 2), smearing was measured as the peak width difference between the 2 and 4 and the 2 and 91 meter coils. The results showed a maximum of 14 meters of tubing which equates to 19 days temporal resolution (Fig. 3-9 and Table 3-2).



**Fig. 3- 9: Spreading distances due to both diffusion and dispersion predicted from equation 2 and directly measured.**

**Table 3- 2: Predicted and measured smearing spread.**

<u>Predicted from Jannasch et al. (2004)</u>		<u>Directly measured</u>	
Tubing length (m)	Spread (m)	Tubing length (m)	Spread (m)
3	1.86	2	0.6
33	6.18	89	9
69	8.94		
153	13.31		
171	14.07		

## 2.5. Analytical methods

Pore water sulfate and chloride concentrations were determined by ion chromatography of 1:100 diluted pore-fluid samples using a 2010i Dionex Ion Chromatograph (Sunnyvale, CA) as described in Martens et al. (1999).

Methane concentrations and carbon stable isotope ratios were analyzed for each depth interval using the same serum vial, as previously described. For methane concentrations, a 5 mL headspace aliquot was analyzed on a Shimadzu Mini II Gas Chromatograph (Kyoto, Japan) equipped with a flame ionization detector. Carbon stable isotope ratios were obtained by isotope ratio monitoring using a 5890 Hewlett-Packard gas chromatograph (Palo Alto, CA), coupled to Finnigan MAT 252 isotope ratio mass spectrometer (Thermo Finnigan, Bremen, Germany) via a combustion interface (GC-C-IRMS) as described in Rice et al. (2001). Results are reported using the standard “del” notation,

$$\delta^{13}\text{C} (\text{‰}) = [R_{(\text{sample})}/R_{(\text{PDB standard})} - 1] * 1000 \quad (1)$$

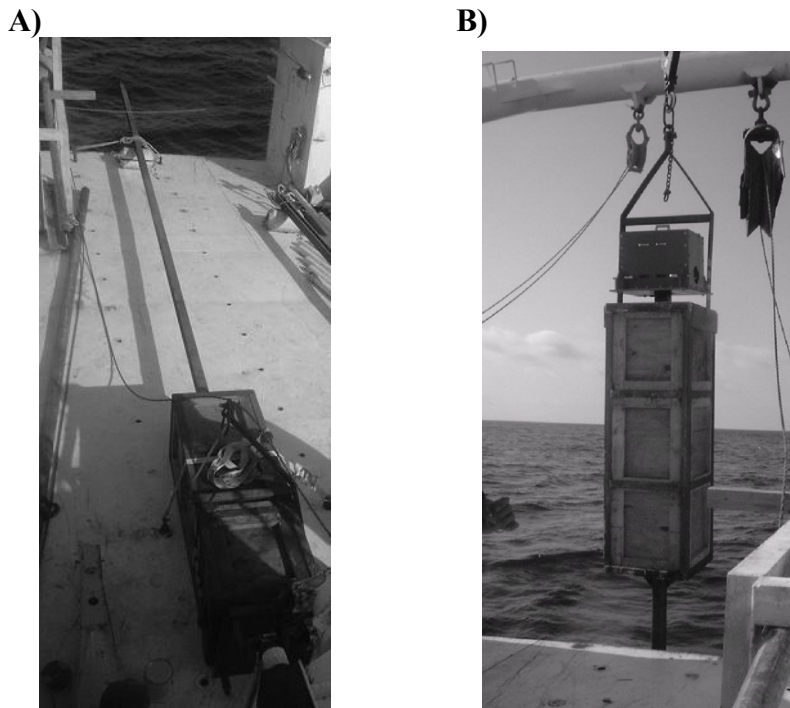
where R is the ratio of the heavy to light isotope. The precision for replicate measurements of single samples was  $\pm 3$  percent for sulfate, chloride, and methane concentrations.

## 3. RESULTS

### 3.1. PFA deployment

On the May 2005 GOMHRC cruise, the fully assembled PFA was connected to an acoustic ranging Benthos release and deployed from the R/V Pelican (Fig. 3-10). Like a gravity core, it was lowered off the side of the ship and dropped into the sediments. The wire was detached and the remaining acoustic release on the PFA was used to locate its position using the ship's differential GPS with WAAS and USCG beacon corrections. The PFA position was triangulated using “Angulate” software to computer position relative to the

onboard GPS. A series of 9 slant range positions were computed with the position estimated to have 5 to 10 meter accuracy (Paul Higley, personal communication). The position was latitude 28°51'28.27262 and longitude 88°29'31.19183. On the same cruise, a geophysical array was also deployed next to the PFA (Fig. 3-1c). This array was outfitted with thermistors collecting a temperature record in the overlying water, 1.5 mbsf, and 4.5 mbsf (Higley, personal communication).



**Fig. 3- 10: Deployment of the pore-fluid array at MC-118 in May, 2005. A) PFA shown as the cement box and 10meter long probe shaft off the stern of the R/V Pelican. B) The PFA ready for deployment, the upper most portion is the interchangeable basket containing the OsmoSamplers, the box below is the cement weight and the probe shaft is barely visible.**

### 3.3. PFA recovery

After 540 days (1.5 years) in September, 2006, the PFA was found at 28°51.4682'N and 88°51.4969'W using the GPS system onboard the manned submersible Johnson Sea-Link operating from the R/V Seward Johnson. The PFA was oriented in a fully upright position,



protruding out of the sediments about 2 meters (Fig. 3-11a). This sediment penetration depth translates to samples collected from overlying water at 1.4 m above seafloor, 1.2 meters below seafloor (mbsf), 3.7 mbsf, and 8.5 mbsf recovered. The instrument package was recovered on September 12, 2006 with minimal bio-fouling, covered only with hydroids (Fig. 3-11b). Before removing the package from the PFA, the submersible successfully closed the high pressure valve in order to seal the PFA sampling tubing (Fig. 3-11c). In a subsequent dive, a replacement instrument package was successfully mated onto the connector and PFA probe. This package will be retrieved in June 2007.



**Fig. 3- 11: Seafloor photos of the PFA retrieval. A) The first sighting of the PFA showed it was standing upright and vertical about 2 meters out of the sediment. B) The OsmoSampler package shown with minimal biofouling and all parts intact. C) Although a little corroded, the high pressure valve was still intact.**

### *3.2.1. Assessment of package condition*

Once the PFA instrument package was on board ship, a detailed survey of its condition was taken. All tubing and unions were in good visual condition. However, upon extraction of each pump, the gold-plated unions failed. Overall, the pumps were in good visual condition, no visible cracks or leaks, and the salt reservoirs were still supersaturated. The only obvious problem was that the OsmoSampler on port #3 had green tinted water within the DI reservoir. Since this pump was connected to copper tubing, the green tint suggested

that although the pumps were working properly, the reaction between pore-fluids containing sulfate and the copper tubing probably formed copper sulfate. Therefore, sulfate concentrations measured in samples from copper coils may be suspect. Although the valve seemed to have closed on the seafloor, upon assessment on the ship, we found that it had corroded and did not properly close (see section 2.4.).

### **3.3. Pore-fluid concentration and $\delta^{13}\text{C-CH}_4$ values**

Chloride, sulfate, and methane concentrations and methane isotopes were measured from coils collected from the overlying water, 1.3 mbsf, 3.2 mbsf, and 8.5 mbsf. Along with coil fluid measurements, chloride concentrations were also measured within the DI-reservoir water itself. Because the OsmoSamplers were deployed for 547 days and had only enough tubing to collect for 95 to 168 days, they overpumped the entire length of the tubing coil into the DI-water reservoir more than twice. This resulted in an increase in the salinity of the DI-reservoir and the new pumping rates are currently being assessed in the laboratory.

Therefore, preliminary sampled time intervals were calculated using the laboratory calculated pumping rates at 4°C from the day of recovery (Sept 12, 2007) back 95-168 days (depending on the coil). Although a temperature record is not available for the specific deployment period of this experiment, a temperature record for May through July 2006 showed the bottom water temperature ranged between 4 to 5°C (Paul Higley, 2006, unpublished data). This range is within the  $\pm 1^\circ\text{C}$  needed for a linear response of the samplers (Jannasch et al., 2004).

Since two of the OsmoSamplers were not plumbed to the high pressure valve and the valve itself did not survive the deployment time, methane concentrations should still be considered minimums.

For pore-fluids collected from 1.4 meters above the seafloor (known as overlying water from now on), chloride concentrations ranged between 456-772 mM and averaged  $549 \pm 76$  mM (Fig. 3-12a). Sulfate concentrations ranged from 25.2-34.6 mM and averaged  $26.6 \pm 9$  mM (Fig. 3-13). For this coil, the average Cl:SO<sub>4</sub> was  $18.4 \pm 1.5$ . Methane concentrations were approximately 0.1 mM at day 0 of the series and decreased to 0.004 mM (Fig. 3-14). The methane  $\delta^{13}\text{C-CH}_4$  values were not measured since concentrations were so low. For this overlying water OsmoSampler, the chloride concentration of the DI-reservoir water was 487 mM (data not shown).

For pore-fluids in the 1.3 mbsf sample coil, chloride concentrations ranged from 467-629 mM and averaged  $560 \pm 42$  mM (Fig. 3-12a), sulfate concentrations ranged from 12.5-22.4 and averaged  $19.3 \pm 2$  mM (Fig. 3-13), and methane concentrations were as high as 14 mM but otherwise ranged between 0.7-8.1 mM and averaged  $4.2 \pm 2$  mM (Fig. 3-14). The average Cl:SO<sub>4</sub> was  $29.7 \pm 2.4$ . The average methane  $\delta^{13}\text{C-CH}_4$  value was  $-32.35 \pm 3.4\%$ ; suggesting either a strong thermogenic methane source or highly microbially oxidized (Fig. 3-15). Three distinct <sup>13</sup>C enriched spikes in the  $\delta^{13}\text{C-CH}_4$  values suggest a possible occasional contribution of extremely <sup>13</sup>C enriched methane. If these spikes are taken out of the averaging statistics, the average  $\delta^{13}\text{C-CH}_4$  value becomes  $-33.94 \pm 1.5\%$ . The average of the three spike values is  $-26.60 \pm 2.2\%$ . From this 1.3 mbsf OsmoSampler, the chloride concentration of the DI-reservoir water was 559 mM (data not shown).

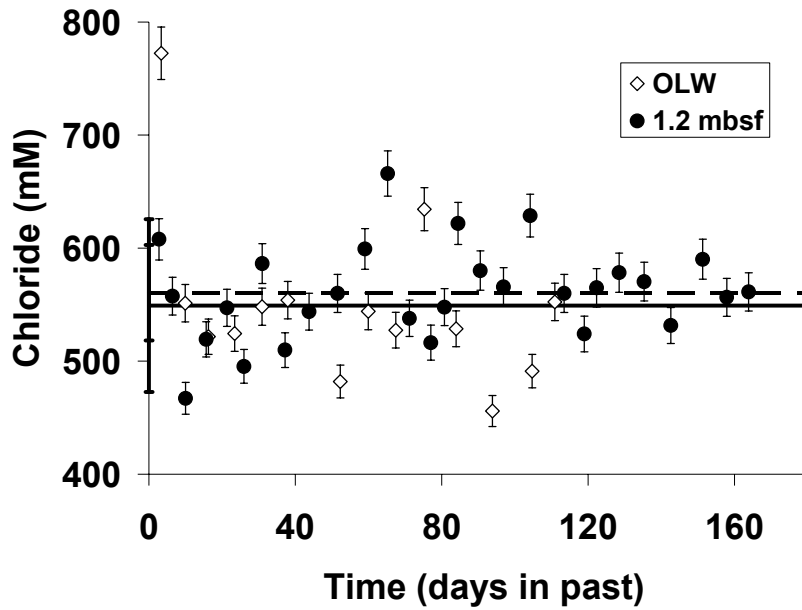
No samples were collected from the coil collected at 3.2 mbsf. However, the DI-reservoir water was measured for chloride concentrations. It measured 2195 mM chloride, four times higher than seawater values (data not shown).

For pore-fluids in the 8.5 mbsf sample coil, chloride concentrations ranged between 3944-4890 mM and averaged  $4561 \pm 254$  mM, 8 times above seawater values (Fig. 3-12b). Sulfate concentrations ranged between 0.3-1.27 mM and averaged  $0.67 \pm 0.2$  mM (Fig. 3-13). Methane concentrations were low and averaged  $0.002 \pm 0.001$  mM (Fig. 3-14). For the DI water reservoir for this OsmoSampler, the chloride concentration was 4288 mM (data not shown).

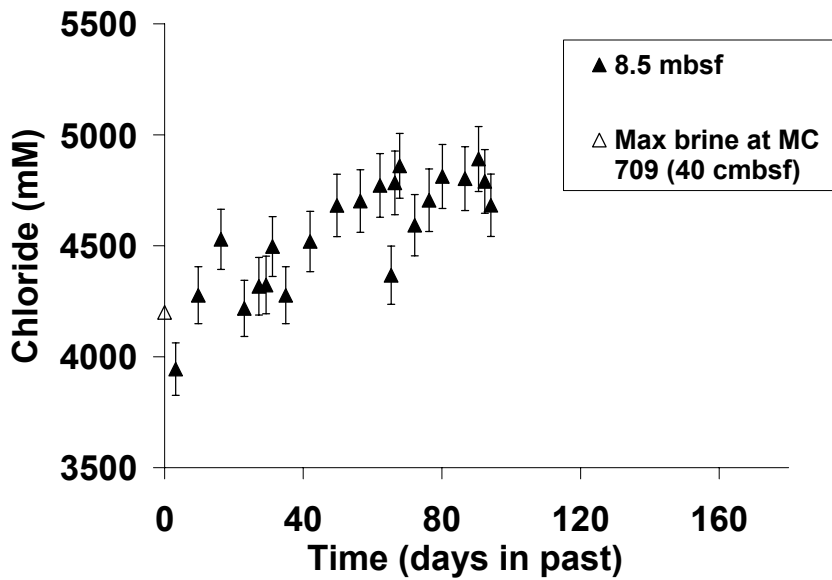
#### **3.4. Post-deployment pumping rates**

Since pumps were deployed long enough to flush the sample tubing coils multiple times, pore-fluids mixed with the DI-water contained within the OsmoSampler DI reservoir. Since these pore fluids sometimes contained brine, they reduced the osmotic potential and probably slowed down pumping rates of the OsmoSamplers. Therefore, flow rates were measured back at the lab with the salty DI-reservoirs in order to establish time intervals for samples recovered in the coils. Determination of the pumping rates within these samplers is still ongoing.

A)



B)



**Fig. 3- 12: A) Chloride concentrations for overlying water (OLW) and 1.2 mbsf. The dashed and solid lines correspond to the overall average concentrations and standard deviations for 1.2 mbsf and OLW samples. B) Chloride concentrations for 8.6 mbsf are plotted in black filled triangles. The open triangle is the chloride concentration measured at a nearby brine field, MC 709. Note the y-axis scale change between A and B. On each point, error bars represent 3% analytical error.**

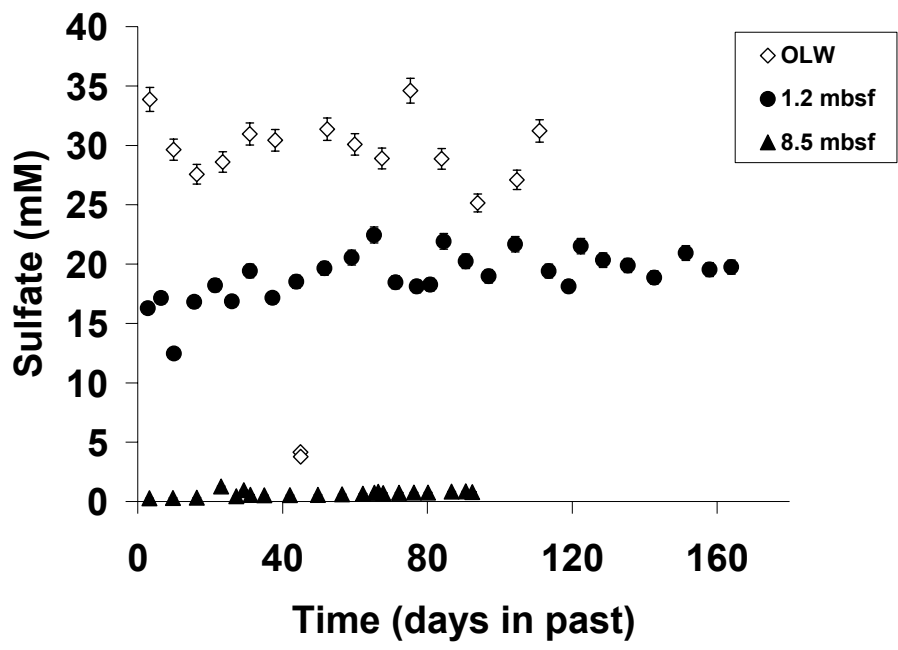


Fig. 3- 13: Sulfate concentrations for all three coils measured. On each point, error bars represent 3% analytical error.

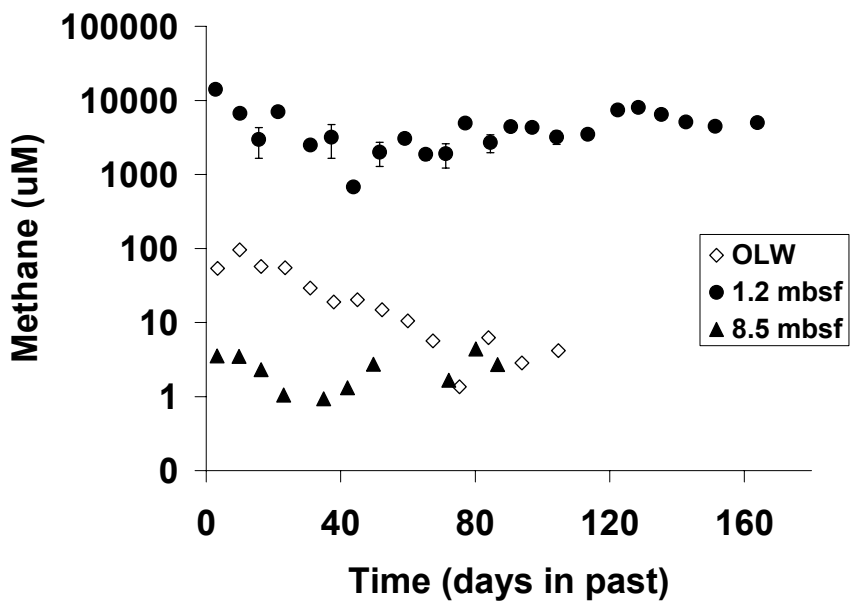
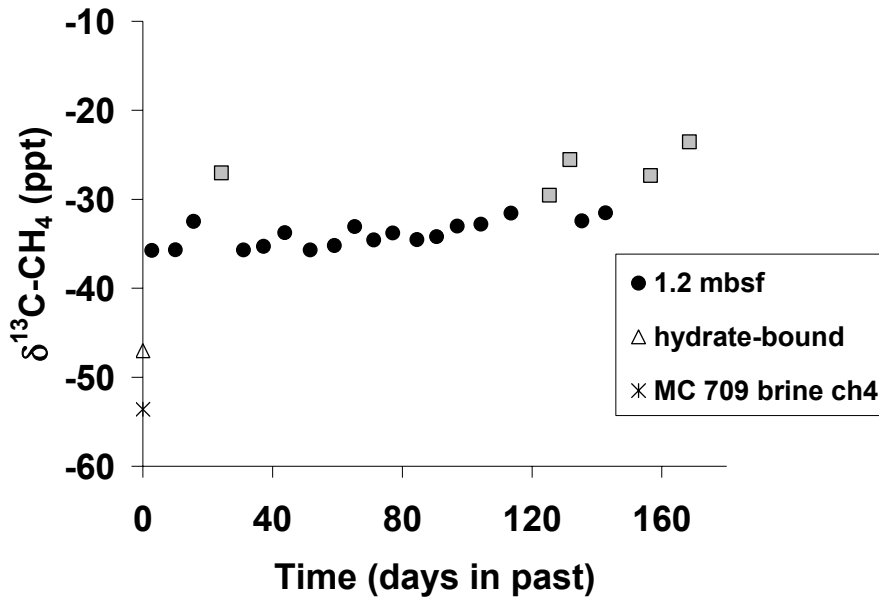


Fig. 3- 14: Methane concentrations for all three coils measured. Note log scale y-axis.



**Fig. 3- 15: Methane isotope composition for 1.2 mbsf shown in black circles and gray squares. Symbols have standard deviation bars on them. Gray squares show values lying outside the average value. Also shown, open triangle is the hydrate-bound methane value as reported in Sassen et al. (2006) and the x-symbol is the methane stable isotope composition measured in brine fluid from a nearby lease block, MC 709 (see dissertation Chapter 6).**

## 4. DISCUSSION

### 4.1. Assessment of PFA design

The first deployment of the PFA allowed us to assess the best possible configurations and materials for future PFA designs. The initial results showed that gold-plated unions corrode and should not be used. Instead, future PFA designs should use the PEEK unions that can withstand the high pressures and long-term seawater exposure. We also found that the high pressure valve did not survive the 1.5 year deployment. Coating it in lithium grease did provide sufficient protection from seawater corrosion. Therefore, future PFA designs will contain the valve contained within a sealed, oil-filled box to minimize corrosion.

Preliminary experiences with sample coils suggests that the ideal tubing for obtaining both *in situ* methane and ion concentrations may not be either copper or the PEEK. Although both materials were able to retain the samples at in situ pressures and were easy to sub-sample using the fraction collector, they each had other problems. First, the copper may have been reactive to sulfate. The OsmoSampler collecting at 1.2 mbsf had a DI-reservoir that was tinted green, possibly due to the precipitation of copper sulfate. Although the fluids sampled within the tubing did not exhibit this discoloration, the sulfate concentrations from the copper tubing are suspect. Long term tests are being conducted in the laboratory to verify this reaction. Secondly, PEEK material may be permeable to methane (i.e. 8.5 mbsf coil). At 8.5 mbsf, where a PEEK coil was used, methane concentrations should have been much higher than measured. Since concentrations were lower than those found in the overlying water, we suspect the PEEK material was permeable to methane. Although methane permeability of PEEK is not known, it has the lowest permeability to oxygen compared to other plastic tubing materials; 14 compared to 881  $\text{cm}^3/100\text{in}^2 \cdot 24\text{hr} \cdot \text{atm}/\text{mil}$  @ 25°C, respectively



(Alltech reports). However, other factors may have contributed to the low observed methane values and laboratory tests are being conducted to measure the methane permeability out of PEEK. Therefore, neither copper nor PEEK may be ideal materials to measure both sulfate and methane concentrations. Future PFA designs will consider other tubing materials such as stainless steel. Stainless steel was originally discounted because of the difficulty in sampling it by traditional cutting techniques and the practical matter of obtaining continuous long lengths. However, since we are using the fraction collector method, cutting it is no longer a problem.

#### **4.2. *In situ* data**

The overall results from the PFA are quite promising. For the first time, we have direct evidence of the occurrence of subsurface brine fluids at MC 118. Geophysical reports have suggested the presence of a sub-seafloor brine deposit (Woolsey et al., 2005). A comparison of the average chloride concentrations at each depth shows that there is a steep concentration gradient with depth. Since brine inhibits hydrate formation, this data can be used to help modify the calculated hydrate stability zone at MC 118 (see section 4.3.).

The results of the PFA data also show that the brine fluid contains high methane concentrations, up to 14 mM, with an average isotopic ratio of  $-32.4 \pm 3.4\%$ . This highly enriched  $^{13}\text{C}$  value was surprising since bubbles and hydrate collected from the southern flank of MC 118 have  $\delta^{13}\text{C}$  values around  $-47\%$  (Sassen et al., 2006). Possible explanations for the enriched methane isotope values are isotope fractionation through diffusion out of the tubing, microbial oxidation or thermogenic methane. Diffusion through copper tubing and subsequent fractionation is unlikely because studies have shown gases do not diffuse through

copper (Lupton et al., 1998). Microbial oxidation and thermogenic methane are discussed below.

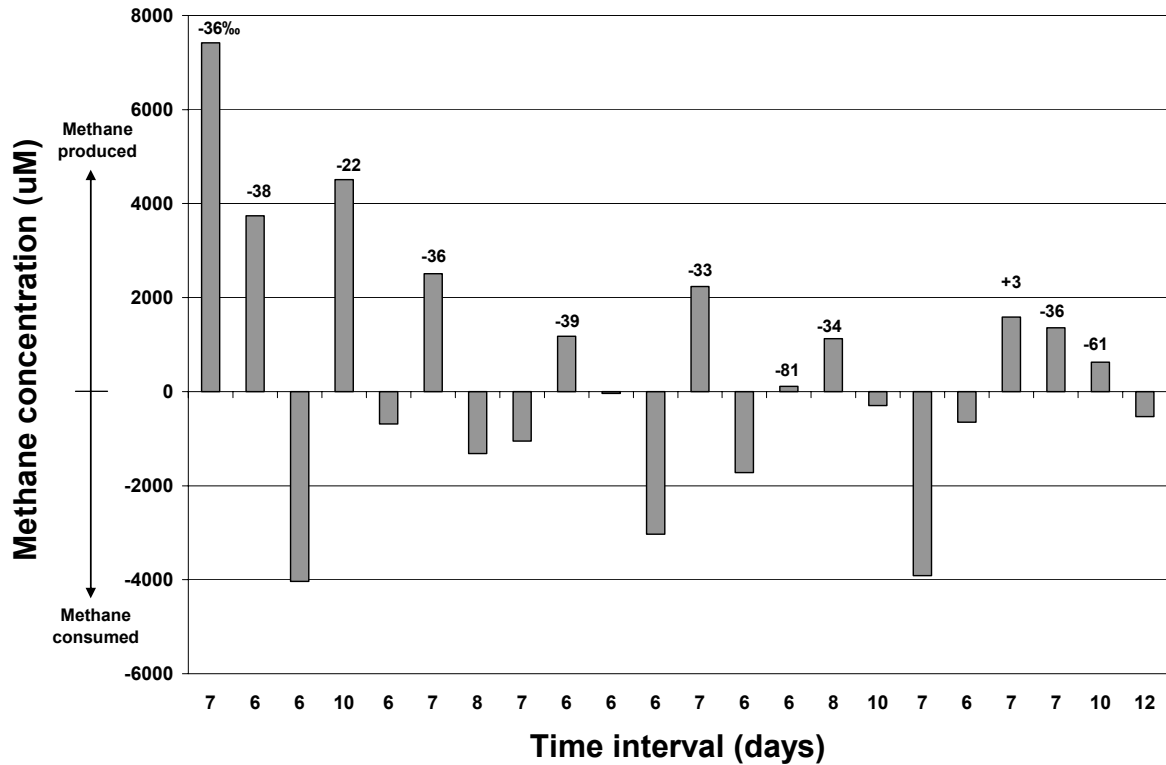
The isotopic signature of the dissolved methane from 3.2 mbsf could be enriched in  $^{13}\text{C}$  due to microbial oxidation. As microbes preferentially consume the lighter isotope, the residual methane becomes more enriched (Alperin et al., 1988). If we evaluate the temporal isotope record, we can better evaluate the source of this methane. Within this record, a trend is clear: the gradual depletion in  $^{13}\text{C}$  over time punctuated by the three spikes of  $^{13}\text{C}$  enriched methane. Since microbial oxidation should result in the isotopic signature becoming more enriched in  $^{13}\text{C}$  over time, the gradual  $^{13}\text{C}$  depletion could not be caused by microbial oxidation. Furthermore, the spikes cannot be from microbial oxidation because they are accompanied by an increase in the methane concentration.

An alternative explanation is that the overall depletion in  $^{13}\text{C}$  over time may be caused by microbial methane production in the sediments with three spike events caused by an increase in the upward flux rate of the purely thermogenic methane. The spike events have an average isotopic signature of  $-26.6 \pm 2.2\%$  which may represent the “end-member” isotopic signature of the purely thermogenic methane. However, these spikes are not associated with an increase in brine since there was no concurrent pulse in the chloride data. To fully understand the role microbial processes play in controlling changes in the methane isotopic signature, additional data are needed such as the isotopic signature of the dissolved inorganic carbon. Although there are still unresolved issues with this data set, it is clear that there are large changes occurring in pore water composition even over 4 months time and that temporal records from PFA samplers can contribute much to our understanding of the impact of those changes on hydrate stability.

The methane isotope data was further evaluated to determine the isotopic signature of the methane either produced or consumed within the concentration and isotope records. This was carried out using the following mass balance equation:

$$(\delta^{13}\text{C} \cdot [\text{CH}_4])_{\text{source}} + (\delta^{13}\text{C} \cdot [\text{CH}_4])_{t1} = (\delta^{13}\text{C} \cdot [\text{CH}_4])_{t0} \quad (2)$$

where  $\delta^{13}\text{C}$  and  $[\text{CH}_4]$  are the stable carbon isotopic signature of methane and methane concentration for the source methane (source), later time point (t1) and earlier time point (t0). The concentrations of the methane source needed to explain the isotopic signature at two time points is the difference of the methane concentrations at those two time points. Solving for  $\delta^{13}\text{C}_{\text{source}}$ , it becomes apparent that a wide range of isotopic values are needed to explain the isotope and concentration results (Fig. 3-16). However, it should be noted that since these concentrations may still be minimums (because the valve failed), these results should be interpreted with caution. The average isotope value for the methane source is  $-37.5 \pm 20.8\text{‰}$  which is similar to the average isotope value over time ( $-32.4\text{‰}$ ). However, the large standard deviation associated with this average is not well understood. For example, in Figure 16, the isotopic signature of one methane source is  $+3\text{‰}$ . Since there is no known methane source to give such isotopically enriched value, this mass balance exercise suggests a possible artifact in the isotope data. At this time, the cause for this artifact is not known.

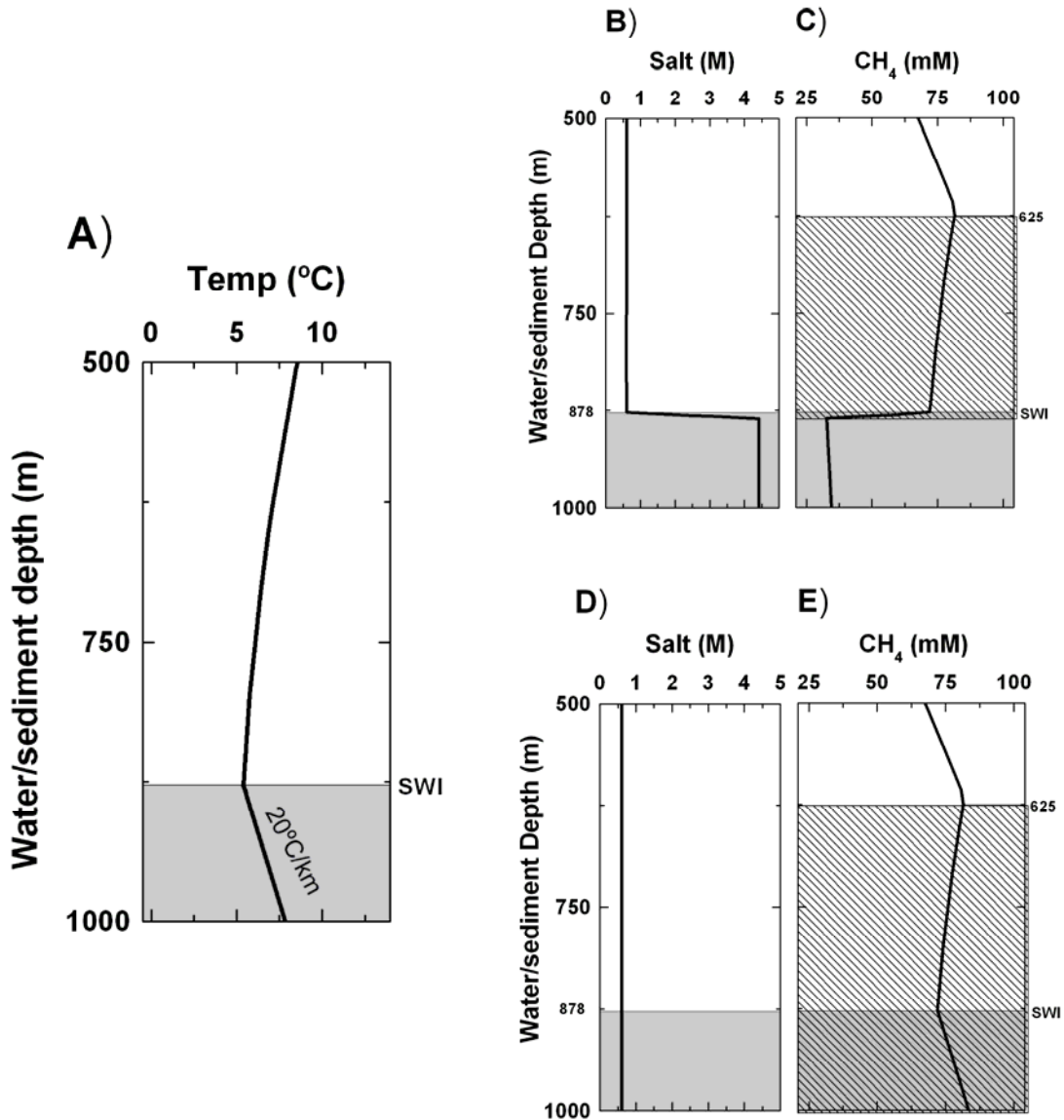


**Fig. 3- 16: For the 1.2 mbsf coil, methane produced and consumed over specific time intervals over the course of the 170 day PFA deployment using equation 2. Numbers above the concentration bars indicate the isotopic composition of the methane source.**

There may also be artifacts in the sulfate and chloride concentrations due to the methods used for sub-sampling. The *in situ* chloride and sulfate concentrations from the overlying water sample coil show a surprising variability over time. This variability is not due to changes in chloride or sulfate alone since the Cl:SO<sub>4</sub> ratio does not change over time. Therefore, the variability may be caused from salt crystals precipitating during the sub-sampling procedure. Until laboratory tests are completed to fully address this issue, the temporal variations in sulfate and chloride should be not be over interpreted.

### **4.3. *In situ* hydrate stability models**

*In situ* chloride and temperature data can be used to improve estimates of the hydrate stability zone (HSZ) at our PFA sampling site. Using the average chloride data at 8.3 mbsf and assuming saturated methane conditions, the HSZ was estimated from a thermodynamic model (Duan and Mao, 2006) to be 256 m thick, spanning from 625 to 881 meters of water and sediment depth (Fig. 3-17). Since the water column is 878 meters, the HSZ only penetrates 3 meters into the seafloor. This explains why no outcropping hydrate was visible near the PFA. Alternatively, at a hydrate outcrop ~500 meters to the south of the PFA, where no brine exists, the HSZ was calculated to be from 625 to 1000 meters water/sediment depth and supports the substantial hydrate outcrops seen. Furthermore, gas vents were observed and when contained within a core tube, quickly precipitated hydrate (Sassen, personal communication, 2006). Obtaining *in situ* ion and temperature data is paramount to understanding the hydrate stability zone.



**Fig. 3- 17: Results of thermodynamic model to determine the hydrate stability zone at MC 118. A) Temperature profile in water column and sediments at MC 118. Water column profile obtained from CTD casts and sedimentary geothermal gradient was assumed to be 20°C/km. SWI = sediment water interface. B) PFA salinity profile. Sedimentary salinity gradient was assumed to be a constant 4.5 M below 10 meter below seafloor. C) Saturated methane concentration profile necessary to precipitate hydrate. Hydrate stability zone shown in hatched area, from 625 and 881 meters water/sediment depth. D) From a site ~500 meters south of the PFA, a constant salinity with depth is assumed. E) Saturated methane concentration profile necessary to precipitate hydrate. The HSZ (hatched area) penetrates down to 1000 m or 122 m below seafloor.**

#### **4.4. Future considerations**

From this first PFA deployment, several issues arose that need to be taken into consideration for the future. First, variability in the overlying water sulfate and chloride concentrations measured was high. Since this variability is unlikely due to natural changes in seawater sulfate and chloride concentrations, it could have been due to issues with the sub-sampling procedure or analytical measurements. The sub-sampling procedure using the fraction collector increased the temporal resolution and may not be able to handle high pressures. To determine the best method for sub-sampling, laboratory tests must be conducted before analyzing the next PFA sample set. Furthermore, considerations of the precision and accuracy needed to determine natural changes over time must be made. It may also be useful to collect overlying water from three individual samplers to assess error over time. While sample replication would be ideal, it may be unrealistic with the limited resources available. These considerations will be made for future deployments of the PFA.

### **5. CONCLUSIONS**

Directly assessing hydrate stability within the sediment column where migrating brine fluids are altering pore water chemical composition requires a tool to collect undecompressed pore-fluid samples that can yield in situ methane and dissolved ion concentration measurements as a proxy for hydrate formation and/or dissociation. We have successfully designed, deployed, and recovered such a tool- the PFA. Several different materials and configurations were tested in order to assess the best possible designs for future long term PFA deployments. The preliminary PFA deployment results showed the potential importance of brine and thermogenic fluids present at MC 118 in effecting hydrate stability. Future deployments of the PFA will be made in concert with geophysical measurements of

seismic events within the hydrate zone to help assess how temporal variability in fluid transport processes induce changes in hydrate stability.

*Acknowledgements.* I would like to thank Hans Jannasch, MBARI, for helping me with the OsmoSampler designs and providing scientific and technical help along the way. Jean Whelan sent me my first OsmoSampler and encouraged me along the way. The design and construction of the connector was provided by Paul Higley, Specialty Devices, Inc. The construction, recovery, and deployment of the PFA would not have been possible without the help of Bob Woolsey, Brian Noakes, Matt Lowe, Andy Gossett, and Larry Overstreet, University of Mississippi Machine Shop. Jim Gambony, Specialty Devices Inc., built the OsmoSampler instrument package box. Don Brewer, University of North Carolina Chemistry Machine Shop, built the OsmoSamplers. And Sam Perkins helped with the OsmoSampler laboratory experiments. Claire Langford ran all the samples for methane concentrations and isotope ratios. This project was funded as part of the Hydrate Research Consortium, University of Mississippi.



## 6. REFERENCES

- Alperin M. J., Reeburgh W. S., and Whiticar M. J. (1988) Carbon and hydrogen isotope fractionation resulting from anaerobic methane oxidation. *Global Biogeochemical Cycles* **2** (3), 279-288.
- Bidle K. A., Kastner M., and Bartlett D. H. (1999) A phylogenetic analysis of microbial communities associated with methane hydrate containing marine fluids and sediments in the Cascadia Margin (ODP site 892B). *FEMS Microbiology Letters* **177**, 101-108.
- Duan Z. and Mao S. (2006) A thermodynamic model for calculating methane solubility, density, and gas phase composition of methane-bearing aqueous fluids from 273 to 523 K and from 1 to 2000 bar. *Geochimica et Cosmochimica Acta* **70**, 3369-3386.
- Fisher A. T., Urabe T., Klaus A., Wheat C. G., Becker K., Davis E. E., Jannasch H. W., Hulme S., Nielsen M., Schroeder D., Dixon R., Pettigrew T., MacDonald R., Meldrum R., Fisk M., Cowen J., Bach W., Edwards K., and Party I. E. S. (2005a) IODP expedition 301 installs three borehole crustal observatories, prepares for three-dimensional, cross-hole experiments in the northeastern Pacific Ocean. *Scientific Drilling* **1**, 6-11.
- Fisher A. T., Wheat C. G., Becker K., Davis E. E., Jannasch H. W., Schroeder D., Dixon R., Pettigrew T., Meldrum R., MacDonald R., Nielsen M., Fisk M., Cowen J., Bach W., and Edwards K. A. T. Fisher, T. Urabe, A. Klaus, and e. al. (2005b) *Scientific and technical design and deployment of long-term, subseafloor observatories for hydrogeologic and related experiments, IODP Expedition 301, Eastern flank of Juan de Fuca Ridge*, College Station, TX.
- Jannasch H. W., Davis E., Kastner M., Morris J., Pettigrew T., Plant J. N., Solomon E., Villinger H., and Wheat C. G. (2003) CORK II: Long-term monitoring of fluid chemistry and hydrology instrumented boreholes at the Costa Rica subduction zone., In *Proceedings of the Ocean Drilling Program, Initial Reports Volume 205* (ed. Morris and Klaus).
- Jannasch H. W., Johnson K. S., and Sakamoto C. M. (1994) Submersible, osmotically pumped analyzers for continuous determination of nitrate in situ. *Analytical Chemistry* **66**, 3352-3361.
- Jannasch H. W., Wheat C. G., Plant J. N., Kastner M., and Stakes D. S. (2004) Continuous chemical monitoring with osmotically pumped water samplers: OsmoSampler design and applications. *Limnology and Oceanography: Methods* **2**, 102-113.
- Joye S. B., Boetius A., Orcutt B. N., Montoya J. P., Schulz H. N., Erickson M. J., and Lugo S. K. (2004) The anaerobic oxidation of methane and sulfate reduction in sediments from Gulf of Mexico cold seeps. *Chemical Geology* **205**, 219-238.

- Kennett J. P., Cannariato K. G., Hendy I. L., and Behl R. J. (2003) *Methane hydrates in Quaternary climate change: The clathrate gun hypothesis*. American Geophysical Union, Washington, DC.
- Lanoil B. D., Sassen R., LaDuc M. T., Sweet S. T., and Nealson K. H. (2001) Bacteria and Archaea physically associated with Gulf of Mexico gas hydrates. *Applied and Environmental Microbiology* **67** (11), 5143-5153.
- Lelieveld J., Crutzen P. J., and Dentener F. J. (1998) Changing concentration, lifetime and climate forcing of atmospheric methane. *Tellus* **50B**, 128-150.
- Lupton J. E., Baker E. T., and Greene R. R. (1998) Anomalous helium and heat signatures associated with the 1998 Axial Volcano event, Juan de Fuca Ridge. *EOS, Transactions, American Geophysical Union* **79**, 8135.
- Marchesi J. R., Weightman A. J., Cragg B. A., Parkes R. J., and Fry J. C. (2001) Methanogen and bacterial diversity and distribution in deep gas hydrate sediments from the Cascadia Margin as revealed by 16S rRNA molecular analysis. *FEMS Microbiology Ecology* **34**, 221-228.
- Milkov A. V. (2004) Global estimates of hydrate-bound gas in marine sediments: how much is really out there? *Earth-Science Reviews* **66**, 183-197.
- Mills H. J., Hodges C., Wilson K., MacDonald I. R., and Sobecky P. A. (2003) Microbial diversity in sediments associated with surface-breaching gas hydrate mounds in the Gulf of Mexico. *FEMS Microbiology Ecology* **46** (39-52).
- Orcutt B. N., Boetius A., Lugo S. K., MacDonald I. R., Samarkin V. A., and Joye S. B. (2004) Life at the edge of methane ice: microbial cycling of carbon and sulfur in Gulf of Mexico gas hydrates. *Chemical Geology* **205**, 239-251.
- Sassen R., MacDonald I. R., Guinasso Jr. N. L., Joye S., Requejo A. G., Sweet S. T., Alcalá-Herrera J., DeFreitas D. A., and Schink D. (1998) Bacterial methane oxidation in sea-floor gas hydrate: Significance to life in extreme environments. *Geology* **26**, 851-854.
- Sassen R. and Roberts H., 2004. Site selection and characterization of vent gas, gas hydrate, and associated sediments. DOE Technical Report.
- Sassen R., Roberts H. H., Jung W., Lutken C. B., DeFreitas D. A., Sweet S. T., and Guinasso Jr. N. L. (2006) The Mississippi Canyon 118 Gas Hydrate Site: A complex natural system. *OTC Paper #18132; Offshore Technology Conference*.
- Sloan E. D. E. D. Sloan (1998) *Clathrate hydrates of natural gases, second edition*. Marcel Dekker, Inc., New York.
- Ussler W. and Paull C. K. (2001) Ion exclusion associated with marine gas hydrate deposits. In *Natural gas hydrates: occurrence, distribution, and detection* (ed. C. K. Paull and W. P. Dillion), pp. 315. American Geophysical Union.

Woolsey J. R., Higley P., Lapham L. L., Chanton J. P., Lutken C., Sleeper K., Culp R., Sharpe S., and Ross D., 2005. Operations report of cruise GOM2-05-MC118 Deployment of the initial components of the sea floor monitoring station- The pore-fluid array and the geophysical line array- via the sea floor probe system and collection of core samplers, Mississippi Canyon 118. Gulf of Mexico Hydrates Research Consortium: University of Mississippi Center for Marine Resources and environmental technology.

## **Chapter 4: Utilization of HYDRA for *in situ* concentrations and $\delta^{13}\text{C}$ values of methane dissolved in pore-fluids surrounding buried gas hydrates: Ramifications for hydrate stability**

**Abstract-** The quantification of *in situ* dissolved methane concentrations is necessary in order to fully understand the stability of hydrates found in shallow oceanic sediments. Yet, such concentrations are difficult to measure in the deep sea because methane is relatively insoluble in seawater and quickly comes out of solution with pressure release during sample ascent through the water column. Therefore, a novel instrument named HYDRA was utilized to collect pore-fluids adjacent to hydrate and retain samples at *in situ* pressures for shipboard methane concentration measurements. This instrument was deployed at Barkley Canyon on the northern Cascadia Margin off the coast of Vancouver Island, British Columbia where several large hydrate outcrops are known to exist. If these outcrops are thermodynamically stable, the surrounding pore-fluids will be saturated with respect to methane and contain ~67 mM concentrations. Yet, due to microbial methane oxidation and diffusive transport processes, we expected the pore-fluids to be undersaturated with respect to methane. To test this, *in situ* methane concentration and stable carbon isotopic compositions were measured from six different locations and distances from the outcrops; such as thin and thick bacterial mats, oily and gassy sediments, clam fields, and reference sediments from 3 to 350 cm distances. Regardless of distance from the hydrate or environment, the maximum concentration measured was 18 mM; seven fold less than the saturation concentration. The

stable carbon isotopic composition of this methane closest to the hydrate was isotopically similar to the hydrate-bound methane and probably resulted from hydrate dissolution. Further from the hydrate, the values became more enriched in  $^{13}\text{C}$  than hydrate-bound methane, which suggests microbial oxidation. This data suggests hydrates are unstable and should be dissolving through diffusion. However, seafloor observations do not support the estimated diffusion controlled dissolution rates. Therefore, this research supports the hypothesis that hydrates may be more stable than theory predicts and their dissolution may be controlled by kinetics rather than thermodynamics.

## 1. INTRODUCTION

Gas hydrates are crystalline ice compounds containing light hydrocarbon gases, primarily methane,  $\text{CO}_2$ , and  $\text{H}_2\text{S}$  (Sloan, 1998). They form in oceanic sediments and arctic permafrost under conditions of high pressure, low temperature, and/or moderate salinities when surrounding fluids are saturated with respect to methane. Hydrates are thought to be Earth's largest methane reservoir, containing ~500 to 2,500 Gt methane carbon (or 1 to  $5 \times 10^{15} \text{ m}^3$  methane, (Milkov, 2004). Currently, this reservoir is relatively stable and considered to be a minor source of atmospheric methane (Lelieveld et al., 1998). However, if destabilized, hydrate deposits have the potential to release enormous amounts of methane into the oceans and possibly directly into the atmosphere; contributing to global climate change (Kvenvolden, 1993; Kennett et al., 2003). Such destabilizations appear to have occurred on geological time scales due to large variations in pressure and temperature (Kennett et al., 2003). On shorter time scales, hydrate destabilizations could occur with changes in surrounding methane concentrations. However, little is known about the *in situ* methane

concentrations surrounding hydrate and, in order to fully assess hydrate stability, the capability to measure and understand controls on *in situ* methane concentrations is needed.

It is commonly assumed that stable hydrates are surrounded by fluids that are saturated with respect to methane (Egorov et al., 1999; Rehder et al., 2004). Using a thermodynamic model, a methane solubility curve can be estimated that predicts the concentrations at which methane saturates the solution and forms gas bubbles or hydrates with the excess (Duan and Mao, 2006). In the oceans, this curve is dependent upon the depth, temperature, and salinity of the water and sediment column (Fig. 4-1). For example, at Barkley Canyon located on the Cascadia margin off British Columbia, Canada, the methane solubility increases from approximately 1.2 mM at the water-atmosphere interface to 100 mM at the top of the hydrate stability zone (HSZ) or 650 meters water depth. The concentration then decreases to the sediment-water interface; where it is ~67 mM. Below this depth, due to the sedimentary geothermal gradient, the concentration increases through the bottom of the HSZ and beyond. The model shows two important points; hydrate is thermodynamically stable when exposed to methane-saturated pore-fluids and pure methane bubbles are not thermodynamically stable within the hydrate stability zone. It is important to note that the methane solubility concentration will be lower if a thermogenic gas mixture is present.

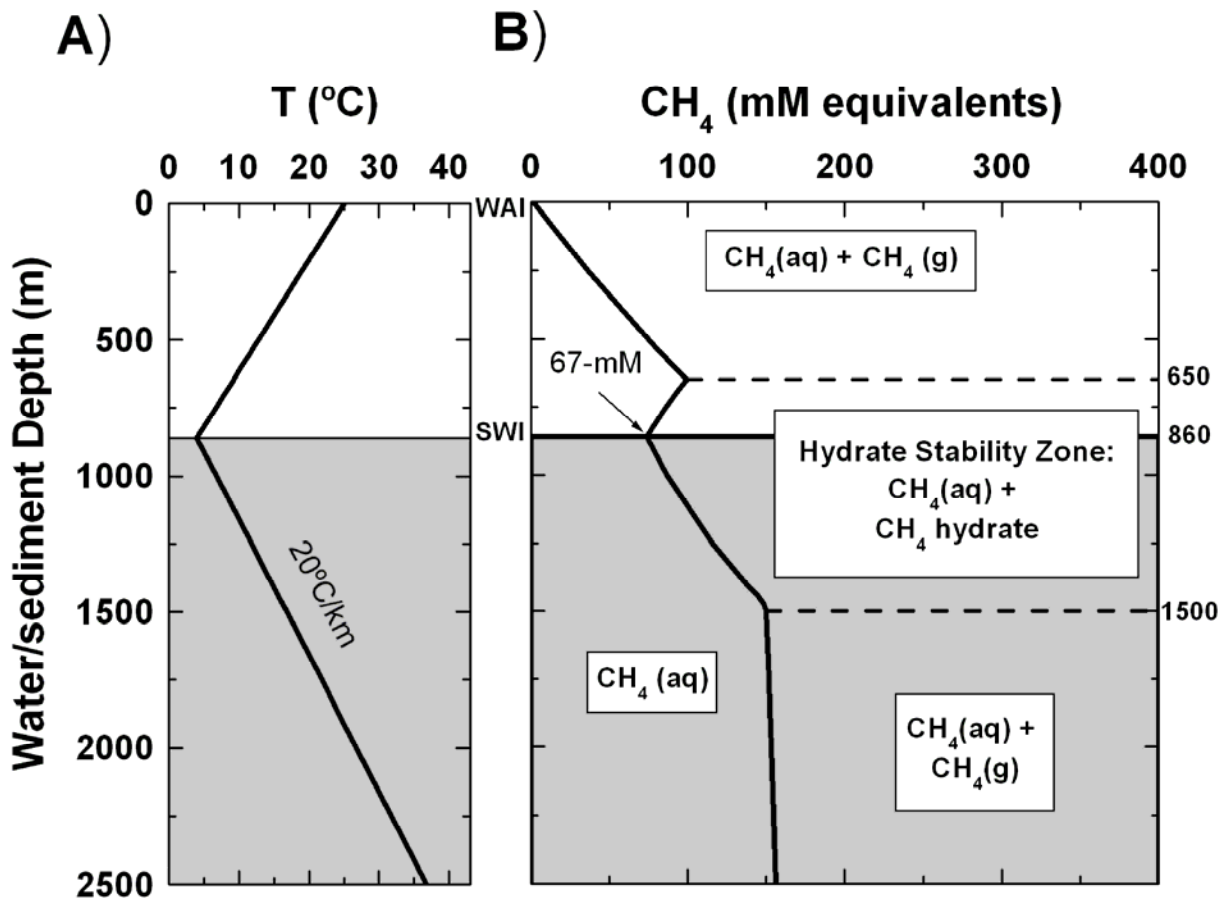


Fig. 4- 1: A) Barkley Canyon temperature and depth profile through the ocean water and sediment column. Geothermal gradient was assumed to be 20°C/km. B) Using a thermodynamic model (Duan and Mao, 2006), the relationship is shown between three phases of methane (CH<sub>4</sub>): aqueous (aq), gaseous (g), and hydrate. Methane concentrations are given in mM equivalents. The solid black line represents the methane solubility curve at thermodynamic equilibrium. The black horizontal dashed lines show the top and bottom of the hydrate stability zone (depths in meters given to right of graph). WAI = water atmosphere interface; SWI = sediment water interface.

When pure methane hydrate is exposed to pore-fluids undersaturated in methane, thermodynamic theory predicts that it will dissolve (Rehder et al., 2004; Duan and Mao, 2006). Hydrates most vulnerable to dissolution are those found outcropping the seafloor or buried by a thin veneer of sediments. Such deposits are in direct or close contact with air-equilibrated seawater that is far undersaturated with respect to pure methane gas bubbles (3 nM methane, Pohlman, 2006). Therefore, theory predicts that the methane contained within the hydrates will diffuse out of the hydrate cage and into the undersaturated surrounding waters thus resulting in hydrate dissolution.

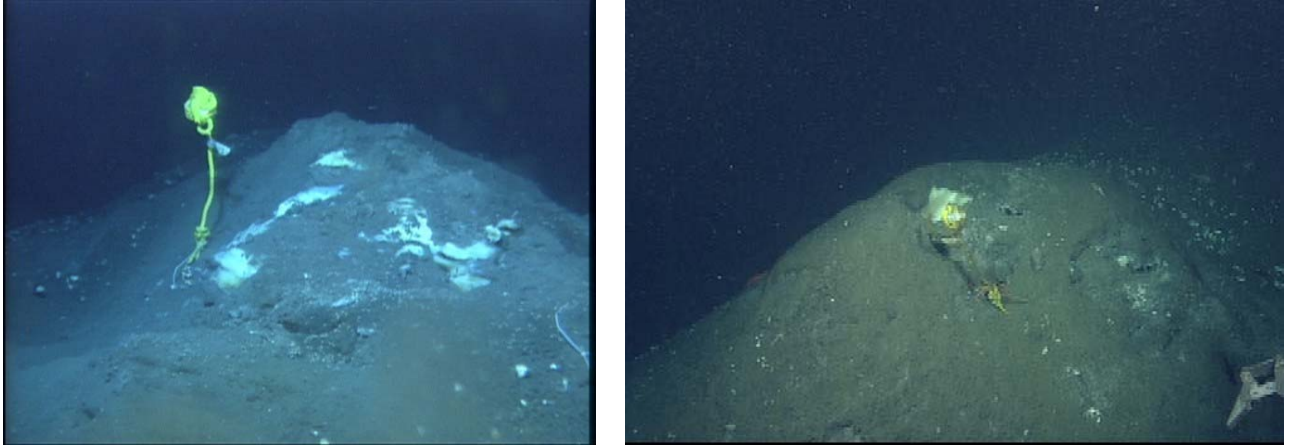
The rate of hydrate dissolution has been both modeled and measured. Modeled rates assume dissolution is controlled by diffusion and thus, can be estimated from Fick's first law. From such a model, outcropping hydrates were estimated to dissolve at ~30 cm/year (Egorov et al., 1999). More recently, measured rates were calculated by bringing laboratory precipitated hydrate to the seafloor and observing its dissolution over time. The hydrate loss rate was found to be 300 cm/year, an order of magnitude higher than predicted rates (Rehder et al., 2004). While there is a clear discrepancy between these predicted and measured values, dissolution experiments need to be conducted with hydrates precipitated under *in situ* conditions.

*In situ* observations of outcropping hydrate should also shed light on the importance of dissolution. At either the predicted or measured dissolution rates, hydrate outcrops should show considerable change over time. However, using seafloor cameras, it was shown that there was little to no morphological change in a hydrate outcrop over 1 year (MacDonald et al., 2005). Also, visual observations during annual visits to Barkley Canyon outcrops



showed little change in outcrop morphology (Fig. 4-2). If these hydrates are more stable than predicted, what is keeping them from dissolving?

Hydrates may be more stable than originally thought because of three possible factors. The first is that their dissolution is not controlled by diffusion alone but also by kinetic barriers associated with the hydrate cage itself or surface barriers. The second is that the hydrates are accreting at the same rate from below (Egorov et al., 1999). And finally, it is possible that the shallow buried hydrates are surrounded by fluids saturated in methane. This possibility is supported by observations of methane-rich bubbles emanating from sediments upon disruption (Pohlman et al., 2005). However, chemical exchange resulting from mixing and vertical diffusion should result in below saturation values close to the sediment water interface. Furthermore, the anaerobic oxidation of methane (AOM) is expected to consume a large fraction of the upwardly migrating dissolved methane via sulfate reduction (Martens and Berner, 1977; Reeburgh and Heggie, 1977). Although these studies were conducted in coastal systems, AOM may be an important process in hydrate-bearing sediments. Recent work sheds light on the mechanism carried out during AOM (Hoehler et al., 1994) and the presence of the consortium of micro-organisms responsible (Boetius et al., 2000). Subsequent work has shown these micro-organisms to be in close contact with the hydrate (Orcutt et al., 2004) or present within surrounding sediments (Lanoil et al., 2001; Joye et al., 2004). In order to assess these three different factors to explain the stability of shallow buried hydrates, the distribution of *in situ* concentrations and  $\delta^{13}\text{C}$  values of methane are needed.



**Fig. 4- 2: Barkley Canyon site “double mound” visited in A) 2004 (photo from ROPOS video archive) and B) 2006 (photo courtesy of Edward Peltzer, MBARI).**

The purpose of this study was to utilize *in situ* sampling techniques in sediments surrounding shallow buried hydrate deposits to determine the spatial distribution of dissolved methane concentration and isotopic composition. Such distributions will aid in assessing the stability of hydrate and the role microbial processes may have in this stability. Although theory predicts stable hydrates (i.e., those observed to not undergo physical changes as described above) should be bathed in saturated methane, we hypothesized that they might be stable for reasons other than thermodynamic equilibrium with surrounding pore-fluids and that methane undersaturation would occur in surrounding pore-water because of losses due to diffusive transport and microbial oxidation processes. To obtain the needed samples, we developed a novel instrument named HYDRA that collected pore-fluid samples and stored them at *in situ* pressures during sample recovery (described in Chapter 2). Traditional coring methods are not ideal because pore-fluids super-saturate and degas upon ascent up through the water column. HYDRA was deployed in shallow sediments to collect concentration and isotope profiles from six different distances from hydrate outcrops within different environments. Along with quantifying the *in situ* methane concentrations, microbial

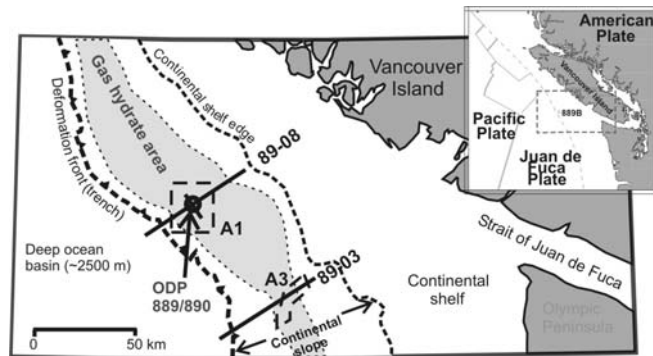
oxidation was also assessed through modeling vertical sulfate concentration gradients and methane  $\delta^{13}\text{C}$  horizontal distributions. To our knowledge, these are the first *in situ* methane concentration and isotope gradients obtained from sediments at a hydrate site.

## 2. MATERIALS AND METHODS

### 2.1. Geological setting

Barkley Canyon is located 80 km west of Vancouver Island, British Columbia on the northern Cascadia Margin (Fig. 4-3;  $48^{\circ}18.84'\text{N}$ ,  $126^{\circ}03.26'\text{W}$ , 860 meters water depth; Spence et al., 2001). The northern

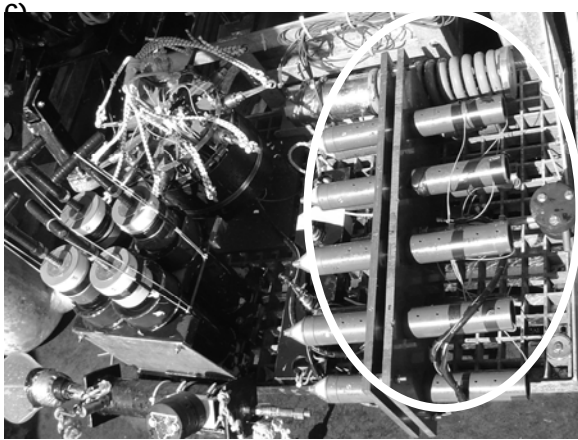
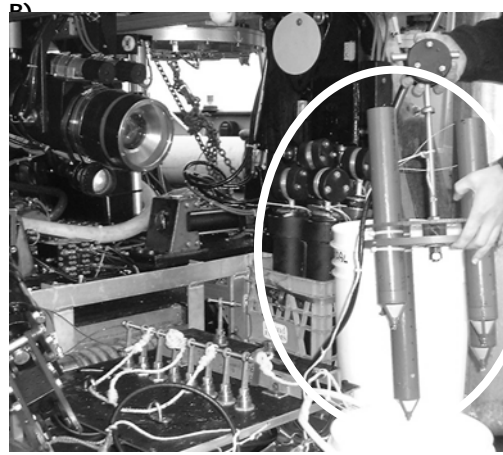
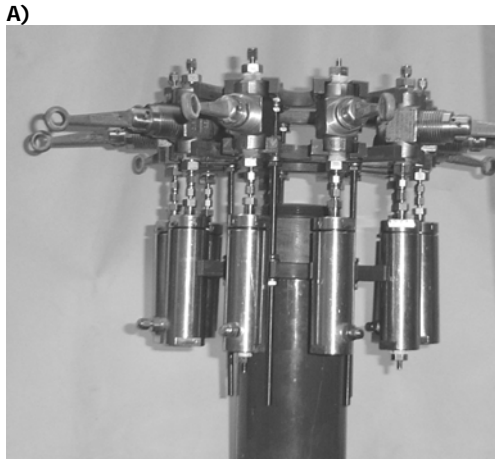
margin is an active accretionary wedge resulting from subduction of the Juan de Fuca plate under the American plate and has proven to be an active site of methane hydrate formation (Hyndman et al., 2001). Barkley Canyon contains gas hydrate deposits both as exposed outcrops and buried deposits in sediment (Chapman et al., 2004). The hydrates are formed from thermogenic methane and other gases that originate from deep source rock kerogen thermal degradation (Pohlman et al., 2005). Outcropping hydrates were associated with bacterial mats and both living and dead clams but not tube worms (Ross Chapman, personal communication). Natural gas and oil venting occurred as well as venting initiated by sediment disturbance.



**Fig. 4- 3: Northern Cascadia Margin (upper right panel). Gas hydrate area is shown along the shelf and includes Barkley Canyon as A3.**

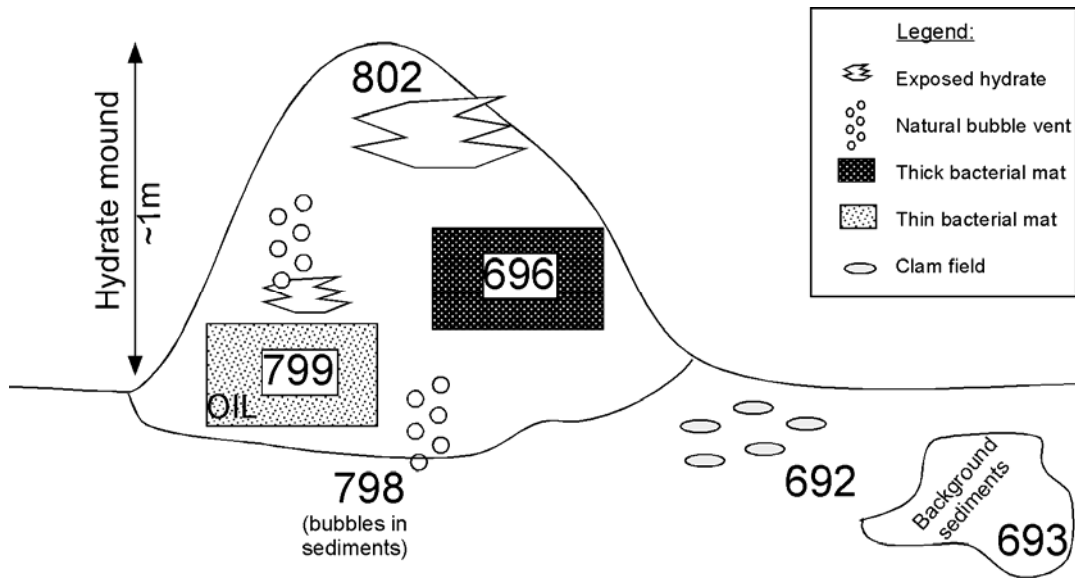
## 2.2. Sample collection

In the summers of 2003 and 2004, the remotely operated vehicle ROPOS (Remotely Operated Platform for Ocean Science) was utilized to collect sediment pore-water samples with a novel *in situ* collection array named HYDRA (Fig. 4-4; described thoroughly in Chapter 2). Using hydraulic suction, HYDRA collects discrete pore-water samples through filtered intake ports and stores them in stainless steel sample chambers (Fig. 4-4a). Using high pressure valves (Fig. 4-4a), chambers retain samples at *in situ* pressures until sampled on board ship, preventing degassing during ascent through the water column. The intake ports are housed within two types of tips; the first has four ports in a rosette configuration (Fig. 4-4b; i.e. dive 693, Table 4-1) and the second has 10 ports in a 3D array (Fig. 4-4c; i.e. dive 798, Table 4-1). The 3D array ports can be set at different depths to accommodate the sedimentary environment. The footprint of the rosette is about 50 cm diameter and the 3D array is about 75 cm x 50 cm. Due to these large footprints, HYDRA collects vertical depth dependent samples as well as samples collected over an approximately 75 cm horizontal distance.



**Fig. 4- 4: Photographs of HYDRA in action. A) Stainless steel sample chambers with high pressure valves shown. B) HYDRA on the front deck of ROV ROPOS with the 4-port probe tip circled in white. The high pressure valves are shown in the background lined up in a row. C) HYDRA on the front deck of ROPOS configuration with the 10-port probe tip circled in white. Sediment push cores are visible to the bottom left of the tip. To the upper left of the tip, the sample chambers and high pressure valves are shown.**

HYDRA was deployed at six different locations and distances from outcropping hydrate on six different dives (Fig. 4-5, Table 4-1, and Table 4-2). On dive 693, HYDRA was deployed in soft sediments, devoid of clams or bacterial mats, about 350 cm away from a large hydrate outcrop (Fig. 4-5 and Table 4-1). On dive 799, HYDRA was deployed in a bacterial mat about 200 cm from exposed hydrate and bubble vents (Fig. 4-5 and Table 4-1). Upon extraction of the tip from the sediments, oil bubbles were released. On dive 798, HYDRA was deployed into sediments on the edge of bacterial mats, about 200 cm from an exposed hydrate outcrop (Fig. 4-5 and Table 4-1). One bubble vent was visible about 10 cm away from one of the tip intakes. During this deployment, the submersible equipment platform disrupted the sediments which resulted in the release of gas bubbles. On dive 692, HYDRA was deployed on the edge of a clam (both live and dead) field, about 150 cm away from a large hydrate mound (Fig. 4-5 and Table 4-2). On dive 696, HYDRA was deployed directly into a thick bacterial mat, about 50 cm from a hydrate exposure (Fig. 4-5 and Table 4-2). And finally, on dive 802, HYDRA was deployed on top of an exposed cliff of hydrate covered with ~15 cm of sediment (Fig. 4-5 and Table 4-2). Although clam shells were visible in these sediments, bacterial mats were not. Upon tip extraction, small chips of hydrate were released into the overlying water.




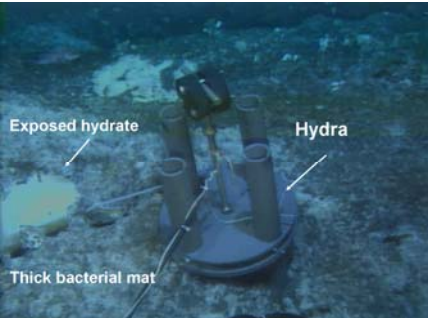
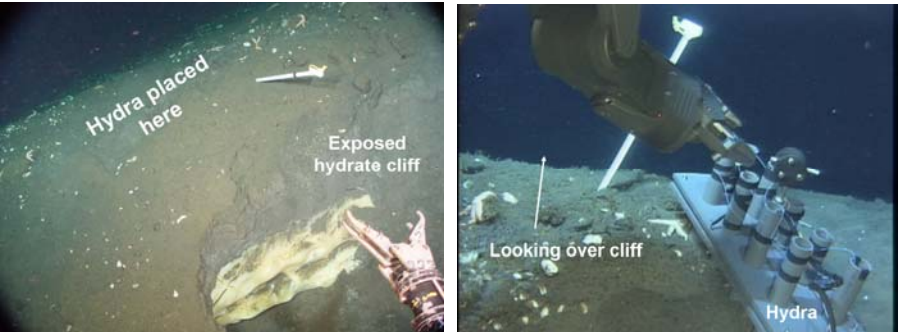
**Fig. 4- 5: Conceptual picture of the HYDRA deployments on a hydrate mound. Numbers refer to submersible dive numbers. It is important to note that not all dives took place on one hydrate mound.**

**Table 4- 1: Pictures of each HYDRA deployment and relative distance to the hydrate outcrop.**

Dive #	Distance from outcrop	Deployment pictures
693	350 cm	
799	200 cm	
798	200 cm	



**Table 4- 2: Pictures of each HYDRA deployment and relative distance to the hydrate outcrop.**

Dive #	Distance from outcrop	Deployment pictures
692	350 cm	
696	50 cm	
802	on top	

### 2.3. Analytical Techniques

Pore-fluids were extracted from HYDRA and placed into evacuated glass serum vials sealed with blue butyl stoppers. To each vial, helium was added to overpressurize the headspace by 6 mL. Samples were then measured for methane concentrations onboard ship (described below). After concentrations were measured, the vials were frozen upside down, with rubber stopper submerged to minimize headspace diffusion, for land-based carbon isotopic composition measurements.

For concentrations, methane was extracted from the dissolved phase into the gas phase by shaking vials for 2 minutes. A 3 mL gas aliquot was then taken from the headspace and injected into a Shimadzu Mini-II gas chromatograph (GC) equipped with a Poroplot-Q column and flame ionization detector. Scott specialty gas standards were used for calibration. CH<sub>4</sub> (ppm) was calculated for each sample by comparing their areas to the standard areas. Dissolved methane concentrations CH<sub>4</sub> (uM) were then calculated by:

$$CH_4 (\mu M) = \frac{P}{RT} [CH_4 (ppm)] \left( \frac{\text{headspace volume (mL)}}{\text{pore water volume (mL)}} \right) \left( \frac{1}{0.95} \right) \left( \frac{1}{\text{correction factor}} \right) \quad (1)$$

where P is 1 atm pressure, R is the gas constant (0.08205 L atm/mol K), T is temperature in K, headspace volume is the volume of headspace (mL) including any helium added to each evacuated vial to slightly over-pressurize it, pore-water volume is the volume (mL) of pore-fluid collected from HYDRA, 1/0.95 is the methane extraction efficiency, and the ‘correction factor’ term refers to two corrections that were made to the methane concentrations. The corrections were made for DI-water dilution and seawater channeling down the probe tip and are thoroughly discussed in chapter 2 and will not be presented further here. In this chapter, concentrations corrected for DI-water dilution are denoted as CH<sub>4</sub>-x and those corrected for

channeling dilution are denoted as CH<sub>4</sub>-f. Furthermore, all concentrations and correction factors are tabulated in chapter 2-table 2-4 and 2-5.

Carbon stable isotope ratios for dissolved methane were analyzed at the UNC stable isotope facility using a pre-concentrating system on-line with a continuous flow 5890 Hewlett-Packard gas chromatograph (Palo Alto, CA) equipped with a Poropak Q column set at 30°C, capillary combustion, and Finnigan Mat 252 isotope ratio mass spectrometer (Thermo Finnigan, Bremen, Germany) as described in Rice et al. (2001). Carbon isotope ratios (<sup>13</sup>C/<sup>12</sup>C) are compared between a sample and internal standard by expressing the relative change in <sup>13</sup>C using the conventional δ notation with units of per mil, ‰:

$$\delta^{13}C(\text{‰}) = \left( \frac{R_{\text{sample}} - R_{\text{standard}}}{R_{\text{standard}}} \right) \times 1000 \quad (2)$$

where  $R = ^{13}\text{C}/^{12}\text{C}$  for both the sample and the Peedee Belemnite standard. The difference between duplicates was ~0.3‰ (n=3).

Gas aliquots were injected into the GC-IRMS by two different methods, depending on the methane concentration. Low concentration samples (<0.08 mM) were analyzed by pre-concentrating a ~1-30mL sample on a 25 meter 1/8 inch stainless steel column packed with Poropak Q column and immersed in a liquid nitrogen/ethanol slush (-130°C). The trap was then warmed with an air gun and then introduced into the GC-IRMS by freezing the sample on a liquid nitrogen frozen section of the capillary column. This sample was then heated and introduced to the IRMS. High concentration samples (>0.08 mM) were injected directly onto the GC column using the septa. Standard deviations are between multiple injections of same sample.

Sulfate and chloride concentrations were also determined on Hydra pore-fluids by ion chromatography. Samples were diluted 1:100 and injected into a 2010i Dionex Ion Chromatograph (Sunnyvale, CA) as described in Martens et al. (1999). For replicate measurements of single samples, the precision was  $\pm 3$  percent. Sulfate concentrations were corrected for DI water dilution as described in Chapter 2 and are reported in Appendix 4.

### 3. RESULTS

On dive 693, ~350 cm away from exposed hydrate, methane concentrations (corrected for DI-water dilution) reached a maximum of 0.5 mM at 16 centimeters below seafloor (cmbsf; Fig. 4-6a). The  $\delta^{13}\text{C-CH}_4$  value was -39.4‰ at the surface and reached -33.8‰ at depth. The depth averaged  $\delta^{13}\text{C-CH}_4$  value was  $-36.9 \pm 2.3$ ‰. The corrected down-core sulfate concentrations averaged  $28.2 \pm 0.6$  mM, showing little change with depth (all sulfate data reported in Appendix 4, not graphically shown here).

On dive 799, ~200 cm from exposed hydrate, methane concentrations (corrected for DI-water and channeling dilutions) reached a maximum of 17.8 mM at 16 cmbsf (Fig. 4-6b). Duplicate measurements at the same depth yielded some variability (i.e. at 9 cmbsf, concentrations were 1.0, 3.0, 2.9 mM). The  $\delta^{13}\text{C-CH}_4$  value was -47.3‰ at the surface and reached -43.3‰ at depth. The depth averaged  $\delta^{13}\text{C-CH}_4$  value was  $-42.8 \pm 2.0$ ‰. Corrected sulfate concentrations decreased rapidly with depth; they were 28.7 mM at the sediment-water interface and decreased to 1.0 mM at 18 cmbsf.

On dive 798, ~200 cm from a hydrate outcrop, methane concentrations (corrected for DI-water dilution) showed a slight increase with depth (Fig. 4-6c). Concentrations were 0.002 mM at the sediment-water interface and increased to 0.9 mM at 22 cmbsf. Near a natural bubble vent, at 7 cmbsf, concentrations only reached 0.002 mM. It is interesting to note that

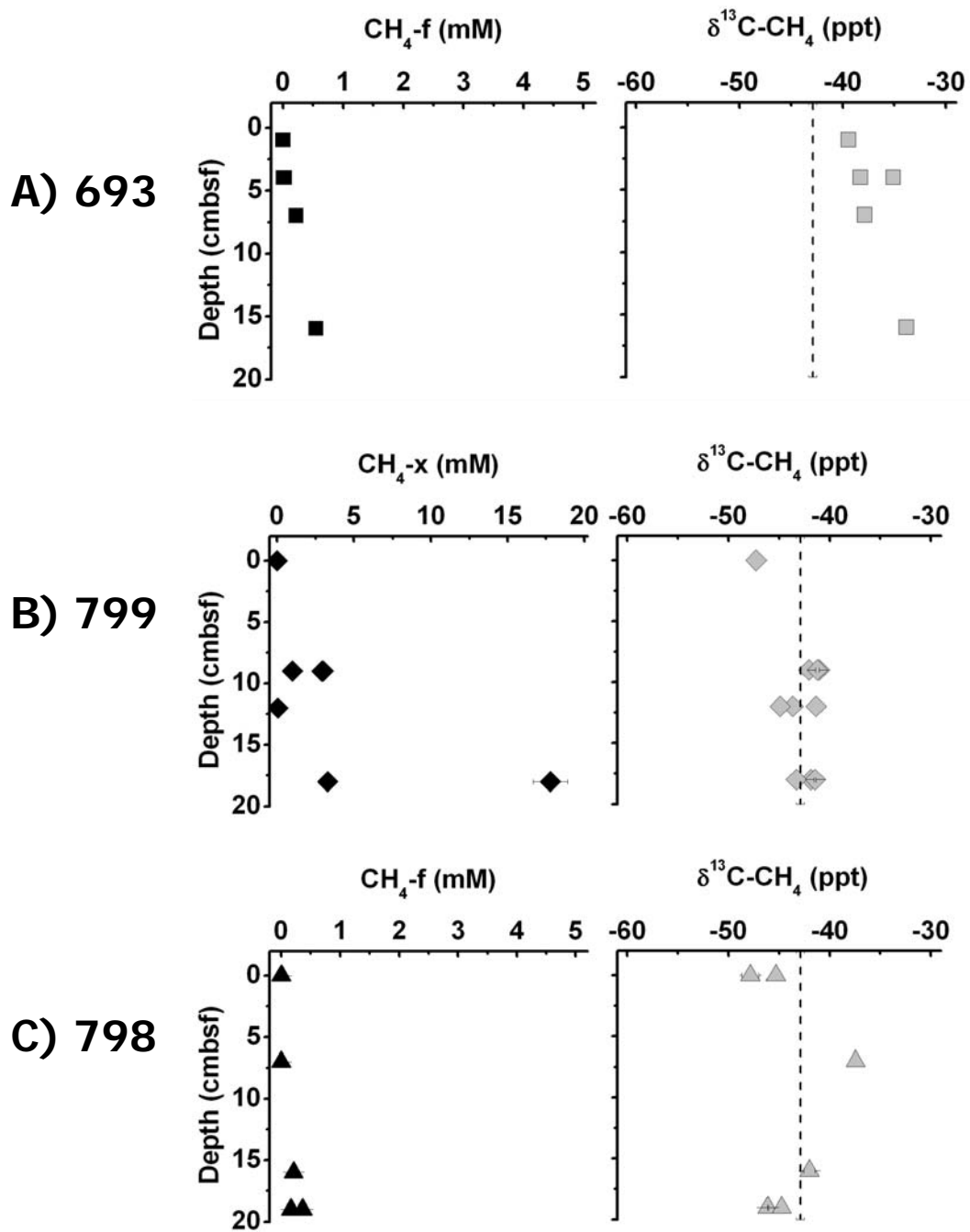
at this depth, the isotopic ratio was the heaviest measured in this deployment; much more enriched in  $^{13}\text{C}$  than the near-by bubble vent gas (-42.1‰; Pohlman et al., 2005). The  $\delta^{13}\text{C}\text{-CH}_4$  was -45.3‰ at the surface and reached -47‰ at depth. The depth averaged  $\delta^{13}\text{C}\text{-CH}_4$  value was  $-43.7\pm 3.4\%$ . Corrected sulfate concentrations decreased markedly with depth; at the sediment-water interface, concentrations were 28 mM and decreased to 0.02 at 22 cmbsf.

On dive 692, ~150 cm from an outcrop, methane concentrations (corrected for DI-water and channeling dilutions) reached a maximum of 3.5 mM at 18 cmbsf (Fig. 4-7a). At the sediment-water interface, values were 0.4 mM, higher than any other surface depth. However, these concentrations could only be corrected for DI-water dilution because the core only penetrated 13.5 cmbsf and the sulfate concentration did not vary with depth; averaging  $28.4\pm 0.1$  mM. Therefore, these concentrations should be considered minimum values. The  $\delta^{13}\text{C}\text{-CH}_4$  value averaged  $-40.1\pm 0.9\%$  (n=7).

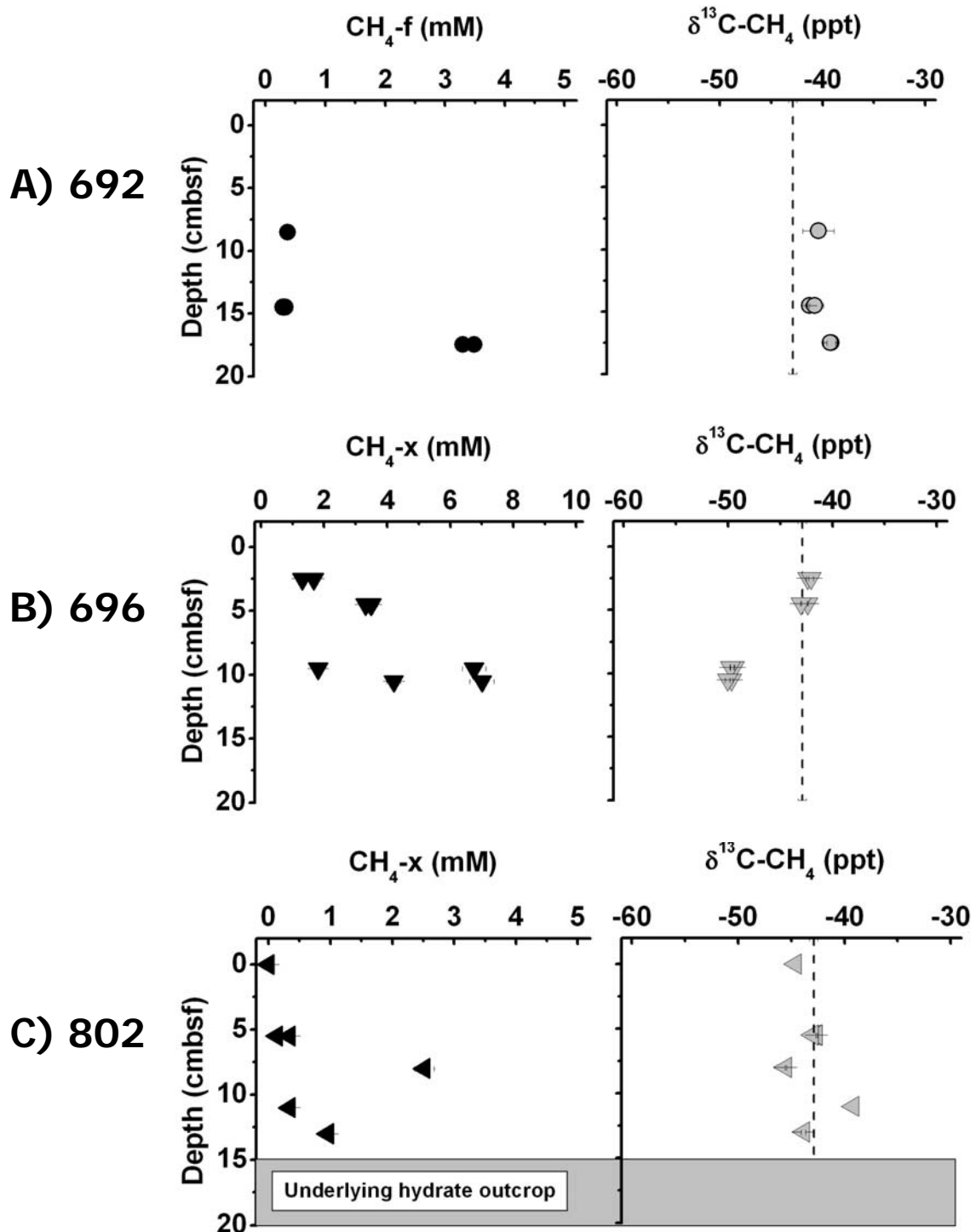
On dive 696, ~50 cm from the outcrop, methane concentrations (corrected for DI-water and channeling dilutions) exhibited an increase with depth (Fig. 4-7b). At 2.5 cmbsf, concentrations were 1.7 mM and reached a maximum of 7 mM at 10.5 cmbsf. The  $\delta^{13}\text{C}\text{-CH}_4$  value became slightly depleted in  $^{13}\text{C}$  with depth. At the surface, the  $\delta^{13}\text{C}\text{-CH}_4$  value was around -42‰ and reached -50‰ at 10.5 cmbsf. The depth averaged  $\delta^{13}\text{C}\text{-CH}_4$  value was  $-46.1\pm 3.8\%$ . Sulfate concentrations decreased with depth; at 2.5 cmbsf, concentrations were around 22 mM and decreased to 0.4 mM at 10.5 cmbsf.

On dive 802, directly overlying an exposed hydrate cliff, *in situ* dissolved methane concentrations (corrected for DI-water and channeling dilutions) were low at the sediment-water interface, 0.0005 mM, increased to 2.5 mM at 8 cmbsf, and decreased to 0.9 mM next to the surface of the hydrate (Fig. 4-7c). The depth averaged  $\delta^{13}\text{C}\text{-CH}_4$  value was -

43.1±2.0‰, similar to the hydrate-bound methane value of -42.9±0.4‰ observed at the same site (Pohlman et al., 2005). Sulfate concentrations decreased from 28 mM at the sediment water interface to 5 mM at 13 cmbsf.



**Fig. 4- 6: Methane concentrations and isotopic ratios for dives A) 693, B) 799, and C) 798. Concentrations contain analytical error and isotope error bars represent 1 SD of multiple injections. Dotted lines represent the hydrate-bound methane value,  $-42.9 \pm 0.4\text{‰}$  (Pohlman et al., 2005).**



**Fig. 4- 7: Methane concentrations and isotopic ratios for dives A) 692, B) 696, and C) 802. Concentrations contain analytical error and isotope error bars represent 1 SD of multiple injections. Dotted lines represent the hydrate-bound methane value,  $-42.9 \pm 0.4\%$  (Pohlman et al., 2005).**



## 4. DISCUSSION

### 4.1. *In situ* methane concentrations and $\delta^{13}\text{C}$ values

At Barkley Canyon, at six different locations around exposed hydrate, dissolved methane concentrations ranged between 0.001 and 18 mM. These values are below the predicted saturation methane concentration of ~67 mM and therefore support our hypothesis that pore-fluids surrounding hydrate are undersaturated with respect to equilibrium with gas hydrate. Along with the low concentrations measured, the overall distribution of methane was patchy and showed no clear correlation to horizontal distance from the hydrate outcrops. In fact, the highest methane was measured about 200 cm away from a hydrate outcrop within a patch of thin, oily bacterial mat (dive 799). This suggests that dissolved methane is controlled by local environmental processes and not by chemical equilibrium with the hydrate solid phase.

Although proximity to the hydrate did not seem to influence the concentration of dissolved methane, there was evidence of hydrate-derived methane in the pore-fluids. Averaging all the stable carbon isotope ratios measured, even up to 350 cm away from the hydrate, resulted in a  $\delta^{13}\text{C}$  value of  $-42.6 \pm 3.7\text{‰}$  ( $n=43$ ); similar to the hydrate-bound methane which has an isotopic signature of  $-42.9 \pm 0.4\text{‰}$  ( $n=4$ ) (Pohlman et al., 2005). So, if hydrate-derived methane is found up to 350 cm away, why are the methane concentrations so low? What factors control the concentrations and isotopes measured? There are three possible explanations. First, methane may be consumed through the microbially mediated process of anaerobic methane oxidation. Second, the sediments are an open system and a significant fraction of methane released from decomposing hydrate may be lost to the overlying water through transport processes such as diffusion. And third, the hydrates are

young enough that the hydrate phase has only been recently formed, or emplaced, thus allowing insufficient time for diffusion to raise methane concentrations to higher levels regardless of how open or closed the system may be. These three factors are elaborated on in the following section.

## **4.2. Factors controlling *in situ* methane concentrations and $\delta^{13}\text{C}$ values**

### *4.2.1. Microbially mediated processes*

The microbially mediated process of the anaerobic oxidation of methane (AOM) has been found in several hydrate-bearing sediments (Boetius et al., 2000; Lanoil et al., 2001; Joye et al., 2004; Orcutt et al., 2004; Orcutt et al., 2005). This process may keep methane concentrations low in sediments surrounding gas hydrates. Using stable carbon isotopes, AOM can be assessed since microbes preferentially consume the isotopically light methane,  $^{12}\text{C}$ , and leave the remaining dissolved methane pool enriched in the heavy isotope,  $^{13}\text{C}$  (Barker and Fritz, 1981; Coleman et al., 1981; Alperin et al., 1988). Assessing the isotopes, we found that the average  $\delta^{13}\text{C}$  value closest to the hydrate ( $-43.1 \pm 2.0\text{‰}$ ) was similar to the hydrate-bound gas ( $-42.9 \pm 0.4\text{‰}$ ; Pohlman et al., 2005). Further from the hydrate, about 350 cm away, the  $\delta^{13}\text{C}$  values were more enriched in  $^{13}\text{C}$ , averaging  $-36.9 \pm 2.3\text{‰}$ . These results show that hydrate-bound methane is contributing to the dissolved methane pool and suggest that microbial methane oxidation is occurring further from the hydrate. Furthermore, they support the hypothesis that although the hydrate is dissolving, microbial consumption is keeping the concentrations low.

The amount of hydrate-derived methane consumed by microbes can be estimated by using a closed system isotope model (Bergamaschi et al., 1998). In this model, the percent methane oxidized,  $f$ , is calculated from:

$$f = \left( 1 - 10^{\frac{\log(\delta_x + 1000)}{\log(\delta_{x+y} + 1000)} / \alpha - 1} \right) \times 100 \quad (3)$$

where  $\alpha$  is the fractionation factor and the terms  $\delta_x$  and  $\delta_{x+y}$  are the  $\delta^{13}\text{C-CH}_4$  values (‰) at distance intervals  $x$  and  $x+y$  (cm) away from the outcrop. Although the fractionation factor for this particular site is not known, the minimum alpha value of 1.009 (Alperin et al., 1988) and the maximum value of 1.030 (Chanton and Liptay, 2000) were used. Using the  $\delta^{13}\text{C-CH}_4$  values found at distances 3 and 350 cm away from the hydrate, the results of this closed system model show that methane oxidation consumes a minimum of 17% ( $\alpha = 1.030$ ) and a maximum of 47% ( $\alpha = 1.008$ ) of the dissolved methane. The assumptions made for this calculation are extensive. First, oxidation within hydrate-bearing sediments does not solely occur horizontally; vertical oxidation is probably occurring. Second, the natural system does not work as a closed system. And third, the fractionation factor is not known for these sediments. Although these assumptions limit the ability to truly interpret the fraction of methane consumed through AOM, the calculation is still useful since we are simply trying to constrain the highest possible rate of oxidation that occurs in these sediments. With this objective, and using the maximum amount of methane consumed  $f=0.47$ , the measured *in situ* methane concentration,  $[\text{CH}_4]_{\text{measured}}$ , was adjusted for AOM,  $[\text{CH}_4]_{\text{adjusted}}$ , with the following equation:

$$[\text{CH}_4]_{\text{adjusted}} = [\text{CH}_4]_{\text{measured}} \times 100 / f \quad (4)$$

Applying equation 4 for all measured methane values, the maximum adjusted methane concentration was 38 mM, which is below the expected value for saturated fluids (Table 4-3). Therefore, even accounting for the maximum microbial oxidation, the *in situ* methane

concentrations were still well below the thermodynamic equilibrium concentration between hydrate and dissolved methane.

**Table 4- 3: Dive, distance to hydrate, measured *in situ* methane concentrations, and the adjusted methane concentrations assuming the maximum amount of anaerobic methane oxidation, 47%, from equation 3.**

Dive	Distance to hydrate (cm)	Depth (cmbsf)	[CH <sub>4</sub> ] <sub>measured</sub> (mM)	[CH <sub>4</sub> ] <sub>adjusted</sub> (mM)	Dive	Distance to hydrate (cm)	Depth (cmbsf)	[CH <sub>4</sub> ] <sub>measured</sub> (mM)	[CH <sub>4</sub> ] <sub>adjusted</sub> (mM)
693	350	1	0.0	0.0	692	150	8.5	0.4	0.8
		4	0.0	0.1			14.5	0.3	0.7
		4	0.0	0.0			14.5	0.3	0.6
		7	0.2	0.5			17.5	3.5	7.4
		16	0.6	1.2			17.5	3.3	7.0
799	200	0	0.0	0.0	696	50	25.5	2.5	5.3
		9	1.0	2.2			2.5	1.7	3.6
		9	3.0	6.4			2.5	1.3	2.8
		9	2.9	6.2			4.5	3.5	7.4
		18	3.3	7.0			4.5	3.3	7.1
798	200	18	17.8	37.8	802	overlying	9.5	6.8	14.4
		0	0.0	0.0			9.5	1.8	3.9
		0	0.0	0.0			10.5	7.0	14.9
		0	0.0	0.0			10.5	4.2	8.9
		7	0.0	0.0			5.5	0.1	0.2
		16	0.2	0.4			5.5	0.3	0.6
		19	0.4	0.8			8	2.5	5.3
		19	0.2	0.4			11	0.3	0.6
		22	0.9	1.9			13	1.0	2.1

#### 4.2.2. Transport processes

Along with AOM, the low methane concentrations measured around the hydrate could also be due to transport processes such as diffusion out of the sediments. Since ocean waters typically contain ~3 nM methane, there is a significant concentration gradient between pore-fluids and the overlying waters which results in significant diffusive loss from the pore-fluids. Evidence for diffusive loss is clearly seen in the vertical profiles of methane concentrations with lowest concentrations occurring systematically at or near the sediment-water interface.

#### 4.2.3. Age of hydrates

When a hydrate is newly formed or emplaced, the surrounding methane concentrations may be below the thermodynamic equilibrium. Assuming that hydrates will dissolve when in disequilibrium with surrounding fluids, we can determine the age of the hydrates by evaluating the concentration change over time due simply to molecular diffusion (Crank, 1975). This can be done using Fick's second law:

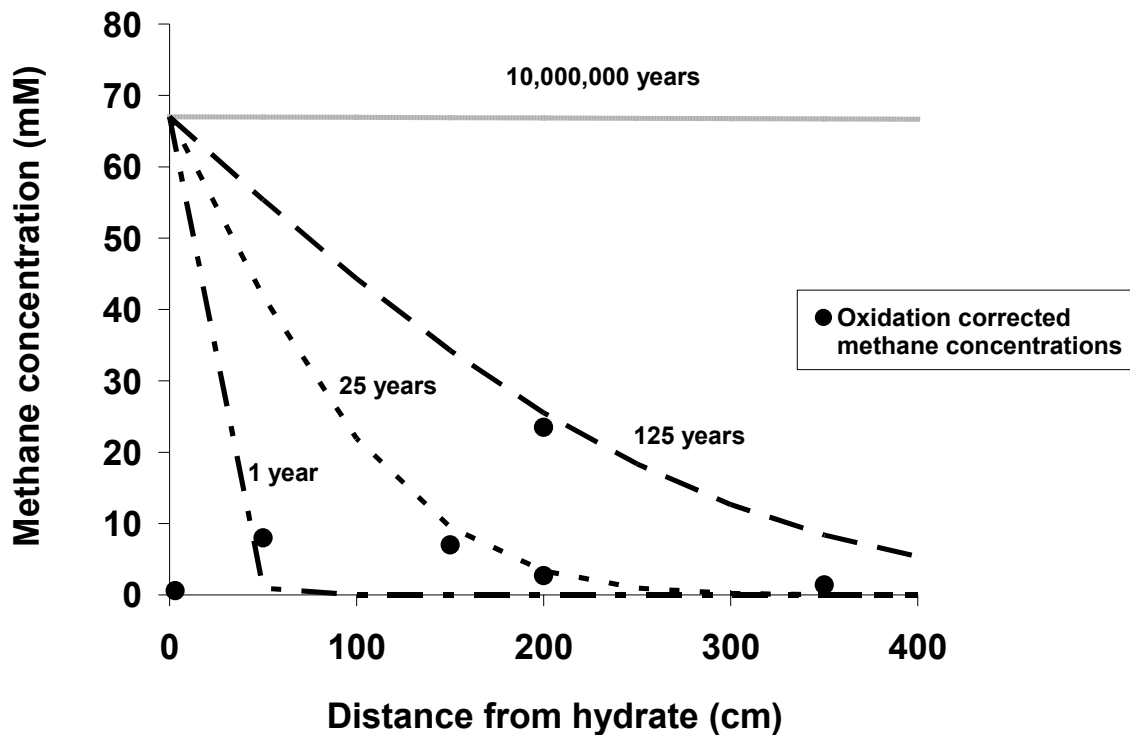
$$\frac{\partial C}{\partial t} = -\frac{\partial J_{CH_4}}{\partial x} = D_s \frac{\partial^2 C}{\partial x^2} \quad (5)$$

where  $C$  is methane concentration,  $t$  is time,  $J_{CH_4}$  is the methane flux,  $x$  is distance, and  $D_s$  is the diffusion coefficient in sediments. The analytical solution to equation 5 is:

$$C(x,t) = C_{int} \left( 1 - \operatorname{erf} \left[ \frac{x}{2\sqrt{D_s t}} \right] \right) \quad (6)$$

where  $C(x, t)$  is the concentration at distance  $x$  from the initial boundary at time  $t$ ,  $C_{int}$  is the concentration at the hydrate-sediment interface and taken as the equilibrium concentration of 67 mM, and  $\operatorname{erf}$  is the error function. The initial boundary conditions are  $C(x,0) = 0$ ;  $C(0,t) = C_{int}$ ;  $C(\infty,t) = 0$ , and  $C(x,\infty) = C_{int}$ . For Barkley Canyon hydrate system, the results show that

the hydrate is at least 1 year old and at most 125 years old (Fig. 4-8). Therefore, we may be measuring pore-fluids that are still attaining equilibrium with the newly formed or emplaced hydrate.



**Fig. 4- 8: Age of hydrate outcrop estimates. Black dots are the maximum microbial oxidation corrected methane concentrations. Each line represents the concentration gradient at different ages.**

### 4.3. Implications of low concentrations: hydrate dissolution

Regardless of the exact mechanism(s) controlling the low concentrations surrounding hydrate, either AOM, transport processes, or hydrate age, the results of this study indicate that methane concentrations are generally low around shallow buried hydrates and suggest two possibilities: the Barkley Canyon hydrates are currently dissolving or they are more

stable, or at least metastable, than predicted with thermodynamics alone. If hydrates are dissolving, they could be contributing a large flux of methane to the overlying water column. Making several assumptions, we could calculate the methane flux from the hydrate to the pore fluids and the dissolution rate.

#### 4.3.1. Estimated methane flux and dissolution rates

The methane flux can be estimated from Fick's first law (following Egorov et al., 1999):

$$J_{CH_4} = -\phi D_s \left( \frac{C_{int} - C_L}{dL} \right) \quad (7)$$

where,  $J_{CH_4}$  is the methane flux (mmol  $CH_4/cm^2/year$ ) from the hydrate to the surrounding pore fluids,  $\phi$  is the porosity,  $D_s$  is the sedimentary methane diffusion coefficient ( $cm^2/sec$ ),  $C_{int}$  is the dissolved methane concentration at the hydrate interface (mM),  $C_L$  is the dissolved methane concentration at the edge of the diffusive sub-layer (mM),  $dL$  is the diffusive sub-layer thickness, and  $C_{int} - C_L/dL$  is the concentration gradient within the diffusive sub-layer. For the flux calculations at Barkley Canyon, constant parameters of porosity and the diffusion coefficient were used. Porosity was 0.9 and  $D_s$  was  $7.34 \times 10^{-6} cm^2/sec$ , corrected for tortuosity and *in situ* pressures (87 atm at 860 meters water depth), temperatures (4°C), and salinity (35ppt).

Using equation 7, the flux was estimated for hydrate outcropping the sediments in direct contact with ocean water and for hydrate buried in shallow sediments (Table 4-4). Following Egorov et al. (1999) for outcropping hydrate, the diffusive sub-layer was estimated to be 1 mm within which the methane concentration decreased from 67 to 0 mM. The corresponding concentration gradient was 67 mM/cm and the methane flux was calculated to be 140 mmol  $CH_4/cm^2/yr$ . For hydrate buried in shallow sediments, the flux was calculated by assuming a



diffusive sub-layer of 1 cm within which the concentration gradient of 67 mM/cm was also assumed (Table 4-4). The flux was then calculated to be 14 mmol CH<sub>4</sub>/cm<sup>2</sup>/yr.

From the methane flux calculations, the dissolution rate or the hydrate loss rate can be estimated by assuming a methane hydrate composition of 160 cm<sup>3</sup> CH<sub>4</sub> gas per 1cm<sup>3</sup> hydrate (Sloan, 1998) in the following equation:

$$DR = J_{CH_4} \left( \frac{22.414 \text{ L } CH_4}{\text{mol } CH_4} \right) \left( \frac{\text{cm}^3 \text{ hydrate}}{160 \text{ cm}^3 \text{ hydrate} \times 0.8} \right) \quad (8)$$

where, DR is the dissolution rate (cm/year), 22.414 L/mol CH<sub>4</sub> is the volume of methane per mol of methane assuming an ideal gas at STP, 0.8 refers to the hydrate cage being filled with 80% methane, as determined by Pohlman et al. (2005). For outcropping hydrate, the hydrate dissolution rate was estimated to be 24 cm hydrate per year and for buried hydrate, the rate was 2.4 cm/year. The methane flux and dissolution rate are sensitive to the thickness of the diffusive sub-layer. For example, for buried hydrate overlain by 15 cm of sediment, as in dive #802, the dissolution rate was calculated to be 0.15 cm/year (Table 4-4). Therefore, when buried within sediments, hydrate is more stable than those outcropping the sediments, as intuition suggests.

**Table 4- 4: For equation 8, the listed parameters were used for outcropping hydrate and buried hydrate using assumed methane concentrations.**

<b>Parameter</b>	<b>Outcropping hydrate</b>	<b>Buried hydrate assumed</b>	<b>Buried hydrate assumed</b>
Theoretical C <sub>interface</sub> (mM)	67	67	67
C <sub>L</sub> (mM)	0	0	0
dL(cm)	0.1	1	15
dC/dL (mM/cm)	670	67	4.5
CH <sub>4</sub> flux (mmol-CH <sub>4</sub> /cm <sup>2</sup> /yr)	140	14	0.9
Hydrate dissolution rate (cm-hyd/yr)	24	2.4	0.16

#### 4.3.2. In situ methane flux and dissolution rates

The methane flux was also estimated by applying the *in situ* methane concentration corrected for this study's maximum microbial oxidation overlying the hydrate. For this flux estimate, the boundary layer thickness was determined by the distance from the hydrate that the *in situ* measurement was taken. For example, in the HYDRA deployment overlying the hydrate (dive 803), the sample was collected 3 cm away from the hydrate surface. Therefore, the boundary layer was taken as 3 cm within which the concentration decreased from 67 to 0.5 mM. The corresponding concentration gradient was 22 mM/cm and the methane flux was 4.6 mmol CH<sub>4</sub>/cm<sup>2</sup>/yr. Applying equation 8, the dissolution rate was then 0.8 cm/year.

And finally, the flux and dissolution rate were also determined solely from the measured *in situ* concentration gradient. Fitting a linear gradient to the concentrations measured at 50, 150, and 350 cm away from the hydrate (data plotted in Fig. 4-8 excluding 3 cm and 200 cm outliers), the slope of this line was 0.03 mM/cm, the corresponding methane flux was 0.007 mmol CH<sub>4</sub>/cm<sup>2</sup>/yr, and the dissolution rate was 0.001 cm/year.

#### 4.3.3. Observations versus theoretical calculations

Although the theoretical dissolution rates include highly conservative estimates of the diffusive boundary layer thickness, they are not supported by *in situ* observations at Barkley Canyon. For example, a hydrate valley has been photographed over the last 3 years (Fig. 4-9). Over this time, the valley itself has widened at a rate of ~7 cm/year (Ross Chapman, personal communication). Although this estimate needs to be experimentally quantified, it is slower than the theoretical prediction for outcropping hydrate of 24 cm/year with a 0.1 cm boundary layer and suggests that natural hydrates are more stable than predicted by diffusion alone. However, a boundary layer thickness of only 0.35 cm is needed to result in a

dissolution rate of the observed 7 cm/year. Since these outcropping hydrates may be sheltered from turbulent forces, a thicker boundary layer is not unreasonable. Using a thicker boundary layer thus suggests that the observations support diffusion controlled dissolution.



**Fig. 4- 9: Annual photographs taken of outcropping hydrate at Barkley Canyon. In 2002, the valley between each hydrate slab was about 10 cm wide. In 2003, this valley widened to ~17 cm and in 2004, it grew to about 24 cm. Photographs courtesy of Ross Chapman, University of Victoria.**

While the stability of hydrates in direct contact with fluids undersaturated with methane is still indeterminable, it appears that yellow tinted hydrates, the majority of outcrops at Barkley Canyon, are more stable than white tinted hydrates (Peltzer et al., 2006). Since the yellow color is a visual sign of entrained oils, it has been hypothesized that the oils stabilize hydrates because of their non-polar hydrophobic characteristics (Peltzer et al., 2006). Therefore, the dissolution of either hydrates outcropping or buried within the sediments may not be solely controlled by diffusion alone but may also be controlled by kinetic processes that act as “armor” on the surface of the hydrate.

Hydrate “armoring” could be controlled by three different factors. The first is the hydrate structure itself. Studies have shown that the formation of a hydrate skin around liquid CO<sub>2</sub> droplets is enough to slow down the diffusion rate (Mori and Mochizuki, 1998). The same

could be true for methane hydrate. The second is the physical presence of microbes, microbial mucous, or biosurfactants that protect the hydrate from dissolving (as discussed by science crew of the GOM Hydrate Research Consortium Fall 2006 cruise). In the Barkley Canyon photos (Fig. 4-9), the microbial mats seem to be growing into the valley over time and their physical presence may slow down the dissociation of hydrate. Similarly, on a recent visit to outcropping hydrate in the Gulf of Mexico, a visible mucous was observed to directly hang from outcropping hydrate (GOM Hydrate Research Consortium September cruise dive video). While the presence of mucous or the microbes themselves may slow down dissolution, their absence may speed up dissolution. This was seen in recent experiments where the measured dissolution rate of laboratory precipitated hydrates on the seafloor was an order of magnitude higher than that predicted by diffusion (Rehder et al., 2004). Furthermore, microbially produced biosurfactants were recently found to act as catalysts to hydrate formation (Zhang et al., 2006) and could also act to help stabilize the hydrate.

And finally, the third factor controlling hydrate “armoring” is the presence of oils entrained within the hydrate itself (Leifer and MacDonald, 2003; Peltzer et al., 2006). Studies of oil coated bubbles showed that the oil allowed the bubble to travel through the water column and reach the surface instead of dissolving immediately upon release from the sediments (Leifer and MacDonald, 2003). The plausibility of any of these three factors needs to be tested in nature and a mechanism is needed to explain how each could suppress hydrate dissolution.

While it is exciting to report direct concentration evidence for the possibility that hydrates are more stable than predicted by diffusion, these results must be taken with caution.

The HYDRA concentrations are still in question due to many issues with the instrument (see Chapter 2). However, several instruments reside on the seafloor at the present moment collecting pore fluids from 1, 2, 3, and 4 cm away from buried hydrate. These instruments may hold the answer to the ultimate question of the concentration of methane directly adjacent to the hydrate and as a gradient away from the hydrate.

## 5. CONCLUSIONS AND IMPLICATIONS

In this chapter, the first *in situ* methane concentration and stable carbon isotope measurements from sediments surrounding gas hydrate outcrops were reported. The measurements were made possible through the utilization of a sampling device that collects pore-fluids and stores them at *in situ* pressures. The instrument was deployed six times in different local environments and at distances ranging from 3-350 cm from outcropping gas hydrate. Regardless of distance from the hydrate, measured concentrations at six locations were between 0-18 mM. Although lower than the equilibrium concentration between dissolved methane and hydrate, these low concentrations were hypothesized to result from both microbial methane oxidation and pore-water transport processes. The occurrence of microbial anaerobic methane oxidation was verified using stable carbon isotopic ratio measurements and quantified using a closed system model. Model results indicated that up to 50% of the methane expected to result from estimated hydrate decomposition could be accounted for by microbial consumption. Even though there was isotopic evidence of dissolved hydrate-bound methane in surrounding pore-fluids, the low methane concentrations observed relative to theoretical predictions and the lack of physical evidence for changes in hydrate morphology over time do not suggest that the outcropping hydrates are rapidly decomposing. This suggests that the hydrates are more stable than theory predicts for an

open system and that their dissolution may not be solely controlled by diffusion but also kinetic barriers such as cage dissociation rates and surface armoring. Future studies should directly address these controlling factors by measuring the *in situ* concentration within the diffusive sub-layer (less than 1 cm scale).

*Acknowledgements.* I would like to thank the captain and crew of the Canadian Coast Guard vessel J. P. Tully and the crew of the ROV ROPOS of the Canadian Submersible Group. I especially thank Chief Scientists Ross Chapman, Ken Grabowski, and Rick Coffin for the opportunity to take HYDRA to sea. Funding was provided through a grant from University of Mississippi Gulf of Mexico Hydrate Research Consortium and Department of Energy. Additional support came from the Link Foundation Ocean and Engineering and EPA-STAR fellowships.

## 6. REFERENCES

- Alperin M. J., Reeburgh W. S., and Whiticar M. J. (1988) Carbon and hydrogen isotope fractionation resulting from anaerobic methane oxidation. *Global Biogeochemical Cycles* **2** (3), 279-288.
- Barker J. F. and Fritz P. (1981) Carbon isotope fractionation during microbial methane oxidation. *Nature* **293**, 289-291.
- Bergamaschi P., Brenninkmeijer C. A. M., Hahn M., Rockmann T., Scharffe D. H., and Crutzen P. J. (1998) Isotope analysis based source identification for atmospheric CH<sub>4</sub> and CO sampled across Russia using the Trans-Siberian railroad. *Journal of Geophysical Research-Atmospheres* **103** (D7), 8227-8235.
- Boetius A., Ravensschlag K., Schubert C. J., Rickert D., Widdel F., Gieseke A., Amann R., Jorgensen B. B., Witte U., and Pfannkuche O. (2000) A marine microbial consortium apparently mediating anaerobic oxidation of methane. *Nature* **407**, 623-626.
- Chanton J. P. and Liptay K. (2000) Seasonal variation in methane oxidation in a landfill cover soil as determined by an in situ stable isotope technique. *Global Biogeochemical Cycles* **14** (1), 51-60.
- Chapman N. R., Pohlman J., Coffin R., Chanton J. P., and Lapham L. L. (2004) Thermogenic Gas Hydrates in the Northern Cascadia Margin. *EOS, Transactions, American Geophysical Union* **85** (38), 361.
- Coleman D. D., Risatti J. B., and Schoell M. (1981) Fractionation of carbon and hydrogen isotopes by methane-oxidizing bacteria. *Geochimica et Cosmochimica Acta* **45**, 1033-1037.
- Crank J. (1975) *The Mathematics of Diffusion*. Oxford University Press, Oxford.
- Duan Z. and Mao S. (2006) A thermodynamic model for calculating methane solubility, density, and gas phase composition of methane-bearing aqueous fluids from 273 to 523 K and from 1 to 2000 bar. *Geochimica et Cosmochimica Acta* **70**, 3369-3386.
- Egorov A. V., Crane K., Vogt P. R., and Rozhkov A. N. (1999) Gas hydrates that outcrop on the sea floor: stability models. *Geo-Marine Letters* **19**, 68-75.
- Hoehler T. M., Alperin M. J., Albert D. B., and Martens C. S. (1994) Field and laboratory studies of methane oxidation in an anoxic marine sediment: Evidence for a methanogen-sulfate reducer consortium. *Global Biogeochemical Cycles* **8** (4), 451-463.

- Hyndman R. D., Spence G. D., Chapman N. R., Riedel M., and Edwards R. N. (2001) Geophysical studies of marine gas hydrate in Northern Cascadia. In *Natural Gas Hydrates: Occurrence, Distribution, and Detection*, Vol. 124 (ed. American Geophysical Union), pp. 273-295.
- Joye S. B., Boetius A., Orcutt B. N., Montoya J. P., Schulz H. N., Erickson M. J., and Lugo S. K. (2004) The anaerobic oxidation of methane and sulfate reduction in sediments from Gulf of Mexico cold seeps. *Chemical Geology* **205**, 219-238.
- Kennett J. P., Cannariato K. G., Hendy I. L., and Behl R. J. (2003) *Methane hydrates in Quaternary climate change: The clathrate gun hypothesis*. American Geophysical Union, Washington, DC.
- Kvenvolden K. A. (1993) Gas hydrates-geological perspective and global change. *Reviews of Geophysics* **31**, 173-187.
- Lanoil B. D., Sassen R., LaDuc M. T., Sweet S. T., and Nealson K. H. (2001) Bacteria and Archaea physically associated with Gulf of Mexico gas hydrates. *Applied and Environmental Microbiology* **67** (11), 5143-5153.
- Leifer I. and MacDonald I. R. (2003) Dynamics of the gas flux from shallow gas hydrate deposits: interaction between oily hydrate bubbles and the oceanic environment. *Earth and Planetary Science Letters* **6638**, 1-14.
- Lelieveld J., Crutzen P. J., and Dentener F. J. (1998) Changing concentration, lifetime and climate forcing of atmospheric methane. *Tellus* **50B**, 128-150.
- MacDonald I. R., Bender L. C., Vardaro M., Bernard B., and Brooks J. M. (2005) Thermal and visual time-series at a seafloor gas hydrate deposit on the Gulf of Mexico slope. *Earth and Planetary Science Letters* **233**, 45-59.
- Martens C. S., Albert D. B., and Alperin M. J. (1999) Stable isotope tracing of anaerobic methane oxidation in the gassy sediments of Eckernforde Bay, German Baltic Sea. *American Journal of Science* **299**, 589-610.
- Martens C. S. and Berner R. A. (1977) Interstitial water chemistry of anoxic Long Island Sound sediments. 1. Dissolved gases. *Limnology and Oceanography* **22**, 10-25.
- Milkov A. V. (2004) Global estimates of hydrate-bound gas in marine sediments: how much is really out there? *Earth-Science Reviews* **66**, 183-197.



- Mori Y. H. and Mochizuki T. (1998) Dissolution of liquid CO<sub>2</sub> into water at high pressures: a search for the mechanism of dissolution being retarded through hydrate-film formation. *Energy Conversion and Management* **39** (7), 567-578.
- Orcutt B. N., Boetius A., Elvert M., Samarkin V. A., and Joye S. B. (2005) Molecular biogeochemistry of sulfate reduction, methanogenesis, and the anaerobic oxidation of methane at Gulf of Mexico cold seeps. *Geochimica et Cosmochimica Acta* **69** (17), 4267-4281.
- Orcutt B. N., Boetius A., Lugo S. K., MacDonald I. R., Samarkin V. A., and Joye S. B. (2004) Life at the edge of methane ice: microbial cycling of carbon and sulfur in Gulf of Mexico gas hydrates. *Chemical Geology* **205**, 239-251.
- Peltzer E. T., Walz P., Brewer P. G., Dunk R., Hester K., and Sloan E. D. (2006) An Experimental Determination of Natural Clathrate Hydrate Dissolution Rates in the Deep Sea. *American Geophysical Union Abstract*.
- Pohlman J. W. (2006) Sediment biogeochemistry of Northern Cascadia Margin shallow gas hydrate systems. Ph. D. Thesis, College of William and Mary.
- Pohlman J. W., Canuel E. A., Chapman N. R., Spence G. D., Whiticar M. J., and Coffin R. B. (2005) The origin of thermogenic gas hydrates on the northern Cascadia Margin inferred from isotopic (<sup>13</sup>C/<sup>12</sup>C and D/H) and molecular composition of hydrate and vent gas. *Organic Geochemistry* **36**, 703-716.
- Reeburgh W. S. and Heggie D. T. (1977) Microbial methane consumption reactions and their effect on methane distributions in freshwater and marine environments. *Limnology and Oceanography* **22** (1), 1-9.
- Rehder G., Kirby S. H., Durham W. B., Stern L. A., Peltzer E. T., Pinkston J., and Brewer P. G. (2004) Dissolution rates of pure methane hydrate and carbon-dioxide hydrate in undersaturated seawater at 1000-m depth. *Geochimica et Cosmochimica Acta* **68** (2), 285-292.
- Rice A. L., Gotoh A. A., Ajie H. O., and Tyler S. C. (2001) High-precision continuous-flow measurement of  $\delta^{13}\text{C}$  and  $\delta\text{D}$  of atmospheric CH<sub>4</sub>. *Analytical Chemistry* **73**, 4104-4110.
- Sloan E. D. E. D. Sloan (1998) *Clathrate hydrates of natural gases, second edition*. Marcel Dekker, Inc., New York.

Spence G. D., Chapman N. R., Hyndman R. D., and Cleary C. (2001) Fishing trawler nets massive "catch" of methane hydrates. *EOS, Transactions, American Geophysical Union* **82** (50).

Zhang G., Rogers R. E., French W. T., and Lao W. (2006) Investigation of microbial influences on seafloor gas-hydrate formations. *Marine Chemistry*  
**doi:10.1016/j.marchem.2006.10.005.**

## **Chapter 5: Utilization of cores and HYDRA to follow biogeochemical processes at three Gulf of Mexico hydrate sites: influence on hydrate stability**

**Abstract-**Biogeochemical processes such as sulfate reduction and the anaerobic oxidation of methane in sediments surrounding gas hydrates may enhance hydrate dissolution. To address this, sediment push cores were collected as transects from outcropping hydrate and from local micro-environments within three Gulf of Mexico hydrate sites (Green Canyon 185, 234, and 232) and a reference site. From these cores, pore-fluids were measured for depth gradients indicative of sulfate reduction and anaerobic oxidation of methane such as sulfate and total organic carbon (TOC) concentrations and the stable carbon isotope ratios of dissolved inorganic carbon (DIC) and TOC. Direct measurements of sulfate reduction rates were also made. Pore-fluids were also collected *in situ* with a novel sampling device, named HYDRA, and measured for methane concentrations and stable carbon isotope ratios. The transect study showed that the steepest sulfate depletion gradients were both adjacent to and as far away as 200 cm from the hydrate outcrops. Regardless of distance from hydrate, these steep gradients were always coupled to an incorporation of  $^{13}\text{C}$ -depleted carbon into the DIC pool suggesting that either methane or petroleum were contributing to sulfate reduction. In micro-environments surrounding hydrate, methane concentrations were found to be as high as 2000  $\mu\text{M}$  under bacterial mats and as low as 2  $\mu\text{M}$  near tubeworms. Sediments under the bacterial mat exhibited the highest rates of sulfate reduction, reaching up to  $8.9 \pm 4.9$

mM/day. Although coupled to high methane concentrations, sulfate reduction was also coupled to high concentrations of total organic carbon that was isotopically depleted in  $^{13}\text{C}$ , possibly from surrounding petroleum. These results suggest that sulfate reduction and the anaerobic oxidation of methane were more dependent upon the availability of dissolved methane and TOC, especially petroleum, than the hydrate-bound methane. This study suggests that AOM is not consistently enhanced directly adjacent to hydrate and may not contribute to hydrate dissolution.

## 1. INTRODUCTION

Gas hydrates are ice-like solids that form in the presence of saturated methane concentrations under high pressures and low temperatures typically found in continental slope sediments and permafrost (Sloan, 1998). They are composed of rigid cages of water that enclose molecules of low molecular weight hydrocarbons, principally methane, along with carbon dioxide and/or hydrogen sulfide. The global hydrate reservoir is estimated to contain around ~500 to 2,500 Gt methane carbon or  $1$  to  $5 \times 10^{15}$  m<sup>3</sup> methane (Milkov, 2004). Therefore, it represents one of the largest source of hydrocarbons on Earth and could be an important future energy reserve (Kvenvolden, 1988; Buffett, 2000). Hydrates may also contribute to climate change if they are rendered unstable (Kvenvolden, 1993). While hydrates are stable under conditions of high pressures, low temperatures, and saturated methane concentrations (Sloan, 1998), changes in these conditions could cause hydrates to become unstable, decompose, and release methane into the oceans and possibly the atmosphere.

From a purely thermodynamic approach, gas hydrate decomposition proceeds through the processes of either dissociation or dissolution (Zhang and Xu, 2003). Hydrates dissociate into gas bubbles and water when they are taken out of their pressure and temperature stability zone. This process has been directly documented when hydrates were transported from the seafloor to the ocean surface (Brewer et al., 2002). Its occurrence was also inferred when seafloor temperature increases of a few degrees were correlated with an increase in bubble vents (MacDonald et al., 1994; Roberts et al., 1999b). Although these temperature increases were not enough to bring the hydrates out of their stability zone (MacDonald et al., 2005). Along with dissociation, hydrates may also decompose through the process of dissolution

when fluids surrounding the hydrate are no longer saturated with respect to methane (Zhang and Xu, 2003). During this process, the hydrate-bound methane dissolves into the surrounding fluids.

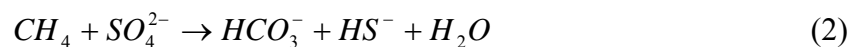
Gas hydrate deposits most vulnerable to dissolution are those outcropping the seafloor or residing in the shallow sediments. While ocean waters are known to be undersaturated with respect to methane (Scranton and Brewer, 1978; Pohlman, 2006), surrounding pore-fluids are also thought to be depleted in dissolved methane (see chapter 4). Thus, the hydrates should be dissolving into surrounding waters and pore-fluids:



where  $CH_4 \cdot 6H_2O(s)$  is pure methane hydrate and  $CH_4(aq)$  is aqueous or dissolved methane.

While the dissolution of hydrate is thought to be controlled by the diffusion of methane from the hydrate to the surrounding pore-fluids to obtain chemical equilibrium (Egorov et al., 1999; Rehder et al., 2004), dissolution may also be enhanced by the consumption of dissolved methane by sedimentary microbial activity.

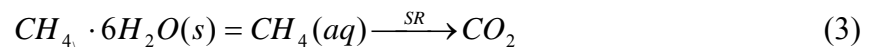
The anaerobic oxidation of methane (AOM) is responsible for consuming ~80% of all methane produced in coastal and oceanic sediments (Reeburgh, 1996) and therefore provides a major control on fluxes of this powerful greenhouse gas. While much geochemical evidence has documented a coupled sulfate reduction and anaerobic methane oxidation zone (as reviewed in Hoehler et al., 1994), the mechanism and organism(s) responsible for these processes were not identified until recently. It was hypothesized that a unique consortium of sulfate reducing bacteria and methanogenic-like archaea, working in reverse, carried out the following net reaction (Hoehler et al., 1994):



where CH<sub>4</sub> is methane, SO<sub>4</sub><sup>2-</sup> is sulfate, HCO<sub>3</sub><sup>-</sup> is bicarbonate, HS<sup>-</sup> is sulfide, and H<sub>2</sub>O is water. Using molecular techniques, the hypothesized organisms in this consortium were identified in hydrate bearing sediments of the Pacific Ocean and found to be physically associated with each other as a spherical cover of sulfate reducing bacteria enclosing methanogens (Boetius et al., 2000).

Coupled sulfate reduction and anaerobic oxidation of methane may also be an important control on hydrate-bound methane in the Gulf of Mexico. Molecular isotope studies suggested that sedimentary anaerobic microbes directly oxidize hydrate-bound methane (Sassen et al., 1999). This was supported by the physical association of bacteria and archaea with the hydrate (Lanoil et al., 2001) and the measurement of high rates of sulfate reduction and anaerobic methane oxidation within sediments in direct contact with the hydrate interface (Orcutt et al., 2004). Furthermore, sulfate reducer lipid biomarkers were found to have a unique molecular content that indicated they played a role in anaerobic methane oxidation and other hydrocarbons (Zhang et al., 2002).

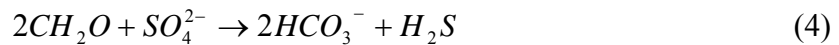
With all this evidence that microbial methane oxidation is occurring in close proximity to the hydrates, does this activity enhance hydrate dissolution and negatively affect hydrate stability? If hydrates are in equilibrium with the surrounding pore-fluids, this dissolved methane may then be available to the microbes and, through sulfate reduction, drive equation (1) further to the right:



where CH<sub>4</sub>.6H<sub>2</sub>O is solid hydrate, CH<sub>4</sub> (aq) is dissolved methane, SR is sulfate reduction coupled to AOM, and CO<sub>2</sub> is carbon dioxide. Therefore, by assessing sulfate reduction

around hydrates, we can begin to understand the role microbial activity plays in hydrate stability.

Measuring solely for sulfate reduction around gas hydrates may overestimate the role AOM plays because sulfate reduction has also been shown to be stimulated by the oxidation of non-methane carbon such as petroleum or organic carbon fixed by chemoautotrophs via the equation:



where  $CH_2O$  is a generic representation organic carbon including petroleum,  $SO_4^{2-}$  is sulfate,  $HCO_3^-$  is bicarbonate, and  $H_2S$  is hydrogen sulfide. Evidence for enhanced sulfate reduction proceeding via petroleum and chemoautotrophic carbon oxidation and not methane oxidation has been reported in hydrate bearing sediments (Aharon and Fu, 2000; Arvidson et al., 2004; Joye et al., 2004). This is supported by laboratory studies that show specific mesophilic and thermophilic sulfate-reducing bacteria capable of oxidizing petroleum anaerobically (Reuter et al., 1994). Furthermore, petroleum collected from hydrate sites at Green Canyon (GC) lease blocks 185 and 234 has been bacterially oxidized (Sassen et al., 1994; 2001). These studies suggest that sulfate reduction may be enhanced independently from methane oxidation. Therefore, it is important to quantify the rates of sulfate reduction and anaerobic methane oxidation surrounding hydrate and sediments to determine the role microbial activity plays in hydrate dissolution.

The goal of this chapter is to determine whether or not microbial activity in sediments surrounding hydrates is enhanced and possibly contributing to hydrate dissolution. Investigations were carried out by conducting a large scale spatial survey of biogeochemical indicators of sulfate reduction and anaerobic methane oxidation. Variations in depth



gradients of sulfate, methane, and total organic carbon (TOC) concentrations, the stable carbon isotopic composition of methane, dissolved inorganic carbon (DIC), and TOC and sulfate reduction rates as transects away from hydrate and within different local micro-environments were utilized to quantify the differences in microbial activity. The specific questions addressed were:

1. In sediments surrounding gas hydrate, what is the source of the dissolved methane and has it been biogeochemically altered?
2. Do rates of sulfate reduction decrease proportional to distance away from hydrate or are they controlled by local variability in methane or non-methane carbon such as petroleum?
3. What is the spatial variability of sulfate reduction and anaerobic methane oxidation around hydrates?
4. What is the relative contribution of methane and non-methane carbon to sulfate reduction?

## **2. METHODS**

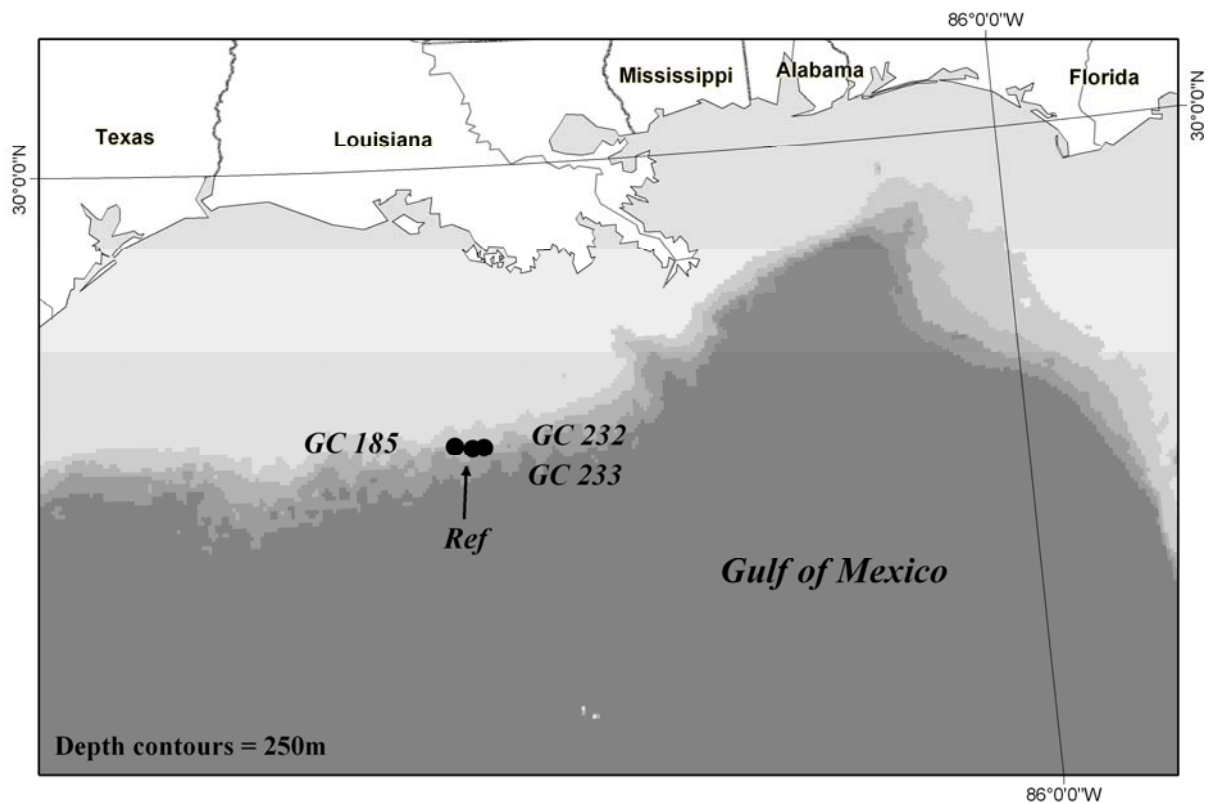
### **2.1. Sites Visited**

In August of 2000 and 2002 aboard the R/V Edwin Link/Seward Johnson, three hydrate seep sites and a nearby reference site were visited (Fig. 5-1, Table 1). The seep sites, Green Canyon (GC) 185, GC 234, and GC 232, contained venting gas streams, outcropping hydrate, tubeworms, mussels, clams, and heterotrophic bacteria. The gas within the venting streams was made up of low molecular weight hydrocarbons such as methane, ethane, and propane (Sassen et al., 2004). There was also visible oil seeping from and entrained within sediments. The reference site contained light brown sediments with no visible disturbances

in the cores due to gas expansion or dissociating hydrates upon collection. Hydrates are not known to exist in this area.

**Table 5- 1: Locations and water depths of sites visited.**

Site	Location	Water depth (m)
GC 185	27°46.9'N, 91°30.4'W	550-580
GC 234	27°44.7'N, 91°13.3'W	525-560
GC 232	27°44.3'N, 91°19.1'W	807
Reference	27°44.9'N, 91°16.63'W	535



**Fig. 5- 1: Map of northern Gulf of Mexico and hydrate sites: GC 185, GC 232, and GC 234. The black circles show each hydrate sites and the arrow shows the reference site. Map generated in ArcGIS 9.1.**

## 2.2. Sample collection

Sediments and pore-waters were collected from the four sites using box cores, submersible cores and HYDRA. An overview of the samples collected is given in Table 2. Cores are referred to as their dive number and core number (i.e. 4213-core 3) and HYDRA samples are referred to as HYDRA and the dive number (i.e. HYDRA-4210).

At the reference site, a box core was collected over the side of the ship. Once the box core was onboard, sediment push cores (5cm x 30cm lexan core barrels) were collected from the center. Cores were immediately stored in the ship's cold room at *in situ* temperatures of 7°C for core sectioning, as described below. The mud was brown in color and showed no signs of hydrate pieces or gas expansion.

From the three hydrate sites, submersible deployed push cores were collected. Upon retrieval of the cores from the submersible, they were placed in the cold room at 7°C. For core sectioning, all push cores were sectioned into 3 cm intervals. Within each interval, triplicate sub-cores were collected with a cut-off 3 mL glass syringe for sulfate reduction rate measurements (described in section 2.2). Remaining sediment patties were placed in a Reeburgh-type squeezer apparatus and pore-waters were expressed by pressure filtration (Reeburgh, 1967). The pore-water volumes were partitioned into one plastic vial with 2 drops of 50% HCl for sulfate concentrations, one plastic vial with no additional treatment for chloride concentrations, and the remainder was placed into an evacuated glass serum vial for dissolved inorganic carbon (DIC) stable carbon isotope ratio analysis. Sulfate and chloride samples were placed at 3°C and the DIC samples frozen until land-based measurements could be completed. Resultant sediment patties were placed in plastic bags and frozen for future analysis of total organic carbon concentrations and solid phase stable carbon isotope ratios.

**Table 5- 2: Overview of sampling sites, environments, sample types, and descriptions. The description of ‘on top of hydrate’ was determined when core hit a hard substrate during sampling.**

Environment	Site	Dive #	Sample type, c=core	Descriptions
Transect from hydrate	GC 234	4215	c4	On top of shallow hydrate, degassed upon retrieval
		4407	c1	adjacent to hydrate
		4407	c4	~50 cm from hydrate
		4407	c5	~200 cm from hydrate
	GC 232	4403	c6	on top of hydrate
		4401	c2	~50 cm from hydrate
		4405	c3	~200 cm from hydrate
In bacterial mat	GC 185	4213	HYDRA	Soft sediments with thin bacterial mat coverage ~300 cm from hydrate outcrop
		4213	c3	next to HYDRA in soft sed
	GC 234	4217	HYDRA	Near thin bacterial mat
		4217	c7	next to HYDRA, sulfate reduction rates
		4218	HYDRA	Description not available
		4218	c7	next to HYDRA, sulfate reduction rates
Near tubeworms	GC 185	4210	HYDRA	Near tubeworm bed, next to bubble stream
	GC 232	4401	c4	near tubeworm bed
		4403	c4	near tubeworm bed
Soft sediments	GC 185	4214	c4	collected ~50 cm from 4214 core 5 in soft sed, sulfate reduction rates
		4214	c5	collected ~50 cm from 4214 core 4 in soft sed, sulfate reduction rates
		4551	c11	Description not available
Reference		No #	c1	Light brown sediments within box core

Additional pore-water samples were also obtained from GC 185 and GC 234 using a submersibly deployed, unique pore-water extraction device named HYDRA (Fig. 5-2). These samples were specifically collected to measure pore-waters for dissolved methane concentrations and stable carbon isotope ratios. A full description of HYDRA is given in Chapter 2 of this dissertation. Briefly, HYDRA has 10 flush and sample chamber sets plumbed to 10 filtered sample ports evenly spaced every 5 cm along a 50 cm long probe tip.

The probe tip was placed into the sediments and pore-waters collected by initiating a suction created from a large pistoned cylinder. At each depth, the suction first extracted ~20 mL of pore-water to flush the system lines and then collected and stored ~7 mL of pore-water sample within a stainless steel chamber. This configuration of HYDRA did not have high pressure valves to maintain the samples at *in situ* pressures so they were allowed to degas upon ascent from the seafloor. Therefore, methane concentrations reported here are considered minimums. On board ship, the pore-waters were taken from each sample chamber and ~2 mL of this fluid was placed into a gas-tight syringe and a helium headspace was added. The syringes were gently agitated to release the methane from the dissolved phase and the headspace was immediately analyzed for dissolved gases (described in section 2.3). Remaining pore-water from the HYDRA sample chambers (~5 mL) was preserved by injecting it into evacuated glass serum vials and freezing the vials upside down for land-based stable carbon isotope measurements.



**Fig. 5- 2: Picture of HYDRA on board ship. The stainless steel 7 mL sample chambers are shown in front of the 20 mL gray-PVC flush chambers. The probe tip is shown immersed in a water-filled plastic tube.**

### **2.3. Analytical methods**

Pore-water sulfate and chloride concentrations were determined by ion chromatography on 1:100 diluted pore-fluid samples using a 2010i Dionex Ion Chromatograph (Sunnyvale, CA) as described in Martens et al. (1999). Percent total organic carbon (TOC),  $\delta^{13}\text{C}$ -TOC, and carbon to nitrogen ratios (C:N) were measured on ~30 mg of freeze-dried sediment pellets that were vapor acidified to remove inorganic carbon prior to combustion to  $\text{CO}_2$  and  $\text{N}_2$  on a Carlo-Erba NA 1500 (CE Elantech, Inc., Milan, Italy) elemental analyzer. The effluent gas stream was introduced to a Finnigan Mat 252 isotope ratio mass spectrometer (Thermo Finnigan, Bremen, Germany) via a modified Finnigan ConFlo<sup>TM</sup> interface (Brenna et al., 1997). Methane, ethane, and propane concentrations were measured on the HYDRA pore water samples by directly injecting the syringe headspace into the Shimadzu Mini II Gas Chromatograph (Kyoto, Japan) equipped with flame ionization detector. Only methane

concentrations are reported. Stable carbon isotope compositions for dissolved methane were obtained using a preconcentrating system on-line with a continuous flow 5890 Hewlett-Packard gas chromatograph (Palo Alto, CA), capillary combustion, and isotope ratio mass spectrometry as described in Rice et al. (2001). Results are reported using the standard “del” notation,

$$\delta^{13}\text{C} (\text{‰}) = [\text{R}_{(\text{sample})}/\text{R}_{(\text{PDB standard})} - 1] \times 1000 \quad (5)$$

where R is the ratio of the  $^{13}\text{C}$  to  $^{12}\text{C}$ . The precision for replicate measurements of single samples was  $\pm 3$  percent for sulfate, chloride, and methane concentrations; 1 percent for TOC and methane isotopes; and 5-10 percent for %TOC and C:N.

Sulfate reduction rates were measured on two cores each from GC 185 and GC 234 and one core from the reference site following procedures from Albert *et al.* (1995). Briefly, sub-cores were line injected with about 40 kBq  $^{35}\text{S}$ -sulfate contained in a 10  $\mu\text{L}$  volume and incubated at *in situ* temperatures ( $7^\circ\text{C}$ ) for about 24 hours onboard ship. After the incubation time, sub-cores were extruded into empty 120 mL glass serum vials and preserved in a slurry of 5 mL saturated (1.6M) zinc sulfate, which stabilized sulfide in the form of insoluble zinc sulfide and stopped biological activity, and 1 mL of 0.1 M sodium sulfide carrier solution. Vials were stoppered with blue butyl rubber stoppers and frozen for later determination of biologically produced  $^{35}\text{S}$ -sulfide at the Chapel Hill laboratory by a modification of an active distillation/chromium reduction technique (Albert et al., 1995). Radioactivity was then counted on a Beckman LS 6800 liquid scintillation counter.

Sulfate reduction rates were calculated using the following equation,

$$\text{Sulfate reduction rate} \left( \frac{\text{mM}}{\text{day}} \right) = \frac{H_2 \text{ } ^{35}\text{S} \cdot [\text{SO}_4^{2-}] \cdot 1.04 \cdot \phi}{^{35}\text{SO}_4^{2-} (\text{added}) \cdot \text{time}} \quad (6)$$

where,  $H_2^{35}S$  is the amount of isotopically labeled sulfide produced during the experiment,  $SO_4^{2-}$  is the concentration of pore water sulfate measured in the cores in mM, 1.04 is the fractionation factor taken into account when bacteria preferentially take up the lighter sulfur isotope rather than the heavier isotope,  $\phi$  is the porosity of the sediments,  $^{35}SO_4^{2-}$  (added) is the amount of labeled sulfate added to the incubations, and time is the incubation time in days.

### 3. RESULTS

From three hydrate sites and one reference site, fifteen locations were sampled for biogeochemical profiles of methane ( $CH_4$ ), sulfate ( $SO_4$ ), and total organic carbon (TOC) concentrations;  $CH_4$ , dissolved inorganic carbon (DIC), and TOC stable carbon isotope ratios; carbon to nitrogen ratios (C:N); and sulfate reduction rates. These profiles were collected as transects from outcropping hydrate, within bacterial mats, near tubeworm beds, and within background sediments.

#### 3.1. Transect from hydrate

At GC 234 and GC 232, cores were collected as transects off two outcropping hydrate mounds. Cores were collected on top, adjacent to, ~50 cm from, and ~200 cm from the mound. At GC 234, on top of the mound, sulfate concentrations did not vary with depth and averaged  $28.8 \pm 0.9$  mM (Fig. 5-3a). The  $\delta^{13}C$ -DIC values were -2‰ at the surface and decreased to -6‰ by the end of the core (Fig. 5-3b). Adjacent to the mound, sulfate concentrations were 30 mM at the surface and decreased to 15 mM by 13 cmbsf (Fig. 5-3a). The  $\delta^{13}C$ -DIC values were -3‰ at the surface and decreased to -29‰ by 13 cmbsf (Fig. 5-3b). Approximately 50 cm from the mound, sulfate concentrations showed little variation with depth and averaged  $30.4 \pm 0.3$  mM down the length of the core (Fig. 5-3a). The  $\delta^{13}C$ -



DIC values were +1‰ at the surface and decreased to -13‰ by 11 cmbsf (Fig. 5-3b). And finally, furthest from the mound, ~200 cm, sulfate concentrations averaged  $29.6 \pm 1$  mM until the bottom of the core where the concentrations decreased to 20 mM (Fig. 5-3a). The  $\delta^{13}\text{C}$ -DIC values were +0.8‰ at the surface and decreased to -11‰ by 22 cmbsf (Fig. 5-3b).

At GC 232, on top of the hydrate mound, sulfate concentrations were 30 mM at the surface and decreased to 19 mM at the bottom of the core (Fig. 5-3c). The  $\delta^{13}\text{C}$ -DIC values were -1‰ at the surface and decreased to -14‰ by 27 cmbsf (Fig. 5-3d). For this transect, a core was not collected adjacent to the mound. Approximately 50 cm from the hydrate, sulfate concentrations were 30 mM at the surface and decreased to 27 mM by 15 cmbsf (Fig. 5-3c). The  $\delta^{13}\text{C}$ -DIC values were 0‰ at the surface, decreased rapidly to -12‰ at 2 cmbsf, and slowly decreased to -19‰ at the bottom of the core (Fig. 5-3d). The steepest sulfate gradients and lowest  $\delta^{13}\text{C}$ -DIC values were measured in the core furthest from the hydrate. Here, sulfate concentrations were 28 mM near the surface and decreased to 4 mM by 22 cmbsf (Fig. 5-3c). The  $\delta^{13}\text{C}$ -DIC values were 0‰ at the surface, decreased to -31‰ at 13.5 cmbsf, and increased to -7‰ by 22 cmbsf (Fig. 5-3d).

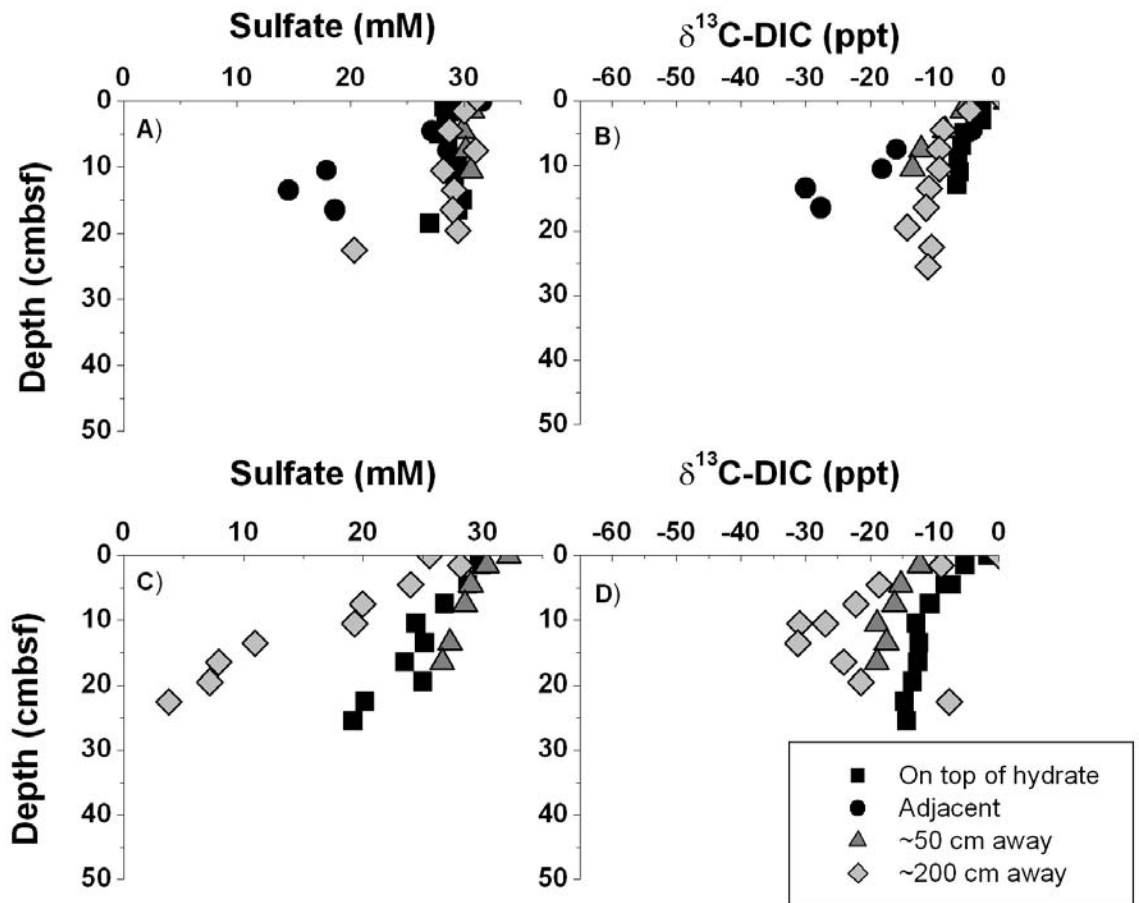
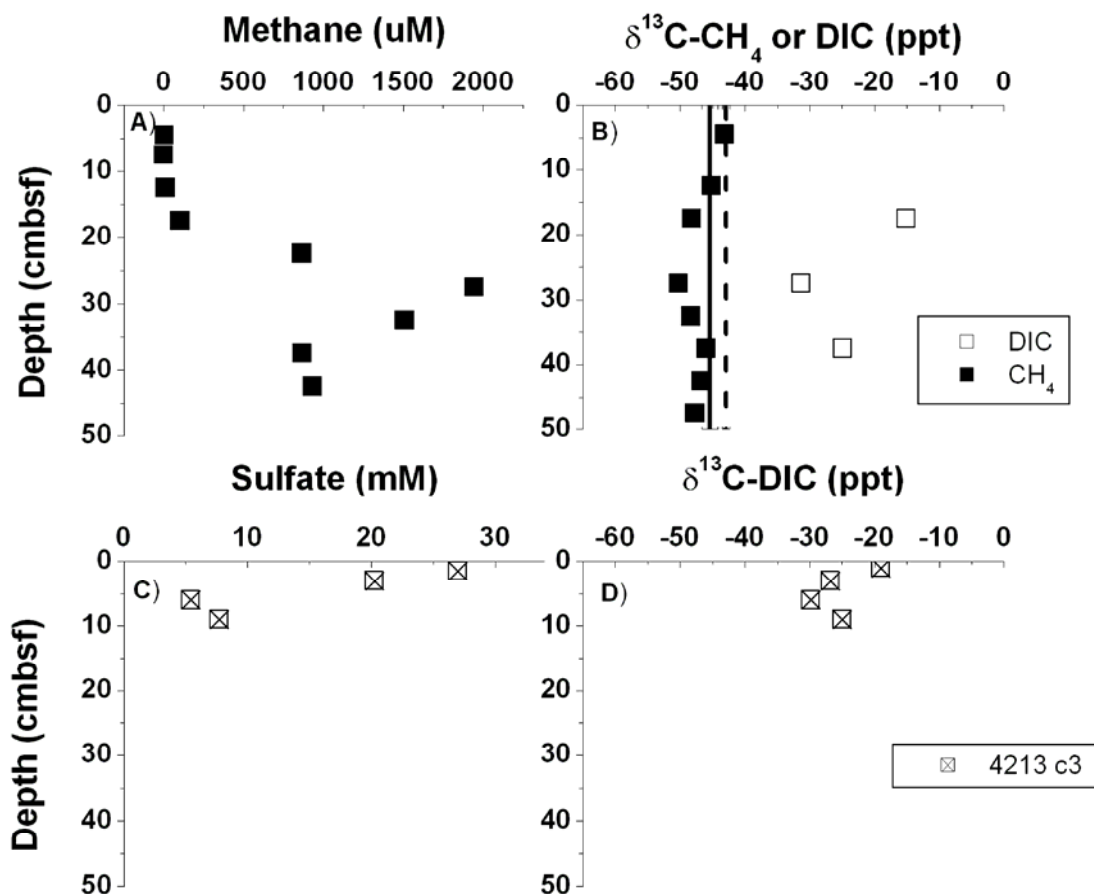


Fig. 5- 3: Geochemical results from two transects from a hydrate outcrop. From GC 234, a) sulfate concentrations and b)  $\delta^{13}\text{C-DIC}$  values. From GC 232, c) sulfate concentrations and d)  $\delta^{13}\text{C-DIC}$  values.

### 3.2. In bacterial mats

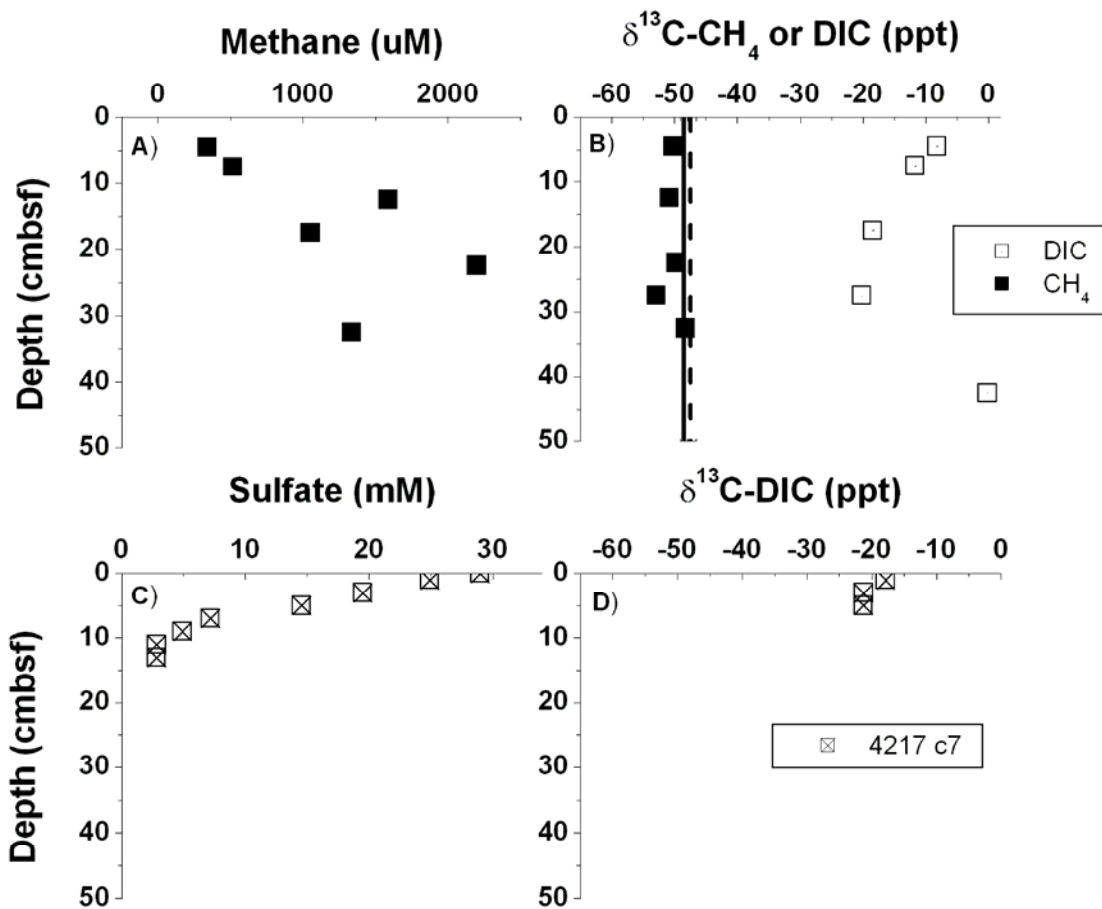
Three deployments of HYDRA and three adjacent cores were collected within bacterial mats at GC 185 and GC 234. At GC 185, the HYDRA pore-fluids, HYDRA-4213, contained dissolved methane concentrations that were low at the surface, increased to a sub-surface maximum peak of 1900  $\mu\text{M}$  at 27.5 cmbsf, and decreased to 750  $\mu\text{M}$  at 43 cmbsf (Fig. 5-4a). This sub-surface maximum trend is probably a result of concentrations above methane saturation at 1 atm that degassed upon ascent through the water column. This result is not surprising since HYDRA did not contain the samples at *in situ* pressures. The methane stable carbon isotope ratios were consistent down core and averaged  $-46.2 \pm 2.2\text{‰}$  (Fig. 5-4b). However, at 27 cmbsf, there was a slight decrease in  $\delta^{13}\text{C}\text{-CH}_4$  values that coincided with the highest methane concentration measured in this profile. The  $\delta^{13}\text{C}\text{-DIC}$  values were depleted in  $^{13}\text{C}$  compared to seawater  $\delta^{13}\text{C}\text{-DIC}$  values and reached as low as  $-30\text{‰}$  at 27 cmbsf (Fig. 5-4b). In the core collected adjacent to HYDRA-4213, the sulfate concentrations were around 30 mM at the sediment water interface and decreased to 8 mM by the deepest depth (Fig. 5-4c). Similar to HYDRA-4213, the  $\delta^{13}\text{C}\text{-DIC}$  values also reached as low as  $-30\text{‰}$  (Fig. 5-4d). Although the  $\delta^{13}\text{C}\text{-DIC}$  values measured between HYDRA and the core are similar, they are offset by about 20 cm. It is possible that either HYDRA was not placed all the way into the sediments or overlying water channeled down the probe shaft and mixed with the pore waters. Unfortunately, dive video of the deployment did not document the actual emplacement of HYDRA into the sediments.



**Fig. 5- 4: Geochemical results from sediments under a thin bacterial mat at GC 185. HYDRA-4213 pore fluids were analyzed for a) methane concentrations and b)  $\delta^{13}\text{C}$  of methane or DIC. The core 4213-c3 was also collected adjacent to HYDRA and its pore fluids measured for c) sulfate concentrations and d)  $\delta^{13}\text{C}$ -DIC. For comparison in panel b, the solid line represents the average value for vent gas,  $-45.4\pm 1.2\text{‰}$ , and the dashed line represents the hydrate-bound methane value of  $-42.9\pm 0.6\text{‰}$  (Sassen et al., 2004).**

The second deployment of HYDRA within a bacterial mat was at GC 234 and exhibited similar trends as those seen at GC 185. In HYDRA-4217 pore-fluids, methane concentrations increased from near zero at the surface to 2200  $\mu\text{M}$  at 22.5 cmbsf but were noisy due to degassing (Fig. 5-5a). The isotopic composition of this methane exhibited little variation with depth and the average  $\delta^{13}\text{C}\text{-CH}_4$  value was  $-50.4\pm 1.7\text{‰}$  (Fig. 5-5b). Alternatively, the  $\delta^{13}\text{C}\text{-DIC}$  values exhibited large variations with depth. Near the sediment-

water interface, the  $\delta^{13}\text{C}$ -DIC values were near -10‰, decreased to -20‰ by 27 cmbsf, and increased to ~0‰ by 42 cmbsf (Fig. 5-5b). In the core collected adjacent to HYDRA, 4217-core 7, sulfate concentrations were near 28 mM at the sediment water interface and decreased to 2.8 mM by the bottom of the core (Fig. 5-5c). The  $\delta^{13}\text{C}$ -DIC values were as low as -21‰ (Fig. 5-5d). Sulfate reduction rates (SRR) were measured in this core and, as expected by the steep sulfate concentration profiles, the rates were very high. SRR were  $3.6 \pm 1.0$  mM/day at the sediment water interface,  $8.8 \pm 4.9$  mM/day at 5 cmbsf and  $0.5 \pm 0.1$  mM/day at the bottom of the core (Fig. 5-9d). The standard deviations reported here were based on triplicate rates measurements at each depth.



**Fig. 5- 5: Geochemical results from sediments under a thin bacterial mat. From GC 234, HYDRA-4217 pore fluids were analyzed for a) methane concentrations and b)  $\delta^{13}\text{C}$  of methane or DIC. The core 4217-c7 was also collected adjacent to HYDRA and its pore fluids measured for c) sulfate concentrations and d)  $\delta^{13}\text{C-DIC}$ . For comparison in panel b, the solid line represents the average value for vent gas,  $-48.5 \pm 0.6\text{‰}$ , and the dashed line represents the hydrate-bound methane value of  $-47.5 \pm 1.0\text{‰}$  (Sassen et al., 2004).**

The third HYDRA deployment, HYDRA-4218 was also made at GC 234 to illustrate the spatial variability of methane concentrations and isotopic compositions within a hydrate site. Unfortunately, the exact environmental location of this HYDRA profile is not known. The dives notes were missing from the dive log and there was no video recording of the dive. In HYDRA-4218, methane concentrations reached a maximum of 80 uM at 27.5 cmbsf (Fig. 5-6a) and the average  $\delta^{13}\text{C-CH}_4$  value was  $-47.2 \pm 2.3\text{‰}$  (Fig. 5-6b). The  $\delta^{13}\text{C-DIC}$  value was

around -10‰ at the sediment water interface and decreased to -15‰ by 50 cmbsf (Fig. 5-6b). Collected adjacent to this HYDRA deployment, the core (4218-core 7) exhibited sulfate concentrations that did not vary with depth and averaged  $28.7 \pm 1.1$  mM until 24 cmbsf where concentrations decreased to 26 mM (Fig. 5-6c). The core  $\delta^{13}\text{C-DIC}$  values were higher than the values measured in HYDRA pore waters. In the core, they reached only as low as -5‰ and showed little variation with depth, averaging  $-2.9 \pm 2.3$ ‰ whereas in HYDRA, these values reached as low as -15‰ (Fig. 5-6d). As expected from a core with little sulfate depletion, the sulfate reduction rates were low and also showed little change with depth (Fig. 5-9c). The average SRR over all depths was  $0.026 \pm 0.005$  mM/day (Fig. 5-9c).

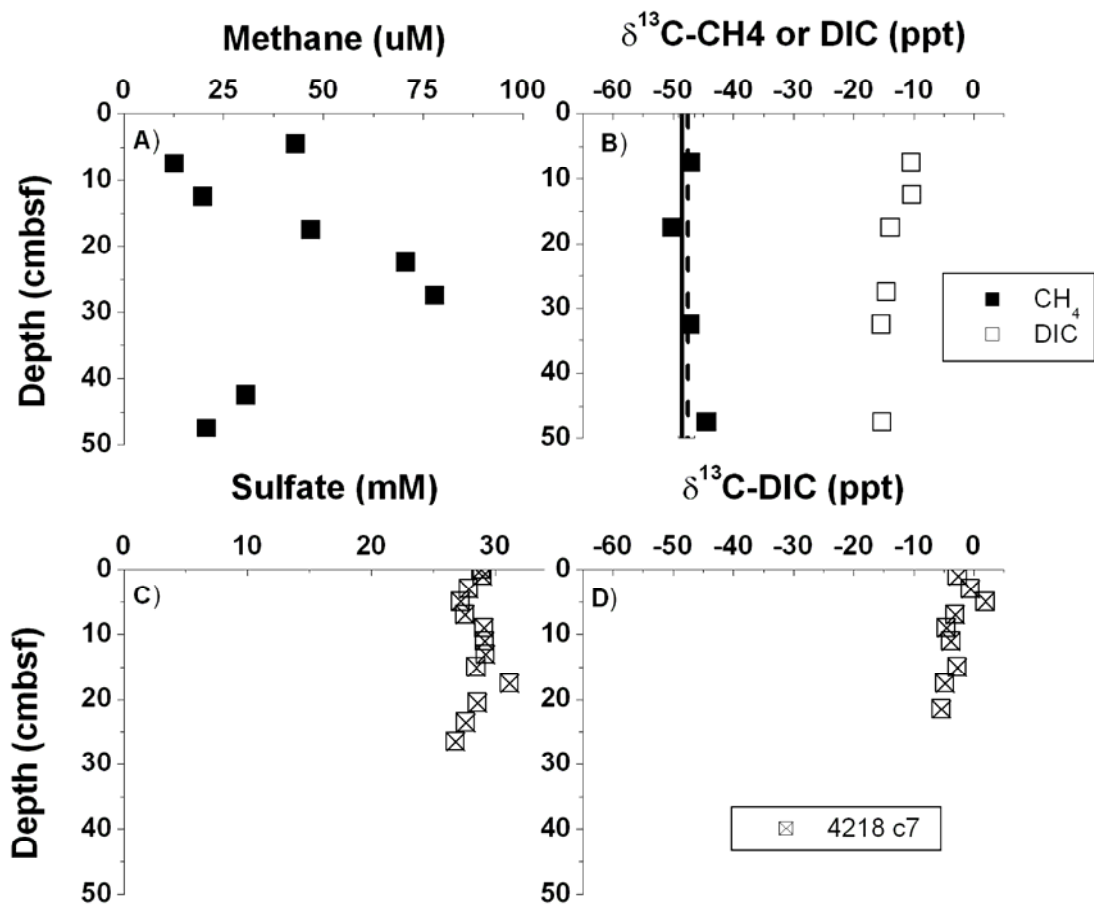
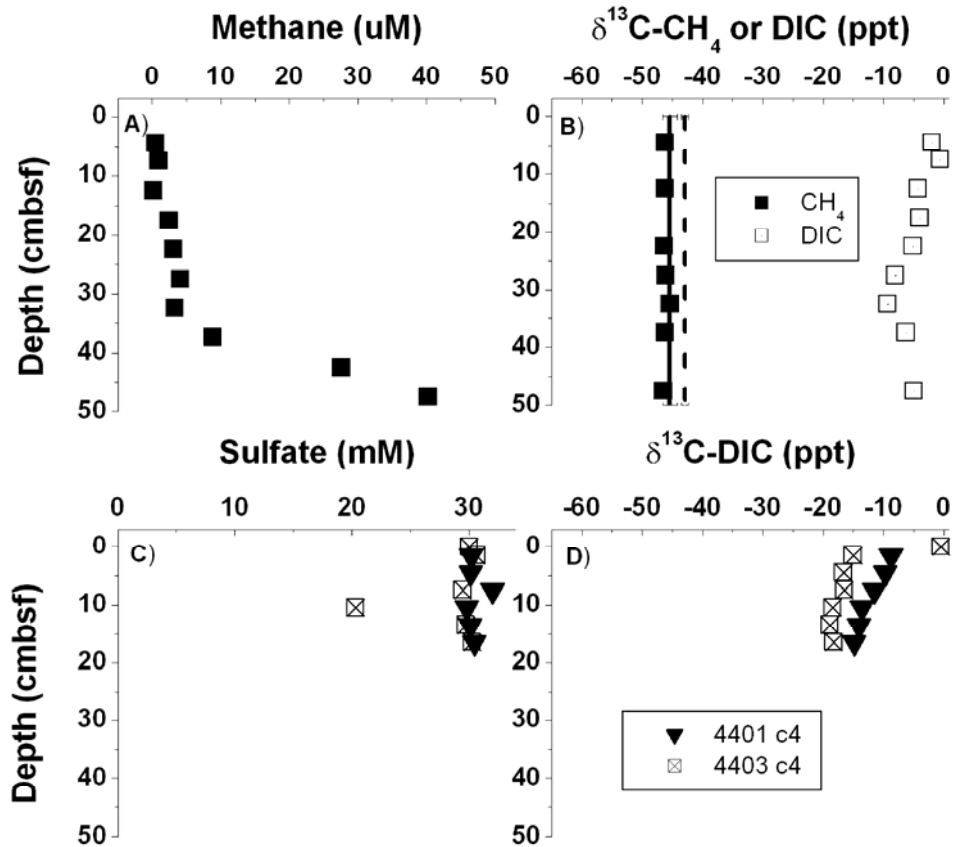


Fig. 5- 6: Geochemical results from sediments under a thin bacterial mat. From GC 234, HYDRA-4218 pore fluids were analyzed for a) methane concentrations and b)  $\delta^{13}\text{C}$  of methane or DIC. The core 4218-c7 was also collected adjacent to HYDRA and its pore fluids measured for c) sulfate concentrations and d)  $\delta^{13}\text{C-DIC}$ . For comparison in panel b, the solid line represents the average value for vent gas,  $-48.5 \pm 0.6\text{‰}$ , and the dashed line represents the hydrate-bound methane value of  $-47.5 \pm 1.0\text{‰}$  (Sassen et al., 2004).



### 3.3. Near a tubeworm bed

In contrast to samples collected within bacterial mats, the biogeochemical profiles of methane, sulfate, and DIC in pore waters near tubeworms exhibited limited microbial activity. At GC 185, HYDRA-4210 pore-waters contained ~5 uM dissolved methane from the surface to 37 cmbsf (Fig. 5-7a). At 48 cmbsf, concentrations sharply increased to 40 uM (Fig. 5-7a). The  $\delta^{13}\text{C-CH}_4$  values showed no down core trend, averaging  $-46.1 \pm 0.4\text{‰}$  (Fig. 5-7b). However, the  $\delta^{13}\text{C-DIC}$  values exhibited a sub-surface minimum at 32 cmbsf (Fig. 5-7b). At the sediment water interface, the  $\delta^{13}\text{C-DIC}$  value was around  $-1\text{‰}$ , decreased to  $-10\text{‰}$  by 32 cmbsf, and then increased to  $-6\text{‰}$  by the end of the profile. Two cores were also collected near the tubeworms, 4401-core 4 and 4403-core 4. In these cores, the sulfate concentrations averaged  $28.6 \pm 3$  mM until 10 cmbsf where they decreased to 20 mM (Fig. 5-7c). The  $\delta^{13}\text{C-DIC}$  values showed variation with depth. For 4401-core 4,  $\delta^{13}\text{C-DIC}$  values were  $-9\text{‰}$  at the sediment water interface and decreased to  $-15\text{‰}$  at the bottom of the core. For 4403-core 4, these values were  $\sim 0\text{‰}$  at the sediment water interface, quickly decreased to  $-15\text{‰}$  at 1.5 cmbsf, and slowly decreased to  $-18\text{‰}$  at the bottom of the core (Fig. 5-7d).



**Fig. 5- 7: Geochemical results from sediments near a tubeworm bed. From GC 185, HYDRA-4210 pore fluids were analyzed for a) methane concentrations and b)  $\delta^{13}\text{C}$  of methane or DIC values. From GC 232, 4401-core 4 and 4403-core 4 were also collected near a tubeworm bed and measured for c) sulfate concentrations and d)  $\delta^{13}\text{C-DIC}$  values. For comparison in panel b, the solid line represents the average value for vent gas,  $-45.4 \pm 1.2\text{‰}$ , and the dashed line represents the hydrate-bound methane value of  $-42.9 \pm 0.6\text{‰}$  (Sassen et al., 2004).**

### 3.4. Background cores

Two types of background cores were collected. The first type was collected off the side of the ship between hydrate sites and referred to as the reference core. The second type of background core was collected from sediments at GC 185 but showed no visible evidence of bacterial mats or other chemosynthetic community influence. These cores were sister cores, taken ~50 cm apart from each other and named 4214-core 4 and 4214-core 5.

From the reference core, sulfate concentrations did not vary with depth and averaged  $28.8 \pm 0.8$  mM (Fig. 5-8a). From 4214-core 4 and 4214-core 5, sulfate concentrations were similar to the reference core and were consistently high with depth (Fig. 5-8a). Sulfate concentrations averaged  $30.5 \pm 0.6$  mM for 4214-core 4 and  $29.4 \pm 0.4$  mM for 4214-core 5 (Fig. 5-8a). For both cores, the  $\delta^{13}\text{C-DIC}$  values were -3‰ from the surface to 7 cmbsf (Fig. 5-8b). For 4214-core 5, the  $\delta^{13}\text{C-DIC}$  value reached -8‰ by the end of the core.

Sulfate reduction rates (SRR) were low in the background cores. For the reference core, SRR averaged  $0.003 \pm 0.0005$  mM/day for the length of the core (Fig. 5-9a). In 4214-core 5, rates were 0.017 mM/day at the sediment water interface, increased to 0.037 mM/day at 5 cmbsf, and decreased back to 0.016 mM/day (Fig. 5-9b). The rates were similar in 4214-core 4 except that the sub-surface maximum reached only 0.026 mM/day (Fig. 5-9b).

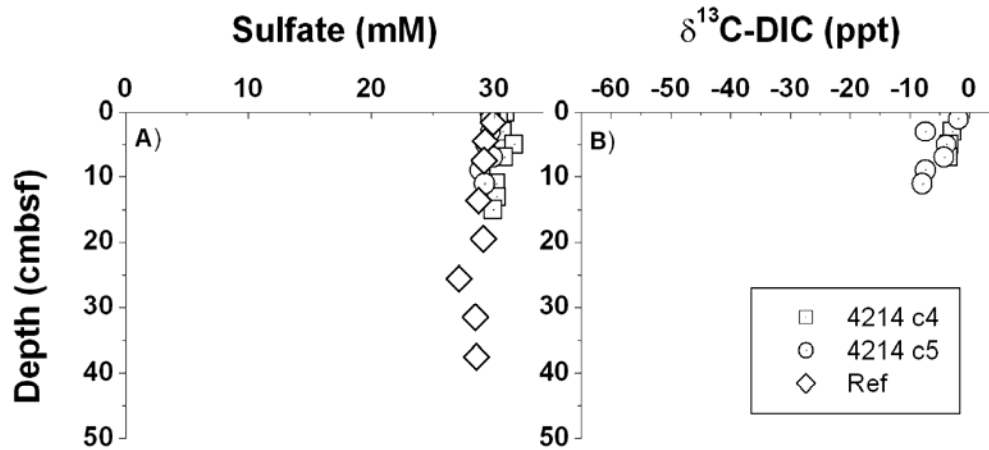


Fig. 5- 8: A) Sulfate and b)  $\delta^{13}\text{C-DIC}$  values from three cores collected in background sediments: 4214-core 4, 4214-core 5, and reference core. The  $\delta^{13}\text{C-DIC}$  values were not measured for the reference core.

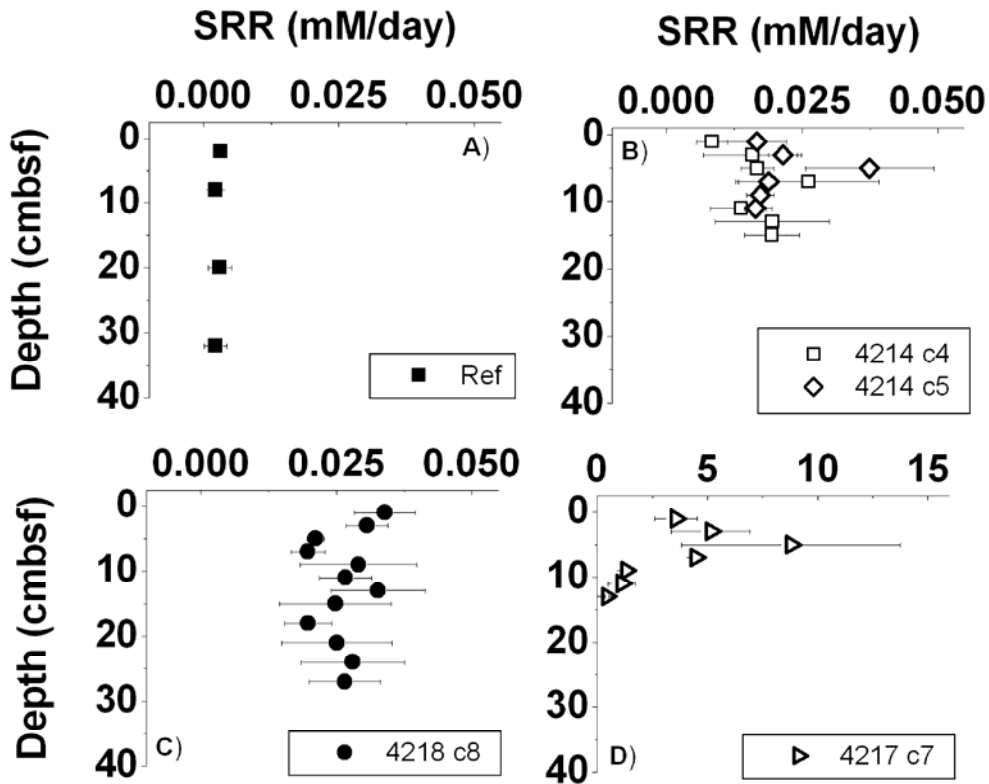


Fig. 5- 9: Sulfate reduction rates (SRR) from four different environments: a) a reference site out of main seepage area, b) two sister background cores from within soft sediments, c) GC 234 core within thin bacterial mat, and d) GC 234 core within thin bacterial mat. Notice x-axis scale change for panel d.

### 3.5. TOC concentrations, $\delta^{13}\text{C}$ -TOC, and C:N

The total organic carbon (TOC) percentage, the  $\delta^{13}\text{C}$ -TOC, and C:N were measured for the reference core, three cores collected at GC 185, and two cores collected at GC 234 (Table 3 and Fig. 5-10). In the reference core, the average TOC concentration was  $1.4\pm 0.2\%$ ,  $\delta^{13}\text{C}$ -DIC was  $-21.3\pm 3.4\%$ , and C:N ratio of  $13.7\pm 6.4$  (Table 3 and Fig. 5-10A-C). At GC 185, for 4213-c3, the average TOC concentration was  $8.3\pm 1.3\%$ ,  $\delta^{13}\text{C}$ -DIC was  $-26.8\pm 0.4\%$ , and C:N ratio of  $27.2\pm 4.0$  (Table 3 and Fig. 5-10D-F). For 4214-c4, the average TOC concentration was  $7.7\pm 1.2\%$ ,  $\delta^{13}\text{C}$ -DIC was  $-23.8\pm 1.6\%$ , and C:N ratio of  $32.5\pm 2.5$  (Table 3 and Fig. 5-10D-F). For 4214-c5, the average TOC concentration was  $8.0\pm 0.6\%$ ,  $\delta^{13}\text{C}$ -DIC was  $-23.5\pm 0.5\%$ , and C:N ratio of  $33.3\pm 3.1$  (Table 3 and Fig. 5-10D-F). At GC 234, for 4217-c7, the average TOC concentration was  $10.7\pm 2.9\%$ ,  $\delta^{13}\text{C}$ -DIC was  $-26.5\pm 0.8\%$ , and C:N ratio of  $22.8\pm 1.3$  (Table 3 and Fig. 5-10G-I). And finally, for 4218-c7, the average TOC concentration was  $5.0\pm 0.8\%$ ,  $\delta^{13}\text{C}$ -DIC was  $-26.1\pm 0.5\%$ , and C:N ratio of  $18.0\pm 2.5$  (Table 3 and Fig. 5-10G-I).

**Table 5- 3: Average statistics on %TOC,  $\delta^{13}\text{C}$ -TOC, and C:N for down core profiles.**

Site	Core	TOC (%)	stdev	$\delta^{13}\text{C}$ -TOC (ppt)	stdev	C:N	stdev
Ref	Ref	1.4	0.2	-21.3	3.4	13.7	6.4
GC 185	4213 c3	8.3	1.3	-26.8	0.4	27.2	4.0
GC 185	4214 c4	7.7	1.2	-23.8	1.6	32.5	2.5
GC 185	4214 c5	8.0	0.6	-23.5	0.5	33.3	3.1
GC 234	4217 c7	10.7	2.9	-26.5	0.8	22.8	1.3
GC 234	4218 c7	5.0	0.8	-26.1	0.5	18.0	2.5

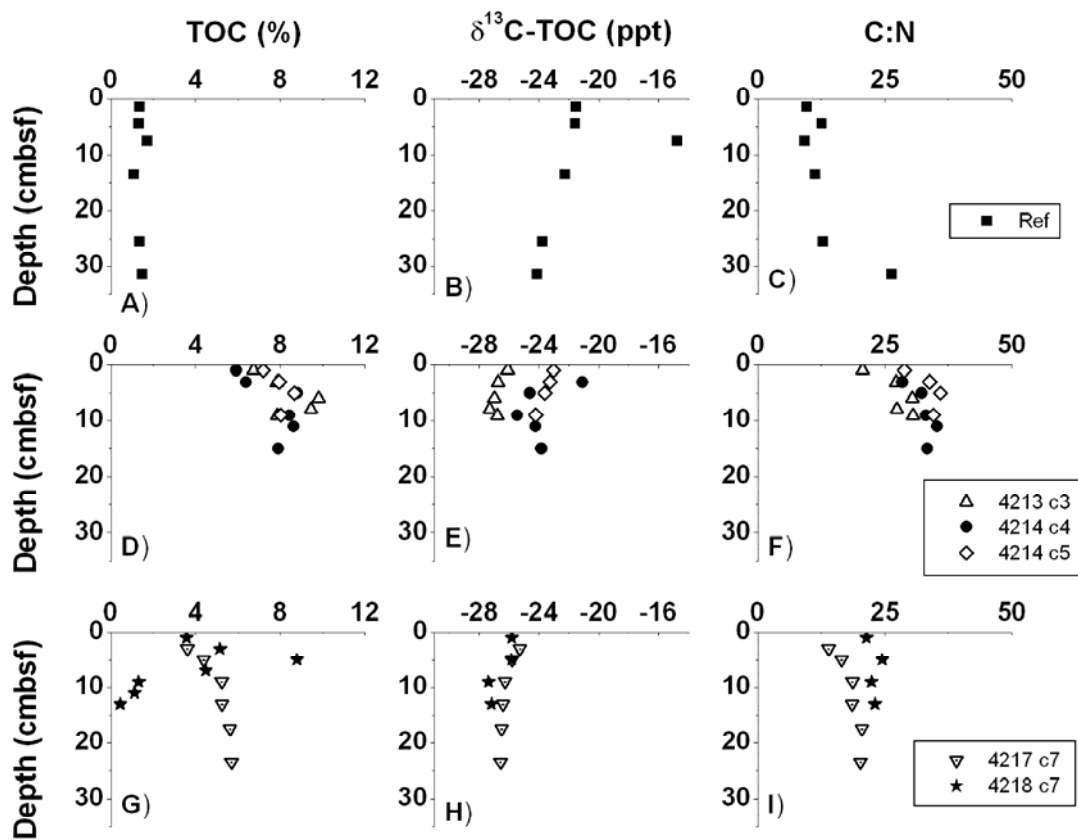


Fig. 5- 10: Total organic carbon (TOC) percentage,  $\delta^{13}\text{C-TOC}$ , and C:N ratios for a)- c) the reference core, d)-f) GC 185 (cores 4213 c3, 4214 c4, and 4214 c5), and g)-i) GC 234 (cores 4217 c7 and 4218 c7).

### 3.6. DOC concentrations

Dissolved organic carbon (DOC) concentrations were measured for a few samples. These concentrations are only reported here and not further discussed. DOC concentrations ranged between 10 uM at the sediment water interface and increased as high as 2200uM at GC 185 (Table 4). These concentrations are within the range reported from other pore water samples (Martin and McCorkle, 1993).

**Table 5- 4: DOC concentrations. OLW = overlying water.**

Site	ID	Interval (cm)	DOC (uM)	stdev
Ref	Ref 2	0-3	228.47	10.25
		6-9	214.04	14.01
		12-15	313.30	8.86
GC 234	4218 c7	OLW	271.49	8.05
		4-6	503.18	14.29
GC 234	4217 c7	OLW	145.75	13.43
		0-2	407.91	14.14
GC 185	4214 c5	0-2	351.58	10.06
		4-6	853.12	13.42
GC 185	4214 c4	OLW	111.91	16.64
		0-2	745.17	18.69
		4-6	612.58	8.63
		10-12	2244.92	26.76

## 4. DISCUSSION

The goal of this study was to assess whether or not microbial activity in sediments surrounding gas hydrates enhances hydrate dissolution. This assessment required an understanding of the source of the dissolved methane surrounding the hydrate, the spatial variability of microbial activity as determined by sulfate reduction within and between hydrate sites, and to determine the relative contribution of methane and oil oxidation coupled to sulfate reduction. In carrying out this assessment, the most significant results were: 1) the source of the dissolved methane pool was a mixture of thermogenic and biogenic processes and the dissolved methane showed no isotopic indication of oxidation, 2) microbial activity was not controlled by proximity to hydrate and was more controlled by availability of high concentrations of methane and TOC, 3) within bacterial mats and next to tubeworm bushes, sulfate reduction rates were elevated above background rates but still exhibited high spatial variability within the hydrates sites, and 4) an isotope mass balance suggested that near the hydrates, anaerobic methane oxidation accounted for ~50% of the sulfate reduction even though this oxidation was not seen in the dissolved methane pool. Collectively, these results suggest that AOM was limited adjacent to the hydrate and does not significantly contribute to hydrate dissolution.

### 4.1. Source of dissolved methane

The source of dissolved methane can be determined using two different approaches. The first generically compares the measured dissolved methane carbon stable isotope and molecular values to established ranges for both thermogenic and biogenic processes. The second approach directly compares the isotopic composition of dissolved methane to possible methane sources such as vent gas and hydrate-bound gas.



For the first approach, the dissolved methane carbon isotopic composition and the ratio of methane to ethane were compared in a Bernard-style plot (Bernard et al., 1978). This plot determines the source of the methane as either biogenic or thermogenic based on established molecular and isotopic ranges of both. For example, biogenic methane typically has  $\delta^{13}\text{C-CH}_4$  values less than -60‰ and  $\text{CH}_4$  to ethane ratios greater than 100 whereas thermogenic methane has  $\delta^{13}\text{C-CH}_4$  values greater than -50‰ and  $\text{CH}_4$  to ethane ratios less than 100 (Bernard et al., 1978). At GC 185 and 234, methane to ethane ratios varied between 1 and 100 and the methane exhibited an isotopic composition ranging from -52 to -45‰ (Fig. 5-11). The Bernard plot shows that the dissolved methane measured in this study was thermogenic in origin. This result is consistent with previous reports of the thermogenic origin of vent gas and the hydrate-bound gas (Sassen et al., 1998, 1999, 2001; Sassen and MacDonald, 1997).

While the Bernard-style plot is appropriate for an overall assessment of the methane source, it is not sensitive enough to distinguish if the dissolved methane originated from the hydrate-bound methane. Therefore, the  $\delta^{13}\text{C-CH}_4$  values of the dissolved methane were directly compared to the isotopic composition of the hydrate-bound and vent gas methane sources. Dissolved methane isotope values more depleted in  $^{13}\text{C}$  than these sources were qualitatively evaluated as being microbially produced methane whereas values enriched in  $^{13}\text{C}$  indicate microbially oxidized methane.

At GC 185, the dissolved methane was slightly depleted in  $^{13}\text{C}$  compared to either the vent gas or hydrate-bound methane (Fig. 5-12). At this site, the isotopic composition of vent gas was  $-45.4 \pm 1.2\text{‰}$  whereas hydrate-bound gas was  $-42.9 \pm 0.6\text{‰}$  (Sassen et al., 2003). The dissolved methane was  $-46.9 \pm 0.4\text{‰}$  (HYDRA-4210) and  $-46.22 \pm 2.2\text{‰}$  (HYDRA-4213).

Since the dissolved methane is slightly depleted in  $^{13}\text{C}$  compared to either the vent gas or hydrate-bound gas, it has a mixed biogenic and thermogenic source component.

At GC 234, the results were slightly different. Here, the isotopic composition of vent gas and hydrate-bound gas were isotopically indistinguishable and averaged  $-48.5 \pm 0.6\text{‰}$  and  $-47.5 \pm 1.0\text{‰}$ , respectively (Sassen et al., 2003). The dissolved methane was measured to have an isotopic composition of  $-50.4 \pm 1.7\text{‰}$  (HYDRA-4217) and  $-47.2 \pm 2.3\text{‰}$  (HYDRA-4218). Therefore, the dissolved methane on dive 4218 was similar to the vent and hydrate-bound gas whereas dive 4217 showed a source from microbially produced methane (Fig. 5-12).

While it was difficult to determine whether or not the dissolved methane originated from the hydrate-bound gas, these results indicate that the dissolved methane had not been microbially oxidized. Therefore, anaerobic methane oxidation is not a major control on the dissolution of the hydrate. Future studies should conduct a transect of methane isotopes from a hydrate to directly test this result.

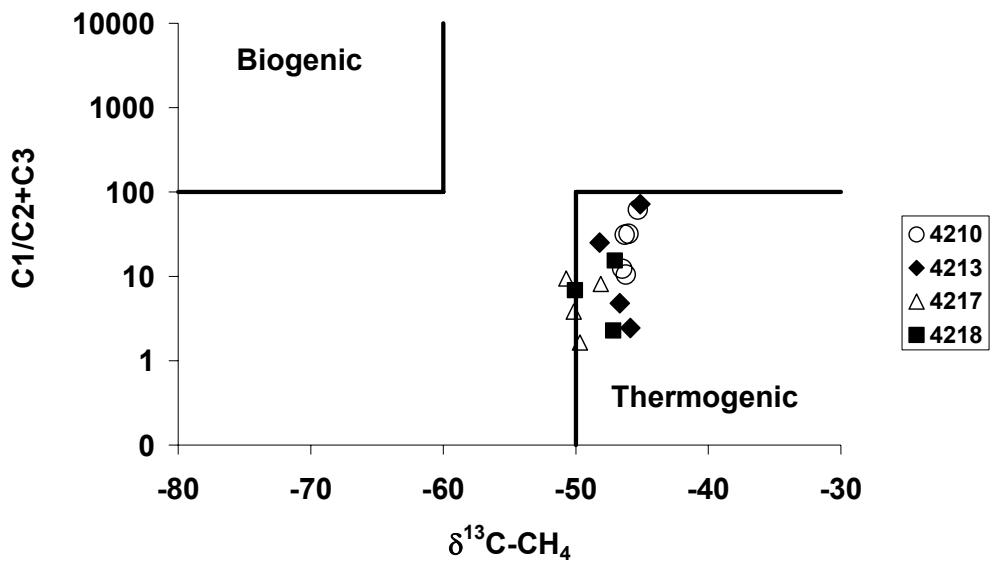


Fig. 5- 11: Bernard style plot to distinguish between biogenic and thermogenic methane (Bernard et al., 1976).

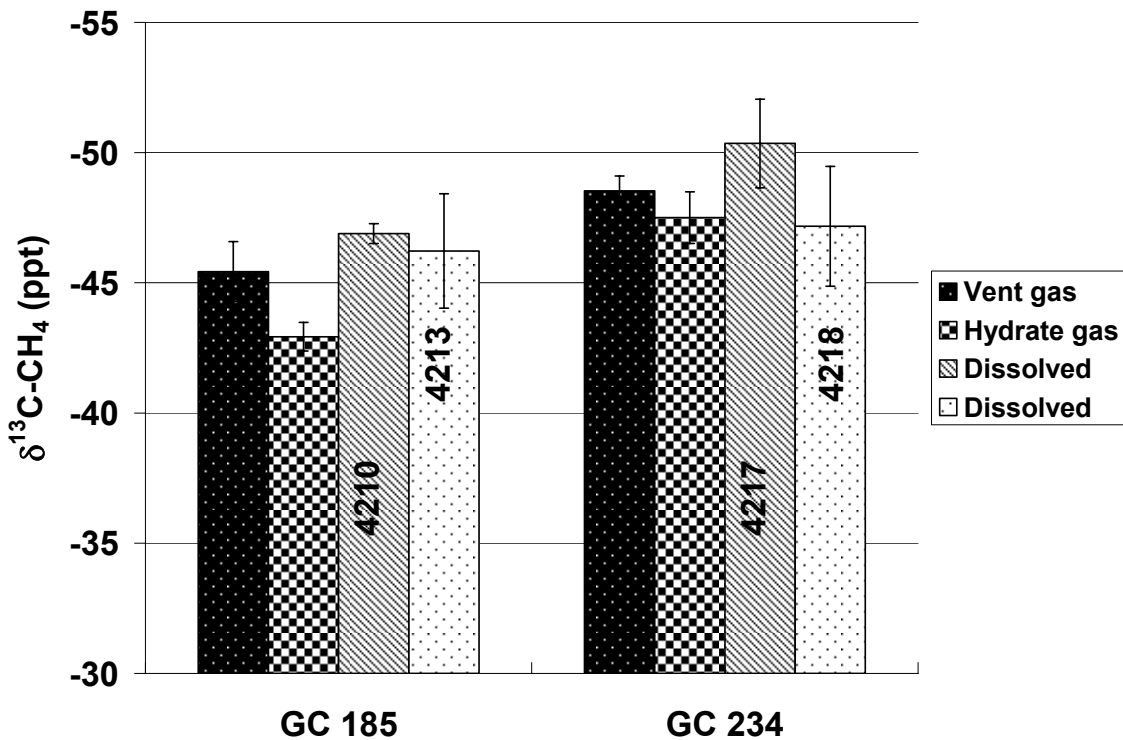


Fig. 5- 12: Synthesis of methane carbon isotopic composition from GC 185 and GC 234. Dissolved = results from HYDRA profiles of this study with dive number displayed. Vent and hydrate gases from Sassen et al. (2003).

#### **4.2. Sulfate reduction and anaerobic methane oxidation as transects away from hydrate**

To address the influence sulfate reduction (SR) and the anaerobic oxidation of methane (AOM) had on hydrate dissolution, these processes were assessed as two transects away from outcropping hydrate at GC 234 and GC 232. The results of these transects were mixed. While both transects showed that SR and AOM were limited on top of the hydrate, these processes were highest adjacent to the hydrate at GC 234 and at GC 232, they were highest furthest from the hydrate. Low rates on top of the hydrate could be due to the path taken by the upward advecting fluids. If these fluids flow around the hydrate and never reach the sediments on top of the hydrate, the rates of SR and AOM may be low because of the lack of reduced carbon. However, this mechanism can not be substantiated with this transect study.

The transect study does, however, suggest that proximity to hydrate does not ultimately control sulfate reduction or methane oxidation. Sulfate reduction was inferred both adjacent to and far from the hydrate. This result supports the lack of an oxidation signal in the isotopes of the dissolved methane (as discussed in the previous section). It is also consistent with other studies that directly measured the rates of sulfate reduction and AOM on the hydrate interface (Orcutt et al., 2004). In these studies, rates of AOM were measurable within the sediments directly adjacent to hydrates but only accounted for ~4% of the rates of sulfate reduction. Therefore, microbial activity may not play a large role in hydrate stability.

#### **4.3. Spatial variability of sulfate reduction rates at hydrate sites**

Rates of sulfate reduction were found to be patchy within and between hydrate sites. Although this has been found by other investigators (Arvidson et al., 2004; Joye et al., 2004; Orcutt et al., 2005), the exact cause for the patchiness is not known. Our study correlates high sulfate reduction rates to high concentrations of methane and TOC (i.e. 4217-core 7)

and suggests a coupling between sulfate reduction and either methane or TOC oxidation. The relative contribution of methane or TOC to sulfate reduction is discussed in section 4.4. Therefore, the patchiness in sulfate reduction could be caused by the patchy availability of such oxidants. Since these oxidants are brought to the seep system from the upward advecting fluids from below, our results suggest that the advecting fluids are also patchy in distribution.

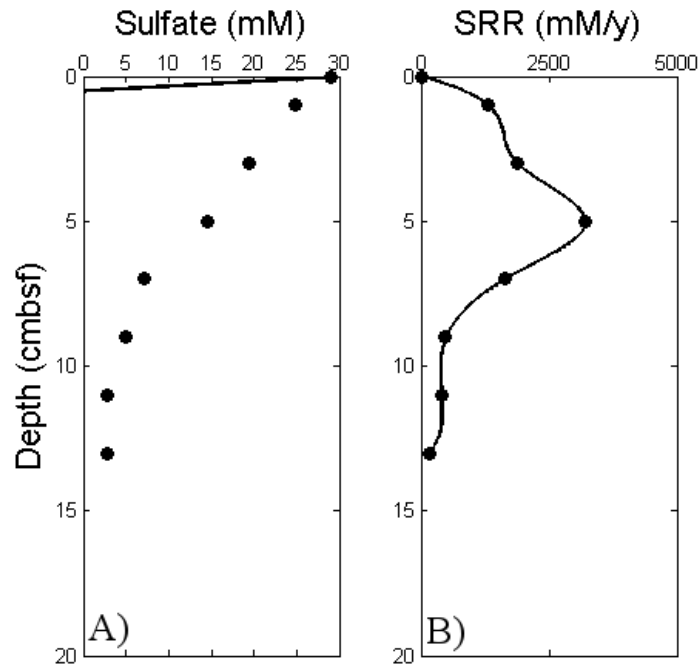
In 4217-core 7, the rates of sulfate reduction were too high to be supported by the diffusive flux of sulfate from overlying water. This was determined by applying the general diagenetic equation that describes the sulfate profiles as a function of diffusion, sediment accumulation, compaction, and any reactions (Berner, 1980). At steady state, the diagenetic equation is:

$$\phi^2 D_o \frac{d^2 C}{dx^2} + \left( 3\phi D_o \frac{d\phi}{dx} - \frac{\omega\phi_\infty}{\phi} \right) \frac{dC}{dx} + R_x = 0 \quad (7)$$

where  $\phi$  is the sediment porosity,  $D_o$  is the free solution diffusion coefficient for sulfate,  $C$  is the sulfate concentration,  $x$  is the depth below the sediment water interface,  $\omega$  is the sediment accumulation rate,  $\infty$  is the depth at which the porosity gradient approaches zero, and  $R_x$  is the depth dependent reaction rate. The sulfate reduction rate measurements and model parameters (Table 5) were used in equation (7) to determine the sulfate concentrations needed to support the rates. The results show that, at the rates measured, the sulfate pool would have been depleted by 1 cmbsf (Fig. 5-13). The modeled rates underestimated measured rates by 97%.

**Table 5- 5: Model parameters.**

Parameters	Description	Values
$\phi-\infty$	porosity at infinite depth	0.796
$\phi$ -coefficient	exponential decay coefficient for porosity	0.9635-0.796
$\phi$ -exponent	exponential decay constant for porosity	-0.456
$\omega$ (cm/year)	sedimentation rate	0.02
$D_0$ (cm <sup>2</sup> /sec)	diffusion coefficient	6.13E-06
$x_{bc1}$ (cm)	upper depth boundary condition	0
$c_{bc1}$ (mM)	upper concentration boundary condition	28.9
$x_{bc2}$ (cm)	lower depth boundary condition	13
$c_{bc2}$ (mM)	lower concentration boundary condition	2.8



**Fig. 5- 13: Measured and modeled results from 4217-core 7. A) sulfate concentrations and b) sulfate reduction rates. Filled circles are the measured data and the solid lines are the model results.**

There are two possible explanations for the discrepancy between the model and measured results (Fig. 5-13). The first is that the measured rates overestimated the *in situ* rates due to an artifact in the rate measurements and the second is that there is an alternative process supplying sulfate that was not considered in equation (7). For the first explanation, the rate measurements were conducted on board the ship at *in situ* temperatures but not at *in situ*

pressures. Although lower pressures could artificially elevate rates, there has been no direct evidence of this in laboratory versus *in situ* rate studies (Weber et al., 2000). Rates could also have been elevated due to exposure to higher temperatures during collection. However, the cores were collected from the submersible, immediately placed into a cold room, and allowed to equilibrate for a few hours in order to minimize this effect. Furthermore, several studies from similar hydrate sites have also reported this discrepancy between measured and modeled rates (Arvidson et al., 2004; Orcutt et al., 2005). Therefore, the discrepancy between measured and modeled rates is best explained by processes other than diffusion supplying sulfate to the sediments.

Additional sulfate may be supplied to surface sediments through four processes: physical replenishment from bubble ebullition (O'Hara et al., 1995), bioirrigation from tube dwelling animals (Fossing et al., 2000), the dissolution of barite ( $\text{BaSO}_4$ ) (Orcutt et al., 2005), and the biologically mediated recycling of sulfate from bacterial mats and tubeworms (Arvidson et al., 2004). The physical process of bubbling out of sediments could replenish interstitial waters with oxygenated, sulfate-rich seawater (O'Hara et al., 1995). Since high concentrations of methane were measured where the highest sulfate reduction rates were also measured, the physical replenishment of sulfate from ebullition is possible. However, when the cores were collected, there was no indication of active bubbling. Bioirrigation from tube dwelling animals could also bring sulfate-rich seawater down into the tubes and ultimately into the interstitial waters. However, no animal tubes were found in the cores. Sulfate could also be supplied through the dissolution of barite (Orcutt et al., 2005). As barite is often found at hydrate sites (i.e. Fu et al., 1994), its dissolution still remains a possibility even though there was no direct evidence of barite in the cores collected for this study.

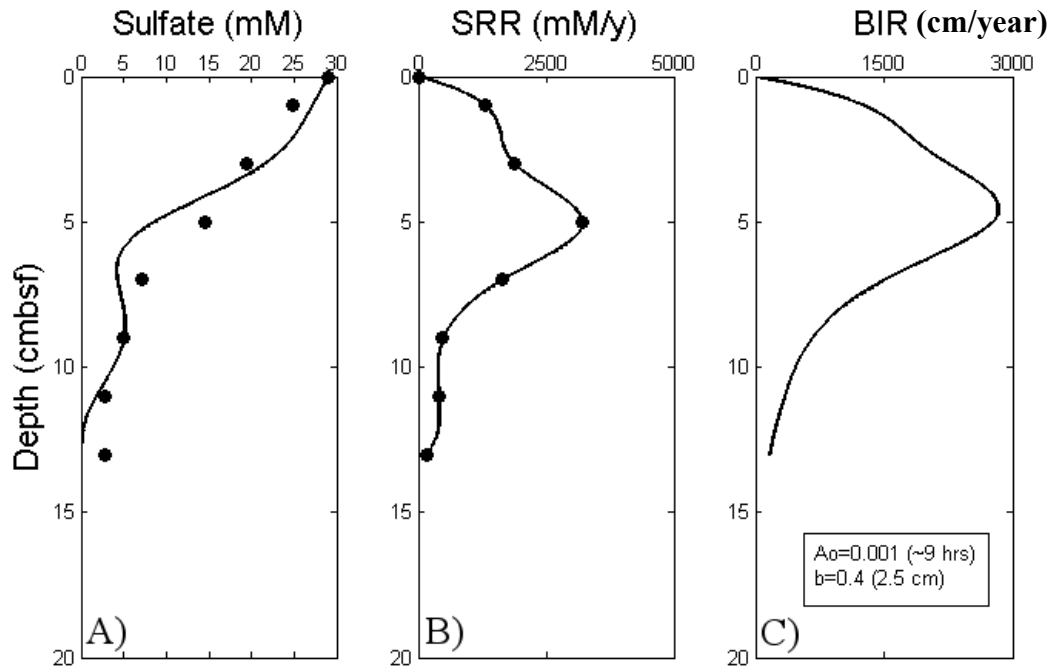
The more likely explanation for an additional sulfate supply is the active pumping and recycling of sulfate from tubeworms and bacterial mats, respectively (Arvidson et al., 2004). Tubeworms obtain their energy from endosymbiotic bacteria that oxidize sulfide. Since these endosymbionts can not access the sulfide directly, tubeworms reside in sediments where sulfate reduction is high in order to actively pump resultant sulfide from their roots (10-25 cm deep) to their endosymbionts (Julian et al., 1999). This action may be complimented by the tubeworms pumping seawater, enriched in sulfate, down their roots and to the sulfate reducers to produce more sulfide (Julian et al., 1999). Likewise, sulfate could simply be recycled by the activity of bacterial mats such as *Beggiatoa*. These bacteria oxidize sulfide to sulfate and, as they migrate vertically in the sediments, could replenish the interstitial sulfate supply. This recycling of sulfate is a viable explanation for the high rates measured in 4217-core 7 because it was collected in a bacterial mat.

Regardless of the exact process providing additional sulfate to the sediments, the discrepancy between the measured and modeled rates is clear. Therefore, the sulfate reduction rates were modeled again with equation (7) to include a bioirrigation term. In order to reconcile the measured and modeled rates, a non-local pore water exchange function of  $0.001 \text{ yr}^{-1}$  had to be applied (Fig. 5-14). This means that every ~9 hours, sulfate was resupplied to the sedimentary microbial community.

Bioirrigation could also explain profiles of limited sulfate depletion yet the incorporation of  $^{13}\text{C}$ -depleted carbon into the DIC pool (i.e. GC 232 core collected ~50 cm from hydrate, Fig. 5-3c and 3d). The replenishment of sulfate from bioirrigators would result in a consistent sulfate profile with depth, even if sulfate reduction is still occurring. This



illustrates the caution that must be taken when interpreting the lack of sulfate depletion with depth as limited sulfate reduction.



**Fig. 5- 14: Measured and model results for 4217-core 7. A) sulfate concentrations, b) sulfate reduction rates (SRR) and c) bioirrigation term defined by an exponential curve  $y=A_0\exp^{-bx}$ , where  $A_0$  and  $b$  are defined in panel c. Filled circles represent data and lines are model results.**

#### **4.4. Future work**

High sulfate reduction rates were correlated to high methane and total (or non-methane) organic carbon concentrations (i.e. 4217-core 7). Was sulfate reduction enhanced because of the availability of methane or other organic carbon at the hydrate site? Due to the decoupling of the methane and DIC isotopes, methane was a small part of sulfate reduction. This supports other studies that have also determined that the majority of sulfate reduction proceeds not by methane oxidation but by the oxidation of petroleum (Joye et al., 2004; Orcutt et al., 2005). Since microbial methane oxidation is an important control on the flux of methane into the overlying water, it is important to quantify the relative contribution from both methane and non-methane carbon oxidation to sulfate reduction. This quantification can be carried out by implementing a reaction transport isotope model which will be done in the future.

### **5. CONCLUSIONS**

The goal of this chapter was to determine whether or not microbial activity in sediments surrounding hydrates was enhanced closer to the hydrate and possibly contributing to hydrate dissolution. To address this, the source of the dissolved methane surrounding the hydrate, the spatial variability of microbial activity as determined by sulfate reduction within and between hydrate sites, and the relative contribution of methane and oil oxidation coupled to sulfate reduction were determined. The source of the dissolved methane was overall thermogenic but had a contribution from microbially produced methane. As transects away from hydrate, sulfate reduction and anaerobic methane oxidation rates were not controlled by proximity to the hydrate but were more controlled by the availability of high concentrations

of methane and total organic carbon. These results suggest that since AOM was limited adjacent to the hydrate, it does not contribute significantly to hydrate dissolution.

*Acknowledgements.* This work was supported by DOE and the Gulf of Mexico Hydrates Research Consortium at the University of Mississippi, DE-FC26-00NT40920

## 6. REFERENCES

- Aharon P. and Fu B. (2000) Microbial sulfate reduction rates and sulfur and oxygen isotope fractionations at oil and gas seeps in deepwater Gulf of Mexico. *Geochimica et Cosmochimica Acta* **64** (2), 233-246.
- Albert D. B., Taylor C., and Martens C. S. (1995) Sulfate reduction rates and low molecular weight fatty acid concentrations in the water column and surficial sediments of the Black Sea. *Deep-Sea Research I* **42** (7), 1239-1260.
- Arvidson R. S., Morse J. W., and Joye S. B. (2004) The sulfur biogeochemistry of chemosynthetic cold seep communities, Gulf of Mexico, USA. *Marine Chemistry* **87**, 97-119.
- Bernard B. B., Brooks J. M., and Sackett W. M. (1976) Natural gas seepage in the Gulf of Mexico. *Earth and Planetary Science Letters* **31**, 48-54.
- Bernard B. B., Brooks J. M., and Sackett W. M. (1978) Light hydrocarbons in recent Texas Continental Shelf and Slope sediments. *Journal of Geophysical Research* **83** (C8), 4053-4061.
- Berner R. A. H. D. Holland (1980) *Early Diagenesis: A theoretical approach*. Princeton University Press, Princeton.
- Boetius A., Ravensschlag K., Schubert C. J., Rickert D., Widdel F., Gieseke A., Amann R., Jorgensen B. B., Witte U., and Pfannkuche O. (2000) A marine microbial consortium apparently mediating anaerobic oxidation of methane. *Nature* **407**, 623-626.
- Brenna J. T., Corso T. N., Tobias H. J., and Caimi R. J. (1997) High-precision continuous-flow isotope ratio mass spectrometry. *Mass Spectrometry Reviews* **16**, 227-258.
- Brewer P. G., Paull C. K., Peltzer E. T., Ussler III W., Rehder G., and Friederich G. (2002) Measurements of the fate of gas hydrates during transit through the ocean water column. *Geophysical Research Letters* **29** (22), 38-1 to 38-4.
- Buffett B. A. (2000) Clathrate Hydrates. *Annual Review of Earth and Planetary Sciences* **28**, 477-507.
- Egorov A. V., Crane K., Vogt P. R., and Rozhkov A. N. (1999) Gas hydrates that outcrop on the sea floor: stability models. *Geo-Marine Letters* **19**, 68-75.
- Fossing H., Ferdelman T. G., and Berg P. (2000) Sulfate reduction and methane oxidation in continental margin sediments influenced by irrigation (South-East Atlantic off Namibia). *Geochimica Cosmochimica Acta* **64** (5), 897-910.
- Fu B., Aharon P., Byerly G. R., and Roberts H. H. (1994) Barite chimneys on the Gulf of Mexico slope: Initial report on their petrography and geochemistry. *Geo-Marine Letters* **14**, 81-87.

- Hoehler T. M., Alperin M. J., Albert D. B., and Martens C. S. (1994) Field and laboratory studies of methane oxidation in an anoxic marine sediment: Evidence for a methanogen-sulfate reducer consortium. *Global Biogeochemical Cycles* **8** (4), 451-463.
- Joye S. B., Boetius A., Orcutt B. N., Montoya J. P., Schulz H. N., Erickson M. J., and Lugo S. K. (2004) The anaerobic oxidation of methane and sulfate reduction in sediments from Gulf of Mexico cold seeps. *Chemical Geology* **205**, 219-238.
- Julian D., Gaill F., Wood E., Arp A. A., and Fisher C. R. (1999) Roots as site of hydrogen sulfide uptake in the hydrocarbon seep Vestimentiferan *Lamellibrachia* sp. *The Journal of Experimental Biology* **202**, 2245-2257.
- Keeling C. D. (1958) The concentration and isotopic abundances of atmospheric carbon dioxide in rural areas. *Geochimica et Cosmochimica Acta* **13**, 322-334.
- Kennicutt M. C., Brooks J. M., and Denoux G. J. (1988) Leakage of deep, reservoired petroleum to the near surface on the Gulf of Mexico continental slope. *Marine Chemistry* **24**, 39-59.
- Kvenvolden K. A. (1988) Methane hydrate-a major reservoir of carbon in the shallow geosphere? *Chemical Geology* **71**, 41-51.
- Kvenvolden K. A. (1993) Gas hydrates-geological perspective and global change. *Reviews of Geophysics* **31**, 173-187.
- MacDonald I. R., Bender L. C., Vardaro M., Bernard B., and Brooks J. M. (2005) Thermal and visual time-series at a seafloor gas hydrate deposit on the Gulf of Mexico slope. *Earth and Planetary Science Letters* **233**, 45-59.
- MacDonald I. R., Guinasso Jr. N. L., Sassen R., Brooks J. M., Lee L., and Scott K. T. (1994) Gas hydrate that breaches the sea floor on the continental slope of the Gulf of Mexico. *Geology* **22**, 699-702.
- Martens C. S., Albert D. B., and Alperin M. J. (1999) Stable isotope tracing of anaerobic methane oxidation in the gassy sediments of Eckernforde Bay, German Baltic Sea. *American Journal of Science* **299**, 589-610.
- Martin W. R. and McCorkle D. C. (1993) Dissolved organic carbon concentrations in marine pore waters determined by high-temperature oxidation. *Limnology and Oceanography* **38** (7), 1464-1479.
- Milkov A. V. (2004) Global estimates of hydrate-bound gas in marine sediments: how much is really out there? *Earth-Science Reviews* **66**, 183-197.
- Mortazavi B. and Chanton J. P. (2004) Use of Keeling plots to determine sources of dissolved organic carbon in nearshore and open ocean systems. *Limnology and Oceanography* **49** (1), 102-108.

- O'Hara S. C. M., Dando P. R., Schuster U., Bennis, Boyle J. D., Chui F. T. W., Hatherell T. V. J., Niven S. J., and Taylor L. J. (1995) Gas seep induced interstitial water circulation: observations and environmental implications. *Continental Shelf Research* **15** (8), 931-948.
- Orcutt B. N., Boetius A., Elvert M., Samarkin V. A., and Joye S. B. (2005) Molecular biogeochemistry of sulfate reduction, methanogenesis, and the anaerobic oxidation of methane at Gulf of Mexico cold seeps. *Geochimica et Cosmochimica Acta* **69** (17), 4267-4281.
- Orcutt B. N., Boetius A., Lugo S. K., MacDonald I. R., Samarkin V. A., and Joye S. B. (2004) Life at the edge of methane ice: microbial cycling of carbon and sulfur in Gulf of Mexico gas hydrates. *Chemical Geology* **205**, 239-251.
- Pohlman J. W. (2006) Sediment biogeochemistry of Northern Cascadia Margin shallow gas hydrate systems. Ph. D. Thesis, College of William and Mary.
- Reeburgh W. S. (1967) An improved interstitial water sampler. *Limnology and Oceanography* **12**, 163-165.
- Reeburgh W. S. M. E. Lidstrom and F. R. Tabita (1996) *"Soft spots" in the global methane budget*. Kluwer Academic Publishers, Intercept, Andover, UK.
- Rehder G., Kirby S. H., Durham W. B., Stern L. A., Peltzer E. T., Pinkston J., and Brewer P. G. (2004) Dissolution rates of pure methane hydrate and carbon-dioxide hydrate in undersaturated seawater at 1000-m depth. *Geochimica et Cosmochimica Acta* **68** (2), 285-292.
- Roberts H. H., Wiseman W. J. J., Hooper J., and Humphrey G. D. (1999) Surficial Gas Hydrates of the Louisiana Continental Slope-Initial results of direct observations and in situ data collection. *Offshore Technology Conference*, 259-272.
- Sassen R., Milkov A. V., Ozgul E., Roberts H. H., Hunt J. L., Beeunas M. A., Chanton J. P., DeFreitas D. A., and Sweet S. T. (2003) Gas venting and subsurface change in the Green Canyon area, Gulf of Mexico continental slope: evidence of a deep bacterial methane source? *Organic Geochemistry* **34**, 1455-1464.
- Sassen R., Roberts H. H., Aharon P., Larkin J., Chinn E. W., and Carney R. (1993) Chemosynthetic bacterial mats at cold hydrocarbon seeps, Gulf of Mexico continental slope. *Organic Geochemistry* **20**, 77-89.
- Sassen R., Roberts H. H., Carney R., Milkov A. V., DeFreitas D. A., Lanoil B., and Zhang C. (2004) Free hydrocarbon gas, gas hydrate, and authigenic minerals in chemosynthetic communities of the northern Gulf of Mexico continental slope: relation to microbial processes. *Chemical Geology* **205**, 195-217.
- Scranton M. I. and Brewer P. G. (1978) Consumption of dissolved methane in the deep ocean. *Limnology and Oceanography* **23** (6), 1207-1213.

- Sloan E. D. E. D. Sloan (1998) *Clathrate hydrates of natural gases, second edition*. Marcel Dekker, Inc., New York.
- Wang X.-C., Chen R. F., Whelan J. K., and Eglinton L. (2001) Contribution of "old" carbon from natural marine hydrocarbon seeps to sedimentary and dissolved organic carbon pools in the Gulf of Mexico. *Geophysical Research Letters* **28** (17), 3313-3316.
- Weber A., Riess W., Wenzhoefer F., and Jorgensen B. B. (2000) Sulfate reduction in Black Sea sediments: in situ and laboratory radiotracer measurements from the shelf to 2000m depth. *Deep-Sea Res. I* **48**, 2073-2096.
- Zhang Y. and Xu Z. (2003) Kinetics of convective crystal dissolution and melting, with applications to methane hydrate dissolution and dissociation in seawater. *Earth and Planetary Science Letters* **213**, 133-148.

## **Chapter 6: Biogeochemical processes and advection rates in Gulf of Mexico brine seeps: field and modeling studies**

**Abstract-** Brine fluids seeping through oceanic sediments that reach the shallow sediment surface may strongly impact the surrounding biogeochemical processes. To address this, pore-fluids were collected from four different brine seeps (GC 233, GB 425, GC 205, and MC 709) to determine how the brine fluids affect local biogeochemical processes and to determine the rate of upward fluid flux. Pore-fluids were measured for variations in depth gradients of chloride, sulfate, and methane concentrations and stable carbon isotopic compositions of methane and dissolved inorganic carbon. From GC 205 and MC 709, steep chloride concentration gradients were measured. Applying these gradients to an advection/diffusion diagenetic model, upward advection rates were estimated to be between 3 and 65 cm/year, depending on the site. After correcting sulfate profiles for this upwardly advecting sulfate-free brine fluid, sulfate profiles were explained primarily by advection and diffusion and very low rates of sulfate reduction were inferred. The brine fluids were enriched with methane, measuring as high as 25,000  $\mu\text{M}$ . Within the brine fluids and mussel beds at GC 233, this methane was biogenic in origin whereas outside the mussels, the methane was a mixture of biogenic and thermogenic methane. Likewise, brine fluids at GB 425, GC 205, and MC 709 also contained methane of a mixed biogenic and thermogenic source.



## 1. INTRODUCTION

Brine seeps are common along the northern Texas-Louisiana Continental shelf and slope in the Gulf of Mexico (Shokes et al., 1977; Brooks et al., 1979; MacDonald et al., 1990b).

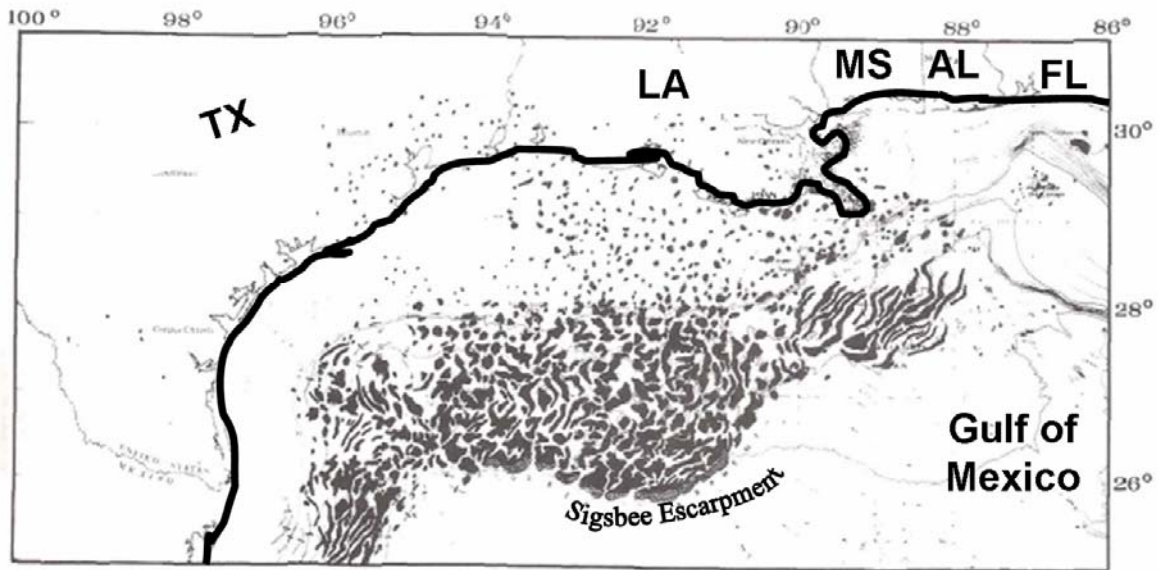
Along with the brine, these seeps bring large amounts of methane and other reduced compounds to the shallow sediments that may fuel biogeochemical processes such as sulfate reduction and anaerobic methane oxidation. However, brine seeps may be an important source of the potent greenhouse gas methane directly to overlying ocean waters since brines inhibit methane hydrate formation (Sloan, 1998). Furthermore, there is some evidence that the anaerobic oxidation of methane (AOM) is inhibited under the high salinity conditions (Joye et al., in review). In addition, the anoxic conditions and availability of organic substrates may also support significant rates of methanogenesis (Joye et al., in review).

Therefore, it is imperative to quantify how fast the methane-enriched seeping fluids reach the sediment-water interface and to understand how advective processes may control the rates of biogeochemical processes such as AOM and methanogenesis that act to control the flux of methane from sediments.

Gulf of Mexico brine seepage occurs because of the basin's unique history. When the basin first formed about 150 million years ago, a thick layer of salt was deposited through a series of flooding and evaporation events (Salvador, 1987). After that, as continental sediments spilled onto the slope, loading pressures forced the deeply layered salt to flow as a horizontal salt-wedge towards the basin center; forming the Sigsbee Escarpment (Fig. 6-1a). Due to density differences between the thickening compacted sediments ( $\rho=2.7 \text{ g/cm}^3$ ) and the deeper salt ( $\rho\sim 2.2 \text{ g/cm}^3$ ), the salt also began to move vertically as finger-like salt diapirs or domes. The movement of these diapirs has resulted in tectonic activity that

continues to create sedimentary faults along which deeply buried fluids rich in thermogenic gases and oil migrate to shallower depths (Fig. 6-1b). Faults that intersect the seafloor typically manifest into mud volcanoes and cold hydrocarbon seeps that are rich in chemosynthetic communities and gas hydrates (Roberts and Carney, 1997). Over time, the diapirs themselves may breach the sediment-water interface and produce brine pools or brine filled sediments (Williams and Lerche, 1987; MacDonald et al., 1990b). At such sites, chemosynthetic communities and mud volcanoes are also typically found.

A)



B)

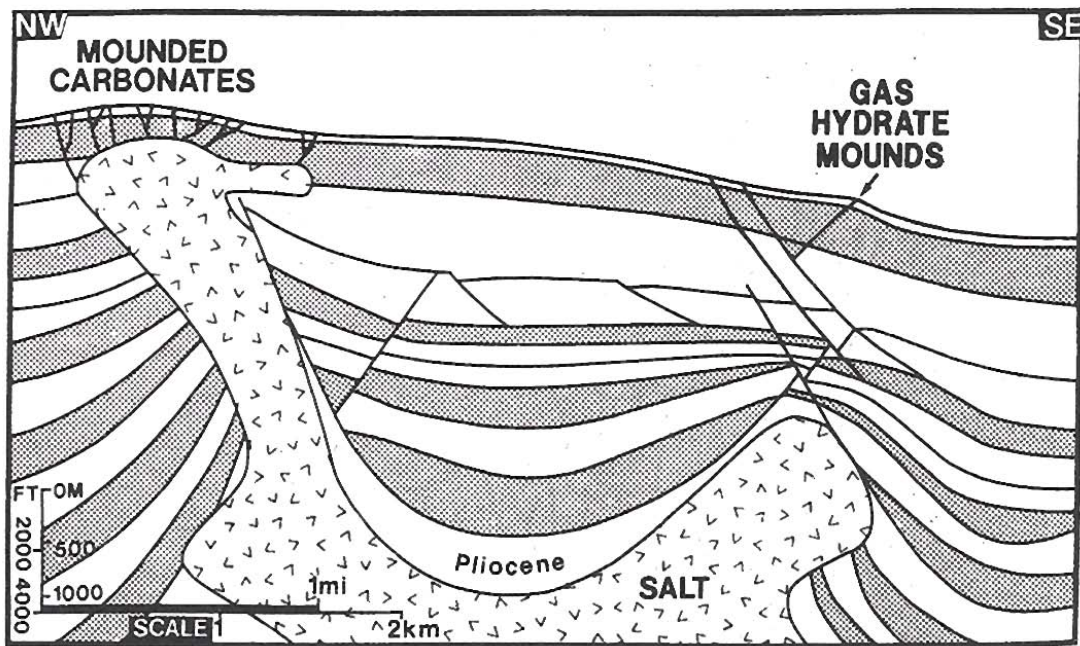


Fig. 6- 1: A) Map of the Texas-Louisiana coast, shelf, and slope (Martin and Bouma, 1982). Dark black line contours the current coastline. Dark gray splotches represent all known salt diapirs. B) Cartoon of the underlying salt diapirs found in Green Canyon Lease Block (Cook and D'Onfro, 1991).

Brine fluids have unique chemical characteristics. Along with hypersaline conditions, fluids are typically warm, anoxic, and enriched in reduced methane and other light hydrocarbon gases (MacDonald et al., 1990b; Joye et al., 2005). The reduced chemicals found in the fluids help support a diverse ecosystem of chemosynthetic communities and sedimentary microbial processes (MacDonald et al., 1990b). Although studies are beginning to shed light on the rates of biogeochemical processes in Gulf of Mexico brines (Joye et al., in review), little is known of such processes.

The rates at which brine fluids reach shallow sediments are also unknown but thought to be quite variable (Martin and Bouma, 1982). Episodic venting is suggested because of pockmarked sediments around brine pools (MacDonald et al., 1990b; MacDonald et al., 2000) and substantial temporal variability in brine fluid temperatures (Joye et al., 2005). This episodic venting could have significant impacts on the rates of temperature-driven microbial processes.

The salinity of overlying seawater in the northern Gulf of Mexico is ~35 psu containing ~550 mM chloride. However, brine fluids have observed salinities up to 130 psu (Brooks et al., 1979; MacDonald et al., 1990b; Joye et al., 2005). Are the high concentrations of salt found in the Gulf toxic to microbial processes? A recent study comparing rates of two brine fields with ostensibly variable upward flow rates showed that sulfate reduction was the primary metabolism process where fluid flow was low and methanogenesis dominated in a high flow system (Joye et al., in review). In laboratory culture studies, salt tolerances were measured for different microbial processes (Oren, 2002). In such studies, methanogens fermenting acetate had the lowest tolerance at 60 psu, methanogens reducing carbon dioxide

could tolerate 120 psu which was similar to sulfate reducers, and methanogens reducing noncompetitive substrates had the highest salt tolerance of 250 psu (Oren, 2002).

The presence of biogenic methane within brine fluids with salinities of 120 psu (n=3; MacDonald et al., 1990b; Sassen et al., 1999) suggests that *in situ* methanogenesis is a dominant microbial process in these fluids. Furthermore, brine filled sediments typically contain reduced compounds such as sulfide and biodegraded oils that can support elevated rates of microbial activity compared to background sediments (MacDonald et al., 1990b). Rates of sulfate reduction were found to be elevated. Studies in sediments surrounding brine pools showed that while SR rates were high, rates of MP and AOM were low (Arvidson et al., 2004; Orcutt et al., 2005). Yet, few studies have directly measured the rates of biogeochemical processes within Gulf of Mexico brine fluids (Joye et al., in review).

We hypothesize that sulfate reduction will be limited to lower salinities and flow rates whereas methanogenesis will dominate in higher salinities and flow rates. The focus of this study was to conduct a spatial survey of pore-fluid chemistry within and amongst brine filled sediments to determine to determine the advective, upward brine flux and how the brine affects the local biogeochemical processes.

The following questions were asked:

1. What are the upward advection rates of brine fluids at our field sites?
2. How do brine fluids affect biogeochemical processes such as sulfate reduction, anaerobic methane oxidation, and methanogenesis?
3. What are the sources of methane in surficial sediments with elevated salinities and how much methane is entrained in migrating brine fluids?

To answer these questions, sediments and pore-waters were sampled from four brine field sites by traditional coring and by use of the novel pore-fluid sampler HYDRA. The pore-fluids were measured for chloride, sulfate, and methane concentrations, and the stable isotopic composition of methane and dissolved inorganic carbon. Advection rates were determined by modeling the steep chloride concentration gradients measured in the sediment cores. Biogeochemical processes were inferred based on established patterns of stable carbon isotope fractionation.

## 2. METHODS

### 2.1. Sites visited

In the Gulf of Mexico, four brine sites were visited on two cruises on the Research Vessel Seward Johnson using the submersible Johnson Sea-Link (JSL; Fig. 6-2 and Table 6-1). A conceptual picture of the sites shows the local environments around the sampling sites (Fig. 6-3) while exact sampling sites are shown in Fig. 6-4.

Green Canyon (GC) 233 is a well known brine pool site at 650 meters water depth where the brine fluid extends into the overlying water, creating the brine pool, and is rimmed by a bed of *Bathymodiolus childressi* mussels (MacDonald et al., 1990b). In 2000, on JSL dive 4222, sediments were sampled outside the mussel bed with the *in situ* pore-fluid sampler, HYDRA, (Fig. 6-4a).

In 2003, on JSL dive 4555, HYDRA was deployed within the mussel bed (Fig. 6-4b). In 2003, JSL visited GC 205 on dive 4566. This site was found in 958 meters water depth and a small mud volcano was evident. Near the eruption, pore-fluids were sampled with HYDRA and sediments were collected with two cores (Fig. 6-4c). Core 5 was collected on the edge of

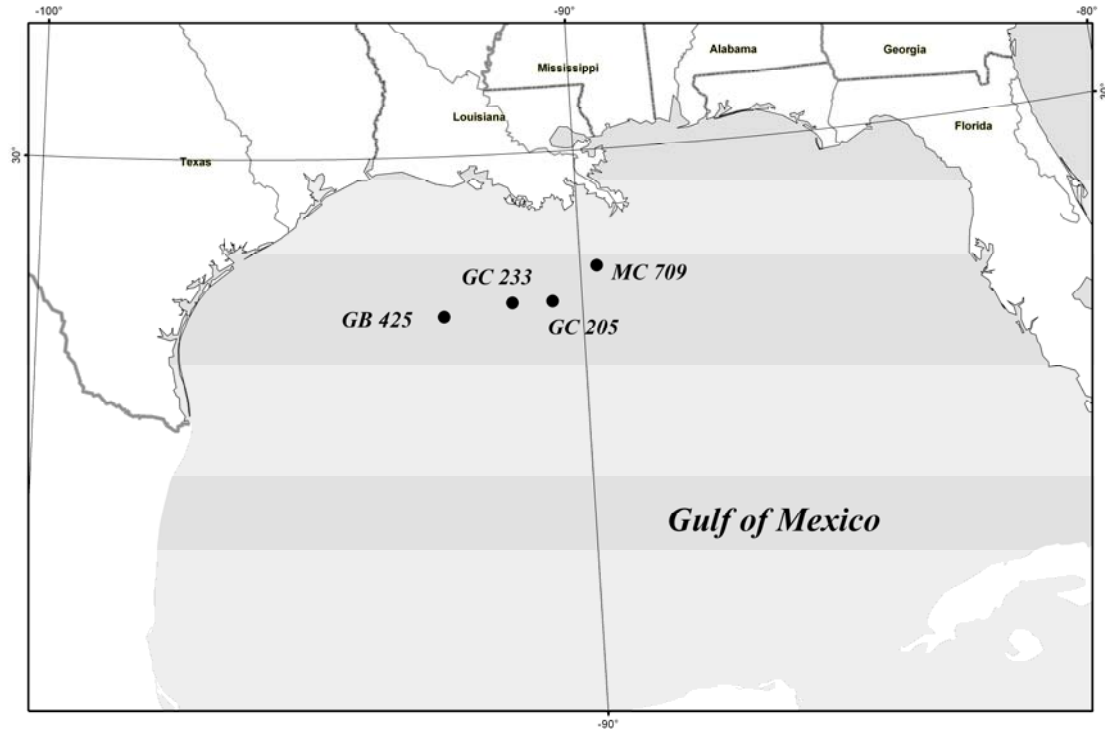
the thin bacterial mat and core 2 was collected within the thick bacterial mat. When core 2 was extracted from the sediments, a viscous, cloudy fluid remained within the core-hole.

Garden Banks (GB) 425 was sampled on JSL dive 4562 (Fig. 6-4d). GB 425 is a brine-dominated cold seep found at 600 meters water depth (MacDonald et al., 2000; Joye et al., 2005). Apparently due to the higher salinity in the brine, hydrates were not found at GB 425 but they have been suggested to have caused gas expansions in other cores collected in a nearby area (Sager et al., 1999). HYDRA was placed into gray mud with no visible indication of bacterial mats.

Mississippi Canyon (MC) 709 was sampled in 2002 on JSL dives 4412 and 4413. MC 709 is found in 740 meters water and is not thought to contain hydrate due to the occurrence of brine fields (Sassen and Roberts, 2004). Although no hydrates were visible during the MC 709 dives, this site was unique in that it featured ledges and walls with black streaks running along and beside them (Fig. 6-3d). Core 3 (dive 4412) was collected within one of the black streaks and core 6 (dive 4413) was collected within a thick bacterial mat with black sediments underneath a bacterial mat (Fig. 6-3d). HYDRA was deployed outside the black streaks in brown mud with few clam shells present (Fig. 6-4e).

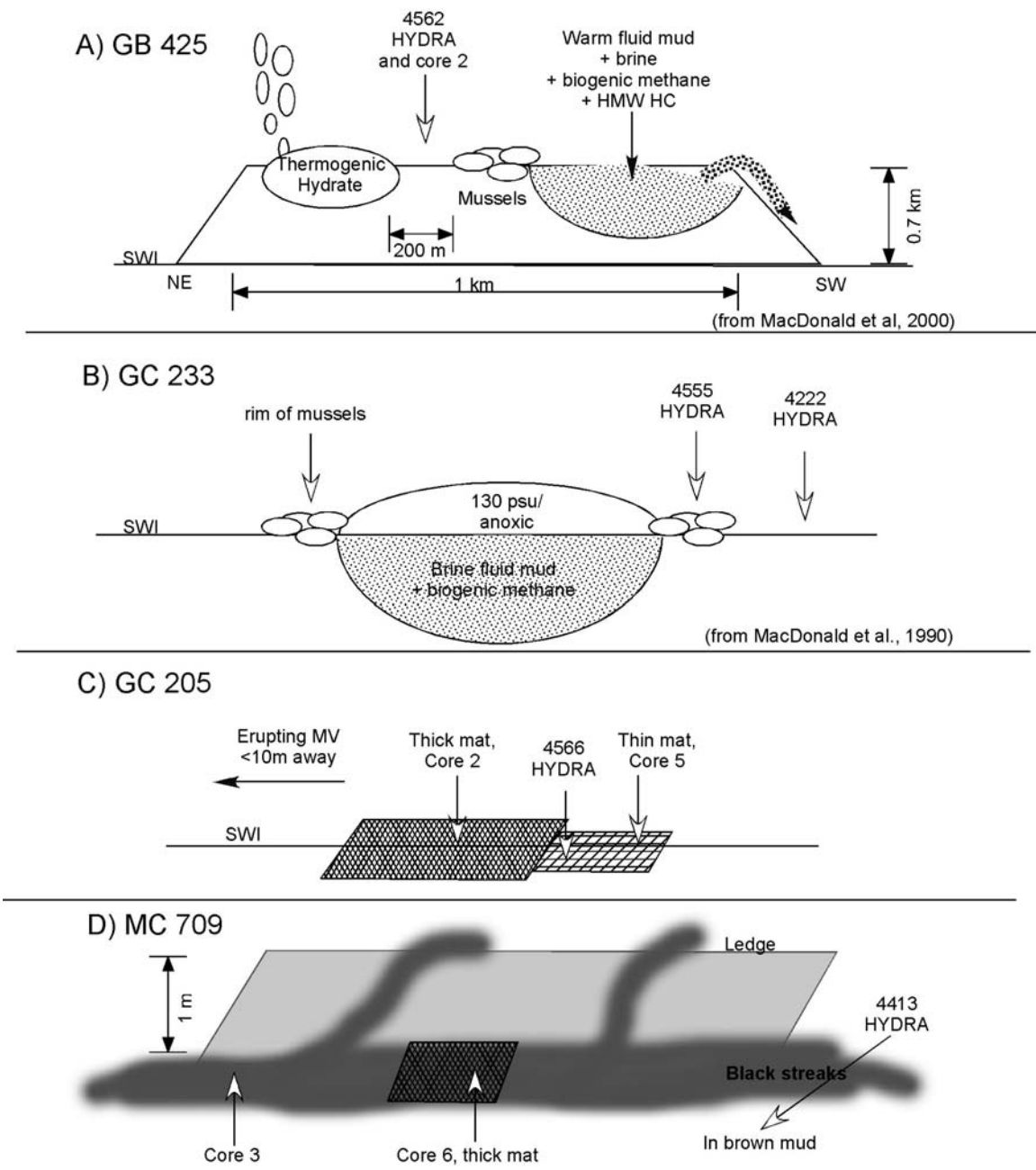
**Table 6- 1: Site, site description, water depth, sample number, and deployment description for samples in this chapter.**

<b>Site</b>	<b>Site description</b>	<b>Water depth (m)</b>	<b>Dive #-sample method</b>	<b>Deployment description</b>
GC 233	Brine pool	650	4222-HYDRA 4555-HYDRA	outside mussels within mussels
GC 205	mud volcano	958	4566-HYDRA 4566-core 2 4566-core 5	Outside bacterial mat patch Thick bacterial mat Edge of thin bacterial mat
GB 425	Brine	600	4562-HYDRA	In gray mud
MC 118	Brine	740	4413-HYDRA 4412-core 3 4413-core 6	Outside black streaks Within black streaks Within thick bacterial mat and black streaks

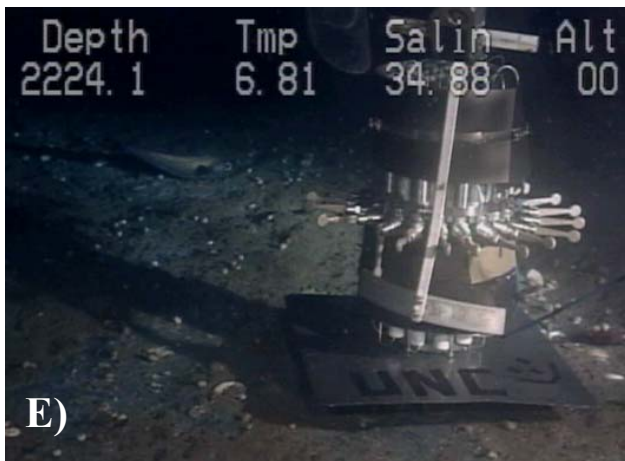
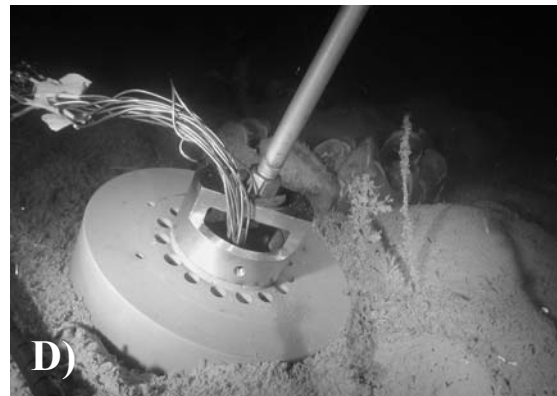
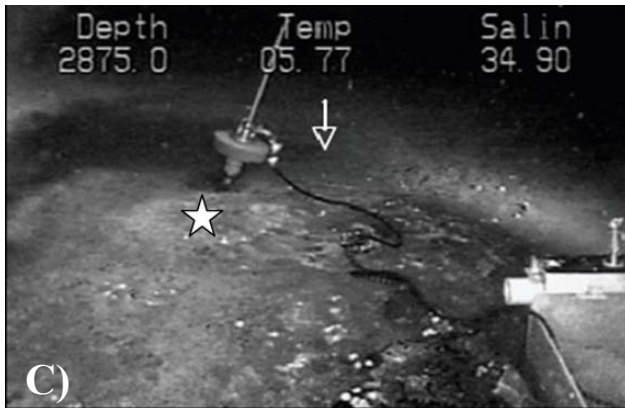
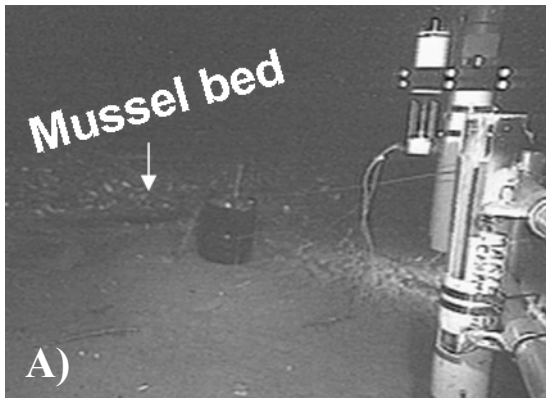


**Fig. 6- 2: Map of Gulf of Mexico sites visited. Garden Banks (GB) 425, Green Canyon (GC) 233, GC 205, and Mississippi Canyon (MC) 709.**





**Fig. 6- 3: Conceptual picture of surrounding environment at A) GB 425, B) GC 233, C) GC 205, and D) MC 709. SWI = sediment water interface and MV = mud volcano.**



**Fig. 6- 4: At GC 233, A) HYDRA was deployed on edge of the mussels (dive 4222) and B) HYDRA was deployed within the mussels (dive 4555). C) At GC 205 (dive 4566), HYDRA was deployed in a thin bacterial mat and two cores were also collected; core 5 was on the outside edge of the bacterial mat (shown with arrow) and core 2 was within the thick mat (shown with star). D) At GB 425 (dive 4562), HYDRA was deployed in floccy gray sediment. E) MC 709 (dive 4413), HYDRA was in gray mud with sparse clam shells present.**

## 2.2. Sample collection

Pore-fluids were collected by an *in situ* pore-fluid collection device named HYDRA and with sediment push cores. HYDRA is thoroughly explained in chapter 2 of this dissertation and so is only briefly explained here. It collects discreet pore-water samples through filtered intake ports every 5 cm and stores them in stainless steel sample chambers. The intake ports are housed along a 50 cm stainless steel shaft (shown deployed in sediments in Fig. 6-4). Once on the ship, the pore-fluids are collected into evacuated vials.

For all dives, except dive 4222, configuration 2 of HYDRA was used. Therefore, the sample and flush chambers had high pressure valves to retain samples at *in situ* pressures and prevent degassing during ascent through the water column (chambers and valves shown in Fig. 6-4e). However, for dive 4222, configuration 1 was used that did not have the high pressure valves and the methane concentrations should be regarded as minimums.

Pore-fluids were also collected from submersible collected sediment push cores. Cores were sectioned every 3 cm and two different pore-water extraction methods were employed. For the first method, each core section was sub-sampled by collecting a 6 mL sediment plug with a cut-off syringe. The plug was placed into a glass serum vial, capped, and stored frozen for future analysis of methane concentrations, stable carbon isotopes, and porosity. Remaining sediment from each section was then collected into 15 mL centrifuge tubes and frozen for later analysis of sulfate and chloride concentrations. This method was employed for cores with dives numbers 4555, 4566, and 4562. For cores 4412-c3 and 4413-c6, a second method was employed to extract the pore-water. For these cores, each 3 cm sediment section was placed into a Reeburgh-type squeezer and the pore-waters extracted from the sediments (Reeburgh, 1967). The resultant water was placed into evacuated glass serum

vials and frozen for future methane concentration and isotope measurements and dissolved inorganic carbon isotope measurements. Squeezing is not an ideal method for measuring methane concentrations because of the large amount of manipulation of the samples. So, from these cores, the methane concentrations should be regarded as minimum values.

### 2.3. Analytical methods

Methane concentrations were measured at sea on a Shimadzu Mini II gas chromatograph (GC). Ten mL of methane-free deionized water was added to each sample vial to displace 10 mL headspace needed for the GC injection. Samples were analyzed by head space extraction. Integrated areas were compared to standards (101.6 ppm CH<sub>4</sub>). Sulfate and chloride concentrations were measured on a Dionex 2010i ion chromatograph (Crill and Martens, 1983). Carbon stable isotope ratios were obtained at our UNC-Chapel Hill laboratory by isotope ratio monitoring using a 5890 Hewlett-Packard gas chromatograph (Palo Alto, CA), coupled to Finnigan MAT 252 isotope ratio mass spectrometer (Thermo Finnigan, Bremen, Germany) via a combustion interface (GC-C-IRMS) as described in Rice et al. (2001). Results are reported using the standard “ $\delta$ ” notation,

$$\delta^{13}\text{C} (\text{‰}) = [R_{(\text{sample})}/R_{(\text{PDB standard})} - 1] \times 1000 \quad (1)$$

where R is the ratio of the heavy to light isotope. The precision for replicate measurements of single samples was  $\pm 3$  percent for sulfate, chloride, and methane concentrations. Total organic carbon (TOC) concentrations and isotopes were run on an Elemental Analyzer coupled to the Finnigan Mat Isotope Ratio Mass Spectrometer (EA-IRMS). For these measurements, sediments were frozen, lyophilized, ground, and  $\sim 30$  mg aliquots weighed out into aluminum boats. Each sample was loaded onto the EA-IRMS, combusted and ran through an oxidation and reduction column.

### 3. RESULTS

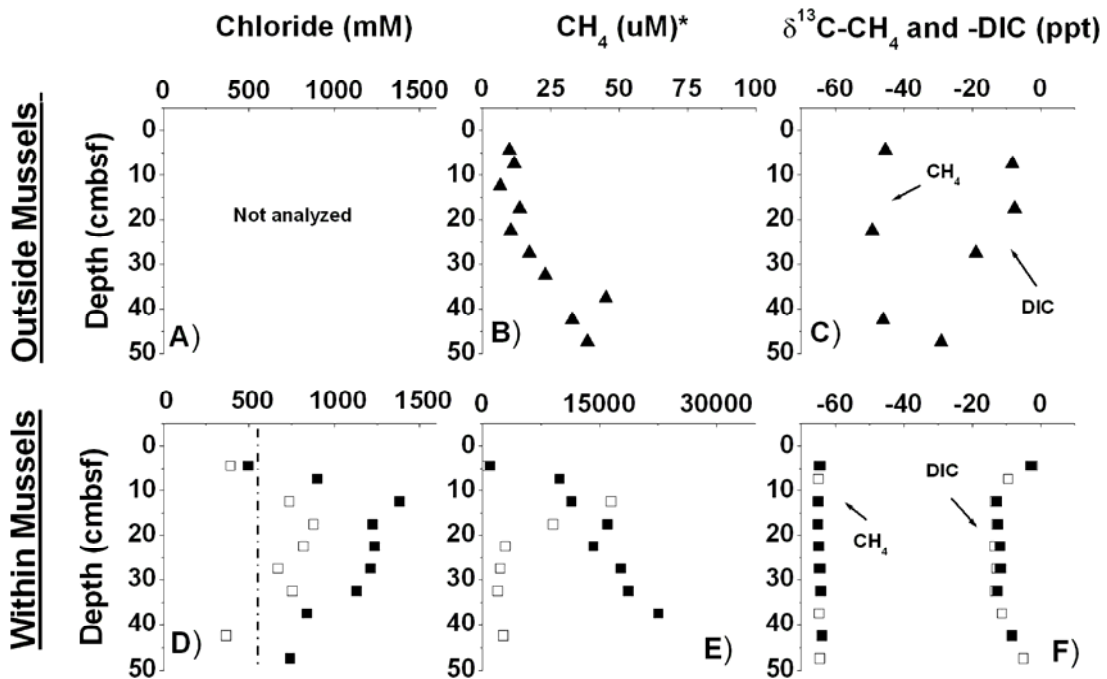
#### 3.1. Notes on HYDRA

Chloride and methane concentrations were measured for each HYDRA deployment. However, these concentrations were subjected to a dilution from deionized water present in the instrument during deployment (see Chapter 2). This dilution is typically corrected for by assuming the original salinity of the sample is normal seawater chloride concentrations. However, for the HYDRA samples in this chapter, the dilution correction could not be applied because the original sample salinity was not known. Therefore, the HYDRA chloride and methane concentrations presented here are minimums. These minimums are still reported to illustrate that, even though the pore-fluid samples were possibly diluted, they were still enriched with brine and methane. This dilution does not affect the isotopic composition of the samples since isotopes are not dependent upon concentration. Also, for each depth of HYDRA, two samples were collected; one from a 'flush' chamber and one from a 'sample' chamber (described in chapter 2). Both sample results are reported in the following figures to illustrate the reproducibility of  $\delta^{13}\text{C-CH}_4$  values between the flush and sample chambers and show that the isotopes are not affected by the possible dilution.

#### 3.2. GC 233 Brine Pool

The GC 233 brine pool was sampled with HYDRA both outside and within the mussel bed that rims the pool itself (pictured in Fig. 6-4a and 6-4b). Outside the bed, methane concentrations reached a maximum of 50  $\mu\text{M}$  (Fig. 6-5b). The  $\delta^{13}\text{C-CH}_4$  values averaged  $-46.9 \pm 2.1\text{‰}$  while the  $\delta^{13}\text{C}$  of the dissolved inorganic carbon (DIC) was  $-8\text{‰}$  near the sediment water interface (SWI) and decreased to  $-29\text{‰}$  (Fig. 6-5c). Results within the mussel bed were quite different. While the chloride concentrations are considered minimums

due to instrument DI-water dilution, they reached as high as 1500 mM; three times seawater values (Fig. 6-5d). Methane concentrations reached as high as 25,000 uM (Fig. 6-5e). The  $\delta^{13}\text{C-CH}_4$  values averaged  $-64.6 \pm 0.4\text{‰}$  with little depth variation. The  $\delta^{13}\text{C-DIC}$  value was  $-2.6\text{‰}$  at the SWI and immediately decreased to an average value of  $-12.8 \pm 0.8\text{‰}$  until 35 cmbsf where values increased to  $-5\text{‰}$  (Fig. 6-5f).



**Fig. 6- 5: At GC 233, outside the mussel bed (dive 4222), A) chloride concentrations, B) methane concentrations, and C) methane and DIC stable carbon isotope ratios. Within the mussel bed (dive 4555), D) chloride concentrations, E) methane concentrations, and F) methane and DIC stable carbon isotope ratios. For results within the mussels, closed symbols represent sample chambers while open symbols represent flush chambers. \*Note axis change between panels B and E. In panel D, the dot-dash line represents typical seawater chloride concentrations or 550 mM.**

### 3.3. GC 205, GB 425, and MC 709

Besides GC 233, three other brine sites were sampled with both HYDRA and sediment push cores. The results from HYDRA are presented first, followed by core results.

#### 3.3.1. HYDRA

For GC 205, chloride concentrations were below seawater values (seawater contains ~550 mM chloride) until the deepest depths where concentrations reached as high as 1241 mM (Fig. 6-6a). Chloride concentrations in the flush cylinders were lower than those measured in the sample cylinders. Methane concentrations were low and ranged between 0 and 225  $\mu\text{M}$  at 27 cmbsf (Fig. 6-6b). The  $\delta^{13}\text{C}\text{-CH}_4$  values averaged  $-53.8 \pm 3.0\text{‰}$  over the 50 cm depth range (Fig. 6-6c). For DIC, at the SWI, the  $\delta^{13}\text{C}\text{-DIC}$  value was  $-2\text{‰}$  and decreased to  $-19\text{‰}$  at 27 cmbsf (Fig. 6-6c).

For GB 425, at the SWI, chloride concentrations were also below seawater values and became more diluted with DI-water with depth; illustrating that HYDRA diluted the samples (Fig. 6-6d). Methane concentrations were low, ranging between 0 and 151  $\mu\text{M}$  from the SWI to 33 cmbsf (Fig. 6-6e). At the SWI, the  $\delta^{13}\text{C}\text{-CH}_4$  value was  $-46.4\text{‰}$  and decreased to  $-57\text{‰}$  at 32 cmbsf (Fig. 6-6f). For  $\delta^{13}\text{C}\text{-DIC}$ , the value was  $-2\text{‰}$  at the SWI and also decreased to  $-7.3\text{‰}$  at 27 cmbsf (Fig. 6-6f).

For MC 709, chloride concentrations were not measured in the HYDRA pore-fluids (Fig. 6-6g). Methane concentrations reached as high as 6,000  $\mu\text{M}$  and exhibited a concave-down shape (Fig. 6-6h). The methane isotopic composition was  $-47.7\text{‰}$  at the sediment water interface, decreased to  $-55\text{‰}$  at 12.5 cmbsf, and increased to  $-53.6\text{‰}$  at 47.5 cmbsf (Fig. 6-6i). This sub-surface minimum was also exhibited in the  $\delta^{13}\text{C}\text{-DIC}$  values: at the SWI, the

isotopic composition was -1.1‰, decreased to -7.2‰ at 12.5 cmbsf, and then increased to -2.55‰ at 47.5 cmbsf (Fig. 6-6i).

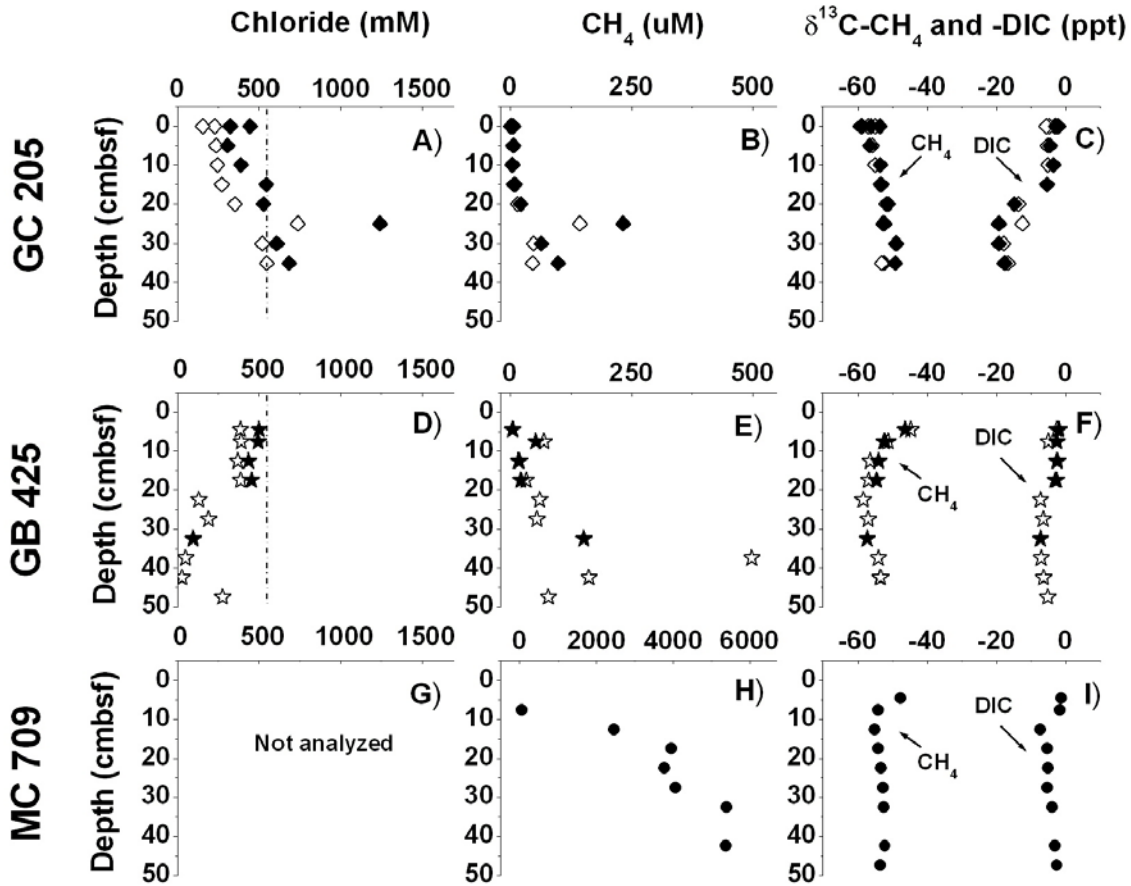


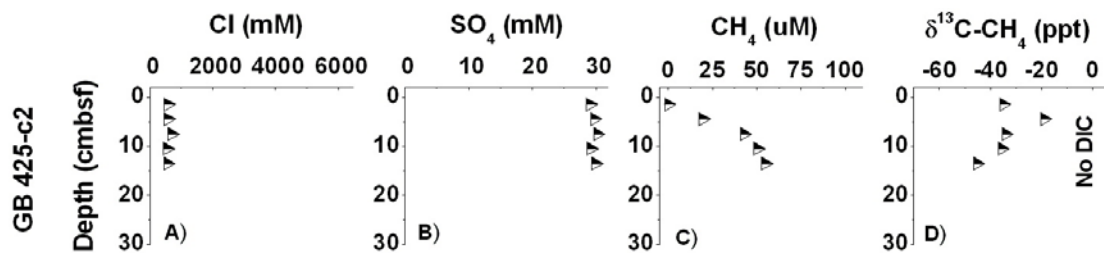
Fig. 6- 6: For GC 205, A) chloride concentrations, B) methane concentrations, and C) methane and dissolved inorganic carbon (DIC) stable carbon isotope ratios. For GB 425, D) chloride concentrations, E) methane concentrations, and F) methane and dissolved inorganic carbon (DIC) stable carbon isotope ratios. For MC 709, G) chloride concentrations, H) methane concentrations, and I) methane and dissolved inorganic carbon (DIC) stable carbon isotope ratios. Open symbols represent ‘flush’ chamber results while filled symbols are the ‘sample’ chamber results. For MC 709, only ‘sample’ chamber pore-fluids were analyzed. For panels A and D, the dot-dash line represents typical seawater chloride concentrations. For panel H, note x-axis scale change.



### 3.3.2. Sediment cores

Along with the HYDRA samples, five cores were also collected at GB 425, GC 205, and MC 709. The core locations compared to HYDRA are shown in Fig. 6-3. Pore-fluids were measured for chloride, sulfate, and methane concentrations and methane and dissolved inorganic carbon (DIC) stable carbon isotope ratios. For some cores, the sediments were also analyzed for total organic carbon (TOC) percent and  $\delta^{13}\text{C}$ -TOC.

For GB 425-core 2 (dive 4562), chloride concentrations averaged  $587 \pm 60$  mM (Fig. 6-7a) and sulfate concentrations averaged  $29.6 \pm 0.5$  mM (Fig. 6-7b). Although the chloride concentrations are slightly enriched above seawater values of 550 mM, the sulfate concentrations are consistent with seawater values of 30 mM. Methane concentrations were low and only reached 55  $\mu\text{M}$  at 13.5 cmbsf (Fig. 6-7c). The isotopic composition of this methane exhibited a sub-surface maximum (Fig. 6-7d). At the SWI, the  $\delta^{13}\text{C}$ - $\text{CH}_4$  value was -35‰, increased to -19‰ at 5 cmbsf, and then decreased to -45‰ at the bottom of the core (Fig. 6-7d). The  $\delta^{13}\text{C}$ -DIC values and %TOC were not measured for this core.



**Fig. 6- 7: For GB 425-core 2, A) chloride concentrations, B) sulfate concentrations, C) methane concentrations, and D) methane carbon stable isotope values. Dissolved inorganic carbon (DIC) stable isotopes were not measured.**

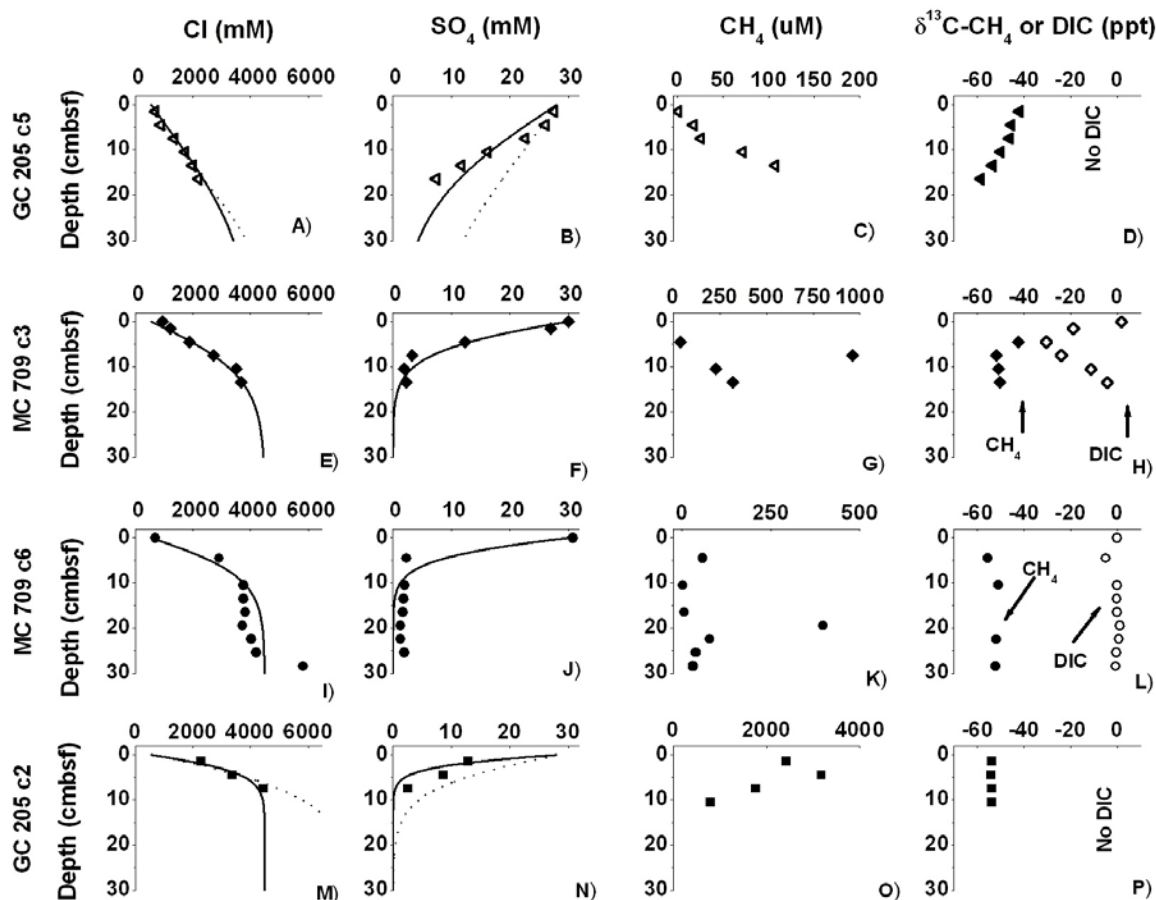
For GC 205-core 5, chloride concentrations increased from 693 near the SWI to 2201 mM at 16.5 cmbsf (Fig. 6-8a). Within this same depth interval, sulfate concentrations decreased from 27.6 to 7.4 mM (Fig. 6-8b). Methane concentrations increased steadily with core depth and reached 233 uM at 16.5 cmbsf (Fig. 6-8c). The  $\delta^{13}\text{C-CH}_4$  values become steadily  $^{13}\text{C}$  depleted with depth: at the sediment-water interface, the  $\delta^{13}\text{C-CH}_4$  value was -42‰ and decreased to -59‰ at 16.5 cmbsf (Fig. 6-8d). The  $\delta^{13}\text{C-DIC}$  values and %TOC were not measured for this core.

For MC 709-core 3 (dive 4412), chloride concentrations increased with core-depth from 1000 mM at the SWI to 3600 mM at 15 cmbsf; 6.5 times normal seawater values (Fig. 6-8e). Sulfate concentrations showed the opposite trend and decreased from 30 mM at the SWI to 2.3 mM at 10 cmbsf (Fig. 6-8f). Methane concentrations were more scattered in this core (probably due to squeezing treatment during collection) but were less than 400 uM except for at 7.5 cmbsf where concentrations reached 900 uM (Fig. 6-8g). The  $\delta^{13}\text{C-CH}_4$  value was -42‰ at the SWI and decreased to -50‰ at 13.5 cmbsf (Fig. 6-8h). The  $\delta^{13}\text{C-DIC}$  value was around 0‰ at the seafloor, reached a minimum of -31‰ at 5 cmbsf, and returned to near 0‰ by 15 cmbsf (Fig. 6-8h). Percent total organic carbon was around 3% and the  $\delta^{13}\text{C-TOC}$  ranged from -31.7 to -26.4‰ (data not shown).

For MC 709-core 6, chloride concentrations were also high; ranging from 694 to 5813 mM for the length of the core (Fig. 6-8i). From 4.5 to 43.5 cmbsf, the average chloride concentration was  $4100 \pm 700$  mM ( $n=12$ );  $\sim 7.5$  times as high as normal seawater values. At the SWI, sulfate concentrations were near seawater values and decreased sharply to 2.4 mM at 4.5 cmbsf (Fig. 6-8j). Below this depth, the average sulfate concentration was  $1.7 \pm 0.3$  mM ( $n=11$ ). The methane concentrations were scattered but ranged between 0 and 400 uM

for the length of the core (Fig. 6-8k). The isotopic composition of the methane showed little variation with depth and averaged  $-51.7 \pm 2.1\%$  (Fig. 6-8l). Similarly, little variation was seen in the isotopic composition of the DIC; it averaged  $-1.0 \pm 2.1\%$  (Fig. 6-8l). Percent total organic carbon was between 1-3% and the  $\delta^{13}\text{C}$ -TOC ranged between -33 and  $-27.7\%$  (data not shown).

And finally, for GC 205-core 2, the chloride concentrations ranged from 2278 mM at 1.5 cmbsf to 4460 mM at 7.5 cmbsf (Fig. 6-8m). Sulfate concentrations were low near the SWI, measuring 13 mM, and decreased to 3 mM at 7.5 cmbsf (Fig. 6-8n). Overall, methane concentrations were highest in this core (Fig. 6-8o). Concentrations were 2400 uM within the upper 3 cm of the core, increased to 3200 uM, and dramatically decreased to 1770 and 800 uM for the deeper sections of the core. This concentration trend was consistent with a core that degasses upon ascent through the water column. The  $\delta^{13}\text{C}$ -CH<sub>4</sub> values showed little change with depth and averaged  $-53.9 \pm 0.2\%$  (Fig. 6-8p). The  $\delta^{13}\text{C}$ -DIC values and TOC were not measured for this core.



**Fig. 6- 8: For GC 205-core 5, A) chloride concentrations, B) sulfate concentrations, C) methane concentrations, and D) methane carbon stable isotope values. For MC 709-core 3, E) chloride concentrations, F) sulfate concentrations, G) methane concentrations, and H) methane and dissolved inorganic carbon (DIC) carbon stable isotope values. For MC 709-core 6, I) chloride concentrations, J) sulfate concentrations, K) methane concentrations, and L) methane and DIC carbon stable isotope values. For GC 205-core 2, M) chloride concentrations, N) sulfate concentrations, O) methane concentrations, and P) methane carbon stable isotope values. Symbols represent all measured data. Black solid and dotted lines represent advection model results. Solid lines assume 4500 mM chloride end-member brine while the dotted lines assume 7390 mM.**

## 4. DISCUSSION

Pore-fluid chemical and molecular constituents were measured at four different Gulf of Mexico brine sites to determine the upward brine advection rates and how brine fluids affect biogeochemical processes. Three important observations came out of this data set. 1) In the cores, the chloride depth profiles clearly exhibit upward brine advection and rates of this fluid flow can be calculated. 2) The steep sulfate concentration depth gradients are controlled by a combination of diffusion from seawater, upward advection of no-sulfate brine fluids, and consumption by bacterial sulfate reduction. And, 3) the brine fluids were enriched in methane that exhibited variable  $\delta^{13}\text{C-CH}_4$  values on both a local and regional scale.

### 4.1. Chloride profiles and advection rates

Typically, deep sea sediment pore-fluids exhibit constant seawater chloride concentrations throughout the depths of the cores. However, in the sediments measured in this study, chloride concentrations became increasingly elevated above seawater values with depth as a result of the upward advection of brine fluids. In fact, the chloride concentrations exhibited steep down-core concentration gradients within the upper 50 cm of sediments. Such gradients suggest not only a hypersaline fluid end-member but one that is currently advecting upwards. The exception to this result was the core collected from GB 425, where the brine fluid was missed altogether, probably because the core was collected outside the brine field (Fig. 6-3). This spatial variability illustrates that the brine fluid advection is focused in certain areas of the Gulf of Mexico seafloor.

Since chloride is a conservative tracer, the measured chloride gradients were used to calculate the rate at which this fluid is advecting. At GC 205 and MC 709, an

advection/diffusion diagenetic model was applied to the chloride profiles (Berner, 1980; Albert et al., 1998). At steady state, chloride profiles can be described by an equation that balances molecular diffusion of chloride into the sediments and advection of brine through the sediments:

$$\frac{d}{dx}(\phi D_s \frac{dC}{dx}) = -\phi \mathcal{G} \frac{dC}{dx} \quad (2)$$

where  $x$  is depth in sediment,  $\phi$  is sediment porosity,  $D_s$  is the sedimentary diffusion coefficient for chloride,  $C$  is the chloride concentration, and  $\mathcal{G}$  is the sum of the downward advection due to sedimentation and the upward advection due to migrating brine fluids.

The model parameters are shown in Table 6-2 and discussed here. For both sites, the upper concentration boundary condition was set at the seawater chloride concentration of 550 mM. The lower depth boundary condition was 100 cm. Since we do not know the depth of the source brine, the model was run at different lower depth boundaries. The exercise showed that up to 10 m, the results were similar to 100 cm. The parameters for the lower concentration boundary condition were not as straight forward. For the MC 709 cores, the lower concentration boundary condition was assumed to be 4500 mM because core 6 exhibited an asymptote around this concentration. However, at 30 cmbsf, the chloride concentration increased to almost 6000 mM (see Fig. 6-8j). Since there was only one point this high and many points with concentrations around 4500 mM, it was assumed that the deepest depth sample was altered during sampling, possibly by water evaporation leaving the residual sample more concentrated in chloride. While this sampling artifact should also have been seen in sulfate analysis, the sample was not analyzed for sulfate. The assumption of a lower concentration boundary condition of 4500 mM is supported by the measurement of chloride concentrations of 4300 mM at 8.5 mbsf at a nearby lease block, MC 118 (see

chapter 3). For GC 205, the end-member chloride concentration also had to be assumed because the cores did not penetrate deep enough to reflect a constant concentration. Therefore, the model was run for both 4500 mM, assuming GC 205 is similar to MC 709, and 7390 mM which is the chloride solubility at the *in situ* pressures and temperatures (Lide, 2006-2007).

The end-member concentrations chosen for the modeling work here are much higher than have been previously reported at brine sites. At GC 233 and GB 425, chloride profiles exhibited an asymptote concentration of 2100 mM (Joye et al., 2005). Therefore, it is clear that we do not know what the actual end-member chloride concentration is or how deep it is found and is a subject for future research.

For the model, sediment accumulation rates (SAR) were estimated from values reported for nearby areas. For MC 709, the SAR was assumed to be 0.07 cm/year as measured from 210-Pb inventories from a nearby site in 985 meters water (Yeager et al., 2004). For GC 205, the SAR was extrapolated from work conducted in GC lease blocks 232 and 272 in 600 m of water and was estimated to be 0.02 cm/year (Hackworth, 2004, personal communication).

The remaining model parameters are the chloride and sulfate diffusion coefficients,  $D_0\text{-Cl}$  and  $D_0\text{-SO}_4$ , respectively. The  $D_0$  values are dependent upon pressure, temperature, and viscosity. Since the chloride concentrations were so high, the viscosity of the fluid changed. Therefore, the  $D_0$  values were corrected for pressure, temperature, and viscosity at each depth (see Appendix 6c for detailed description of this correction).

**Table 6- 2: Diagenetic model parameters.**

<b>Model parameters</b>	<b>GC 205</b>	<b>MC 709</b>
Water depth (m)	958	741
Bottom water temperature (dC)	6	7
Upper boundary concentration (mM)	550	550
Upper boundary depth (cm)	0	0
Saturated brine solution (mM)	7385	7382
Lower boundary concentration (mM)	4500	4500 and 7380
Lower boundary depth (cm)	100	100
Sediment accumulation rate (SAR, cm/yr)	0.02 <sup>^</sup>	0.07 <sup>*</sup>
Do-Cl (cm <sup>2</sup> /sec)	1.13E-05	1.17E-05
Do-SO <sub>4</sub> (cm <sup>2</sup> /sec)	5.96E-06	6.16E-06

<sup>\*</sup>(Hackworth, 2004, personal communication)

<sup>^</sup>(Yeager et al., 2004)

After correcting the D<sub>o</sub>-Cl values, the model parameters were applied to equation (2) for GC 205, cores 2 and 5 and MC 709, core 3 and 6. The upward advection rate was varied until a best fit of the theoretical chloride profile to the *in situ* data was achieved. At GC 205, assuming an end-member chloride concentration of 4500 mM resulted in advection rates of 7 cm/year for core 5 and 65 cm/year for core 2 (Table 6-3 and solid lines in Figs. 6-8a and 6-8m). Assuming an end-member chloride concentration of 7400 mM resulted in lower rates; 3 cm/year for core 5 and 31 cm/year for core 2 (Table 6-3 and dotted lines in Figs. 6-8a and 6-8m). At MC 709, the advection rates were 22 cm/year for core 3 and 31 cm/year for core 6 (Figs. 6-8e and 6-8i). These results show that the choice of an end-member chloride concentration makes a significant difference in the overall calculated advection rates. Without additional knowledge about the site, the appropriate advection rate for GC 205 can not be determined. However, this exercise illustrates that the fluids are controlled by advection, that advection rates are rapid and that the advection rates are highly variable between and within sites.



**Table 6- 3: Modeled advection rates for GC 205 and MC 709 cores.**

<b>Site</b>	<b>Core #</b>	<b>End-member chloride concentration (mM)</b>	<b>Advection rate (cm/year)</b>
GC 205	5	4500	7
		7390	3
	2	4500	65
		7390	20
MC 709	3	4500	22
	6	4500	31

#### **4.2. Sulfate profiles and biogeochemical processes**

Down-core sulfate profiles are the result of a combination of diffusion, advection, and reaction processes. At first assessment, the steep sulfate gradients measured in the cores suggest high rates of sulfate reduction (i.e. Fig. 6-8f). However, since brine fluids are thought to be depleted in sulfate, the measured down-core sulfate depletion could also be explained by the upward advection of sulfate-free brine fluids (Joye et al., 2005). To determine how these fluids would affect the sulfate profile, the advection/diffusion chloride model was modified for sulfate (equation 2).

Using the calculated advection rates from the chloride model (Table 6-3) and the viscosity-corrected sulfate diffusion coefficients, the sulfate model resulted in sulfate profiles that represent diffusion and advection while ignoring any reactions such as sulfate reduction (results plotted as black solid and dotted lines in Fig. 6-8). Therefore, if the measured data fall along the modeled sulfate profile, then the data can be explained by upward advection of brine fluids and diffusion of sulfate from the overlying ocean water. However, if the data fall to the left of the modeled sulfate profiles, a consumption reaction is needed such as sulfate reduction. Conversely, if the data fall to the right of the modeled profiles, a production reaction is needed such as bioirrigation.

The results of the sulfate model show that at low advection rates, the modeled sulfate profiles do not explain the measured sulfate profiles as well as they do at higher advection rates. For example, in GC 205-core 5, the measured sulfate concentration data deviate to the left of the modeled sulfate profiles and, depending on which chloride end-member was used, this deviation was quite extreme (Fig. 6-8b). The deviation of the data from the model suggests that advection and diffusion are not the only processes controlling the sulfate concentrations and that bacterial sulfate reduction is occurring. Although rates of sulfate reduction were not measured, high rates are supported by geochemical evidence of the coupled reaction of anaerobic methane oxidation (Figs. 6-8c and 6-8d). Within the zone of sulfate reduction, the methane concentrations exhibit a concave-up profile and the  $\delta^{13}\text{C}\text{-CH}_4$  values become more enriched in  $^{13}\text{C}$  up the core. These trends suggest an important role for anaerobic methane oxidation (AOM), during which the microbes preferentially take up the isotopically lighter methane and leave the heavier methane behind (Alperin et al., 1988). Studies show a viable community of ANME-1 and sulfate reducers within this core (Lloyd et al., 2006). High rates of sulfate reduction are also supported by the observation of thin bacterial mats which oxidize sulfide, a byproduct of sulfate reduction, on the surface of the core. At the low advection rates estimated for GC 205 core 5, biogeochemical processes still play an important role in controlling the sulfate and methane profiles.

While sulfate reduction was needed to explain the sulfate profiles for GC 205 core 5, the good fit between measured and modeled sulfate concentrations suggests that diffusion and advection are the only processes needed to explain the measured sulfate data for MC 709-core 3 (Fig. 6-8f). However, the trends exhibited in the  $\delta^{13}\text{C}$  values of  $\text{CH}_4$  and DIC suggest the possibility of sulfate reduction above 8 cmbsf. The  $^{13}\text{C}$  enrichment in the  $\text{CH}_4$  and DIC

values from 8 cmbsf to the surface suggest that the methane is being oxidized to DIC within this zone (Fig. 6-8h). Since anaerobic methane oxidation is typically coupled to sulfate reduction, the isotopic enrichment further suggests sulfate reduction is occurring which does not support the agreement between the model and measured sulfate data. It is possible that the sulfate reduction is balanced by sulfate production introduced through bioirrigation. Regardless, the dominant processes controlling the sulfate concentration profiles are advection and diffusion.

Deeper in core 3 at MC 709, below the zone of sulfate reduction (8 cmbsf), the  $\delta^{13}\text{C}$  values of  $\text{CH}_4$  and DIC are decoupled (Fig. 6-8h). Typically, methanogenesis is the dominant microbial process below the zone of sulfate reduction and is evidenced with an increase in  $\delta^{13}\text{C}$ - $\text{CH}_4$  values with depth. If methanogenesis occurs via carbon dioxide reduction, this increase with depth is also coupled to an increase in  $\delta^{13}\text{C}$ -DIC values. However, because this coupling was not seen between the  $\text{CH}_4$  and DIC  $\delta^{13}\text{C}$  values below 8 cmbsf and the  $\delta^{13}\text{C}$ - $\text{CH}_4$  values are constant with depth, the constant  $\delta^{13}\text{C}$ - $\text{CH}_4$  values may be the isotopic signature of biogenic methane produced deeper within the brine.

Since brine is thought to be enriched in methane, the increase in methane concentrations with increase in flow rate (Figs. 6-8c, 6-8g, 6-8k, and 6-8o) also supports the possibility of source brine origin for these fluids. The question then becomes, why do the  $\delta^{13}\text{C}$ -DIC values change with depth (i.e. Fig. 6-8h)? The sub-surface minimum in  $\delta^{13}\text{C}$ -DIC could be from incorporation of light carbon from AOM and below this minimum, this  $\delta^{13}\text{C}$ -DIC values may result from a mixing of brine with a  $\delta^{13}\text{C}$ -DIC value of 0‰ and the AOM light carbon. This decoupling between  $\delta^{13}\text{C}$  values of  $\text{CH}_4$  and DIC was also seen at GC 205 (Fig. 6-6c).

While the isotope results complicate interpretation of the processes controlling sulfate and methane in MC 709 core 3, the results of core 6 are clearer. In MC 709 core 6, the modeled sulfate profiles agree with the measured sulfate concentrations and suggest that advection and diffusion are the dominant processes controlling the sulfate concentrations (Fig. 6-8j). The only deviation from this result was at 5 cmbsf where the measured sulfate concentrations were ~27% less than the model results. Since the measured chloride also deviates from the model results ~17%, only ~10% of the measured sulfate profile is not explained by diffusion and advection alone. However, the analytical precision of sulfate and chloride measurements is approximately +/- 3% so the deviation between measured and modeled sulfate results in core 6 is considered negligible. Furthermore, the isotopic composition of methane and DIC do not exhibit any large variations that would result from sulfate reduction. Therefore, for MC 709, advection and diffusion are the dominant processes controlling the sulfate profiles.

GC 205 core 2 exhibited the highest advection rates where brine fluids containing 4300 mM chloride were found within 10 cm of the seafloor (Fig. 6-8m). While advection and diffusion can explain the majority of the sulfate data, depending on the chloride end-member used, sulfate reduction and sulfate production are needed to explain the remainder of the data. Sulfate reduction is not supported based on the methane concentration distribution or stable isotope depth profiles (Figs. 6-8o and 6-8p). Methane concentrations are too high and show too little variation with depth to support sulfate reduction. Sulfate production is supported by the fact that the core was collected within a thick bacterial mat which could supply additional sulfate via sulfide oxidation. However, mats are not known to actively pump sulfate. For

this core, additional information is needed to fully understand the control biogeochemical processes have on the sulfate profile.

### 4.3. Methane enriched brine

By employing the *in situ* pore-fluid collection device and collecting cores, we found that the brine fluids were highly enriched in dissolved methane (Figs. 6-5, 6-6, 6-7, and 6-8). Although such high concentrations have been inferred from the degassing of brine fluids upon core sampler ascent through the water column (MacDonald et al., 1990a), this study documented the highest methane concentrations ever measured at a brine site<sup>3</sup>. This was especially evident at the brine pool, GC 233, where methane concentrations reached values as high as 25,000 uM within the mussel bed and barely reached 50 uM outside of the mussels (Fig. 6-5). It is also important to note that these concentrations are still minimums since HYDRA typically dilutes samples with internal deionized water (see chapter 2). Even though the concentrations were high, they are still less than the equilibrium solubility concentration with respect to pure methane gas bubbles (58,000 uM; Duan and Mao, 2006). Our data show the presence of high concentrations of methane contained within the brine and limited anaerobic methane oxidation. This supports recently reported geochemical data that suggests brine filled sediments could be an important source for methane to ocean waters (Joye et al., in review).

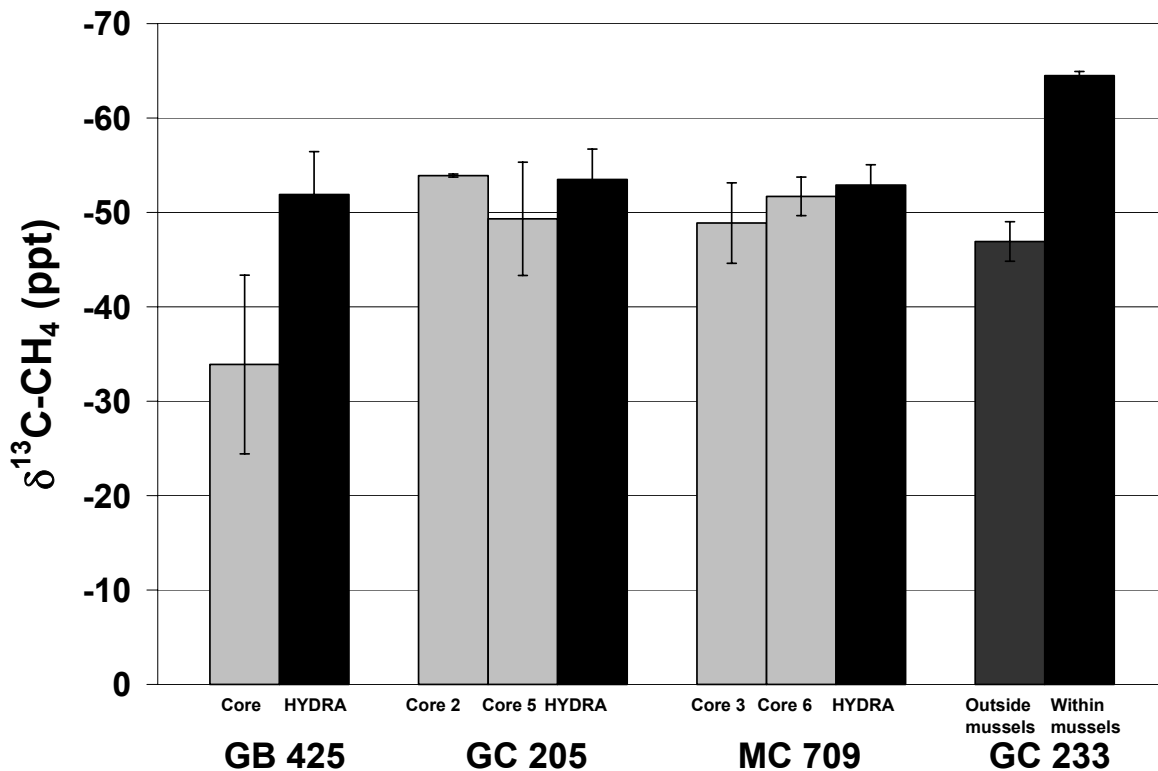
The methane carbon isotope results from both HYDRA and cores showed that the source of the methane contained within the brine varied between and within the different sites (Fig. 6-9). At the GC 233 brine pool, the methane measured within the mussel bed was more biogenic ( $\delta^{13}\text{C-CH}_4 = -64.5 \pm 0.4\text{‰}$ ) than the methane found outside the mussel bed ( $\delta^{13}\text{C-}$

---

<sup>3</sup> In Joye et al. (2005), methane concentrations within the brine fluids are reported in ppm concentrations which can not be directly compared with concentrations measured in this study.

CH<sub>4</sub> = -46.9±2.1‰). This agrees with reported values for brine pool methane (-65‰; MacDonald et al., 1990a; Sassen et al., 1999) and GB 425 mud volcano methane -60‰ (Joye et al., 2005). Between the other three brine sites, not including GC 233, the average δ<sup>13</sup>C-CH<sub>4</sub> value was -51.7±2.5‰ which is isotopically enriched in <sup>13</sup>C compared to the brine pool and surprisingly consistent between the three different brine sites. The exception to this was GB 425-core 2, which was the most enriched methane measured (δ<sup>13</sup>C-CH<sub>4</sub> was -33.9±9.5‰). However, since the chloride concentrations in this core were normal seawater values, its isotopic composition reflects processes outside the brine field.

Why is the methane contained within the brine at GC 233 more isotopically depleted than the three other brine fields? Previous investigators have described GC 233 to be a more quiescent and well established brine (Joye et al., 2005). It is possible that the GC 233 site has had more time for methanogenic populations to establish and contribute isotopically depleted methane. Our data would support this possibility if there was a correlation between the δ<sup>13</sup>C-CH<sub>4</sub> and the advection rates, i.e. the faster fluid flow indicated a newer seep. However, no such correlation exists. Future studies need to independently determine the depth of the source brine (i.e. the salt diapir), the rates of biogeochemical processes within the brine fluids themselves, and the source of the methane.



**Fig. 6- 9: Methane  $\delta^{13}\text{C}$  values averaged over the depth profiles of cores (gray) and HYDRA (black and off-black). Error bars represent  $1\sigma$  of all averaged values.**

## 5. CONCLUSIONS

Overall, the results of the geochemical data show evidence of sulfate reduction and anaerobic methane oxidation in cores with lower brine advection rates compared to cores with higher advection rates. This is possibly because the chloride concentrations exceed the salt tolerances of these microbes or the advection rates themselves are too high to support active sulfate reduction. These analyses highlight the importance of conducting rate measurements within brine-filled sediments. If it is true that biogeochemical processes are inhibited within brine fluids, especially methane oxidation, then brine seeps could be a potentially important source of methane directly to the overlying ocean water.

## 6. REFERENCES

- Albert D. B., Martens C. S., and Alperin M. J. (1998) Biogeochemical processes controlling methane in gassy coastal sediments- Part 2: groundwater flow control of acoustic turbidity in Eckernforde Bay Sediments. *Continental Shelf Research* **18**, 1771-1793.
- Alperin M. J., Reeburgh W. S., and Whiticar M. J. (1988) Carbon and hydrogen isotope fractionation resulting from anaerobic methane oxidation. *Global Biogeochemical Cycles* **2** (3), 279-288.
- Arvidson R. S., Morse J. W., and Joye S. B. (2004) The sulfur biogeochemistry of chemosynthetic cold seep communities, Gulf of Mexico, USA. *Marine Chemistry* **87**, 97-119.
- Berner R. A. H. D. Holland (1980) *Early Diagenesis: A theoretical approach*. Princeton University Press, Princeton.
- Brooks J. M., Bright T. J., Bernard B. B., and Schwab C. R. (1979) Chemical aspects of a brine pool at the East Flower Garden Bank, Northwestern Gulf of Mexico. *Limnology and Oceanography* **24** (4), 735-745.
- Cook D. and D'Onfro P. (1991) Jolliet field thrust fault structure and stratigraphy Green Canyon Block 184, Offshore Louisiana. *Transactions-Gulf Coast Association of Geological Sciences* **XLI**, 100-121.
- Crill P. M. and Martens C. S. (1983) Spatial and temporal fluctuations of methane production in anoxic coastal marine sediments. *Limnology and Oceanography* **28** (6), 1117-1130.
- Duan Z. and Mao S. (2006) A thermodynamic model for calculating methane solubility, density, and gas phase composition of methane-bearing aqueous fluids from 273 to 523 K and from 1 to 2000 bar. *Geochimica et Cosmochimica Acta* **70**, 3369-3386.
- Joye S. B., MacDonald I. R., Montoya J. P., and Peccini M. (2005) Geophysical and geochemical signatures of Gulf of Mexico seafloor brines. *Biogeosciences* **2**, 295-309.
- Joye S. B., Samarkin V. A., Orcutt B. N., Hinrichs K.-U., MacDonald I. R., Meile C. D., Elvert M., and Montoya J. P. (in review) Deeply sourced brines fuel microbial activity along the seafloor in the Gulf of Mexico. *submitted to Nature*.
- Lide D. R. D. R. Lide (2006-2007) *CRC, Handbook of Chemistry and Physics, 87th Ed.* CRC Press, Inc., Cleveland, OH.



- Lloyd K. G., Lapham L., and Teske A. (2006) An anaerobic methane-oxidizing community of ANME-1b archaea in hypersaline Gulf of Mexico sediments. *Applied and Environmental Microbiology* **72** (11), 7218-7230.
- MacDonald I. R., Buthman D. B., Sagar W. W., Peccini M. B., and Guinasso Jr N. L. (2000) Pulsed oil discharge from a mud volcano. *Geology* **28** (10), 907-910.
- MacDonald I. R., Callender W. R., Burke Jr. R. A., McDonald S. J., and Carney R. S. (1990a) Fine-scale distribution of methanotrophic mussels at a Louisiana cold seep. *Prog. Oceanogr.* **24**, 15-24.
- MacDonald I. R., Reilly II J. F., Guinasso Jr N. L., Brooks J. M., Carney R. S., Bryant W. A., and Bright T. J. (1990b) Chemosynthetic mussels at a brine-filled pockmark in the northern Gulf of Mexico. *Science* **248**, 1096-1099.
- Martin R. G. and Bouma A. H. (1982) Active diapirism and slope steepening, Northern Gulf of Mexico Continental Slope. *Marine Geotechnology* **5** (1), 63-91.
- Orcutt B. N., Boetius A., Elvert M., Samarkin V. A., and Joye S. B. (2005) Molecular biogeochemistry of sulfate reduction, methanogenesis, and the anaerobic oxidation of methane at Gulf of Mexico cold seeps. *Geochimica et Cosmochimica Acta* **69** (17), 4267-4281.
- Oren A. (2002) Diversity of halophilic microorganisms: Environments, phylogeny, physiology, and applications. *Journal of Industrial Microbiology and Biotechnology* **28**, 56-63.
- Reeburgh W. S. (1967) An improved interstitial water sampler. *Limnology and Oceanography* **12**, 163-165.
- Roberts H. H. and Carney R. S. (1997) Evidence of episodic fluid, gas and sediment venting on the Northern Gulf of Mexico Continental Slope. *Economic Geology* **92**, 863-879.
- Sager W. W., Lee C. S., MacDonald I. R., and Schroeder W. W. (1999) High-frequency near-bottom acoustic reflection signatures of hydrocarbon seeps on the Northern Gulf of Mexico continental slope. *Geo-Marine Letters* **18**, 267-276.
- Salvador A. (1987) Late Triassic-Jurassic Paleogeography and Origin of Gulf of Mexico Basin. *The American Association of Petroleum Geologists Bulletin* **71** (4), 419-451.
- Sassen R., Joye S., Sweet S. T., DeFreitas D. A., Milkov A. V., and MacDonald I. R. (1999) Thermogenic gas hydrates and hydrocarbon gases in complex chemosynthetic communities, Gulf of Mexico continental slope. *Organic Geochemistry* **30**, 485-497.

Sassen R. and Roberts H., 2004. Site selection and characterization of vent gas, gas hydrate, and associated sediments. DOE Technical Report.

Shokes R. F., Trabant P. K., Presley B. J., and Reid D. F. (1977) Anoxic, hypersaline basin in the Northern Gulf of Mexico. *Science* **196** (4297), 1443-1446.

Sloan E. D. E. D. Sloan (1998) *Clathrate hydrates of natural gases, second edition*. Marcel Dekker, Inc., New York.

Williams D. F. and Lerche I. (1987) Salt domes, organic-rich source beds and reservoirs in intraslope basins of the gulf coast region. In *Dynamical geology of salt and related structures* (ed. I. Lerche and J. J. O'Brien), pp. 751-786. Academic Press, Inc.

Yeager K. M., Santschi P. H., and Rowe G. T. (2004) Sediment accumulation and radionuclide inventories (<sup>239,240</sup>Pu, <sup>210</sup>Pb, and <sup>234</sup>Th) in the northern Gulf of Mexico as influenced by organic matter and macrofaunal density. *Marine Chemistry* **91** (1-4), 1-14.

## **Chapter 7: Spatial variability in microbial activity associated with acoustic wipe-out zones in the northern Gulf of Mexico**

**Abstract-** At cold seep sites, microbial activity is known to be enhanced due to the abundance of reduced compounds entrained in upwardly advecting, hydrocarbon-rich fluids. Yet, it remains to be seen how this microbial activity influences sedimentary gas fluxes and composition on local and regional scales. An integrated biogeochemical and geophysical approach was used to investigate the local and regional role microbial activity plays at hydrate-bearing cold seeps in the northern Gulf of Mexico. Thirty sediment cores were collected both outside and within acoustic wipe-out zones that defined the vent system at Mississippi Canyon Lease Block 118 (MC 118), 100 miles offshore of Louisiana. Variations in depth gradients of sulfate and methane concentrations and stable carbon isotopic composition of methane and dissolved inorganic carbon (DIC) between cores were utilized to quantify differences in microbial activity between coring sites. Three distinct zones featuring low, moderate, and high levels of microbial activity including sulfate reduction, methane production and methane oxidation were recognized. Low microbial activity was always found outside the seismic wipe-out zones whereas both moderate and high microbial activities were found within the wipe-outs, possibly due to the availability of methane and petroleum. Evidence for temporal variability of microbial activity was also found. At sites where microbial activity was high, the carbon isotopic compositions of authigenic carbonates and the DIC pool were similar, suggesting current carbonate precipitation. However, at sites

with only moderate microbial activity the isotopic compositions of the carbonates and DIC were different, suggesting their precipitation at some time in the past when microbial activity was higher. Overall, this study shows that microbial activity is contained within the wipe-out zones, controls the methane flux out of the sediments, and is variable not only spatially but also temporally.

## 1. INTRODUCTION

As a direct link between the deep thermosphere and shallow biosphere, hydrocarbon-rich seeps are recognized as an important source of the powerful greenhouse gas methane today (Kvenvolden, 1993) and in the past (Kennett et al., 2003). Within specific pressure and temperature ranges, methane migrating from deep thermogenic sources may become trapped as part of the largest known methane reservoir, gas hydrate, or expelled through mud volcanoes or bubble vents from the seafloor into the oceans and possibly delivered to the atmosphere (Brewer et al., 2002; MacDonald et al., 2002). If the fluid migration is slow enough, methane may also be quantitatively consumed by microbial oxidation and the resulting dissolved inorganic carbon sequestered within authigenic carbonates (Sassen et al., 2004). To understand the importance of seeps as a methane source, it is imperative to quantify the amount of methane cycling through the seep system. While estimates exist for the standing stocks of methane contained within hydrates (Kvenvolden and Lorenson, 2001; Milkov, 2004) and mud volcanoes (Milkov et al., 2003), less is known about what fraction of this methane is consumed by microbial activity. Quantification of the role of methane oxidation requires knowledge of the spatial distribution of the microbial activity, as it is likely to be patchy within individual seep sites (see Chapter 5).

Microbial activities such as sulfate reduction, anaerobic methane oxidation, and methane production have been shown to be enhanced at seep sites (Aharon and Fu, 2000; Joye et al., 2004; Arvidson et al., 2004; Orcutt et al., 2005; de Beer et al., 2006). Bacterial sulfate reduction quantitatively converts sulfate to sulfide through the oxidation of organic matter. The abundant methane available at some seep sites supports a consortium of sulfate reducers and methanogens that act together to oxidize methane (Hoehler et al., 1994; Boetius et al., 2000; Lanoil et al., 2001). As a direct result of enhanced sulfate reduction, sulfide is then utilized by sulfide-oxidizing bacteria such as *Beggiatoa sp.* to form large mats of filaments on the seafloor (Sassen et al., 1993; Nikolaus et al., 2003). Sulfide and methane are also used by endosymbiotic bacteria living within chemosynthetic organisms such as tubeworms, mussels, and clams. As this sedimentary microbial activity produces dissolved inorganic carbon concentrations that exceed carbonate saturation, authigenic carbonates may precipitate (Ferrell Jr. and Aharon, 1994; Aharon et al., 1997). When dissolved sulfate is exhausted, CO<sub>2</sub>, molecular hydrogen and other substrates then become available for the biogenic production of methane or methanogenesis via acetate fermentation or carbon dioxide reduction. Thus, microbial activity plays a direct role in the formation of the most common seep features such as vast chemosynthetic communities, bacterial mats, and authigenic carbonates.

While microbial activity controls the presence of some seafloor features found at seep sites, the extent of their occurrence is ultimately dependent upon the magnitude of the upward flux of reduced compounds. A conceptual model of the relative flux rates has been proposed that identifies three different vent types based on observations of distinct seep-related features and assumptions about the activity of sedimentary microbial communities

(Roberts and Carney, 1997). First, “mud prone” vents directly inject fluid mud into ocean water and are typically devoid of chemosynthetic communities due to the relatively high fluid flux rates. Second, “transitional” vents are often associated with outcropping hydrate, microbial mats visible on the seafloor, and vast communities of chemosynthetic organisms. Here, the relative fluid flux is slow enough for hydrates to precipitate and for sedimentary microbes to become active and produce substrates needed for the chemosynthetic communities. Although transitional vents typically contain few carbonates, over time, the high rates of microbial activity support the precipitation of abundant carbonates. And finally, the third vent observed is a “mineral-prone” vent where microbial mats are no longer visible and only dead shells and authigenic carbonates remain. For these vents, the relative fluid flux is so low that the microbial communities can no longer thrive. However, biogenic carbonate minerals produced during more active phases are left behind. Since all three of these vent types have been observed at individual seep sites (Roberts and Carney, 1997), the above conceptual model suggests that flux rates wax and wane over time, even over small spatial scales, and suggests that variability in the microbial activity may be tied to such venting variability (Roberts and Carney, 1997).

The purpose of the present study is to understand how spatial variability in upward gas flux and composition may affect observed spatial variability in associated microbial activity. The questions addressed in this chapter are:

- 1) What is the spatial distribution of microbial activity within the MC 118 seep zone compared to non-seep areas outside this zone?
- 2) What carbon source(s) support the sulfate reducers and related microbial consortia?

3) What can the spatial distribution of microbial activities reveal about methane venting history at MC 118?

4) Can the biogeochemical distributions of microbial activity observed at this site be related to the existing Roberts and Carney (1997) vent evolution model?

To address these questions, microbial activity was assessed through pore-water biogeochemical measurements including gas composition in a suite of thirty sediment cores. From each core, pore-waters were analyzed for biogeochemical gradients in sulfate and methane concentrations and the dissolved methane and dissolved inorganic carbon stable isotopic ratios. As exemplified in Alperin et al. (1988) and Whiticar (1999), concentration and isotope depth gradients are suggestive of distinct biogeochemical zones. For example, sulfate concentration depletion with depth is indicative of sulfate reduction and methane concentration increase with depth is indicative of methanogenesis. Due to the kinetic isotope effect, depth gradients in  $\delta^{13}\text{C-CH}_4$  and  $\delta^{13}\text{C-DIC}$  can be used to determine zones of anaerobic oxidation of methane and methane production. As microbes preferentially oxidize the  $^{12}\text{C-CH}_4$ , the residual methane pool becomes enriched in  $^{13}\text{C-CH}_4$ . Therefore, the measurement of an enrichment of  $^{13}\text{C-CH}_4$  up through the sulfate reduction zone suggests anaerobic methane oxidation. Likewise, methanogenesis is associated with an enrichment of  $^{13}\text{C}$  down-core. As methane is produced from the DIC pool, the DIC pool becomes progressively more enriched in  $^{13}\text{C}$  down-core and thereby produces  $\text{CH}_4$  that is more enriched in  $^{13}\text{C}$  down-core. If the DIC and methane isotope pools are decoupled, methanogenesis may proceed via the reduction of other substrates. Therefore, these zonations were used to determine the activity of microbial communities at MC 118.

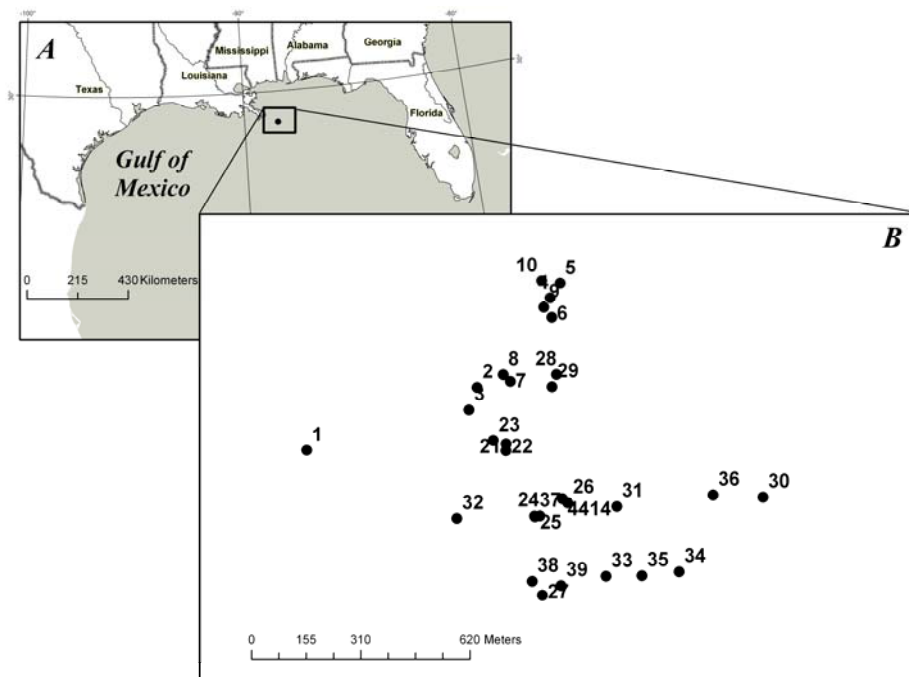
The seep site focused on was Mississippi Canyon Lease Block 118 (MC 118) which covers an area of  $\sim 1\text{-km}^2$  and is known to harbor gas hydrates, authigenic carbonates, and chemosynthetic communities. In addition to these biogeochemical measurements, acoustic measurements by collaborating investigators were utilized to define the spatial scales of the seep system. The MC 118 seep was defined by the presence of acoustic wipe-out zones, thought to signify active venting. Therefore, half of the sediment cores were collected within the wipe-out zones and half were collected outside.

## **2. METHODS**

### **2.1. Geological context**

Our survey area is located in Mississippi Canyon Lease Block 118 (MC 118), located  $\sim 100$  miles offshore of southern Louisiana in 970 meters of water ( $28^{\circ}51.47$ ,  $88^{\circ}29.52$ ; Fig. 7-1). To date, this is the easternmost deposit of gas hydrate in the Gulf of Mexico (Sassen and Roberts, 2004). Bottom water temperatures range from 4.3 to  $5^{\circ}\text{C}$  (Paul Higley, unpublished data). The host sediment is hemiplagic clay with no sand. The regional bathymetry is dominated by the Mississippi Canyon to the west and a smaller, fault controlled, canyon to the east (Woolsey et al., 2005). Hydrate occurs as mounds and veins that form in a circular pattern  $\sim 25$  meters in diameter and massive outcrops (Fig. 7-2; Sassen and Roberts, 2004 and Consortium Sept 2006 cruise report). Chemical analysis of the hydrate-bound gas and vent gas has determined its thermogenic origin (Sassen et al., 2006). Oil and complex chemosynthetic communities such as bacterial mats and clams are present in the sediments. MC 118 has been chosen as the site for a long term gas hydrate monitoring station by the Gulf of Mexico Gas Hydrate Research Consortium.





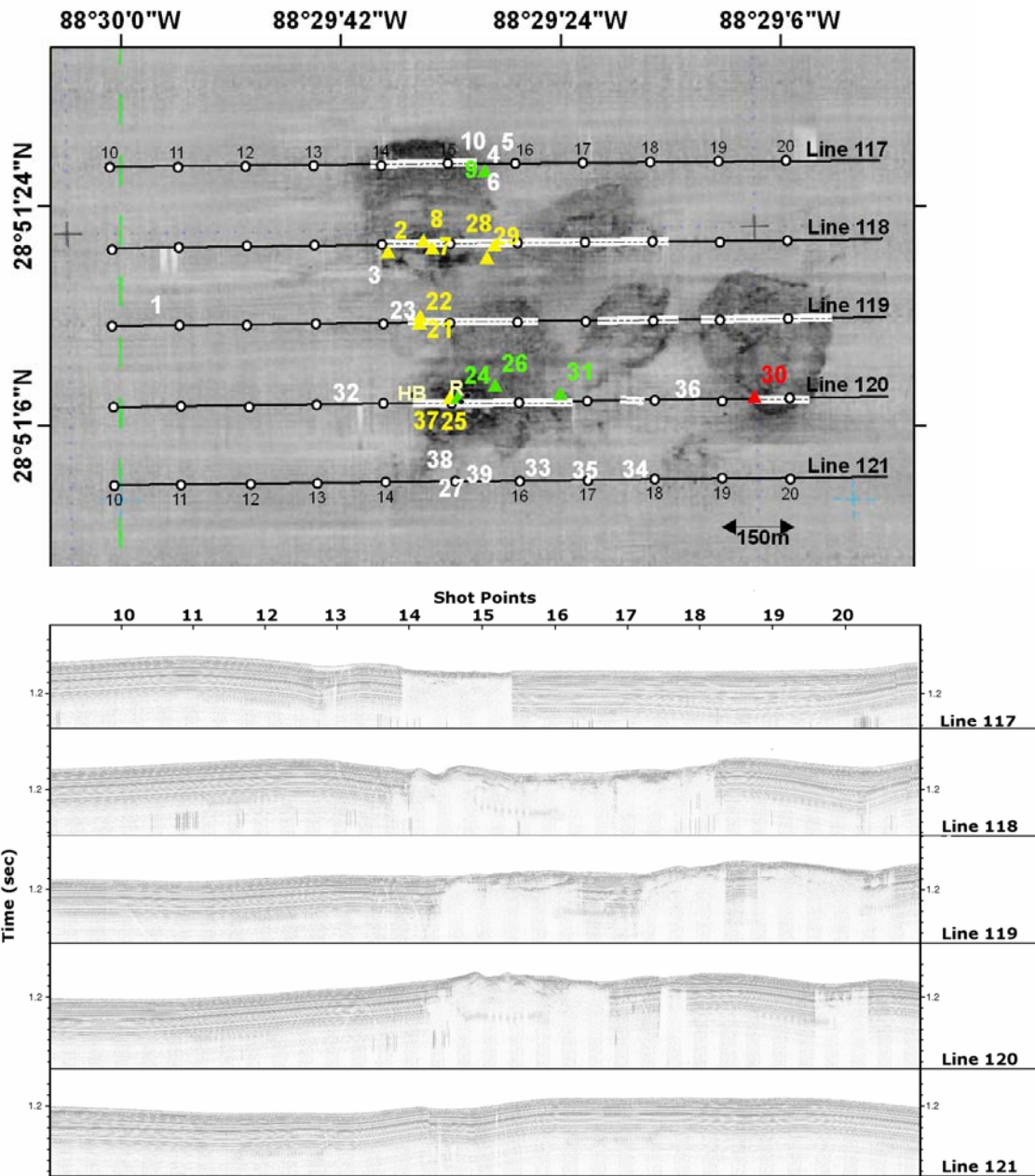
**Fig. 7- 1: A) Gulf of Mexico showing Mississippi Canyon 118, water depth 970 meters. B) Location of all sediment cores at MC 118. Dots represent physical location of cores and numbers represent core numbers.**



**Fig. 7- 2: Seafloor pictures taken at MC 118. A) JSL dive 4414 in 2002. Bottom right hand shows clam shells, diagonally in the middle shows yellow outcropping hydrate with white bacterial mat surrounding it and the top left of the picture is sediment. B) JSL dive 3573 in 2006. Large hydrate outcrop with sediment drape and ice worms.**

## 2.2. Geophysical data

Geophysical data were generated as part of the Gulf of Mexico Gas Hydrate Research Consortium's activities by C+C Technologies Survey Services on May 3, 2005 using a Hugin 3000 automated underwater vehicle (AUV) equipped with 200kHz swath bathymetric system, a dual frequency (120 and 240kHz) side-scan sonar, and a 2-10kHz chirp sonar subbottom profiler (Sleeper et al., 2006). Bathymetry and side-scan sonar data were used to locate vents/seeps as anomalous seafloor features (Fig. 7-3a). These features cover an area 800 m by 1050 m. Survey lines 117-121 are 200 m apart (Fig. 7-3). Along the survey lines, shot points every 150 m denote where sub-bottom chirp profiles were taken. The results show several acoustic wipe-out zones used to target core sites (Fig. 7-3b).



**Fig. 7- 3: Geophysical maps of MC 118. A) Side scan sonar plan view of MC 118. Superimposed are acoustic lines 117-121 with shot points 10-20 (white circles) for reference. White segments along acoustic lines represent the wipe-out zone regions, detailed in B. Colored numbers and symbols represent cores collected; white and red, yellow, and green exhibit microbial activity that is low, moderate, and high, respectively. The positions of white cores are under the white numbers while other core positions have symbols. Off-white letters “HB” and “R” along acoustic line 120 refer to areas of outcropping hydrate as shown in Fig. 7-2b. B) Chirp sub-bottom profiles for acoustic lines 117-121 with shot points for reference. The wipe-out zones are the areas missing visible stratified sediments, such as the region on line 117 between shot points 13.8 and 15.4. Notice that line 119 and 120 each have 3 wipe-out zones.**

### **2.3. Core collection**

Thirty cores were collected at MC 118; one push core and 29 gravity cores. The push core (PC4414) was collected in August 2002 with the Johnson Sea-Link manned submersible deployed from the Research Vessel (R/V) Seward Johnson. The dive site contained outcropping hydrate, bacterial mats, and clam shells. The push core was collected ~2 meters from hydrate outcrop using 30 cm long, 5 cm diameter Lexan core barrels (28°51.1319N, 88°29.5502W). The twenty-nine gravity cores were collected on two cruises in May and October 2005 off the R/V Pelican (operated by Louisiana University Consortium). Previously collected chirp sonar sub-bottom profile data (Fig. 7-3b) was used to target core positions. However, exact core positions were determined by triangulating three surface positions during the May deployment and are given in Appendix 7d. In October, an ultra short baseline transponder (USBL; LinkQuest Inc., California, USA) was connected to the core barrel wire to target exact locations. Accuracy of USBL is estimated to be better than 8 meters (Paul Higley, personal communication).

### **2.4. Core sectioning**

The push core was sectioned every 2-3 cm and pore-waters were expressed by pressure filtration (Reeburgh, 1967). Two-milliliters of pore-water was stored at 4°C in 2 mL o-ring sealed plastic microcentrifuge tubes and frozen for later analysis of dissolved sulfate and chloride by ion chromatography (Crill and Martens, 1983). The remaining pore-water volume was placed in evacuated glass vials for determination of dissolved inorganic carbon (DIC) stable carbon isotope ratios. Remaining sediment patties from the pressure filtration were frozen in plastic bags for future determination of total organic carbon (TOC) concentrations and stable carbon isotope ratios.

The remaining 29 cores were collected as gravity cores off the side of the ship. Once the cores were retrieved, they were sliced lengthwise; one half was used for core descriptions (data not presented here) and the other half sampled for geochemistry. Of the 29 cores collected, two did not return sediment but contained carbonate rocks and are still included in the results. For the other 27 cores, they were sub-sampled every 50 cm using 3 mL cut-off plastic syringes to collect sediment plugs (6-9 mL). Sectioned intervals were about 5 cm. Plugs were then placed into 30 mL glass serum vials, capped, and frozen for future analysis of methane concentrations, stable carbon isotope ratios, and porosity. Remaining sediment from each interval was then collected into two-15 mL centrifuge tubes and frozen for later analysis of pore-water ion (sulfate, chloride, nitrate, phosphate, and ammonium) concentrations and dissolved inorganic carbon (DIC) stable carbon isotope compositions. Immediately back at the laboratory (<3 days after cruise), tubes were thawed and centrifuged at 3000xg for 5 minutes. Resultant supernatant from one set of tubes was transferred to 2 mL o-ring sealed plastic microcentrifuge tubes and frozen for future analysis for ion concentrations. The supernatant from the other set of tubes was injected into evacuated 7 mL glass serum vials and saved for determination of DIC stable carbon isotope compositions at the Florida State University isotope laboratory.

## **2.5. Analytical methods**

Core sub-sections were measured for dissolved methane concentrations on a Shimadzu Mini II Gas Chromatograph (GC). A 5 mL gas aliquot was needed for each GC injection. To ensure no isotopic fractionation while collecting sample aliquots, each sample vial was injected with 10 mL of methane-free deionized water to displace 10 mL headspace needed for GC injections. Dissolved gas was extracted following agitation of the sample vials. Five

milliliter headspace aliquots were then taken and injected into the GC external sample loop (1 mL). Constant volume samples were then carried into the GC with a helium stream. Peak areas were integrated and compared to Scotty methane standards (101.6 ppm CH<sub>4</sub>). Methane concentrations were calculated as presented in Chapter 2, equation 3.

Aliquots of the remaining methane and previously prepared dissolved inorganic carbon (DIC) samples were then analyzed for stable carbon isotope ratios using a gas chromatograph-isotope ratio mass spectrometer (GC-IRMS) with a Hewlett-Packard 5890 GC equipped with a 6 m Poroplot Q column set at 35°C and a Finnigan Mat Delta S at Florida State University. Results are reported using the standard “del” notation,  $\delta^{13}\text{C} (\text{‰}) = (R_{(\text{sample})}/R_{(\text{PDB standard})} - 1) * 1000$ , where R is the ratio of the heavy to light isotope. DIC samples were prepared by adding H<sub>3</sub>PO<sub>4</sub> to release the DIC from solution. Microliter volumes of headspace gas were directly injected onto the GC column and introduced to the mass spectrometer. Methane and carbon dioxide standards were run to calibrate the GC-IRMS.

Sulfate and chloride concentrations were measured by diluting 100 µL of sample with 10 mL carbonate buffer eluent and injecting 1 mL into a Dionex Ion Chromatograph. Standards ranging from 10-100% seawater were run for calibration curves each day and sample concentrations were determined from this curve.

Sediment patties were freeze-dried and ground for determination of total organic carbon concentrations and stable carbon isotope ratios. Approximately 30 mg of sample was vapor acidified with 12 M HCl for 12 hours to release carbonates and then introduced by flash combustion into a Carlo Erba Elemental Analyzer and resultant carbon dioxide flushed into the GC-IRMS system as described above.

Nutrients (nitrate/nitrite, phosphate, and ammonium) were measured on a Lachat QuickChem 8000 autoanalyzer using colourmetric techniques. Dilutions of 48 $\mu$ M ammonium, 8 $\mu$ M phosphate, and 4 $\mu$ M nitrate+nitrite standards were run for the standard curve. Nutrient concentrations were only measured on the May 2005 cruise samples (core numbers 1-10).

Carbonate nodules and shell fragments were hand-picked from cores and stored frozen for stable carbon isotope ratio analysis. At the Florida State University Isotope Lab, the nodules and shells were rinsed with tap water and then dried at 60°C for 12 hours. Samples were then ground and about 0.5 grams placed into a 20 mL glass serum vial, stoppered and capped. Then, each vial was flushed with nitrogen for a few minutes and ~1 mL of 85% phosphoric acid was added to fully convert the sample as CO<sub>2</sub> gas for several hours while shaking. Five microliters of the evolved CO<sub>2</sub>/N<sub>2</sub> gas mixture was then directly injected into the mass spectrometer for isotopic analysis. Samples were run in duplicate.

The stable carbon isotope ratio were also determined on the disseminated carbonate found in whole sediments. Disseminated carbonates are defined as all carbonate that evolves as CO<sub>2</sub> when acidified. After sediments were freeze dried, ~1g was placed into a serum vial. The vial was capped and nitrogen gas flushed through the vial. Then, the vial was injected with 1 mL of 10% H<sub>3</sub>PO<sub>4</sub> and shook for 3 hours to evolve the CO<sub>2</sub> gas. Headspace gas aliquots (100  $\mu$ L) were then directly injected into IRMS for determination of the stable carbon isotope ratio of the disseminated carbonate.

### **3. RESULTS**

A total of thirty cores were collected at MC 118 to contrast and compare the spatial distribution of microbial processes outside and within surface sediments above acoustic

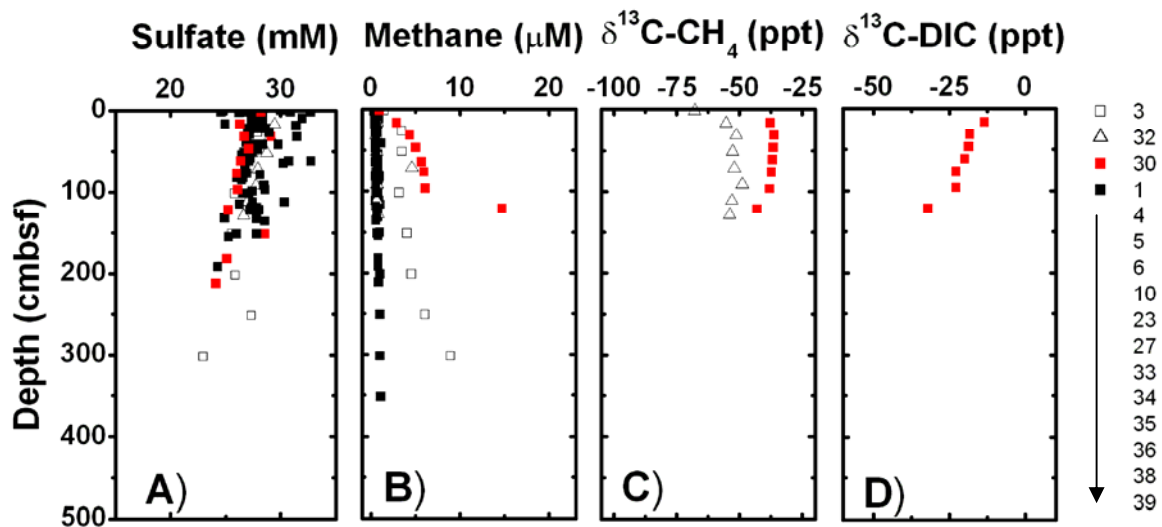
wipe-out zones. Sixteen cores were collected outside and fourteen cores were collected within the wipe-out zones. Of the 14 collected within the wipe-out zones, 2 cores did not collect sediments but were still included in the analysis. Petroleum was only observed visually in cores within wipe-out zones. All cores fell into one of three microbial activity groups as defined by sulfate and methane concentration depth gradients, sulfate-methane interface (SMI) depths, and methane concentrations. In some cases, the sulfate-methane interface depths were not reached in the low and moderate activity cores. Therefore, these SMI depths were extrapolated assuming linear sulfate gradients. The defining gradients for each group are discussed below. The low activity group was collected outside the wipe-out zones whereas the moderate and high activity groups were collected from sediment above the wipe-out zones.

### **3.1. Low microbial activity cores**

The low activity group was defined by sulfate concentration gradients that averaged  $28 \pm 15$   $\mu\text{M}/\text{cm}$  and ranged from 11-63  $\mu\text{M}/\text{cm}$ , methane gradients that averaged  $0.01 \pm 0.03$   $\mu\text{M}/\text{cm}$  and ranged from 0.0003-0.115  $\mu\text{M}/\text{cm}$ , sulfate-methane interface (SMI) depths that averaged 1250 centimeters below seafloor (cmbsf) and ranged between 530-2200 cmbsf, and methane concentration maximums  $<15$   $\mu\text{M}$  (Fig. 7-4, Table 7-1). For all sixteen cores (Fig. 7-4), sulfate concentrations ranged between 32 mM at the sediment water interface and 23 mM at 300 cmbsf (Fig. 7-4a). Sulfate concentrations averaged  $27 \pm 3$  mM over all depths. Methane concentrations ranged 0.2-2  $\mu\text{M}$  except for cores 3, 30, and 32 whose methane concentrations reached as high as 15  $\mu\text{M}$  at the bottom of the cores (Fig. 7-4b). Although concentrations in core 30 were  $<15$   $\mu\text{M}$ , they exhibited a concave down profile, indicating possible upward fluid advection. Methane isotopes were only measured in cores 32 and 30



due to limited amount of gas in other cores. For core 32, the  $\delta^{13}\text{C-CH}_4$  value was  $-68\%$  near the sediment water interface and increased to an average value of  $-52 \pm 2\%$  below 16 cmbsf (Fig. 7-4c). For core 30, the isotopic signature was enriched in  $^{13}\text{C}$  and consistent with depth at a value of  $-38 \pm 4\%$  ( $n=7$ ). In this same core, the  $\delta^{13}\text{C}$  values of dissolved inorganic carbon (DIC) were decoupled from the methane values. It became steadily more depleted in  $^{13}\text{C}$  from  $-18$  to  $-32\%$  with depth (Fig. 7-4d). All these cores were collected outside the wipe-out zone, except for core 30 which was located on the border of the south eastern most wipe-out zone (Fig. 7-3a).



**Fig. 7- 4: Low microbial activity cores. Sixteen sediment cores collected outside wipe-out zones, except core 30 that was collected on the edge of a wipe-out zone and is plotted in red (see Fig. 7-3a). Depth dependent profiles are shown of A) sulfate concentrations, B) methane concentrations, C)  $\delta^{13}\text{C-CH}_4$  values, and D)  $\delta^{13}\text{C}$  values of dissolved inorganic carbon (DIC). Thirteen cores with nearly identical profiles are shown as filled black squares, while cores 3, 32, and 30 are shown with the open square, open triangle, and red square, respectively. Isotopic values were not measured for all cores due to lack of gas.**

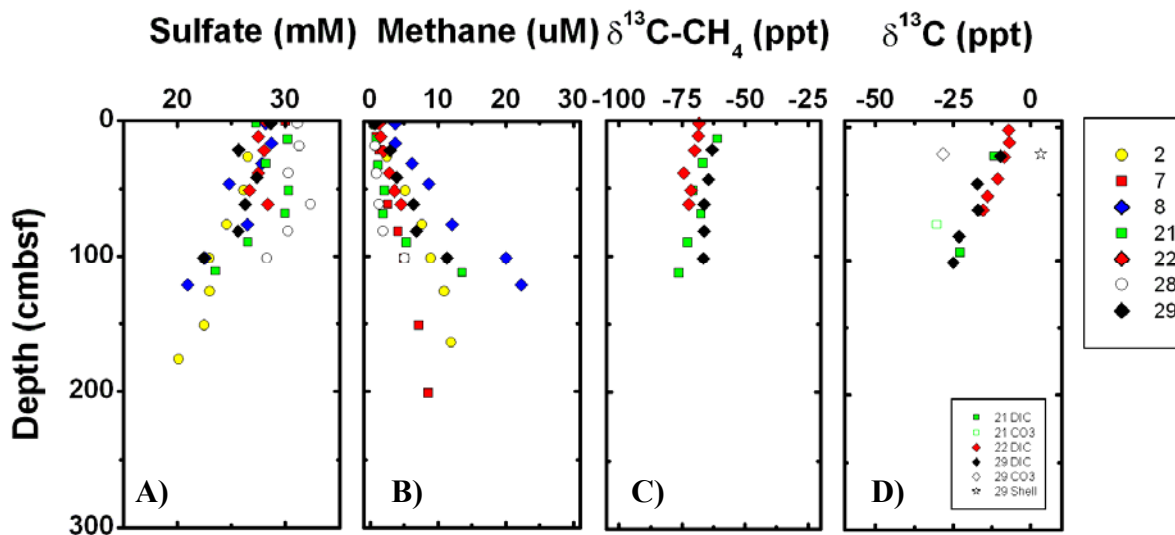
**Table 7- 1: Sulfate gradients calculated from linear fits to sulfate concentration depth profiles. All cores within the low microbial activity group were collected outside the wipe-out zones, except core 30 shown in bold. Core numbers in red were not used for average calculations. Cores within the moderate and high microbial activity groups were collected within the wipe-out zones. Average values are shown in bold, SD= standard deviation. r<sup>2</sup> values were calculated using linear fits to the concentration versus depth profiles. Na = data not available.**

Microbial activity level	Core #	SO <sub>4</sub> gradient (uM/cm)	R <sup>2</sup>	CH <sub>4</sub> gradient (uM/cm)	SMI depth (cmbfs)*	CH <sub>4</sub> maximum (uM)
Low	1	41.72	0.57	0.0005	754	0.9
	3	20.81	0.74	0.0250	1402	8.9
	4	15.05	0.97	0.0011	1838	0.8
	5	21.58	0.93	0.0008	1331	0.8
	6	20.95	0.93	0.0003	1330	0.8
	10	Na				1.1
	27	19.92	0.53	0.0005	1313	0.7
	33	35.61	0.96	0.0016	913	0.7
	32	29.65	0.73	-0.0020	1008	0.8
	34	62.85	0.68	-0.0006	527	0.6
	39	10.83	0.99	0.0038	2222	0.8
	<b>30</b>	<b>26.30</b>	<b>0.82</b>	<b>0.1150</b>	<b>1064</b>	<b>14.7</b>
	<b>Average (SD)</b>	<b>27.75(14.62)</b>		<b>0.01(0.03)</b>	<b>1246(480)</b>	<b>2.6</b>
		<b>23</b>	<b>79.30</b>	<b>0.45</b>	<b>435</b>	<b>0.6</b>
	<b>35</b>	<b>2564.10</b>	<b>0.003</b>	<b>62.16</b>	<b>0.7</b>	
	<b>36</b>	<b>39.28</b>	<b>0.42</b>	<b>762</b>	<b>0.7</b>	
	<b>38</b>	<b>131.41</b>	<b>0.36</b>	<b>152</b>	<b>0.7</b>	
Moderate	2	44.60	0.98	0.07	633	11.9
	7	Na				8.6
	8	73.21	0.92	0.16	407	22.3
	21	107.41	0.57	0.17	313	13.6
	28	59.10	0.60	0.05	568	4.5
	29	68.21	0.82	0.11	432	5.6
	22	66.53	0.40	0.06	445	11.3
	<b>Average (SD)</b>	<b>70.51 (23.32)</b>		<b>0.61 (0.06)</b>	<b>466 (116)</b>	<b>11.1</b>
High	9	172.41	0.98	206.17	51	4285.0
	24	862.07	0.99	3.89	34	56.4
	26	617.28	0.97	46.86	45	2064.4
	31	75.70	0.93	36.63	104	4309.2
	PC4414	943.40	0.97	Na	28	Na
	<b>Average (SD)</b>	<b>534.17 (394.64)</b>		<b>73.39 (90.40)</b>	<b>52 (30)</b>	<b>2678.8</b>

### 3.2. Moderate microbial activity cores

Moderate microbial activity was defined by sulfate concentration gradients that averaged  $70 \pm 21$  uM/cm and ranged from 45-107 uM/cm, methane gradients that averaged  $0.61 \pm 0.06$  uM/cm and ranged from 0.05-0.17 uM/cm, SMI depths that ranged between 313-633 cmbsf, and methane concentration maximums between 5 and 22 uM (Fig. 7-5, Table 7-1). For cores 2, 7, 8, 21, 22, 28, and 29, sulfate concentrations were  $\sim 28$  mM at the sediment water interface and decreased to  $\sim 20$  mM by 150 cmbsf (Fig. 7-5a). Methane concentrations showed the inverse pattern with depth; concentrations were near zero at the surface and increased to  $\sim 20$  uM at 100 cmbsf (Fig. 7-5b). Cores 21, 22, and 29 were analyzed for methane and DIC stable carbon isotope ratios. The  $\delta^{13}\text{C-CH}_4$  values ranged from -61 to -76‰ over all depths, with an average of  $-68.6 \pm 4.1$ ‰ (n=17; Fig. 7-5c). Likewise, the  $\delta^{13}\text{C-DIC}$  values for these three cores were also similar to each other. At the sediment water interface, isotope values were around -10‰ and became  $^{13}\text{C}$ -depleted with depth to -25‰ at 100 cmbsf (Fig. 7-5d).

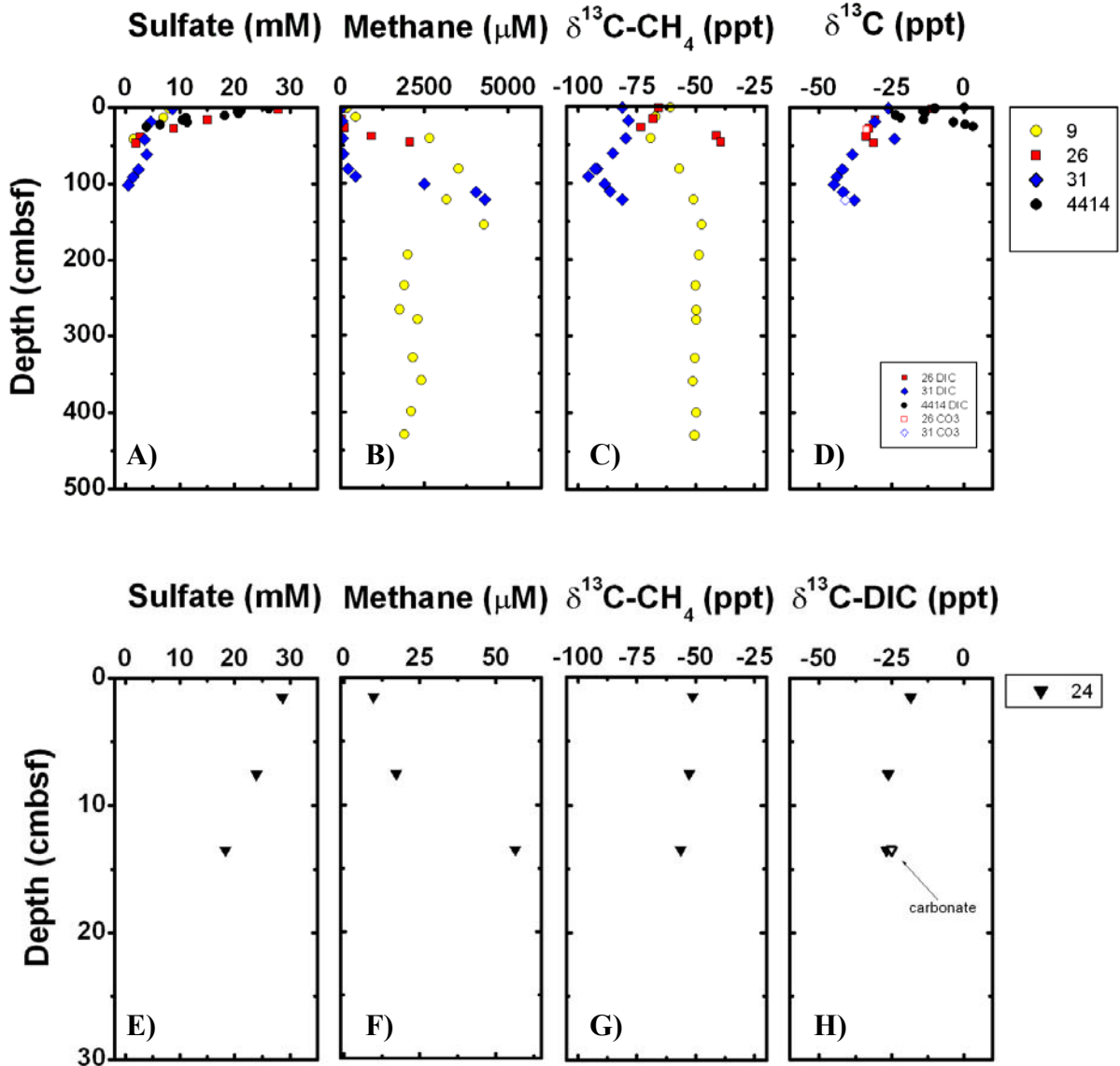
Within the moderate microbial activity group, cores 25 and 37 were included even though coring was attempted and returned little or no sediment during recovery. These cores hit near the center of the acoustic feature on line 120 (Fig. 7-3). In core 25, the core catcher was bent and contained carbonate rocks, suggesting it hit hard bottom. Core 37 also hit hard bottom and the core catcher was caked in dark mud, possibly because it hit hydrate instead of carbonate. Neither core was analyzed further due to lack of material.



**Fig. 7- 5: Moderate microbial activity cores collected within the wipe-out zones. Depth dependent profiles are shown of A) sulfate concentrations, B) methane concentrations, C) methane carbon isotopic compositions, and D) isotopic composition of both dissolved inorganic carbon (DIC), carbonate nodules (CO<sub>3</sub>), and shell.**

### 3.3. High microbial activity cores

High microbial activity was seen in the remaining five cores (9, 24, 26, 31, and PC4414). They were defined by sulfate concentration gradients that averaged  $534 \pm 394$  uM/cm and ranged from 75-943 uM/cm, methane gradients that averaged  $73.39 \pm 90.4$  uM/cm and ranged from 3.9-206.2 uM/cm SMI depths that averaged 52 cmbsf and ranged from 28 to 104 cmbsf and maximum methane concentrations reaching 4300 uM (Fig. 7-6, Table 7-1). Cores 9, 26, and 31 were visibly degassing upon core recovery and therefore, methane concentrations represent minimums, at least for samples with concentrations above ~1200 uM. Above 1200 uM, at 1 atm pressure, methane exceeds equilibrium and comes readily out of solution.



**Fig. 7- 6: High microbial activity cores collected within wipe-out zones. For cores 9, 26, 31, and 4414, depth dependent profiles are shown of A) sulfate concentrations, B) methane concentrations, C) methane carbon isotopic compositions, and D) isotopic composition of both dissolved inorganic carbon (DIC), carbonate nodules (CO<sub>3</sub>), and shell. Core 24 is distinct from these profiles because it was so short; the depth dependent profile is shown of E) sulfate concentrations, F) methane concentrations, G) methane carbon isotopic compositions, and H) isotopic composition of dissolved inorganic carbon (DIC) and carbonate nodule found at 13 cmbsf. Note depth and methane concentration scale changes between A-D) and E-F). The sulfate concentration scale is also different from Figs. 7-4 and 7-5.**

For core 9, sulfate concentrations were around 8 mM at 1.5 cmbsf and decreased to 1 by 42 cmbsf (Fig 6a). Methane concentrations were 190 uM at the sediment water interface and increased to 4300 uM by 120 cmbsf (Fig. 7-6b). Below this depth, concentrations decreased but averaged around  $2000 \pm 200$  uM ( $n=8$ ) for the remainder of the core. The SMI was estimated to be around 50 cmbsf where it coincided with a subsurface minimum  $\delta^{13}\text{C-CH}_4$  value of  $-70\text{‰}$  (Fig. 7-6c). Below the SMI, the isotope ratio became more enriched in  $^{13}\text{C}$  to a value of  $-49.7 \pm 1.1\text{‰}$  ( $n=10$ ), indicating a narrow zone of methanogenesis above a thermogenic source gas from deep below (Fig 6c). In depths above the SMI, the isotope ratio also became enriched in  $^{13}\text{C}$  to  $-60.7 \pm 0.2\text{‰}$ , suggesting anaerobic methane oxidation.  $\delta^{13}\text{C-DIC}$  values were not measured in this core.

For core PC 4414, sulfate concentrations were 26 mM at 1.5 cmbsf and decreased to 4 mM by 26 cmbsf (Fig. 7-6a). Since methane concentrations were not measured, the SMI depth of  $\sim 10$  cmbsf was estimated based on the depth of the minimum  $\delta^{13}\text{C-DIC}$  value of  $-25\text{‰}$  (Fig. 7-6d). Above and below this depth, isotope values become enriched in  $^{13}\text{C}$  to  $\sim 0\text{‰}$ .

For core 31, sulfate concentrations did not show a smooth, linear decrease with depth as the other cores did (Fig. 7-6a). At 1.5 cmbsf, the concentration was low, 8 mM, decreased to 4 mM by 20 cmbsf, stayed consistently  $\sim 4$  mM from 20 to 60 cmbsf, and then decreased to 0.5 mM for the rest of the core. Methane concentrations were 11 uM near the sediment water interface and increased to 4300 uM by the bottom of the core (Fig. 7-6b). The sulfate and methane concentration trends corresponded to a SMI depth of 90 cmbsf where the  $\delta^{13}\text{C-CH}_4$  values exhibited a minimum of  $-95\text{‰}$ . Above and below the SMI depth, the methane became enriched in  $^{13}\text{C}$  to  $-80\text{‰}$  (Fig. 7-6c). The  $\delta^{13}\text{C-DIC}$  values also followed the same trend with

the minimum of -50‰ at the SMI (Fig. 7-6d). Above this depth, the  $\delta^{13}\text{C}$ -DIC reached -25‰ at the sediment water interface and below this depth, the value reached -37‰ (Fig. 7-6d).

For core 26, the sulfate concentrations were 28 mM near the sediment water interface and decreased to 2 mM by 47 cmbsf (Fig. 7-6a). The methane concentrations were 2  $\mu\text{M}$  near the sediment water interface and increased to 2100  $\mu\text{M}$  by 47 cmbsf (Fig. 7-6b). These concentration trends corresponded to a SMI depth of  $\sim 30$  cmbsf (Figs. 7-6a and 7-6b). This depth corresponded to a minimum  $\delta^{13}\text{C}$ - $\text{CH}_4$  value of -73‰ (Fig. 7-6c). Above and below this depth, the  $\delta^{13}\text{C}$ - $\text{CH}_4$  values became enriched in  $^{13}\text{C}$  to -65‰ near the sediment water interface and -40‰ at 50 cmbsf, respectively. The  $\delta^{13}\text{C}$ -DIC also followed the same trend with the minimum -34‰ at the SMI (Fig. 7-6d). Above this depth, the  $\delta^{13}\text{C}$ -DIC reached -11‰ at the sediment water interface and below this depth, the value reached -31‰, at the bottom of the core.

Within the high microbial activity group, core 24 showed some unique trends (Fig. 7-6e-f). This core penetrated only 15-cmbsf and contained oil and carbonate rock on the bottom. Sulfate concentrations decreased with depth but did not deplete by the end of the core (Fig. 7-6e). With this decrease, there was a simultaneous increase in methane (Fig. 7-6f). Yet, methane concentrations were low compared to other cores in this high activity group. However, core 24 exhibited one of the highest sulfate gradients (Table 7-1). At the bottom of this core, the  $\delta^{13}\text{C}$ - $\text{CH}_4$  value was -56‰ (Fig. 7-6g) and the  $\delta^{13}\text{C}$ -DIC value was  $\sim -27$ ‰ (Fig. 7-6h), no clear trend with depth was evident because the core was too short.

### **3.4. Carbonate nodules and shells**

No carbonates were observed outside the wipe-out zones. Within the wipe-out zones, five cores contained carbonate nodules and shell fragments that were individually measured

for their  $\delta^{13}\text{C}$  content (Figs. 7-5d, 7-6d, 7-6h) and summarized in Table 7-2). In the moderate activity group, the carbonate isotope values were  $-28.3 \pm 0.04\text{‰}$  at 18 cmbsf in core 29 and  $-30.3 \pm 0.08\text{‰}$  at 72 cmbsf in core 21 (Table 7-2). In the high activity group, the average carbonate  $\delta^{13}\text{C}$  value was  $-25 \pm 0.1\text{‰}$  at 13 cmbsf for core 24,  $-33.6 \pm 0.28\text{‰}$  at 28 cmbsf for core 26, and  $-40.8 \pm 0.06\text{‰}$  at 123 cmbsf for core 31 (Table 7-2). The shell found in core 29 was isotopically distinct at  $+3.2 \pm 0.04\text{‰}$ . The  $\delta^{13}\text{C}$ -DIC values are also summarized to compare with carbonate values (Table 7-2).

**Table 7- 2: Carbonate, shell, and DIC carbon isotopic signatures for the moderate and high microbial activity groups. Na means shells were not found in cores.**

Activity group	Core #	Depth (cmbsf)	$\delta^{13}\text{C}$ -CaCO <sub>3</sub> (‰; n=2)	$\delta^{13}\text{C}$ -shell (‰)	$\delta^{13}\text{C}$ -DIC (‰)
Moderate	29	18	$-28.3 \pm 0.04$	$+3.2 \pm 0.04$	-8.4
	21	72	$-30.3 \pm 0.08$	Na	-20
High	24	13	$-25 \pm 0.10$	Na	-27
	26	28	$-33.6 \pm 0.28$	Na	-32.6
	31	123	$-40.8 \pm 0.06$	Na	-37.7

Since there were a limited number of carbonate nodules, disseminated carbonates in the whole sediments were also analyzed (Figs. 7-7 and 7-8). On average, the isotopic ratio of the disseminated carbonates was more enriched in  $^{13}\text{C}$  than in the carbonate nodules. This result is most likely due to the presence of shell fragments skewing the values towards 0‰. Future experiments should selectively choose authigenic carbonates from whole sediments to eliminate this potential problem.



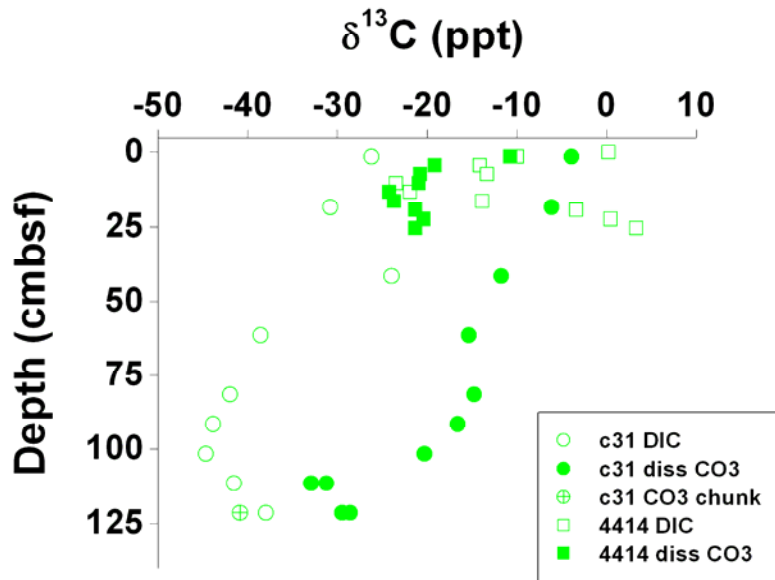


Fig. 7- 7: High microbial activity stable isotopic composition of dissolved inorganic carbon (DIC), disseminated carbonate (diss CO<sub>3</sub>), and carbonate chunk (CO<sub>3</sub> chunk).

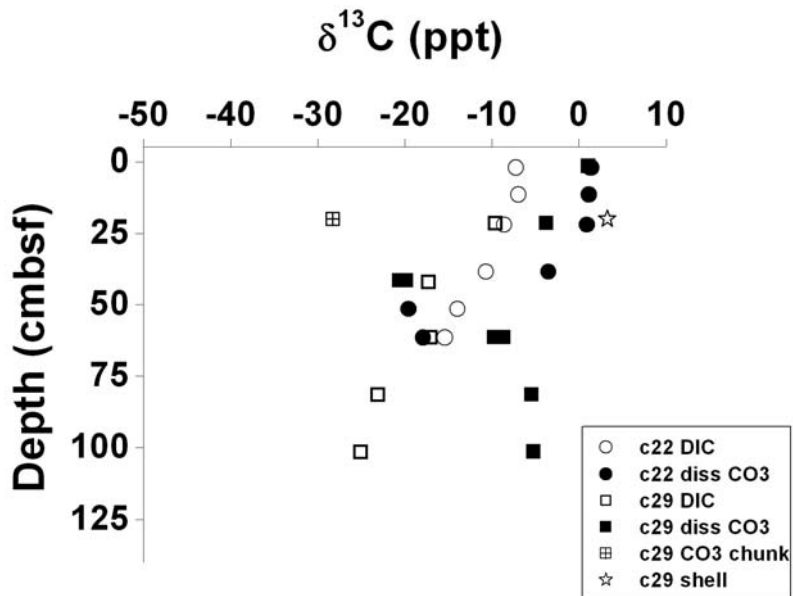
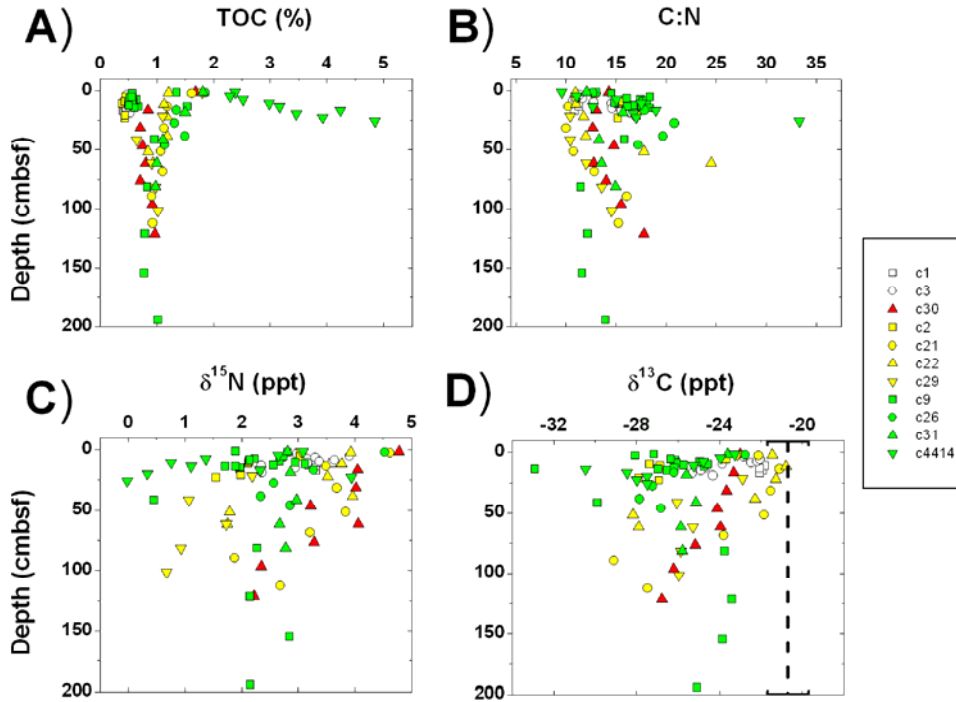


Fig. 7- 8: Moderate microbial activity stable isotopic composition of dissolved inorganic carbon (DIC), disseminated carbonate (diss CO<sub>3</sub>), carbonate chunk (CO<sub>3</sub> chunk), and shell fragment.

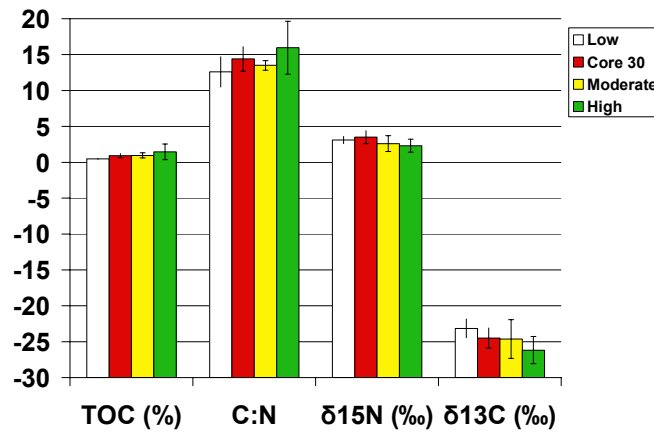
### 3.5. Bulk organic matter chemical composition and stable isotopes

For representative cores within each microbial activity group, the bulk organic matter was evaluated for total organic carbon (TOC) concentrations, C:N ratios,  $\delta^{15}\text{N}$ -total organic nitrogen (TON), and  $\delta^{13}\text{C}$ -TOC (Figs. 7-9 and 7-10). For all cores analyzed, the TOC ranged between 0.4 and 1.8% (Fig. 7-9a). The exception to this was PC4414 where %TOC increased from ~2.5% at the surface to 5% at the 30 cmbsf. C:N varied between 10 and 22, with two outliers in cores 22 and PC4414 reaching up to 34 (Fig. 7-9b). The  $\delta^{15}\text{N}$ -TON values were between 0-5‰ with no clear trends (Fig. 7-9c). And the  $\delta^{13}\text{C}$ -TOC varied between -33 and -22‰ (Fig. 7-9d).

Within each activity group, average values were evaluated (Fig. 7-10). For the low activity group, TOC was  $0.47 \pm 0.04\%$ , C:N of  $12.6 \pm 2.1$ ,  $\delta^{15}\text{N}$ -TON value of  $3.1 \pm 0.5\%$ , and  $\delta^{13}\text{C}$ -TOC value of  $-23.14 \pm 1.3\%$ . For core 30, TOC was  $0.92 \pm 0.3\%$ , C:N of  $14.4 \pm 1.7$ ,  $\delta^{15}\text{N}$ -TON value of  $3.5 \pm 0.9\%$ , and  $\delta^{13}\text{C}$ -TOC value of  $-24.5 \pm 1.4\%$ . For the moderate activity group, TOC was  $0.96 \pm 0.36\%$ , C:N of  $13.5 \pm 0.67$ ,  $\delta^{15}\text{N}$ -TON value of  $2.6 \pm 1.1\%$ , and  $\delta^{13}\text{C}$ -TOC value of  $-24.61 \pm 2.7\%$ . For the high activity group, TOC was  $1.45 \pm 1.1\%$ , C:N of  $15.96 \pm 3.7$ ,  $\delta^{15}\text{N}$ -TON value of  $2.3 \pm 0.9\%$ , and  $\delta^{13}\text{C}$ -TOC value of  $-26.17 \pm 1.9\%$ .



**Fig. 7- 9: Bulk organic matter a) total organic carbon (TOC) percentage, b) carbon to nitrogen ratios, c)  $\delta^{15}\text{N}$ -total organic nitrogen (TON) and d)  $\delta^{13}\text{C}$ -TOC (dotted line represents marine organic matter from Goni et al. (1997)). Open, red, yellow and green symbols represent low, core 30, moderate, and high microbial activity cores, respectively. Colors also correspond to colors of activity groups in Fig. 7-3a.**

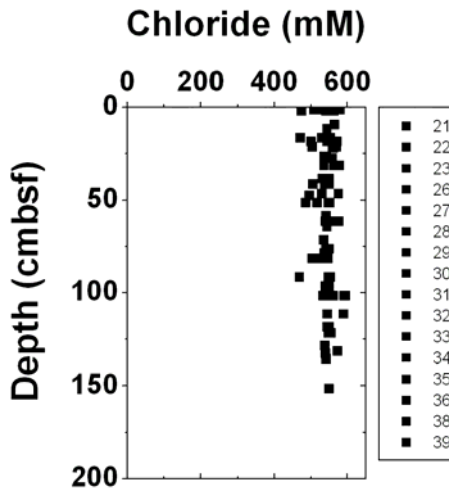


**Fig. 7- 10: Bulk organic matter averages plus standard deviations for total organic carbon (TOC) percentage, carbon to nitrogen ratios,  $\delta^{15}\text{N}$ -total organic nitrogen (TON), and  $\delta^{13}\text{C}$ -TOC. Open, red, yellow and green symbols represent low, core 30, moderate, and high microbial activity cores, respectively. Colors also correspond activity group colors in Figs. 7-3a and 7-9.**

### 3.6. Chloride concentrations

Chloride concentrations averaged  $543.7 \pm 24.7$  mM for all cores (Fig. 7-11). This average value is indistinguishable from the average seawater chloride concentration of 550 mM.

There was no indication of brine fluid advecting from below.



**Fig. 7- 11: Chloride concentrations for most cores.**

### 3.7. Nutrient concentrations

Dissolved ammonium, phosphate, and nitrate/nitrite were measured in cores 1-10 (Fig. 7-12). Overall patterns of nutrient concentrations and wipe-out zones were not as obvious as methane concentrations and stable carbon isotope profiles. However, individual patterns within the data set were seen. For ammonium, sediment seawater interface concentrations exhibited a large range between 26 to 123  $\mu$ M (Fig. 7-12a). Although overlying water concentrations were not directly measured, these values are consistent with an average value of bottom water of 65  $\mu$ M (Joye et al., 2005). Concentrations increased down-core for most cores but core 9 was consistently  $\sim 53 \pm 14$   $\mu$ M until 300 cmbsf where concentrations increased to 350  $\mu$ M within 150 cmbsf. Phosphate concentrations for cores 1-8 were all  $< 5$   $\mu$ M, yet

concentrations were shifted to  $\sim 10$   $\mu\text{M}$  for cores 9 and 10 at the seawater interface (Fig. 7-12b). Core 10 remained at this value down-core but core 9 increased to 25  $\mu\text{M}$  by 350 cmbsf, although there is scatter in the data. Nitrate/nitrite concentrations in all cores were between 0-30  $\mu\text{M}$  (Fig. 7-12c). Cores 7, 8, and 9 exhibited subsurface maxima of 15  $\mu\text{M}$  around 50 cmbsf.

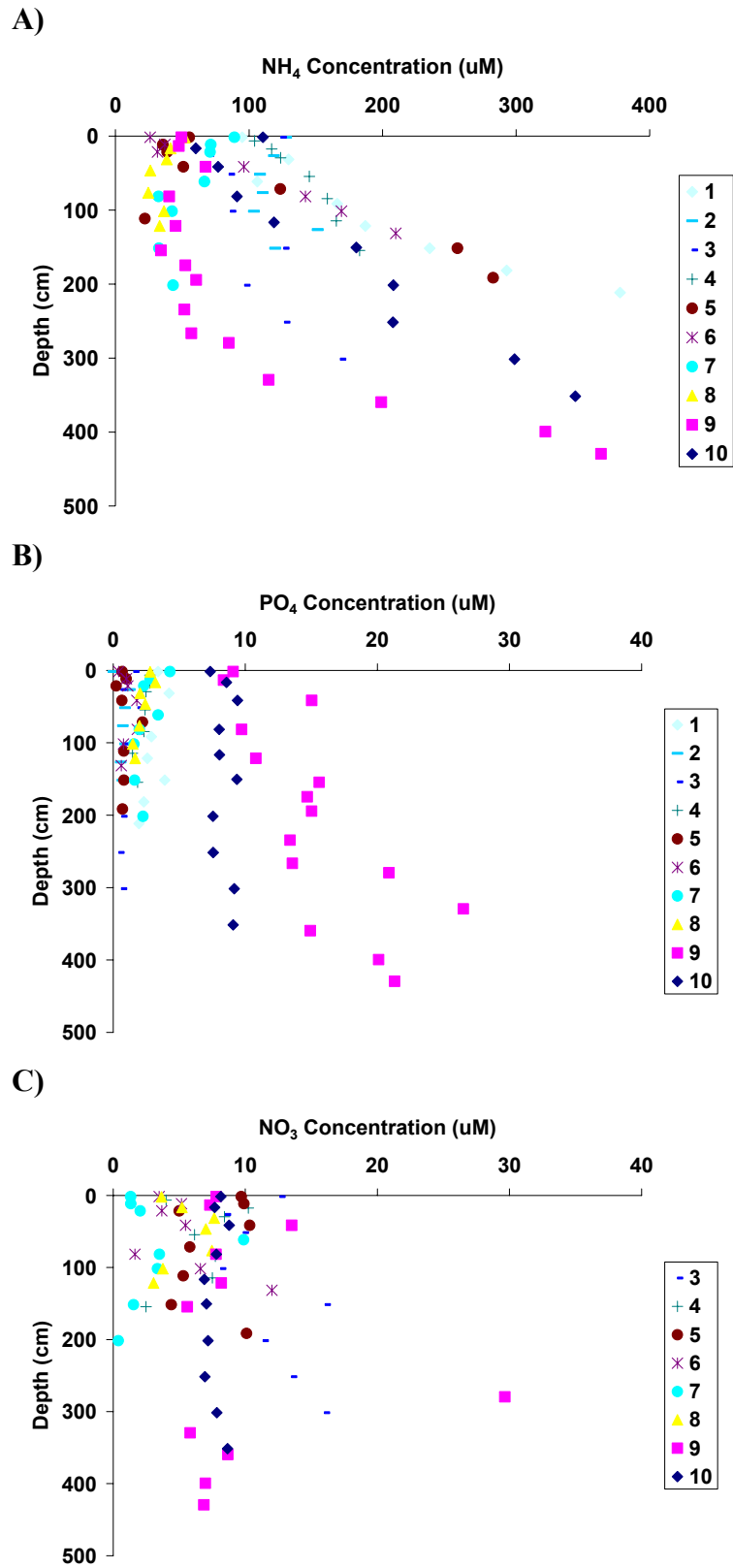


Fig. 7- 12: a) Ammonium, b) phosphate, and c) nitrate/nitrite concentrations for cores 1-10.

## 4. DISCUSSION

Within a 1 km<sup>2</sup> area at Mississippi Canyon 118, microbial activity was assessed through pore-water chemical measurements including gas composition in a suite of thirty sediment cores. Acoustic measurements in this area determined areas of active venting (within wipe-out zones) and inactive venting (outside wipe-outs). In the context of these measurements, the following discussion focuses on the spatial distribution of microbial activity, the carbon source utilized by the microbial communities, and a possible indication of venting history at MC 118 with this geochemical data set.

### **4.1. The spatial distribution of microbial activity outside and within the MC 118 seep zone**

At MC 118, the area of active seepage was defined by the presence of acoustic wipe-out zones. Cores collected outside these zones exhibited little to no variation in pore water chemistry and very low dissolved methane concentrations, and were therefore characterized by low microbial activity. The exception to this pattern was core 30, whose location outside the wipe-out zone is questionable, however, the methane and sulfate gradients were low enough to warrant placement within the low activity group. Although the chemical gradients were low in core 30, it was distinct from the other low activity cores because the methane was relatively enriched in <sup>13</sup>C and the DIC was depleted in <sup>13</sup>C. This data suggests core 30 may have been exposed to previously high rates of microbial activity that will be discussed further below.

In contrast to the low activity cores, cores collected within the wipe-out zones showed evidence of active microbial processes, contained high concentrations of dissolved methane with clear vertical zones of biogenic and thermogenic sources, and exhibited interesting

connections to surrounding authigenic carbonates. As has been reported in other studies (Aharon and Fu, 2000; Arvidson et al., 2004; Joye et al., 2004), these geochemical characteristics provide evidence that seep sites are more microbially active than background sediments. They also show that the microbial activity within the seep site is variable and heterogeneous. While these results are not surprising, what is surprising is that this variable microbial activity falls into one of two different groups: moderate or high microbial activity. An assessment of the small-scale processes within these two groups provides a picture of how microbial activity is affected by large-scale venting processes that ultimately gives information about MC 118's venting history.

Within the moderate activity cores, the biogeochemical profiles suggested active microbial sulfate reduction (SR) and methanogenesis (MP) but limited anaerobic oxidation of methane (AOM). Sulfate reduction is supported by a decrease in sulfate concentrations with depth and, similarly, methanogenesis is supported by an increase in methane concentrations with depth. The lack of a  $\delta^{13}\text{C}\text{-CH}_4$  gradient with depth suggests that AOM is limited within the sulfate reduction zone. Since DIC is a byproduct of SR, its isotope gradient with depth suggests that SR is proceeding via the oxidation of an isotopically light carbon source. Since there is no coupled change in the  $\text{CH}_4$  isotope values, SR is probably using petroleum or chemosynthetically produced organic carbon.

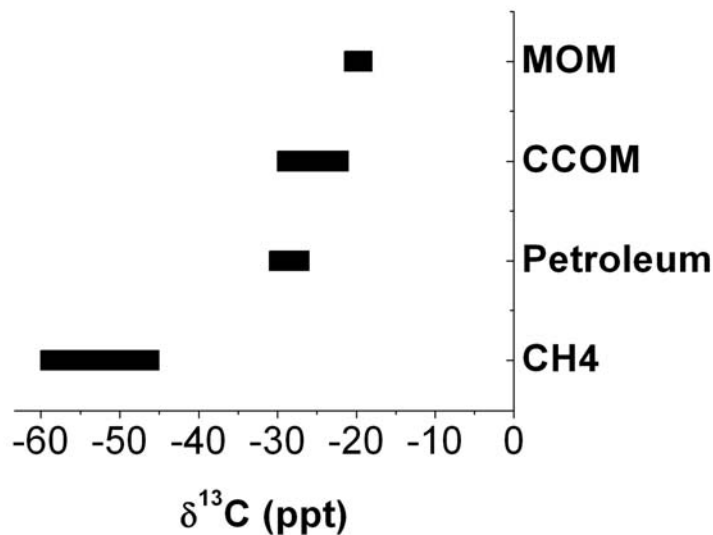
In contrast to the moderately active cores, the high microbial activity cores showed evidence of high rates of SR, AOM, and MP. In these cores, sulfate concentrations were typically depleted within 50 cmbsf and methane concentrations reached as high as 4300  $\mu\text{M}$ , as high as could be measured with coring techniques. This distinct zonation suggests that sulfate reduction was proceeding within the upper depths of the core and, when sulfate was



exhausted, methanogenesis took over. Within the SR zone, the increase in  $\delta^{13}\text{C}\text{-CH}_4$  values up the core suggested an active zone of AOM. AOM was further verified by the coupling between the isotope trends of the  $\text{CH}_4$  and DIC. Below the SR zone, there was also distinct vertical zonation of microbially produced methane and thermogenically produced methane rising from below. It is possible that the high activity cores were more dependent upon the availability of methane than other carbon sources.

#### **4.2. Carbon source(s) utilized by sulfate reducers**

The microbial activity within the MC 118 seep site was highly variable and the microbial communities, specifically the sulfate reducers, used a mixture of carbon sources. At seep sites, the available carbon sources are methane and petroleum derived from seep fluids, marine organic matter (MOM) derived from surface phytoplankton productivity, and organic carbon derived from chemosynthetic communities (CCOM; Fig. 7-13). Using unique chemical and stable carbon isotope ratio characteristics, these sources can be qualitatively teased apart. For example, methane is depleted in  $^{13}\text{C}$  compared to most carbon sources,  $< -47\text{‰}$  (Sassen et al., 2006; current study). While methane is distinctly depleted in  $^{13}\text{C}$ , MOM is uniquely enriched in  $^{13}\text{C}$  from  $-18$  to  $-22\text{‰}$  (Fig. 7-13; Peterson and Fry, 1987; Goni et al., 1997). Ranging between these isotope values for methane and MOM are the values for petroleum and CCOM (Fig. 7-13). The isotopic composition of petroleum is  $\sim -26\text{‰}$  (Kennicutt et al., 1988) and CCOM is between  $-22$  and  $-31\text{‰}$  (Sassen et al., 1993). While petroleum and CCOM are difficult to tease apart, the C:N ratio can be used to decipher between petroleum which is mostly carbon and should have an higher C:N and MOM that is assumed to have a Redfield C:N ratio of 7. Little is known of the C:N ratios of CCOM so only qualitative assessments can be made.



**Fig. 7- 13: Stable carbon isotope ratio ranges of organic carbon sources available to seep microbial communities. MOM is marine organic matter and CCOM is chemosynthetic community organic matter.**

Using the isotope and chemical composition distinctions described above, the carbon source used for sulfate reduction was qualitatively determined in both the high and moderate activity cores. In the high activity cores, the majority of sulfate reduction occurs via methane oxidation because the methane and DIC isotope profiles were tightly coupled within the sulfate reduction zone. However, from the sulfate and methane fluxes calculated in Table 7-1, the upward methane flux was not always supported by an equal sulfate flux suggesting a possible contribution from other organic matter.

In the moderate activity cores, determining the pathway for sulfate reduction was more difficult. In these cores, the isotope values of methane and DIC were decoupled, suggesting that methane was not a major source of carbon. Since the C:N ratios averaged 14 with a δ<sup>13</sup>C-TOC of -25‰, pelagically derived organic carbon was also not a major carbon source. However, these C:N and isotope values may still signify a source of carbon from petroleum or chemosynthetic community derived organic carbon and can not be determined exclusively.

### **4.3. Distribution of microbial activity reveals venting history at MC 118**

Since a large fraction of the microbial activity is dependent upon methane and petroleum entrained within the seep fluids, can the distribution of this activity reveal something about the venting history? While the variable rates of microbial activity within the seep suggest that venting is not homogenous and that there are “hot spots” of microbial activity, it does not reveal any indication of a temporal change in the venting rates. However, temporal change in venting rates may be revealed with the isotopic composition of the dissolved inorganic carbon (DIC) pools and the surrounding carbonates.

Authigenic carbonates precipitate from pore-fluids super-saturated with bicarbonate. Assuming the carbon isotope fractionation between the carbonates and bicarbonate or DIC pool was minimal (Turner, 1982; Boehme et al., 1996), the carbonates should exhibit the stable carbon isotope values of the DIC pool from which they precipitated. As expected, in the high activity group of cores, the isotope values of the DIC pool and the authigenic carbonates were similar, suggesting that the microbial activity was high enough to sustain the current precipitation of carbonates (Table 7-2). In contrast, the moderate activity cores exhibited distinctly different isotope values between the carbonates and DIC pool (Table 7-2). While this result suggests that the carbonates are no longer precipitating in association with current microbial activity, it more importantly suggests that at some time in the past, microbial activity had been high enough to sustain a super-saturated DIC pool and the precipitation of carbonate. This interpretation of the isotope values provides indirect evidence that supports other reports of episodic venting at seep sites (Roberts and Carney, 1997; MacDonald et al., 2000). It further suggests that the episodic venting has led to significant temporal variations in microbial activity.

Episodic venting may also explain the results from core 30 (Fig. 7-4). In this core, the concentrations of sulfate and methane were low, suggesting little to no microbial activity. Yet, the isotopic signature of the methane was highly enriched in  $^{13}\text{C}$  compared to other low activity cores (Fig. 7-4c). This suggests that either the methane has been highly oxidized or it was produced thermogenically. Two pieces of evidence do not support the occurrence of oxidation in this core. First, if anaerobic methane oxidation is occurring via sulfate reduction, a decrease in sulfate concentrations with depth would be expected. Yet, in core 30, the sulfate concentrations did not decrease with depth. Secondly, the methane concentration depth profile exhibits a concave-down shape, suggesting methane production or advection is occurring, not oxidation. An alternative explanation is that the methane was thermogenically produced and that this source fluid is actively venting through sediments in the southeastern vent at MC 118. More coring is needed to fully understand this area's venting history.

#### **4.4. Possible causes for acoustic wipe-out zones**

The large scale methane gas distribution from the current study allows a preliminary assessment of the cause of the wipe-out zones found at MC 118. It has been suggested that seafloor features such as hydrate, carbonate, gas bubbles, and chaotically mixed sediments can all result in acoustic anomalies such as wipe-out zones (Bouma et al., 1990; Roberts et al., 1990; Roberts et al., 1999a; Sager et al., 1999). Since these features suggest a range of upward venting rates (Roberts and Carney, 1997), the presence of acoustic anomalies could not be used to assess the activity of a seep site. Therefore the possible causes for wipe-out zones at MC 118 need to be determined.

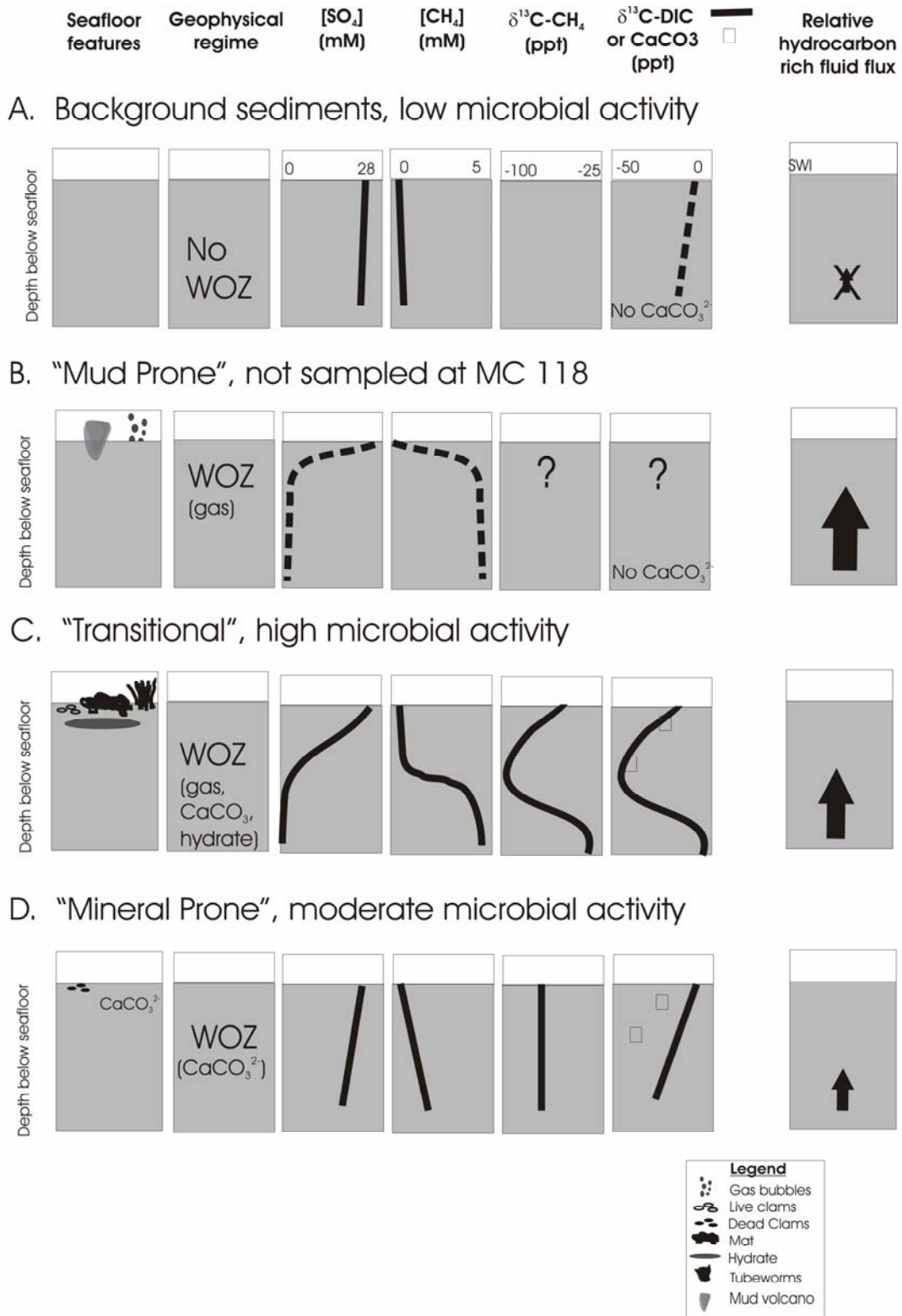
By measuring the methane gas concentrations outside and within the wipe-out zones at MC 118, we tested the hypothesis that the wipe-outs were caused by gas bubbles. In the large methane survey, only four of the fourteen cores collected within the wipe-out zones resulted in high methane concentrations which suggests that the wipe-outs were not solely caused from gas bubbles. However, gas bubbles can not be ruled out because the cores may not have actually reached the depths that were acoustically wiped-out. With the abundance of carbonate collected and visualized on the seafloor at MC 118, carbonates are also thought to contribute to the acoustic signal. It was determined that chaotic sediments were not the cause of the wipe-outs at MC 118 because the biostratigraphy and lithostratigraphy of cores collected outside (cores 10 and 33) and within (cores 9, 21, 26, and 31) the wipe-out zones did not exhibit patterns of mixing (Charlotte Brunner, unpublished data). Therefore, the possible causes of the acoustic wipe-outs at MC 118 are still a mixture of gas, carbonate, and hydrate.

#### **4.5. Biogeochemical distributions of microbial activity integrated into an existing vent evolution model**

The geochemical and microbial distributions at MC 118 support the idea of episodic venting at hydrocarbon-seep sites. Therefore, the general biogeochemical distributions measured in the present study were integrated into an observational model first proposed by Roberts and Carney (1997). This integration includes the estimated relative fluid flux rates and seafloor observations from Roberts and Carney (1997) as well as the geophysical and geochemical data from this study (Fig. 7-14). The geophysical data is based on the presence or absence of acoustic wipe-out zones and suggests possible causes for these zones. The geochemical data follow those presented from the geochemical survey conducted at MC 118;

including depth-dependent gradients of sulfate and methane concentrations, methane and DIC stable carbon isotope values, and the carbonate isotope values. Although the model's sediment depth scale is arbitrary, it is typically focused on the shallow sediments above ~10 meters depth.

The integrated model begins with background 'vents' (Fig. 7-14a). These vents are background sediments that lack seep-related features, acoustic anomalies, and geochemical concentration or isotope gradients. As exhibited in the low microbial activity group, sulfate concentrations remain near seawater values with no depth gradients, dissolved methane concentrations are typically too low to measure, and, if measurable, DIC isotope ratio depth gradients are indicative of typical organic matter decomposition. Furthermore, authigenic carbonates are not present. Background vents contain little to no microbial activity because of the limited upward hydrocarbon fluid flux (Roberts and Carney, 1997).



**Fig. 7- 14: The integrated observational, geochemical, and geophysical seep evolution model.**

Where the seafloor is intersected by faults and fissures and migrating fluids reach the sediment water interface at a high rate, a “mud prone” vent will result (Fig. 7-14b). These vents are also known as mud volcanoes (Dimitrov, 2003; Milkov et al., 2003). Since these fluids are typically enriched in gases, the geophysical regime suggests acoustic anomalies are caused by bubbles entrained within the fluids. Although the biogeochemical regime remains speculative at this time because a mud prone vent was not sampled at MC 118, biogeochemical data was extrapolated from a similar mud volcano system (de Beer et al., 2006). Using this data, sulfate will be depleted at shallow sediment depths and allow methane to increase near the sediment water interface. The original model suggested that microbial activity would be limited due to the fast flux at mud prone vents (Roberts and Carney, 1997). This discrepancy illustrates the need to directly measure the geochemical regime at a mud volcano. Even though not measured, the methane and DIC isotope values would reflect the isotope values of the methane and DIC entrained within the seeping fluids. At mud prone vents, the relative hydrocarbon-rich fluid flux is high (Roberts and Carney, 1997).

Over time and as the high thermogenic fluid flux slows down, the mud prone vent turns into a “transitional” vent (Fig. 7-14c). As presented by Roberts and Carney (1997), transitional vents contain seafloor features such as bacterial mats, other chemosynthetic communities, and gas hydrates. The geophysical regime is defined by acoustic anomalies that are caused by the presence of gas, carbonate, or hydrate. For these transitional vents, the geochemical profiles are similar to those measured in the high activity cores at MC 118. For example, sulfate is depleted within the shallow sub-surface and, when depleted, methane increases. The methane isotope values indicate clear depth-dependent zones of anaerobic



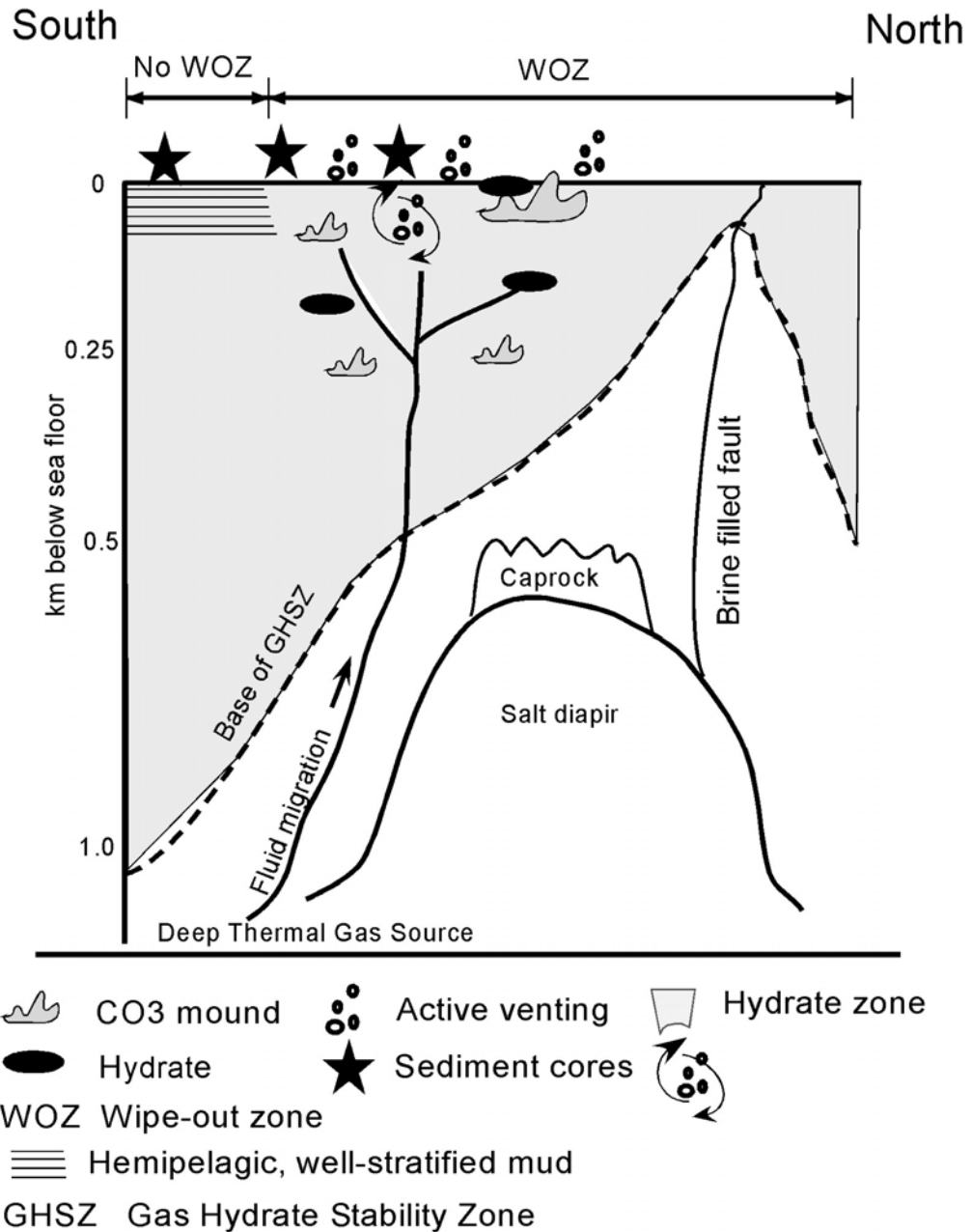
methane oxidation and methanogenesis. As a consequence of the enhanced microbial sulfate reduction, bicarbonate concentrations begin to increase and probably exceed saturation; allowing authigenic carbonate to precipitate. This results in similar stable carbon isotope values between the carbonates and the DIC pool. Due to the high rates of methanogenesis in the shallow sediments, the methane isotope values exhibit distinct depth-dependent zonation between the biogenic and thermogenic methane. At transitional seeps, the relative hydrocarbon-rich fluid flux is moderate (Roberts and Carney, 1997).

As the fluid flux ceases altogether, the transitional vent evolves into a “mineral prone” seep (Fig. 7-14d). Due to the absence of an influxing carbon source, microbial activity will slow down and eventually stop. The lack of microbial activity will thus affect the viability of the surrounding chemosynthetic communities. Therefore, seafloor features at the mineral prone seeps are limited to dead clam shells and authigenic carbonates. Although these vents are no longer active, the presence of the shells and carbonates still cause acoustic anomalies. However, geochemical gradients would be low, much like background vents. The distinguishing characteristic between mineral prone vents and transitional vents is that the isotopic signature of the carbonates will be indicative of past high microbial activity yet, dissimilar to the current DIC pool. At MC 118, the moderate activity group is much like a mineral prone seep. At mineral prone seeps, the relative fluid flux is low; similar to background vents (Roberts and Carney, 1997).

#### **4.5. Overview of MC 118**

From the work presented in this chapter and earlier chapters, conversations at meetings with geophysicists, and building on a map presented by Roger Sassen in 2005, a conceptual cartoon of processes occurring at MC 118 is presented (Fig. 7-15). As has been reported in

many studies, the system is foremost driven by the movement of an underlying salt diapir that underlies the MC 118 seep area. As the salt moves, it creates faults that radiate to the shallow sediments and allow hydrocarbon-rich fluids to migrate to the hydrate stability zone and possibly reach the sediment water interface (Roberts and Carney, 1997). To this well-known understanding of the salt driven tectonics, the present study adds direct evidence of how this fluid migration affects sedimentary biogeochemical processes. In the southern region at MC 118, the shallow sediments are impacted by episodic venting of thermogenic fluids rich in methane and petroleum. This venting fuels high microbial activity and hydrate precipitation forming transitional vents. Over time, fluid flow slows down and the vents evolve into a mineral prone area with the production of authigenic carbonate precipitation. In the northern region, brines fill faults that reach near the sediment water interface which pushes the hydrate stability zone to shallower depths and does not allow for the precipitation of hydrates (chapter 3 data supports this idea). Within these brine filled sediments, microbial activity is therefore limited to methanogenesis (as extrapolated from chapter 6). Future geophysical and geochemical data will either support or reject this interpretation.



**Fig. 7- 15: A conceptual cartoon of a north-south cross section through MC 118. Figure adapted from conversations with Roger Sassen.**

## 5. CONCLUSIONS

This study presented a large scale survey of biogeochemical concentration and isotope profiles within the context of geophysical anomalies to show that while microbial activity was contained within acoustic wipe-out zones, it was still spatially and temporally variable even within these zones. Furthermore, microbial activity within the shallow sediments controls the methane flux out of the sediments and may be an important sequestration process for methane carbon. Future work should directly measure the rates of biogeochemical processes to understand the role the microbial communities play in both carbon sequestration and production. The integrated vent model should be tested by directly measuring biogeochemical processes within a mud prone vent. The link between the authigenic carbonates and DIC pool also needs to be verified with more data. And finally, a more comprehensive understanding of what causes acoustic wipe-out zones is needed.

*Acknowledgements.* This study was funded by EPA STAR fellowship and the Gulf of Mexico Hydrate Research Consortium with a grant from DOE. Cruise time was also supported by the GOMHRC. We thank the R/V Pelican captain and crew. We thank Claire Langford for analyzing methane concentrations and stable carbon methane and DIC isotopes and the stable carbon isotope values for carbonates. We also thank Sam Perkins for running sulfate and chloride concentrations.

## 6. REFERENCES

- Aharon P. and Fu B. (2000) Microbial sulfate reduction rates and sulfur and oxygen isotope fractionations at oil and gas seeps in deepwater Gulf of Mexico. *Geochimica et Cosmochimica Acta* **64** (2), 233-246.
- Aharon P., Schwarcz H. P., and Roberts H. H. (1997) Radiometric dating of submarine hydrocarbon seeps in the Gulf of Mexico. *GSA Bulletin* **109** (5), 568-579.
- Alperin M. J., Reeburgh W. S., and Whiticar M. J. (1988) Carbon and hydrogen isotope fractionation resulting from anaerobic methane oxidation. *Global Biogeochemical Cycles* **2** (3), 279-288.
- Arvidson R. S., Morse J. W., and Joye S. B. (2004) The sulfur biogeochemistry of chemosynthetic cold seep communities, Gulf of Mexico, USA. *Marine Chemistry* **87**, 97-119.
- Boehme S. E., Blair N. E., Chanton J. P., and Martens C. S. (1996) A mass balance of  $^{13}\text{C}$  and  $^{12}\text{C}$  in an organic-rich methane-producing marine sediment. *Geochimica et Cosmochimica Acta* **60** (20), 3835-3848.
- Boetius A., Ravensschlag K., Schubert C. J., Rickert D., Widdel F., Gieseke A., Amann R., Jorgensen B. B., Witte U., and Pfannkuche O. (2000) A marine microbial consortium apparently mediating anaerobic oxidation of methane. *Nature* **407**, 623-626.
- Bouma A. H., Roberts H. H., and Coleman J. M. (1990) Acoustical and geological characteristics of near-surface sediments, upper continental slope of northern Gulf of Mexico. *Geo-Marine Letters* **10**, 200-208.
- Brewer P. G., Paull C. K., Peltzer E. T., Ussler III W., Rehder G., and Friederich G. (2002) Measurements of the fate of gas hydrates during transit through the ocean water column. *Geophysical Research Letters* **29** (22), 38-1 to 38-4.
- Crill P. M. and Martens C. S. (1983) Spatial and temporal fluctuations of methane production in anoxic coastal marine sediments. *Limnology and Oceanography* **28** (6), 1117-1130.
- de Beer D., Sauter E. J., Niemann H., Kaul N., Foucher J. P., Witte U., Schluter M., and Boetius A. (2006) In situ fluxes and zonation of microbial activity in surface sediments of the Hakon Mosby Mud Volcano. *Limnology and Oceanography* **51** (3), 1315-1331.

- Dimitrov L. I. (2003) Mud volcanoes- a significant source of atmospheric methane. *Geo-Marine Letters* **23**, 155-161.
- Ferrell Jr. R. E. and Aharon P. (1994) Mineral assemblages occurring around hydrocarbon vents in the northern Gulf of Mexico. *Geo-Marine Letters* **14**, 74-80.
- Goni M. A., Ruttenberg K. C., and Eglinton T. I. (1997) Sources and contribution of terrigenous organic carbon to surface sediments in the Gulf of Mexico. *Nature* **389**, 275-278.
- Hoehler T. M., Alperin M. J., Albert D. B., and Martens C. S. (1994) Field and laboratory studies of methane oxidation in an anoxic marine sediment: Evidence for a methanogen-sulfate reducer consortium. *Global Biogeochemical Cycles* **8** (4), 451-463.
- Joye S. B., Boetius A., Orcutt B. N., Montoya J. P., Schulz H. N., Erickson M. J., and Lugo S. K. (2004) The anaerobic oxidation of methane and sulfate reduction in sediments from Gulf of Mexico cold seeps. *Chemical Geology* **205**, 219-238.
- Joye S. B., MacDonald I. R., Montoya J. P., and Peccini M. (2005) Geophysical and geochemical signatures of Gulf of Mexico seafloor brines. *Biogeosciences* **2**, 295-309.
- Kennett J. P., Cannariato K. G., Hendy I. L., and Behl R. J. (2003) *Methane hydrates in Quaternary climate change: The clathrate gun hypothesis*. American Geophysical Union, Washington, DC.
- Kennicutt M. C., Brooks J. M., and Denoux G. J. (1988) Leakage of deep, reservoired petroleum to the near surface on the Gulf of Mexico continental slope. *Marine Chemistry* **24**, 39-59.
- Kvenvolden K. A. (1993) Gas hydrates-geological perspective and global change. *Reviews of Geophysics* **31**, 173-187.
- Kvenvolden K. A. and Lorenson T. D. (2001) The global occurrence of natural gas hydrates. In *Natural Gas Hydrates: Occurrence, Distribution and Detection*, Vol. 124 (ed. C. K. Paull and W. P. Dillion), pp. 315. American Geophysical Union.
- Lanoil B. D., Sassen R., LaDuc M. T., Sweet S. T., and Nealson K. H. (2001) Bacteria and Archaea physically associated with Gulf of Mexico gas hydrates. *Applied and Environmental Microbiology* **67** (11), 5143-5153.

- MacDonald I. R., Buthman D. B., Sagar W. W., Peccini M. B., and Guinasso Jr N. L. (2000) Pulsed oil discharge from a mud volcano. *Geology* **28** (10), 907-910.
- MacDonald I. R., Leifer I., Sassen R., Stine P., Mitchell R., and Guinasso Jr N. L. (2002) Transfer of hydrocarbons from natural seeps to the water column and atmosphere. *Geofluids* **2** (95-107).
- Milkov A. V. (2004) Global estimates of hydrate-bound gas in marine sediments: how much is really out there? *Earth-Science Reviews* **66**, 183-197.
- Milkov A. V., Sassen R., Apanasovich T. V., and Dadashev F. G. (2003) Global gas flux from mud volcanoes: A significant source of fossil methane in the atmosphere and the ocean. *Geophysical Research Letters* **30** (2), doi: 10.1029/2002GL016358.
- Nikolaus R., Ammerman J. W., and MacDonald I. R. (2003) Distinct pigmentation and trophic modes in *Beggiatoa* from hydrocarbon seeps in the Gulf of Mexico. *Aquatic Microbial Ecology* **32**, 85-93.
- Orcutt B. N., Boetius A., Elvert M., Samarkin V. A., and Joye S. B. (2005) Molecular biogeochemistry of sulfate reduction, methanogenesis, and the anaerobic oxidation of methane at Gulf of Mexico cold seeps. *Geochimica et Cosmochimica Acta* **69** (17), 4267-4281.
- Peterson B. J. and Fry B. (1987) Stable isotopes in ecosystem studies. *Annual Review of Ecology and Systematics* **18**, 293-320.
- Reeburgh W. S. (1967) An improved interstitial water sampler. *Limnology and Oceanography* **12**, 163-165.
- Roberts H. H., Aharon P., Carney R., Larkin J., and Sassen R. (1990) Sea floor responses to hydrocarbon seeps, Louisiana Continental Slope. *Geo-Marine Letters* **10**, 232-243.
- Roberts H. H. and Carney R. S. (1997) Evidence of episodic fluid, gas and sediment venting on the Northern Gulf of Mexico Continental Slope. *Economic Geology* **92**, 863-879.
- Roberts H. H., Kohl B., Menzies D., and Humphrey G. D. (1999) Acoustic wipe-out zones - a paradox for interpreting seafloor geologic/geotechnical characteristics (an example from Garden Banks 161). *Offshore Technology Conference. Paper # OTC 10921*.
- Sager W. W., Lee C. S., MacDonald I. R., and Schroeder W. W. (1999) High-frequency near-bottom acoustic reflection signatures of hydrocarbon seeps on the Northern Gulf of Mexico continental slope. *Geo-Marine Letters* **18**, 267-276.

- Sassen R. and Roberts H., 2004. Site selection and characterization of vent gas, gas hydrate, and associated sediments. DOE Technical Report.
- Sassen R., Roberts H. H., Aharon P., Larkin J., Chinn E. W., and Carney R. (1993) Chemosynthetic bacterial mats at cold hydrocarbon seeps, Gulf of Mexico continental slope. *Organic Geochemistry* **20**, 77-89.
- Sassen R., Roberts H. H., Carney R., Milkov A. V., DeFreitas D. A., Lanoil B., and Zhang C. (2004) Free hydrocarbon gas, gas hydrate, and authigenic minerals in chemosynthetic communities of the northern Gulf of Mexico continental slope: relation to microbial processes. *Chemical Geology* **205**, 195-217.
- Sassen R., Roberts H. H., Jung W., Lutken C. B., DeFreitas D. A., Sweet S. T., and Guinasso Jr. N. L. (2006) The Mississippi Canyon 118 Gas Hydrate Site: A complex natural system. *OTC Paper #18132; Offshore Technology Conference*.
- Sleeper K., Lowrie A., Bosman A., Macelloni L., and Swann C. T. (2006) Bathymetric mapping and high resolution seismic profiling by AUV in MC 118 (Gulf of Mexico). Paper #OTC 18133 PP. *Offshore Technology Conference*.
- Turner J. V. (1982) Kinetic fractionation of carbon-13 during calcium carbonate precipitation. *Geochimica et Cosmochimica Acta* **46** (7), 1183-1191.
- Whiticar M. J. (1999) Carbon and hydrogen isotope systematics of bacterial formation and oxidation of methane. *Chemical Geology* **161**, 291-314.
- Woolsey J. R., Higley P., Lapham L. L., Chanton J. P., Lutken C., Sleeper K., Culp R., Sharpe S., and Ross D., 2005. Operations report of cruise GOM2-05-MC118 Deployment of the initial components of the sea floor monitoring station- The pore-fluid array and the geophysical line array- via the sea floor probe system and collection of core samplers, Mississippi Canyon 118. Gulf of Mexico Hydrates Research Consortium: University of Mississippi Center for Marine Resources and environmental technology.



## Appendix 1

### 1a. Publications

- N. R. Chapman, J. Pohlman, R. Coffin, J. P. Chanton, and **L. L. Lapham**. (2004). Thermogenic Gas Hydrates in the Northern Cascadia Margin, *EOS, Transactions, American Geophysical Union* 85, 361.
- Lapham, L.L.**, J. P. Chanton, C. S. Martens, and H. P. Mendlovitz. 2004. Innovations in sampling pore fluids at deep sea hydrate sites. In: *Energy, Simulation-Training, Ocean Engineering and Instrumentation: Research Papers of the Link Foundation Fellows*. Thompson, B. J (Ed.), 4.
- Proctor LM, E. Toy, **L. L. Lapham**, J. Cherrier, and J. P. Chanton. 2001. Enhancement of orimulsion biodegradation through the addition of natural marine carbon substrates. *Environ. Sci. Technol.* **35 (7)**: 1420-1424.
- Gee, K.R., E.A. Archer, **L.L. Lapham**, M.E. Leonard, Z. Zhou, H. Bingham, and Z. Diwu. 2000. New ratiometric fluorescent calcium indicators with moderately attenuated binding affinities. *Bioorganic and Medicinal Chemistry Letters*, **10 (14)**: 1515-1518.
- Lapham, L.L.**, L. Proctor, and J. Chanton. 1999. Using respiration rates and stable carbon isotopes to monitor the biodegradation of Orimulsion by marine benthic bacteria. *Environ. Sci. Technol.*, **33**: 2035-2039.

### 1b. Conference abstracts and meeting presentations

- Lapham, L. L., J. P. Chanton, C. S. Martens, P. D. Higley, H. W. Jannasch and J. R. Woolsey. 2007. Monitoring long term hydrate stability: in situ methane and the Pore Fluid Array (PFA). Oral presentation, Gulf of Mexico Hydrates Research Consortium Annual Meeting. Oxford, MS.
- Lapham, L. L., J. P. Chanton, C. S. Martens, P. D. Higley, H. W. Jannasch and J. R. Woolsey. 2006. Pore Fluid Array Construction and Deployment at Mississippi Canyon Site 118, Gulf of Mexico. (OTC-18170-PP). Oral presentation, Offshore Technology Conference.
- Lapham, LL, J. C. Chanton, C. S. Martens, J. P. Pohlman, and R. Chapman. 2005. In situ light hydrocarbon concentrations and stable carbon isotope values in hydrate-bearing sediments of Cascadia Margin, Vancouver Island. Oral presentation. European Geosciences Union Annual Meeting, Vienna, Austria.

Lapham, L.L., J. P. Chanton, C. S. Martens, H. Scheafer, R. Chapman, and J. Puhlman. 2003. Innovations in Sampling Pore Fluids From Deep-Sea Hydrate Sites. Oral Presentation. Transactions of the American Geophysical Union, 84 (46), F862.

Lapham, L. L., C. S. Martens, and R. B. Coffin. 2003. Controls on the isotopic composition of dissolved methane in the pore waters of sediments containing disseminated gas hydrate off of Cascadia Margin. Oral Presentation. American Society of Limnology and Oceanography annual meeting program, p. 82.

Lapham, L.L., D. A. Albert, J. P. Chanton, and C. S. Martens. (2001). Light hydrocarbon distributions and sulfate reduction rates in sediment porewaters near exposed gas hydrates. Oral Presentation. American Society of Limnology and Oceanography annual meeting program.

### **1c. Oceanographic cruises**

1. August 2000, several hydrate sites on Texas-Louisiana Continental Shelf, Gulf of Mexico. Measured pore water chemistry in sediments surrounding hydrates. Also, I addressed rates of microbial sulfate reduction in several sites around hydrates.

2. July-August 2001, Cascadia Margin, offshore Vancouver Island, Canada, Pacific Ocean. The goal of the cruise was to visit several hydrate sites in order to understand the cycling of carbon and sulfur through the system. I was invited on this cruise to measure pore water chemistry in sediment cores.

3. May 2002, two hydrate sites on Texas-Louisiana Continental Shelf, Gulf of Mexico. As part of the hydrate consortium, I deployed the first in situ methane concentration instrument at hydrate sites. The system was deployed from a manned submersible. These samples were analyzed for dissolved gases and ions. In situ gas concentrations in deep sea systems are still difficult to obtain but this work was one step closer to the goal.

4. August 2002, Blake Ridge diapir offshore South Carolina, Atlantic Ocean. Blake Ridge hydrate system has been extensively studied, with an ODP cruise visiting it in late-1990s. However, little is known about the diapir and how it affects the hydrates. Therefore, the goal of this cruise was to visit the diapir and collect many cores on a large spatial scale to understand the cycling of carbon and sulfur. I was invited to measure pore water chemistry in these cores.

5. June 2003, Cascadia Margin, offshore Vancouver Island, Canada, Pacific Ocean. Visiting a newly discovered thermogenic methane hydrate site, I was invited to deploy the in situ methane concentration instrument. The instrument was modified for deployment from a remotely operated vehicle (ROV).

6. August 2003, several sites on Texas-Louisiana Continental Shelf, Gulf of Mexico. With the previous success of the in situ methane concentration instrument, the hydrate consortium

funded me again to deploy the instrument to address sources and sinks of dissolved methane at several different outcropping hydrate sites. Five deployments were made.

7. June 2004, Barclay Canyon offshore Vancouver Island, Canada, Pacific Ocean. Understanding the in situ gas conditions surrounding outcropping hydrate is crucial to addressing hydrate stability. So, I was invited to deploy the in situ methane concentration instrument at an outcropping hydrate site to collect samples as a gradient off the hydrate mounds.

8 and 9. May and August 2005, Gulf of Mexico, MC 118. The main goal of the hydrate consortium is to maintain a long term hydrate monitoring station on the seafloor. This station will follow a hydrate system over time, measuring both geochemical and geophysical indicators of hydrate formation and decomposition. In 2004, the site was chosen as Mississippi Canyon 118 and these two cruises were set up to collect background information on the biogeochemical processes occurring in the shallow sediments and to deploy a long term pore fluid array system. My part in these cruises was to develop and deploy the pore fluid array system and to collect ~30 gravity cores to determine spatial variability of microbial processes such as sulfate reduction, anaerobic methane oxidation, and methanogenesis. These processes were then tied into particular geophysical signatures that are unique to methane hydrate sites. The pore fluid array system was deployed during the May cruise and will be retrieved in August 2006.

10. September 2006, Gulf of Mexico, MC 118. We retrieved the pore fluid array system from MC 118 and deployed peepers and the osmolander.

11. March 2007, Gulf of Mexico, MC 118. We retrieved one peeper sampler from Mandyville.

## Appendix 2

### 2a. Gulf of Mexico HYDRA deployments.

Site	Dive #	Port #	Depth (cm)	Sample volume (mL)	SO <sub>4</sub> (mM)	Cl (mM)	[CH <sub>4</sub> ] <sub>measured</sub> (uM)	Avg δ <sup>13</sup> C-CH <sub>4</sub> (‰)	stdev	Ethane (uM)	Propane (uM)	Avg δ <sup>13</sup> C-DIC (‰)	stdev	NH <sub>4</sub> (uM)	PO <sub>4</sub> (uM)	NO <sub>3</sub> /NO <sub>2</sub> (uM)	
GC 185	4210		4.5		30.47	552.37	0.48	-46.20				-2.32	0.57				
			7.5		30.81	571.30	0.96			0.04		-0.62					
			12.5		19.67	369.06	0.20	-46.21				-4.21					
			17.5		31.31	584.17	2.47	-42.85		0.06		-3.93					
			22.5		30.02	586.41	3.12	-46.31		0.10		-5.11					
			27.5		29.56	577.59	4.16	-46.03		0.13		-8.04					
			32.5		29.63	592.23	3.33	-45.32		0.05		-9.24					
			37.5		30.34	590.04	8.88	-46.23		0.85		-6.22					
			42.5		29.56	570.21	27.61			1.95		-8.36					
		47.5		28.67	557.82	40.27	-46.50		3.27		-4.97						
		4213		4.50		30.37	575.01	5.11	-43.07								
			7.50		31.90	578.55	0.84			0.06							
			12.50		27.03	556.43	12.58	-45.13		0.18							
			17.50		22.55	513.07	104.75	-48.21		4.17		-15.11					
			22.50		16.79	520.26	867.15			371.19	511.00						
			27.50		4.64	543.95	1947.44			2399.71	1241.00	-31.25					
			32.50		4.52	629.03	1511.85			1412.03	1891.00						
			37.50		4.06	558.73	868.84	-45.89		355.65		-24.85					
			42.50		6.89	542.28	933.23	-46.68		194.27	105.00						
	47.50						-47.68										
	4553	F10	4.5	7	12.46	252.75	1.13	-40.45				-4.95					
		F9	7.5	7	13.8	267.83	1.62					-6.13					
		F8	12.5	7	10.46	229.82	0.62	-40.08				-6.25					
		F7	17.5	5	11.77	215.36	0.80	-40.04				-6.89					
		F6	22.5	5	5.09	91.16	0.73	-41.98				-9.62					
		F5	27.5	5	7		0.80	-43.13				-9.82					



	S10	4.5	7	25.34	496.56	10.05	-37.91			-2.36	
	S9	7.5	7	24.35	463.17	22.62	-45.41	0.4031		-2.55	
	S8	12.5	0								
	S7	17.5	2	19.28	376.86	150.72	-48.95			-9.53	
	S6	22.5	5	6.89	167.26	29.71	-51.03			-10.1	
	S5	27.5	0								0.57 0.25 1.45
	S4	32.5	0								
	S3	37.5	0								
	S2	42.5	0								
	S1	47.5	7	12.53	420.22	1435.70	-47.34			10.15	0.28 0.21 0.55
GC 234	4217	4.5		29.44	566.19	343.99	-50.16	46.72	43.53	-8.10	0.12
		7.5		19.50	393.62	517.88	-48.13	41.64	22.00	-11.68	
		12.5		22.80	517.96	1590.82	-50.73	117.90	51.33		
		17.5		19.86	491.42	1053.82		71.38	25.35	-18.40	
		22.5		14.58	491.59	2199.67	-49.69	450.25	886.26		
		27.5								-20.11	
		32.5		12.45	497.19	1337.86	-48.26	562.67	1355.60		
	4218	4.5		26.04	707.46	43.08	-47.06	1.39	1.40	-10.39	
		7.5		27.85	556.68	12.72		0.38		-10.69	0.61
		12.5		25.55	540.28	19.93	-50.07	1.54	1.37	-13.82	
		17.5		28.14	489.09	46.95		3.12	1.04	-9.58	
		22.5		27.07	550.86	70.69		7.20	4.68	-14.52	
		27.5		28.92	556.63	77.99	-47.18	14.52	19.74	-14.02	1.87
		32.5		26.91	569.30						
		42.5		24.28	492.00	30.71		0.98		-15.19	
		47.5		27.59	553.97	20.75	-44.37				
	4557	F10	4.5	7	14.23	294.52	54.46	-48.85		-12.61	
		F9	7.5	7	10.03	241.24	1231.26	-43.26		-9.75	
		F8	12.5	7	9.93	253.70	554.70	-54.66		-15.58	
		F7	17.5	7	9.46	233.69	1135.54	-54.26		-12.09	
		F6	22.5	7	9.06	252.08	599.02	-53.83		-9.77	
		F5	27.5	7	9.26	224.80	657.35	-51.58		-6.71	
		F4	32.5	7	6.8	152.05	417.43	-50.82		-3.86	

F3	37.5	7	11.99	269.57	2819.02	-50.35	0.3253	3.25	
F2	42.5	7	6.91	156.95	613.36	-48.5		2.07	
F1	47.5	7	10.05	256.87	6479.43	-50.92		6.26	
S10	4.5	7	19.02	422.92	64.35	-48.28		-12.54	0.25
S9	7.5	7	14.28	357.93	2591.64	-54.35	0.0919	-13.05	
S8	12.5	7	11.44	315.72	369.21	-54.97		-15.88	
S7	17.5	7	14.06	387.81	1412.03	-53.44	0.1485	-12.51	
S6	22.5	7	10.06	271.88	406.30	-53.43		-10.04	
S5	27.5	7	5.91	169.34					
S4	32.5	7	6.49	180.46	635.78	-50.83		-2.35	
S3	37.5	7	5.86	291.45	2636.41	-50.53	0.3465	3.64	
S2	42.5	7	4.63	131.82	342.79	-49.62	0.7707	1.23	0.01
S1	47.5	7	16.82	425.24	5589.29	-50.91	0.2192	7.22	0.15

---

**2b. Cascadia Margin, Barkley Canyon HYDRA deployments from 2003.**

Dive #	Port #	Depth (cm)	Sample volume (mL)	SO <sub>4</sub> (mM)	Cl (mM)	[CH <sub>4</sub> ] (uM)	δ <sup>13</sup> C-CH <sub>4</sub> (‰)	δ <sup>13</sup> C-CH <sub>4</sub> (‰)	Ethane (uM)	avg δ <sup>13</sup> C-ethane (‰)	stdev	Propane (uM)	δ <sup>13</sup> C-propane (‰)	Butane (uM)	δ <sup>13</sup> C-DIC (‰)
692	1F	8.5	7	18.58	387.06	266.57	-39.33	-41.46	60.88			20.57		1.02	-5.95
	2F	14.5	7	19.55	374.94	234.72	-41.30	-41.28	33.05			223.40		9.52	-3.03
	3F	17.5	7	10.49	365.95	2377.80	-39.44	-38.85	366.11	-21.08	0.09	116.40	-20.03	0.98	-25.93
	4F	25.5	7	13.71	472.38	2019.84	-40.23	-38.79	262.78	-22.97	0.70	383.06	-20.63	5.87	-26.47
	2S	14.5	7	23.99	466.92	255.55	-41.37	-40.14	33.49			35.11		0.78	-2.92
	3S	17.5	7	10.43	410.35	2520.53	-39.71	-38.79	387.36	-21.21	0.25	136.08		1.44	-26.74
	4S	25.5	7	12.59	447.64	2073.92	-40.28	-39.26	261.21	-22.97	0.42	394.23	-33.46	6.50	-25.90
693	1F	1	7	17.06	330.38	3.30	-39.44		0.81			0.32		0.13	-5.15
	2F	4	2.5	6.62	121.65	6.85	-38.28		1.54			0.81		0.29	-10.16
	3F	7	2	8.42	163.88	67.67	-35.08		11.32			1.38		0.27	-6.17
	2S	4	4	10.64	224.65	4.34	-37.88		1.00			0.60		0.22	-9.76
	4S	16	1.5	4.84	72.40	73.96	-33.83		9.66			3.82		1.10	-8.57
696	2F	2.5	7	17.74	368.00	559.97	-42.31	-42.46	100.61			1.51		0.58	-18.22
	1F	4.5	7	16.37	400.93	1521.16	-42.42	-42.34	318.17	-21.76	0.09	1.68		0.35	-25.15
	4F	9.5	7	5.72	322.10	3017.88	-49.41	-49.33	399.28	-21.79	0.39	14.18		0.40	-25.90
	3F	10.5	7	3.96	290.41	2841.10	-49.55	-49.74	258.18	-22.39	0.25	10.37		0.63	-21.33
	2S	2.5	7	21.20	451.32	633.27	-42.20	-41.89	113.54	-22.00	0.37	1.86		0.46	-17.02
	1S	4.5	7	19.48	475.32	1698.60	-42.98	-43.05	351.03	-23.32	0.33	1.24		0.37	-25.07
	4S	9.5	7	5.22	362.91	999.96	-49.73	-49.76	165.74	-22.26	0.06			0.90	-26.79
	3S	10.5	7	5.54	466.56	2853.46	-49.87	-50.17	343.28	-23.29	1.65			1.39	-29.97



## 2c. Cascadia Margin, Barkley Canyon HYDRA deployments from 2004.

Dive #	Port #	Depth (cm)	Sample volume (mL)	SO <sub>4</sub> (mM)	Cl (mM)	[CH <sub>4</sub> ] <sub>measured</sub> (uM)	color (absorbance)	δ <sup>13</sup> C-CH <sub>4</sub> (‰)	δ <sup>13</sup> C-CH <sub>4</sub> (‰)	avg δ <sup>13</sup> C-CH <sub>4</sub> (‰)	stdev	δ <sup>13</sup> C ethane (‰)	δ <sup>13</sup> C - DIC (‰)	δ <sup>13</sup> C - DIC (‰)
798	P10	0	11	16.98	346.09	1.39	0.952	-45.33					-5.21	
	P10	0	11	16.98	346.09	1.30								
	P3	0	11	2.72	54.06	0.63	2.097	-47.81	-47.21	-47.51	0.42		-6.37	
	P6	7	11	5.02	108.14	0.48	1.917	-37.44					-4.51	
	P9	13.5						-46.29				-24.67	-7.27	
	P5	14						-45.12	-45.12	-45.12	0.00		-6.17	
	P8	16	11	19.10	389.86	181.76	0.821	-42.01	-42.41	-42.21	0.29		-7.27	
	P1	19	10	13.67	284.75	219.28	1.121	-46.13	-46.09	-46.11	0.02		-10.29	
	P4	19	11	4.41	108.30	39.83	1.916	-44.76					-11.58	
	P7	22	11	8.44	244.12	482.22	1.334	-42.70	-42.78	-42.74	0.06		-26.7	
799	P10	0	11	17.72	342.96	0.01	1.021	-47.25					-0.2	
	P1	9	11	12.74	257.64	0.12	1.406	-42.07					-1.91	
	P7	9	11	13.56	251.35	0.06	1.388	-41.35	-41.11	-41.23	0.17	-23.44	-6.23	
	P4	9	11	19.60	387.27	0.41	0.84	-41.03				-23.41	-2.83	
	P3	12	6	3.71	44.21	0.05	2.32	-41.36					-8.06	
	P6	12	6	3.30	54.34	0.01	2.22	-43.65				-24.3	-6.79	
	P9	12	5	4.49	94.32	0.00	2.082	-44.92					-4.71	
	P8	18	11	17.07	360.24	2.05	0.975	-43.31				-23.68	-13.04	
	P5	18	12	8.28	220.64	0.56	1.613	-41.51	-41.38	-41.45	0.09		-19.81	-19.55
802	P2	18	11	3.27	55.20	4.39	2.195	-41.87					-5.89	
	P10	0	11	19.45	365.89	0.00	0.993	-44.63					0.1	
	P10	0	11		365.89	0.00								
	P2	5.5	11	2.65	41.24	0.01	2.358	-42.6	-42.7	-42.65	0.07		-7.85	
	P1	5.5	10	11.79	224.78	0.01	1.549	-43.02				-24.98	-2.2	
	P8	5.5	9	18.30	360.74	0.02	0.965	-42.73				-22.62	-1.19	
	P6	6						-42.4	-42.49	-42.45	0.06		-8.09	-8.71
	P4	8	11.5	14.15	321.54	0.54	1.195	-45.59	-45.51	-45.55	0.06	-23.67	-12.07	
	P7	9						-38.11					-7.01	-7.49
P5	11						-40.15				-24.32	-9.25		
P9	11	10	8.15	197.81	0.06	1.724	-39.21					-13.37		



BC	799	2	2.5		27.92	534.33	277.89	-46.61		0.27		8.90	8.35	1.00	
			2.5				3.41	-46.17		0.30					
			5.5		24.76	537.31	12.12	-46.22		1.36	-4.67		17.35	8.10	6.80
			5.5				9.52	-46.44	-47.39	1.02	-4.84				
			8.5		15.06	530.65	84.21	-47.29		7.10	-8.21				
			8.5				46.41	-48.33	-48.86	6.50	-7.49	-7.43			
			11.5		7.04	532.07	4794.88	-58.18		280.25	-22.85	-23.06			
			11.5				295.99	-56.27	-56.05	13.52	-11.59				
			14.5		1.81	534.27	2168.64	-61.21		81.32	-22.32	-23.05			
			14.5				2374.47	-62.00		1.11	-21.73				
			17.5		2.51	526.78	1415.39	-58.26		138.97	-24.10				
			17.5				3570.27	-58.44		321.75	-24.32				
			21.5				2677.15	-55.58		370.42	-24.42				
			21.5				227.15	-53.90	-54.19	540.98	-24.39				
			BC	803	1	1.5		24.33	537.60	281.68	-32.03			-19.38	-19.29
4.5		14.54				536.69	3654.68	-46.75	-45.93		-23.76	-23.39			
7.5		9.00				528.98	19465.93	-49.33			-24.04				
10.5		6.66				519.36	25713.49	-49.21	-50.82		-25.31	-24.57			
13.5		4.57				528.75	1984.00	-48.62			-24.79				
GOM	4557	c11	1.5	0.87	28.60	506.90	0.00	-50.96							
			4.5	0.97	23.19	432.48	4.23	-54.65							
			7.5	0.95	28.24	515.76	4.46	-61.04							
			10.5	0.84	29.00	515.58	3.14	-59.72							
			13.5	0.85	25.97	485.66	3.33	-56.62							
			16.5	0.81	28.95	526.33	5.16	-57.16							
GOM	4564	c11	19.5	0.81	28.95	533.62	6.52	-50.89							
			1.5	0.87	27.44	508.60	0.00	-47.94							
			1.5	0.00	0.00	0.00	0.00	-47.61							
			4.5	0.97	25.07	500.06	4.82	-50.75							
			7.5	0.95	24.59	542.38	10.73	-44.57							
			10.5	0.84	19.44	505.42	21.54	-43.52							
			13.5	0.85	18.77	539.10	74.86	-46.32							
			16.5	0.81	17.01	552.41	128.67	-48.40							
19.5	0.81	6.92	553.93	3709.51	-57.68										

## Appendix 3

### 3a: Pore-fluid concentrations and stable carbon isotopic ratios for Pore-Fluid Array.

Depth (mbsf)	Sample ID	Days	SO <sub>4</sub> (mM)	Cl (mM)	[CH <sub>4</sub> ] (uM)	std dev	δ <sup>13</sup> C-CH <sub>4</sub> (‰)	std dev
-1.4	1-1	7	33.87	772.30	53.93			
	1-2	13	29.64	551.27	95.72			
	1-3	19	27.57	521.68	57.11			
	1-4	27	28.60	524.49	55.02			
	1-5	34	30.95	548.23	29.18			
	1-6	41	30.43	554.03	18.90			
	1-7	48	4.17	277.95	20.36			
	1-8	56	31.36	481.99	14.88			
	1-9	64	30.08	544.05	10.50			
	1-10	71	28.90	527.41	5.64			
	1-11	79	34.61	634.40	1.35			
	1-12	88	28.87	528.65	6.27			
	1-13	99	25.15	455.93	2.86			
	1-14	110	27.09	491.18	4.19			
	1-15	112	31.21	552.44				
1.2	3-1	6	16.29	607.79	14131.98	81.39	-35.75	0.36
	3-2	7	17.15	557.51	0.00	0.00		
	3-3	13	12.46	467.16	6711.29	328.17	-35.68	0.29
	3-4	18	16.82	519.39	2971.53	1325.00	-32.48	0.10
	3-5	24	18.22	547.17	7004.25	652.45	-27.05	0.49
	3-6	28	16.86	495.41	0.00	0.00		
	3-7	34	19.42	586.28	2491.68	22.86	-35.69	0.12
	3-8	40	17.15	509.83	3182.61	1536.83	-35.30	0.52
	3-9	47	18.52	543.76	679.07	31.54	-33.75	0.32
	3-10	56	19.64	559.91	1997.55	715.53	-35.69	0.59
	3-11	62	20.55	599.26	3049.59	28.68	-35.19	0.01
	3-12	68	22.44	666.00	1870.01	321.25	-33.08	0.06
	3-13	74	18.46	537.91	1908.75	690.02	-34.58	0.70
	3-14a	80	18.11	516.36	4943.07	529.30	-33.79	0.13
	3-14b	82	18.27	547.81	0.00	0.00		
	3-15	87	21.91	621.80	2704.66	734.48	-34.54	0.67
	3-16	94	20.24	580.08	4428.02	398.71	-34.20	0.45
	3-17	100	18.98	565.69	4318.90	212.14	-33.03	0.64
	3-18	108	21.67	628.72	3196.52	653.79	-32.80	0.55
	3-19a	119	19.41	559.92	3492.99	261.07	-31.56	0.41
	3-19b	119	18.13	524.09	0.00	0.00		
	3-20	125	21.51	564.89	7407.61	424.50	-29.56	0.64
	3-21	132	20.33	578.25	8055.70	169.62	-25.55	0.52
	3-22	139	19.88	570.33	6470.83	392.63	-32.42	0.01
	3-23	146	18.87	531.54	5108.41	241.36	-31.52	0.03
3-24a	156	20.93	590.14	4481.89	355.96	-27.33	0.27	
3-24b	159	19.54	556.49	0.00	0.00			
3-25	168	19.75	561.29	5012.98	331.22	-23.54	0.40	

8.5	8-1	6	0.28	3944.11	3.56
	8-2	13	0.30	4276.93	3.49
	8-3	20	0.33	4528.81	2.31
	8-4	26	1.27	4218.14	1.05
	8-5	28	0.44	4317.75	
	8-6	31	0.96	4323.43	
	8-7	32	0.56	4496.79	
	8-8	38	0.53	4276.84	0.93
	8-9	46	0.55	4519.30	1.32
	8-10	54	0.56	4681.99	2.73
	8-11	59	0.61	4701.54	
	8-12	65	0.66	4772.14	
	8-13	66	0.74	4367.23	
	8-13b	67	0.83	4783.54	
	8-13c	68	0.72	4860.24	
	8-13d	76	0.74	4592.69	1.66
	8-14a	77	0.76	4704.88	
	8-14b	84	0.76	4812.42	4.40
	8-15a	90	0.84	4802.77	2.70
	8-15b	91	0.85	4890.92	
	8-16a	93	0.80	4789.98	
	8-16b	95		4682.67	

---

## Appendix 4

### 4a. HYDRA concentrations and isotopic compositions for data presented in Chapter 4.

Dive	Distance to hydrate (cm)	Depth (cm)	Measured concentrations				Correction factors		Corrected concentrations and isotope			
			Cl (mM)	SO <sub>4</sub> (mM)	CH <sub>4</sub> (mM)	Core SO <sub>4</sub> (mM)	DI-water dilution, f	Channel dilution, x <sup>#</sup>	SO <sub>4</sub> (mM)*	CH <sub>4</sub> (mM)^	δ <sup>13</sup> C-CH <sub>4</sub> (‰)	st dev (n=2)
693	350	1	330.4	17.1	0.003	28.69	0.6		28.45	0.01	-39.44	
		4	121.7	6.6	0.007	28.39	0.2		29.98	0.03	-38.28	
		4	224.7	10.6	0.004	28.39	0.4		26.10	0.01	-35.08	
		7	163.9	8.4	0.068	28.09	0.3		28.31	0.23	-37.88	
		16	72.4	4.8	0.074	n/a	0.1		36.83	0.56	-33.83	
799	200	0	343.0	17.7	0.006	28.70	0.6	1.42	28.16	0.00	-47.25	
		9	257.6	12.7	0.095	14.67	0.5	0.20	26.95	0.48	-42.07	
		9	387.3	19.6	0.337	14.67	0.7	0.16	27.58	2.14	-41.03	
		9	251.4	13.6	0.053	14.67	0.5	0.04	29.40	1.35	-41.23	0.17
		12	44.2	3.7	0.048	8.38	0.1	-0.73	45.74	-0.07	-41.36	
		12	54.3	3.3	0.006	8.38	0.1	-0.14	33.10	-0.04	-43.65	
		12	94.3	4.5	0.002	8.38	0.2	0.19	25.94	0.01	-44.92	
		18	55.2	3.3	3.626	1.00	0.1	-0.08	32.29	-46.01	-41.87	
		18	220.6	8.3	0.440	1.00	0.4	0.33	20.45	1.33	-41.45	0.09
		18	360.2	17.1	1.692	1.00	0.7	0.14	25.82	11.76	-43.31	
798	200	0	346.1	17.0	0.001	28.00	0.6		26.74	0.00	-45.33	
		0	346.1	17.0	0.001	28.00	0.6		26.74	0.00		
		0	54.1	2.7	0.001	28.00	0.1		27.42	0.01	-47.81	0.84
		7	108.1	5.0	0.000	19.48	0.2		25.30	0.00	-37.44	
		16	389.9	19.1	0.150	n/a	0.7		26.70	0.21	-42.01	0.57
		19	284.8	13.7	0.191	n/a	0.5		26.16	0.36	-46.13	0.05
		19	108.3	4.4	0.033	n/a	0.2		22.19	0.17	-44.76	
		22	244.1	8.4	0.398	n/a	0.4		18.84	0.89	-42.70	0.11

# negative numbers mean HYDRA DI water corrected sulfate concentrations were greater than 30 mM, empty cells were not calculated because core did not penetrate deep enough

\* HYDRA sulfate concentrations corrected for DI water dilution, f.

^ non-shaded cells were corrected for DI water dilution; shaded cells corrected for both DI water and channeling dilution

n/a core did not penetrate any deeper

#### 4b HYDRA concentrations and isotopic compositions for data presented in Chapter 4.

Dive	Distance to hydrate (cm)	Depth (cm)	Measured concentrations				Correction factors		Corrected concentrations and isotope			
			Cl (mM)	SO <sub>4</sub> (mM)	CH <sub>4</sub> (mM)	Core SO <sub>4</sub> (mM)	DI-water dilution, f	Channel dilution, x <sup>#</sup>	SO <sub>4</sub> (mM)*	CH <sub>4</sub> (mM)^	δ <sup>13</sup> C-CH <sub>4</sub> (‰)	st dev (n=2)
692	150	8.5	387.1	18.6	0.267	28.58	0.7		25.78	0.37	-40.40	1.51
		14.5	374.9	19.6	0.235	28.45	0.7		28.00	0.34	-41.29	0.01
		14.5	466.9	24.0	0.256	28.45	0.9		27.59	0.29	-40.76	0.87
		17.5	366.0	10.5	2.378	n/a	0.7		15.39	3.49	-39.15	0.42
		17.5	410.4	10.4	2.521	n/a	0.8		13.65	3.30	-39.25	0.65
		25.5	447.6	12.6	2.074	n/a	0.8		15.10	2.49	-39.77	0.72
696	50	2.5	368.0	17.7	0.560	22.44	0.7	0.49	26.27	1.14	-42.39	0.11
		2.5	451.3	21.2	0.633	22.44	0.8	0.58	25.60	1.09	-42.05	0.22
		4.5	400.9	16.4	1.521	16.92	0.7	0.59	22.25	2.57	-42.38	0.06
		4.5	475.3	19.5	1.699	16.92	0.9	0.59	22.34	2.90	-43.02	0.05
		9.5	322.1	5.7	3.018	3.12	0.6	0.76	9.68	3.99	-49.37	0.06
		9.5	362.9	5.2	1.000	3.12	0.7	0.82	7.84	1.21	-49.75	0.02
		10.5	290.4	4.0	2.841	0.36	0.5	0.76	7.43	3.73	-49.65	0.13
		10.5	466.6	5.5	2.853	0.36	0.9	0.79	6.47	3.59	-50.02	0.21
802	overlying	0	365.9	19.5	0.000	28.18	0.7	0.57	28.18	0.00	-44.63	
		0	365.9	19.5	0.000	28.18	0.7	0.57	28.18	0.00		
		5.5	360.7	18.3	0.012	13.12	0.7	0.14	13.12	0.09	-42.73	
		5.5	41.2	2.7	0.008	13.12	0.1	-0.30	13.12	-0.03	-42.65	0.07
		5.5	224.8	11.8	0.012	13.12	0.4	0.08	13.12	0.14	-43.02	
		8	321.5	14.2	0.430	9.27	0.6	0.29	9.27	1.48	-45.55	0.06
		11	197.8	8.2	0.039	6.11	0.4	0.32	6.11	0.12	-39.21	
		13	159.3	7.0	0.069	4.63	0.3	0.24	4.63	1.15	-43.87	0.21

# negative numbers mean HYDRA DI water corrected sulfate concentrations were greater than 30 mM, empty cells were not calculated because core did not penetrate deep enough

\* HYDRA sulfate concentrations corrected for DI water dilution, f.

^ non-shaded cells were corrected for DI water dilution; shaded cells corrected for both DI water and channeling dilution

n/a core did not penetrate any deeper

## Appendix 5

### 5a. Gulf of Mexico reference core pore-fluid and solid phase concentration and stable isotope ratios.

Site	Depth (cm)	SO <sub>4</sub> (mM)	Cl (mM)	H <sub>2</sub> S (mM)	Ca (ppm)	std dev	Mg (ppm)	std dev	SRR (mM/day)	std dev	%TOC	C/N	δ <sup>15</sup> N-TOC (‰)	δ <sup>13</sup> C-TOC (‰)
Ref 1	0	33.06	603.83											
	1	32.30	575.36	-0.08	416.97		1279.66							
	3	31.56	554.91	-0.08	410.42		1271.29							
	5.5	31.49	572.19	-0.08	415.51		1280.14							
	8.5	32.44	585.65		403.72		1268.76							
	11.5	33.13	599.11	-0.05	396.32	2.66	1276.30	16.34						
	14.5	34.04	591.35	-0.07	396.83	4.04	1252.15	11.29						
	17.5	32.79	585.65	-0.08	395.79		1260.46							
	20.5	32.01	604.74	-0.09	396.43		1262.27							
	26.5	31.64	587.19		390.93		1244.51							
	32.5	31.26	571.32		393.42		1255.49							
	38.5	31.70	596.05		394.34		1252.38							
Ref 2	1.5	29.90	557.13	-0.04	412.13	0.53	1273.61	4.18	0.00319	0.00069	1.34	9.65	3.12	-21.50
	4.5	29.25	555.06		411.05		1268.71				1.32	12.63	3.35	-21.58
	7.5	29.17	552.39	-0.04	406.19		1267.13		0.00230	0.00125	1.72	9.24	3.66	-14.77
	13.5	28.72	543.12	-0.05	397.73		1247.76				1.07	11.31	3.00	-22.25
	19.5	29.11	567.52		398.59		1256.70		0.00308	0.00212				
	25.5	27.13	529.38		393.31		1261.64				1.35	12.81	2.62	-23.75
	31.5	28.44	555.28		397.01		1262.42		0.00228	0.00213	1.48	26.32	2.22	-24.13
	37.5	28.53	562.78		417.46		1324.17							



**5b: Gulf of Mexico GB 425 core pore-fluid and solid phase concentration and stable isotope ratios.**

Dive #	Core #	Depth (cm)	SO <sub>4</sub> (mM)	Cl (mM)	CH <sub>4</sub> (mM)	CH <sub>4</sub> (uM)	δ <sup>13</sup> C-CH <sub>4</sub> (‰)
4562	c1	1.5	29.08	571.72	0	0	-35.03
		4.5	29.75	570.8	0.01	14.41	-19.04
		4.5					-19.05
		7.5	30.23	692.86	0.03	31.73	-34.26
		10.5	29.18	542.84	0.03	33.49	-35.7
		13.5	29.93	557.63	0.04	38.06	-45.45

**5c: Gulf of Mexico GC 185 core pore-fluid and solid phase concentration and stable isotope ratios.**

Dive #	Depth (cm)	SO <sub>4</sub> (mM)	Cl (mM)	H <sub>2</sub> S (mM)	Ca (ppm)	std dev	Mg (ppm)	std dev	δ <sup>13</sup> C-DIC (‰)	SRR (mM/day)	std dev	%TOC	C/N	δ <sup>15</sup> N-TOC (‰)	δ <sup>13</sup> C-TOC (‰)
4209	0.00				399.33		1286.19								
	1.50	30.05	551.18		434.68		1312.75								
	4.50	27.81	544.77		431.06		1326.60								
	7.50	28.59	563.42		418.25		1296.57								
	10.50	30.11	551.04		412.92		1287.51								
	13.00	30.35	549.52		417.20		1290.07								
	15.00	29.95	546.38		413.04		1287.39								
	17.00	30.00	539.26		404.01		1284.55								
4211	0.00				407.30		1280.26								
	1.00	30.46	572.83	0.00	448.17		1400.46								
	3.00	30.91	570.27	0.00	418.35		1301.63								
	5.00	29.95	608.50	0.00	415.33		1302.52								
	7.00	29.12	580.62	0.41											
	10.00	27.85	530.04	0.17	409.79		1289.66								
	13.00	29.12	557.21	0.12	397.92		1259.63								
4212	17.00	29.83	600.28	0.01	396.13		1269.44								
	0.00	32.68	583.12		419.48		1339.45								
	1.00	31.21	598.04	0.06	405.64		1316.28					10.88	39.50	1.18	-27.01
	3.00	29.06	610.67	1.47	407.16		1291.40					13.37		1.53	-27.03
	5.00	29.24	598.38	2.10	417.84	1.92	1314.79	5.23				14.74	34.26	1.46	-27.16
	7.00	30.32	579.23	1.47	395.76		1270.42					13.82	37.85	1.71	-27.03
	11.00	28.33	578.24	2.38	401.08		1259.54								
	18.00	26.88	568.50	2.62	404.05		1266.02					12.69	33.02	1.78	-27.03
24.00	28.37	598.71													
4213 c3	1.00	26.95	560.80	2.03	359.70		1237.27		-19.02			6.74	20.59	1.08	-26.11
	3.00	20.24	538.24	6.25	349.20	1.25	1249.14	4.67	-26.78			7.84	27.22	0.83	-26.75
	6.00	5.41	574.65	7.40	312.59		1235.69		-29.83			9.82	30.39	1.37	-27.00
	8.00			7.10								9.44	27.38	1.21	-27.29
	9.00	7.71	589.75	5.40	277.76		1188.17		-24.97			7.86	30.51	1.40	-26.79



	4.50	28.29	509.10
	7.50	29.15	517.74
	10.50	29.79	535.00

4553 c11	1.50	15.93	494.08
	4.50	16.15	536.94
	7.50	24.35	540.88
	10.50	23.64	537.09
	13.50	23.87	544.68

4556 c2	1.50	26.28	509.48
	4.50	26.41	498.93
	7.50	30.12	575.40

4551 c11	1.5	27.11	524.18
	4.5	27.42	562.51
	7.5	28.92	514.71
	7.5		
	10.5	28.55	424.84
	13.5	27.50	531.05
	16.5	26.63	531.89
	19.5	26.77	526.85
	19.5		

---

**5d: Gulf of Mexico GC 232 core pore-fluid and solid phase concentration and stable isotope ratios.**

Dive #	Core #	Depth (cm)	SO <sub>4</sub> (mM)	Cl (mM)	%CO <sub>3</sub>	δ <sup>13</sup> C-DIC (‰)	DIC (mM)	NH <sub>4</sub> (uM)	PO <sub>4</sub> (uM)	NO <sub>3</sub> /NO <sub>2</sub> (uM)	CH <sub>4</sub> (uM)	δ <sup>13</sup> C-CH <sub>4</sub> (‰)
4401	2	0	32.18			0.65	3.92	78.36	17.88	38.64		
		1.5	30.33		23	-12.29	11.82					
		4.5	29.01				-15.30	13.56	333.12	26.64	1.68	
		7.5	28.52		30	-16.27	14.00	214.92	21	2.1		
		10.5					-19.00	14.41				
		13.5	27.27				-17.45	15.10	179.16	23.22	1.74	
		16.5	26.61		32	-19.00		188.46	19.14	2.28		
4401	4	1.5	30.17		33	-8.73	11.17	718.56	37.32	12.06		
		4.5	30.14			-9.72	9.15	658.32	38.4	10.92		
		7.5	32		34	-11.50	9.61	544.8	14.88	5.52		
		10.5	29.8		30	-13.58	11.09	568.08	17.22	4.98		
		13.5	30.08			-14.08	12.29	535.14	32.58	5.1		
4403	4	16.5	30.44		31	-14.84	5.21	476.4	5.34	4.5		
		0	30.02			-0.52	4.47					
		1.5	30.64		40	-15.02	14.25					
		4.5	37.24			-16.62	17.54					
		7.5	29.47		50	-16.49	7.36					
		10.5	20.32			-18.44	9.77					
4403	6	13.5	29.73			-18.89	12.34					
		16.5	30.26		62	-18.26	14.76					
		0	29.78			-1.66	7.77					
		1.5	29.92		20	-5.23	3.51					
		1.5				-5.22	3.09					
		4.5	28.79		32	-8.31	8.36					
		4.5				-7.27	7.28					
		7.5	26.85			-10.58	10.00					
		7.5				-10.81	7.96					
		10.5	24.46			-12.85	11.31					
		13.5	25.19			-12.39	0.00					
		16.5	23.49		19	-12.55	11.26					
19.5	25.02			-13.39	13.77							
22.5	20.19			-14.59	32.98							

4405	2	25.5	19.18		-14.32							
		0	30.98		-6.60	4.00	43.26	20.7	6.24			
		1.5	20.96	38	-22.80	16.98	409.56	57.36	40.5			
		1.5			-22.12	60.51						
		4.5	13.48		-18.05	26.32						
		7.5	6.77	62	-14.50	11.69	94.62	34.92	12.3			
		10.5			-13.77	58.92						
		10.5			-13.92	52.02						
		13.5	8.11	46	-12.52	61.87	83.94	46.32	6.9			
		16.5	6.12		-6.53							
		19.5	3.03	24	-2.86	72.82	106.02	24.6	14.28			
		22.5	3.23		-0.44	87.02	117.54	37.68	7.86			
		4405	3	25.5	3.65		0.62	86.31				
0	25.57				0.06	5.31	48	8.1	63.9			
1.5	28.15				-8.98	9.33	841.44	55.62	654.96			
4.5	23.98			33	-18.61	9.63	572.28	23.46	32.04			
7.5	19.96				-22.26	9.22	402.3	9.06	23.34			
10.5				32	-26.85	29.70	329.52	26.94	38.82			
10.5	19.28				-30.86							
13.5	10.95				-31.16	25.95	1831.9	374.5	133.74			
16.5	7.96				-24.11	65.39	416.04	92.46	26.94			
19.5	7.23			55	-21.47	28.17	351.36	41.04	10.14			
4564	11	22.5	3.8		-7.73	49.44	348.48	36.36	12.84			
		1.5	27.44	508.6						0.00	-47.94	
		1.5								0.00	-47.61	
		4.5	25.07	500.06						4.78	-50.75	
		7.5	24.59	542.38						9.65	-44.57	
		10.5	19.44	505.42						20.00	-43.52	
		13.5	18.77	539.1						72.85	-46.32	
		16.5	17.01	552.41						125.76	-48.4	
		19.5	6.92	553.93						3152.89	-57.68	

**5e: Gulf of Mexico GC 233 core pore-fluid and solid phase concentration and stable isotope ratios.**

Dive #	Depth (cm)	so <sub>4</sub> (mM)	Cl (mM)	H <sub>2</sub> S (mM)	Ca (ppm)	Mg (ppm)	%TOC	C/N	δ <sup>15</sup> N-TON (‰)	δ <sup>13</sup> C-TOC (‰)
4555 c8	1.5	27.8	577.25							
	4.5	26.2	551.02							
	7.5	28.27	586.66							
	10.5	27.33	579.63							
	13.5	25.95	596.52							
	16.5	23.49	617.24							

5f: Gulf of Mexico GC 234 core pore-fluid and solid phase concentration and stable isotope ratios.

Dive #	Core #	Depth (cm)	SO <sub>4</sub> (mM)	Cl (mM)	H <sub>2</sub> S (mM)	Ca (ppm)	std dev	Mg (ppm)	std dev	CH <sub>4</sub> (uM)	δ <sup>13</sup> C-CH <sub>4</sub> (‰)	%CO <sub>3</sub>	δ <sup>13</sup> C-DIC (‰)	DIC (mM)	NH <sub>4</sub> (uM)	PO <sub>4</sub> (uM)	NO <sub>3</sub> /NO <sub>2</sub> (uM)	SRR (mM/day)	Std dev	%TOC	C/N	δ <sup>15</sup> N-TON (‰)	δ <sup>13</sup> C-TOC (‰)			
4215	4	0.0	29.59	580.17		418.21	0.18	1317.97	1.38																	
		1.0	28.25	581.08	0.00	403.45			1256.13					-2.58												
		3.0	28.49	571.88	0.00	399.05			1240.99					-2.59												
		5.0	27.84	543.10		386.67	0.21		1205.50	0.55				-5.35												
		7.0	28.67	530.54	0.00	406.32			1273.95					-5.73												
		9.0	29.48	551.60	0.00	407.70			1269.06					-6.31												
		11.0	29.05	566.79	0.00	398.07			1258.72					-6.08												
		11.0		560.57																						
		13.0	29.22	560.84	0.00	412.56			1294.97						-6.47											
		15.0	29.92	572.30	0.00	406.56	0.01		1274.80	3.92																
		16.5	29.51	565.87	0.00	416.05			1280.94																	
		18.5	27.02	521.24	0.00	370.94			1167.99																	
		4216	1	1.0	29.68	567.06	0.01																			
3.0	29.69			566.61	0.09																					
5.0	29.26			569.44	0.27																					
7.0	28.90			588.08	0.54																					
9.0	27.39			575.48	0.45																					
11.0	27.19			570.29	1.11																					
13.5	26.47			564.12	2.20																					
4217	7	17.5	25.41	554.07	2.82																					
		0.0	28.95	577.29		408.77			1292.84																	
		1.0	24.90	590.00	0.99	398.82			1267.86					-17.83					3.57	1.0	13.56	21.41	0.91	-25.81		
		3.0	19.47	558.53	1.37	387.51	14.17		1234.38	17.40				-21.21					5.15	1.8						
		5.0	14.54	553.93	3.29	366.06			1250.54					-21.26					8.79	5.0	12.50	24.52	1.19	-25.83		
		7.0	7.18	509.82	2.55	297.23			1200.52										4.48	0.2						
		9.0	4.91	560.28	1.37	273.92			1258.26										1.31	0.2	9.22	22.41	1.82	-27.38		
4218	7	11.0	2.84	571.34	1.42	280.30			1278.35										1.11	0.6						
		13.0	2.83	567.77	1.26	287.51			1309.24										0.45	0.1	7.35	23.09	1.57	-27.17		
		0.0	28.84	553.21		416.58			1307.13																	
		1.0	28.97	544.60	0.00	410.28			1299.32					-2.67						0.03	0.0					
		3.0	27.83	539.99	0.00	394.98	2.16		1256.04	6.10				-0.58						0.03	0.0	3.60	13.91	2.48	-25.26	
		5.0	27.19	544.04	0.00	402.61			1294.40					1.93						0.02	0.0	4.37	16.47	2.41	-25.79	
		7.0	27.54	542.87	0.00	418.28			1331.28					-3.10						0.02	0.0					
		9.0	29.08	585.36	0.00	403.77			1263.23					-4.53						0.03	0.0	5.23	18.60	1.67	-26.28	
		11.0	29.14	579.79	0.00	402.60			1254.62					-3.78						0.03	0.0					
		13.0	29.22	567.45	0.01	405.43			1264.31					0.00						0.03	0.0	5.24	18.54	1.91	-26.40	
		15.0	28.45	536.12		409.89			1278.47					-2.78						0.02	0.0					
		17.5	31.16	554.50	0.01	421.63			1314.49					-4.82						0.02	0.0	5.62	20.48	1.85	-26.50	
		20.5	28.57	526.63	0.24	409.34			1267.80					-5.41						0.03	0.0					
23.5	27.62	528.87	1.10	406.55			1256.17											0.03	0.0	5.69	20.27	2.19	-26.57			
26.5	26.76	565.25	1.37	416.32			1307.55											0.03	0.0							
4221	1	1.0	15.01	570.59	8.74	319.98			1229.55																	



		3.0	12.18	578.06	8.87	306.02		1191.23						
		5.0	7.54	573.27	10.36	281.19		1169.71						
		9.5	2.14	613.70	11.99	237.48		1188.31						
		12.5	2.45	572.37	13.41	220.46		1236.78						
		18.5	4.44	591.12	16.14	233.35	0.71	1214.44	2.21					
		24.5	5.99	611.38	17.81	238.99		1213.80						
		27.5	6.44	577.05	25.64	267.19		1267.02						
4407	1	0.0	31.6						0.76	4.90	38.1	3	12.3	
		1.5	29.22					51.7	-3.75	10.09	202.62	21.96	25.98	
		1.5							-4.13	9.92				
		4.5	27.17						-4.1	9.08	148.56	2.82	14.94	
		7.5	28.59					42.89	-15.91	5.41	80.4	24	2.04	
		10.5	17.86						-18.16	36.83	277.02	28.5	13.5	
		13.5	14.5						-29.95	37.36	92.1	19.32	9.66	
		16.5	18.63					59.56	-27.54	18.84	96.18	15.06	6.54	
4407	4	0.0	30.63						1.03	2.14	31.5	4.5	8.7	
		1.5	30.73					44.89	-5.64		158.58	15.24	14.16	
		4.5	29.92						-8.38	7.31	316.44	23.94	14.88	
		7.5	30.18						-12.06	6.14	399.48	15.72	20.46	
		10.5	30.61					41.43	-13.44	8.73	494.1	12.06	16.56	
4407	5	0.0	30.94						0.82		39	24.6	12	
		1.5	30.04						-4.54		222	49.26	46.62	
		4.5	28.75						-8.67		277.02	28.14	23.22	
		7.5	31.03						-9.3		374.7	5.1	26.64	
		10.5	28.21						-9.24		258.42	24.12	5.76	
		13.5	29.14						-10.86					
		16.5	29.03						-11.34		229.92	7.08	10.62	
		19.5	29.47						-14.21		262.32	24.66	21.78	
		22.5	20.32						-10.48		266.52	21	15.48	
		25.5	36.79						-11.03		244.98	10.08	25.62	
4557	1	1.5	29.76	556.2										
		4.5	25.34	530.5										
4557	11	1.5	28.6	506.9					0				-50.96	
		4.5	23.19	432.5					4.19				-54.65	
		7.5	28.24	515.8					4.013				-61.04	
		10.5	29	515.6					2.914				-59.72	
		13.5	25.97	485.7					3.24				-56.62	
		16.5	28.95	526.3					5.039				-57.16	
		19.5	28.95	533.6					5.655				-50.89	

---

**5g: Gulf of Mexico MC 118 core pore-fluid and solid phase concentration and stable isotope ratios.**

Dive #	Core #	Depth (cm)	$\delta^{13}\text{C-DIC}$ (‰)	DIC (mM)	$\text{SO}_4$ (mM)	Cl (mM)	$\text{NO}_3^-/\text{NO}_2^-$		
							$\text{NH}_4$ (uM)	$\text{PO}_4$ (uM)	$\text{NO}_2$ (uM)
4414	1	0.00	0.26	1.17					
		1.50	-9.93	7.85	26.30	2031.91	62.88	275.10	
		4.50	-14.12	7.86	16.96	29656.76	5.82	424.86	
		7.50	-13.30	5.48	20.75	15220.06	2.40	153.84	
		10.50	-23.46	6.90	18.20	14612.46	7.20	107.40	
		13.50	-21.87	56.33	11.09	1654.32	69.18	188.22	
		16.50	-13.84	24.07	10.55	2001.66	125.22	56.28	
		19.50	-3.39	27.82	11.39	2975.90	43.26	67.98	
		22.50	0.47	59.26	6.41	1501.51	68.88	119.22	
25.50	3.31	39.84	3.91		79.86	132.24			

**5h: Gulf of Mexico VK 826 core pore-fluid and solid phase concentration and stable isotope ratios.**

Dive #	Core #	Depth (cm)	SO <sub>4</sub> (mM)	Cl (mM)	δ <sup>13</sup> C-DIC (‰)	DIC (mM)	%CO <sub>3</sub>	NH <sub>4</sub> (uM)	PO <sub>4</sub> (uM)	NO <sub>3</sub> /NO <sub>2</sub> (uM)		
4410	6	0	31.55		1.34	1.99		37.86	15.30	85.32		
		1.5	32.13		-2.37	0.81		100.08	20.70	52.92		
		4.5	32.53		-2.80	5.81		72.30	8.76	9.60		
		7.5	32.19		-3.58	4.24	60.01	340.80	37.80	51.00		
		10.5	34.37		-3.57	4.83		555.30	20.76	33.36		
		13.5	32.67		-4.16	4.42		462.78	22.62	33.48		
		16.5	31.44					566.10	23.82	39.30		
		16.5			-4.06							
		19.5	31.16		-4.77	2.56	39.70	617.52	18.60	22.62		
		22.5	30.91		-5.88	5.38		831.24	16.50	36.48		
		25.5	30.78		-7.74	6.59		837.42	4.92	45.06		
		4411	1	0	29.31		1.26	1.17		55.44	17.04	2.28
				1.5	30.12		-2.92	5.84		72.00	30.00	60.48
7.5	29.76				-4.99	7.39		173.28	29.64	69.54		
13.5	33.94				-5.89	6.17		174.54	15.06	52.62		
19.5	33.45				-5.98	7.29		51.90	3.42	14.70		
25.5	29.38				-6.77	9.56		255.72	14.16	25.98		
28.5	29.62											
31.5	28.87				-12.34	-1.15		386.22	34.32	9.00		
4411	2	0	28.93		1.36	2.28		35.04	6.48	56.88		
		1.5	29.39		-1.66	4.79		86.40	22.26	66.00		
		4.5	29.83		-3.64	5.77		152.76	34.14	38.46		
		10.5	30.01		-5.33	8.42		237.90	19.32	45.78		
		13.5	30.02		-6.65	5.87		42.48	6.12	6.78		
		19.5	30.58		-3.98	7.75		246.36	22.20	86.58		
		22.5	30.76		-3.79			187.62	20.58	58.26		
		28.5			-5.02	5.70		239.40	25.14	68.34		
		31.5	30.06		-4.75	5.10		272.28	13.26	48.00		

**5i: Core numbers and locations collected on Blake Ridge Hydrate cruise 2002.**

Core #	core type	Latitude*	Longitude*	Core Length (cm)	Sulfide onset (cm)	Comments^
1	piston			1000		two samples for Thomas and one for J.P.
1	gravity			70		
2	piston			594	82	badly bent pipe top of section #3 and we took three gas samples
2	gravity			94		bivalves at top
3	piston	32.29.6515	76.11.5502	416		additional sample for J.P. for carbonates H2S bottom of S2
3	gravity	32.29.6515	76.11.5502	141		no water over core.
4	piston	32.29.6543	76.11.4840	128	402	bent pipe on section #2 carbonate lump in the nose, collected for J.P.
4	gravity	32.29.6543	76.11.4840	0		pipe was empty
5	gravity					gravity core for Thomas
6	gravity			104		gravity core for Thomas shell and holes in sediment
7	gravity			99		gravity core for Thomas, sample for J.P. carbonates
8	gravity			86		gravity core for Thomas
9	gravity			98		gravity core for Thomas, copepod sample for J.P.
10	piston	32.29.6278	76.11.3628	566		worm holes 1 cm diameter
10	gravity	32.29.6278	76.11.3628	126		
11	piston	32.29.6648	76.11.3259	429	302	worm holes 1 cm diameter
11	gravity	32.29.6648	76.11.3259	106		raining while taking samples, no over lying water
12	piston	"32.29.6527"	"76.11.3379"	842	602	worm holes to 150 cm
12	gravity	"32.29.6527"	"76.11.3379"	69		one section for Thomas
13	piston	"32.29.6050"	"76.11.4570"	407	382	on section for Steve Newell
13	gravity	"32.29.6050"	"76.11.4570"	0		hit twice
14	gravity			empty		one section for Thomas, and had carbonate
15	gravity			47		one section for Thomas
16	gravity	"32.29.66"	"76.11.5230"	80		gravity core for Thomas
17	gravity	"32.29.66"	"76.11.53"	95		one section for Thomas
18	piston	"32.29.6500"	"76.11.5140"	249	236	worm holes, condensation, was cool
18	gravity	"32.29.6500"	"76.11.5140"	85		worm holes, and black micro pockets, one section for Thomas
19	piston	32.30.0510	76.11.2366	465	452	one section for Steve, two section for Thomas, and one alien creature, indentation from core catcher
19	gravity	32.30.0510	76.11.2366	138		discarded it was over filled

20	piston	32.29.9542	76.11.6386	60	bent the core head, brown layer followed by shells, followed by another brown layer the gray, sediments samples no pore water.
20	gravity	32.29.9542	76.11.6386	17	J.P 4-17, lots of large shells.
21	gravity	"32 29.966"	"76 11.613"	96	gravity core for Thomas
22	gravity	"32 30.015"	"76 11.43"	60	orange worm, H2S smell
23	gravity	"32 30.01"	"76 11.83"	94	brown top 10 cm, grey downcore below, no smell
24	pgravity	"32.30.035"	"76.11.418"	304	seas were to rough for piston core used the piston as a gravity core, brown worm holes some surface may have been lost, took sample from "worm hole"
25	pgravity	32.29.2587	76.09.3708	301	some surface was lost, carbonate where we found the alien in bottom layer
26	pgravity	"32.29.283"	"76.08.884"	empty	
27	piston	"32.29.281"	"76.08.881"	809	one section for Thomas, 5 sections for Matsu, 0-15, light gray w/sand,0-30 fine carbonate, 30-200.5 gray,200.5-500 marbling light dark gray.
27	gravity	"32.29.281"	"76.08.881"	138	one section for Thomas
28	piston	32.29.685	76.11.2623	1065	strong H2S, began to crack at 1000 cm
28	gravity	32.29.685	76.11.2623	106	one section for Thomas
29	piston	32.29.6547	76.11.3428	1015	Six sections for Matsu, one for Thomas
29	gravity	32.29.6547	76.11.3428	143	One section for Thomas, no over laying water
30	piston	32.29.6241	76.11.2968	1018	four of the NRL sample were checks, one Thomas, and 15 Matsu, lots of notes on color of core
30	gravity	32.29.6241	76.11.2968	139	One section for Thomas
31	piston	32.29.6660	76.11.3370	1039	14 Matsu samples, gas sample at 935 cm, gas cracks to 870 cm, from pushing the piston cable into the core, water was forced out the bottom of S1.
31	gravity	32.29.6660	76.11.3370	no data	blank page
32	piston			hydrate	gas sampled between 255-300, hydrate in core catcher, two pieces of hydrate at 406 cm.
32	gravity			88	
33	gravity				to look for hydrate, none found
34	piston	32.29.6707	76.11.4120	hydrate	bubbling profusely while setting in surface water, pipe is straight, 0-40 sediment, 40-50 gas pockets, 50-129 sediment, s2 water, hydrate found at sect 4 of bottom section ~215 cm from end
34	gravity	32.29.6707	76.11.4120		worked on hydrates left gravity core in holder
35	gravity	32.29.6916	76.11.432	no data	to look for hydrate, none found
36	gravity	32.29.6640	76.11.4227	no data	to look for hydrate, none found

\*Latitude and longitudes in parentheses are best guesses.

^J. P. is John Pohlman and Thomas was the camera guy from Hawaii. Not sure who Matsu or Steve Newell are.

**5j: Blake Ridge ‘unremarkable’ core pore-fluid concentrations and stable isotope ratios.**

Core #	Depth (cm)	SO <sub>4</sub> (mM)	H <sub>2</sub> S (mM)	δ <sup>13</sup> C-CH <sub>4</sub> (‰)	CH <sub>4</sub> (uM)
1	2	29.19	0.00		
	57	29.82	0.00		
	57	32.90	-0.02		
	502	26.03	-0.01	-57.04	
	587		0.02		
	302	29.46	0.01	-51.49	
	687	19.68	-0.05	-66.02	0.64
	887	14.81	0.11	-73.25	0.90
	987		0.95	-76.90	1.63
2	0	30.00			
	7	28.96	0.00		
	22	29.06	0.00		
	37	27.44	0.02		
	67	28.61	0.00		
	52	30.30	0.00		
	82	28.18	0.19		
3	0	29.74			
	2		0.03		
	32	29.07	0.15		
	59	31.73	0.11		
	2		0.11		
	87	30.91	0.09		
	202	30.99	0.07		
	317	29.25	0.09		
	387	28.38	0.18		
4	2	30.33	0.00		
	52	30.25	-0.01		
	82	30.09	0.01		
	102	30.52	0.01		
	202	29.72	0.00		
	302	27.33	-0.01		
	402	27.56	0.04		
11	0	28.76			
	2	27.83	0.00		
	37	28.15	0.08		
	91	28.20	0.02		
	87	28.45	0.01		
	202	27.49	0.01		
	302		0.10		
	402	22.11	1.95		
12	52	30.20	0.02		
	52	30.61	0.02		
	67		0.01		
	202	30.23	0.01		
	402	29.21	0.01		
	602	25.83	0.28		

	802	20.18	1.60
13	2	29.80	-0.01
	67	29.46	
	87	28.96	0.01
	202		-0.02
	252	29.51	0.02
	302	30.31	0.01
	352	28.84	0.02
	382	26.56	0.55
	402		0.07
18	2	28.65	0.03
	32	30.15	0.00
	72	29.09	0.02
	72	28.54	0.00
	137	28.94	0.00
	235.5	27.68	0.08
19	2	29.33	0.01
	52		0.04
	102		0.01
	202		0.01
	302	28.65	0.01
	352	27.49	0.02
	402	27.29	
	452	26.14	0.08
20	0	30.04	0.00
24	2	28.61	0.00
	52	28.40	0.00
	102	27.12	0.00
	152	28.99	0.00
	202	28.99	0.00
	252	28.55	0.00
	283	28.43	
25	17	28.84	
	102	27.72	
	152	25.59	
	202	26.01	
	277	24.35	
27	2	28.89	-0.01
	102	28.29	0.00
	102	28.51	0.00
	197.5	26.69	0.01
	302	25.68	-0.01
	402	24.06	-0.01
	482	23.81	0.01
	602	22.92	0.02
	652	23.97	0.05
	702	22.31	0.17
	752	21.40	0.01
	791	20.71	0.01

---

5k: Blake Ridge 'remarkable' core pore-fluid concentrations and stable isotope ratios.

Core #	Depth (cm)	SO <sub>4</sub> (mM)	H <sub>2</sub> S (mM)	δ <sup>13</sup> C-CH <sub>4</sub>	CH <sub>4</sub> (uM)	DIC (mM)	δ <sup>13</sup> C-DIC (‰)	δ <sup>13</sup> C-TOC	%TOC	δ <sup>13</sup> C-TIC	%TIC	%CO <sub>3</sub>	porosity
28	0	29.90				2.76	0.52						
	2	28.07	0.00										
	87	28.73	0.00	-47.93		2.91	-1.19	-22.65	0.47	1.00	2.11		0.61
	87	27.96	0.01					-23.06	0.44	1.29	1.85		0.65
	202	28.03	2.20	-51.33	1.29	2.86	-0.79	-19.59	0.39	1.36	6.87		0.63
	302	28.03	2.34	-59.76		2.84	-2.08	-20.63	0.51	-0.73	7.05		0.64
	402	27.64	0.13	-68.76	1.25	3.26	-7.49	-20.70	0.35	0.88	6.96		0.61
	502	25.06	1.75	-76.94	7.37	4.49	-19.39	-22.97	0.24	-3.90	4.36		0.55
	602	20.68	3.72	-80.54	13.08	6.60	-30.15	-21.67	0.30	-0.38	2.49		0.60
	702	15.60	5.61	-83.94	23.74	9.16	-36.01	-21.25	0.67	0.36	4.62		0.62
	749	12.77	5.26	-85.31	32.60	9.78	-38.78	-20.27	0.48	0.01	6.60		0.63
	802	14.02	6.46	-87.68	50.81	8.77	-37.50	-21.00	0.41	-0.07	7.02		0.61
	852	6.93	9.20	-88.16	64.80	11.79	-42.64	-23.00	0.66	-1.78	3.58		0.62
	902		12.22	-88.73	97.61	13.25	-44.56	-22.34	0.26	-1.27	2.65		0.55
	952			-86.54	443.57			-21.24	0.18				0.55
29	1002	1.54	11.55	-82.16	1900.13	14.59	-43.56	-20.92	0.59	-1.19	5.42		0.59
	1047	1.23	7.47	-78.14	2602.25	14.62	-41.14	-21.32	0.61	-0.61	4.18		0.61
	2	28.33		-48.74		3.05	-0.90	-18.81	0.74	1.85	6.84		0.69
	102	28.80				2.87	-1.47	-21.69	0.73	0.65	2.33		0.67
	102	29.07		-49.94		2.85	-1.04	-21.61	0.22				0.55
	202	28.56		-53.93		2.92	-1.47						
	390	26.91	0.22	-80.89	3.56	4.07	-14.70	-19.55	0.47	1.16	6.91		0.62
	502	22.66	5.47	-85.03	11.14	5.93	-29.48	-21.70	0.65	0.76	3.05		0.68
	602	19.13	9.93	-88.07	17.14	7.12	-36.04	-21.05	0.42	0.29	6.05		0.61
	698	12.41	5.68	-90.80	27.18	9.59	-43.05	-19.46	0.33	-1.92	8.31		0.63
	802			-93.74	58.02	11.78	-46.82	-22.04	0.21	-2.55	3.24		0.55
	802	7.16	6.01	-93.89									
	902	2.14	9.41	-96.31	228.59	15.24	-49.86	-23.92	0.29	-1.59	3.47		0.57
	997	1.24	7.80	-80.50	1331.00	14.40	-44.92	-21.47	0.62	-3.23	4.75		0.59
	30	2	30.93				2.68	-0.30	-18.91	0.63	2.00	6.41	
87		28.65				2.77	-0.89	-22.37	0.21	0.71	2.49		0.59



	102	28.54			3.07	-0.82	-19.97	0.58	2.26	6.42	0.67	
	202	28.65			2.99	-1.17	-20.67	0.77	1.01	3.77	0.71	
	302	28.33	-55.67		3.08	-2.16	-19.58	0.42	1.51	6.35	0.64	
	382	27.89	-62.14	0.10	3.16	-4.17	-22.04	0.53	0.36	3.64	0.62	
	502	27.31	-70.91	1.05	3.86	-12.82	-22.20	0.57	0.05	2.59	0.67	
	552	26.35	-73.31	1.21	4.12	-15.95	-20.81	0.61	-2.77	6.81	0.66	
	592	24.02			4.38	-18.79						
	596	24.07			4.57	-19.62						
	602	25.63	-74.49	1.61	4.66	-19.44	-21.22	0.41	0.80	4.19	0.62	
	652	24.27	-76.97	2.26	5.42	-22.85	-20.75	0.34	0.65	5.62	0.63	
	682	21.86			5.34	-24.95						
	686	23.43			5.57	-24.93						
	692	21.48	-77.61	2.70	5.61	-25.20	-20.46	0.34	0.28	6.22	0.61	
	752	19.16	-79.83	4.62	6.86	-29.47	-22.24	0.24	-1.10	4.99	0.58	
	802	17.27	-80.54	2.58	7.11	-31.18	-21.73	0.14	-0.62	3.01	0.53	
	842	17.67			8.35	-33.36						
	846	15.46			8.43	-33.48						
	852	15.73	-82.97	2.54	8.46	-33.71	-22.92	0.23	-0.01	2.30	0.53	
	902	13.21	-83.04	11.06	9.18	-35.14	-22.05	0.28	-0.19	2.46	0.58	
	952	11.61	-83.28	6.50	9.82	-36.91	-20.89	0.51	0.25	3.78	0.61	
	982	10.22			10.25	-38.40						
	986	9.83			10.39	-37.43						
	992	9.93	-84.74	6.10	10.28	-37.84	-21.47	0.54	-0.65	5.32	0.61	
31	102	29.60	-59.34		3.04	-2.79	-21.10	1.24	4.85	1.87	0.65	0.56
	202	29.31	-72.55	1.57	3.06	-3.91	-22.01	0.35	0.63	2.29	0.57	0.69
	302	27.31	-79.59	5.43	3.52	-9.87	-20.12	1.23	2.80	4.78	1.09	0.60
	402	24.64	-83.92		4.70	-23.13	-20.93	0.62	1.32	6.11		0.62
	502	19.83	-85.75	17.77			-20.42	0.61	0.82	4.47	1.73	0.62
	602	14.12	-88.73	27.31	8.16	-40.93	-18.23	0.65	-0.98	5.51	1.69	0.61
	652		-90.00		9.46	-43.44	-21.55	1.01	1.23	4.36	2.00	
31	652	11.81	-90.57									0.57
	702	7.93	-90.42		10.50	-46.27	-20.56	0.34	-1.71	5.94		0.63
	752	3.79	-92.89	195.13	12.42	-48.91	-20.58	0.45	-2.36	6.44	1.83	0.56
	802	1.87	-84.70	1553.27	12.48	-47.35	-16.11	0.44	-9.69	4.32	1.16	0.51
	852		-77.73	2285.11	12.43	-44.25	-22.71	0.17	-8.26	3.77	1.52	0.53

902	0.97	-76.47	2856.96	12.66	-41.44	-23.39	0.27	-10.39	2.61	1.18	0.60
937	1.04	-75.66	1898.67	12.31	-40.05	-22.59	0.49	-0.08	2.49	1.28	0.62
952	0.81	-75.18	2172.62	12.25	-38.97					1.07	0.69
1032			1033.77		-37.11	-22.09	0.45	-0.61	3.93	1.60	

**5l: Blake Ridge core dissolved sulfate  $\delta^{34}\text{S-SO}_4$**

Core #	Depth (cm)	avg $\delta^{34}\text{S-SO}_4$ (‰)	stdev
1	57	20.45	0.21
	502	23.30	0.14
28	0	20.15	0.07
	302	20.95	0.07
	802	24.50	0.00
29	202	20.70	0.28
30	992	29.35	1.20
31	202	20.75	0.21
	602	26.40	0.14
	702	29.15	0.07

5m. Northern Cascadia Margin 2002 cruise sites

Core number	Site name	Latitude	Longitude	Water depth (m)	Cores for whom?	Date
1	Vent Site	48.6673	126.8458	1267	Chem	7/26/2001
2	Cucumber Ridge	48.7074	126.8788	1321	Phys/Chem	7/27/2001
3	Cucumber Ridge	48.7056	126.9174	1315	Chem	7/27/2001
4	Vent Site	48.7072	126.9196	1327	Chem	7/28/2001
5	Vent Site	48.7052	126.9128	1325	Phys	7/28/2001
6	Vent Site	48.6661	126.8511	1265	Chem	7/29/2001
7	Vent Site	48.6675	126.8518	1264	Hydrate	7/29/2001
8	Vent Site	48.6683	126.8503	1259	Hydrate	7/30/2001
9	Fish Boat/Barkley Canyon	48.3032	126.0761	840	Chem	8/1/2001
10		48.3032	126.0760	840	Phys	8/1/2001
11	Fish Boat/Barkley Canyon	48.3013	126.0800	871	Chem(AMO)	8/1/2001
12	Fish Boat/Barkley Canyon	48.3009	126.0780	884	Phys/Chem	8/2/2001
13						
14		49.3467	127.1368	lost core barrel		
15		49.3333	127.1500	184	5cm recovered	
16		49.0006	126.7266	240	nothing recovered	
17					no core here	
18	Ocean Basin	49.1783	127.8634	2458	Chem	8/6/2001
18P	Vent Site	49.1667	127.7832	2493	Phys/Chem	8/7/2001
19	Vent Site					
20	Vent Site					
21	Vent Site					

### 5n. Cascadia Margin 'Vent Site' pore-fluid concentration and isotope data

Core #	Depth (cm)	SO <sub>4</sub> (mM)	stdev	Cl (mM)	CH <sub>4</sub> (uM)	δ <sup>13</sup> C-CH <sub>4</sub> (‰)	δ <sup>13</sup> C-TOC (‰)
Core 1	0	28.87		501.04			
	6	30.59	1.22	558.57			
	16	31.50		599.68			
	26	31.30	0.23	603.65			
	46	29.83		637.25		-47.38	
	56	30.22	3.86	603.81			
	66	27.44		563.82			
	76	26.49		565.68			
	86	28.85	0.60	556.95			
	96	26.88		556.97			
	106	25.61		529.03			
	216	16.95		551.08		-52.82	
	306	4.11		548.91		-78.82	
	516	2.12		612.59			
	576						-97.22
Core 4	0	28.46		551.24			
	3	30.00	1.21	562.02			
	15						
	2.5	29.48	1.02	540.80			-24.20
	12.5						
	27.5						-23.55
	37.5	28.98	0.25	604.10			
	47.5						-25.28
77.5						-23.10	
Core 6	2.5	30.44		540.76	215.99	-60.20	
	12.5	29.61		540.77	0.12	-69.94	
	22.5	27.74		510.04	0.24	-73.30	
	32.5	28.75		574.71	0.20		
	42.5	28.61		547.62	0.30		
	52.5	27.25		555.74	0.33		
	62.5	29.18		553.08	0.28	-74.22	
	72.5	27.46		571.54	0.32		
	92.5	25.74		561.07	0.51		
	122.5	23.55		572.99	0.42		
	172.5	20.47		553.05	0.70		
	202.5	17.45		540.55	0.61		
	282.5	11.43		563.16	1.12		
	322.5	8.36		560.47	1.56		
	362.5	5.82		564.08	1.38	-80.77	
	402.5	2.14		552.74	26.76	-109.37	
	452.5	1.55		573.33	58.69	-94.09	
	532.5	1.51		545.84	3098.05	-86.14	
592.5	1.44		585.64	2631.28	-83.56		
642.5	1.15		579.74	1044.05	-80.54		
692.5	1.85		616.29	1417.33	-78.53		
722.5	1.16		530.60	1558.92	-77.53		

Core 7	20	6.20		597.84		
	46	3.92		609.23		
	68	3.13		645.36		
	in hyd zone	2.24		504.35		
	Bot Water	26.97		509.42		
	Hyd water	3.36		63.37		
Core 8	68	4.88		508.61		
	126	3.43		540.25		
	Hydrate water	10.11	0.11	151.11		
Core 18P	5	28.37		552.54		-21.69
	45	29.92		572.49		
	85	30.01		587.76		-21.71
	145	31.02		577.04		
	353	0.00		0.00		-21.49
	426	20.07		619.30		
	500	15.96		0.00	-56.91	-23.23
Core 19	575	11.99		569.29		
	0	27.84	0.26	546.04		
	2.5	27.88		571.67	0.78	-21.76
	2.5	0.00		0.00	0.78	
	17.5	29.15		542.41	0.72	
	32.5	27.61		559.83	0.91	-19.29
	32.5	0.00		0.00	0.90	
	52.5	26.55		583.56	1.09	
	52.5	0.00		0.00	0.57	
	82.5	25.60		580.29	1.08	-19.82
	82.5	0.00		0.00	1.02	
	132.5	22.11		541.65	1.18	
	132.5	0.00		0.00	1.18	
	182.5	22.78		556.13	1.60	-65.95
	182.5	0.00		0.00	1.53	-67.00
	252.5	17.21		0.00	0.00	-67.50
	252.5	0.00		0.00	1.25	-65.92
	302.5	1.77		556.08	1.55	-72.22
	302.5	0.00		0.00	1.69	-70.40
	402.5	9.99		619.24	3.89	-82.31
402.5	0.00		0.00	3.83	-83.60	
502.5	4.22		579.63	16.35	-102.98	
502.5	0.00		0.00	18.09	-102.86	
602.5	1.42		623.81	0.00	-102.86	
602.5	0.00		0.00	0.00	-101.78	
697.5	1.08		581.67	2582.09	-94.31	
727.5	0.95		576.60	3099.66	-91.55	
762.5	1.18		590.87	2011.92	-86.60	
792.5	0.81		566.31	1708.82	-83.43	
Core 20	5	30.89		593.82		
	35	29.89		567.29		
	65	31.47		576.57		
	95	27.78		575.68		
	135	29.34	0.37	585.17		

Core 21	5	2.95	574.00	-20.37
	55	1.16	568.13	-23.41
	105	1.17	563.84	-22.94
	155	1.20	581.92	-23.39
	205	1.28	570.87	-20.12

### 5o. Cascadia Margin 'Cucumber Ridge' pore-fluid concentration and isotope data

Core #	Depth (cm)	SO <sub>4</sub> (mM)	stdev	Cl (mM)	δ <sup>13</sup> C-CH <sub>4</sub> (‰)
Core 2	35	30.425		554.64	
	134	26.33	0.947523	619.69	
	272.5	27.065	6.35689	556.41	
	348	23.09		593.33	
	430	21.8		581.525	-47.63
	505.5	20.65		528.01	-48.44
Core 3	10	8.3		216.79	
	30	32.47		560.85	

### 5p. Cascadia Margin 'Fish Boat/Barkley Canyon' pore-fluid concentration and isotope data

Core #	Depth (cm)	SO <sub>4</sub> (mM)	stdev	Cl (mM)	CH <sub>4</sub> (uM)	δ <sup>13</sup> C-CH <sub>4</sub> (‰)	δ <sup>13</sup> C-TOC (‰)
Core 9	2.5	32.65		608.92			
	12.5	25.09		517.00			
	22.5	25.38		577.88			
	32.5	24.11		575.10			
	42.5	23.61		561.34			
	72.5	22.34		563.82			
	102.5	20.56		550.80			
	142.5	20.07		615.44			
	292.5	13.35		525.93			
	402.5	11.34		574.27			
Core 11	0						
	12.5	28.99		557.94	0.37	-51.56	-21.88
	32.5	32.91		653.30	0.27	-55.81	-23.51
	60	11.44	0.25	562.98	1.45	-75.85	-23.99
	80	8.61		562.61	1.28	-77.95	
	100	8.09		599.99	1.49	-85.35	-25.50
	170	1.60		571.06	246.48	-91.25	
	220	1.85		567.63	637.42	-84.73	-23.57
	280	2.60			959.23	-82.29	
	340	1.59		532.23	1585.68	-80.17	-24.07
400	0.89		574.81	1932.93	-77.24	-24.37	
460	0.85		556.94	2124.14	-74.55		

	530	0.70	521.58	1652.81	-72.97	-20.86
	580	1.01	584.14	1449.01	-71.82	-21.21
	620	0.93	548.63	1966.88	-71.28	-22.63
Core 12	36.5	26.29	551.99	0.22		
	86	24.11	591.39	0.23		
	148	21.51	580.30	0.23		
	238	16.43	523.04	0.34		
	310	14.46	561.66	0.34		
	384.5	12.24	557.77	0.27		
	460	12.66	656.85	0.29		
	528	7.68	587.77	0.36		
	603	5.75	538.34	0.53		
	677	3.32	552.89	0.89		
	752	3.23	593.87	0.77		

### 5q. Cascadia Margin 'Ocean Basin' pore-fluid concentration and isotope data

Core #	Depth (cm)	SO <sub>4</sub> (mM)	Cl (mM)	δ <sup>13</sup> C-CH <sub>4</sub> (‰)
c18	2.5	28.52	527.79	
	12.5	26.99	541.46	
	22.5	23.57	573.89	
	32.5	27.31	521.73	
	42.5	12.98	558.62	
	77.5	28.48	567.25	
	102.5	27.42	526.58	
	132.5	27.31	551.55	
	192.5	26.56	546.87	-61.51
	252.5	26.99	539.27	-78.43
	312.5	4.29	547.88	-90.4
	363.5	2.53	577.48	-77.53
	395.5	4.00	571.49	-75.82
	442.5	2.82	573.05	-74.03
	472.5	1.94	579.64	-74.83
	492.5	2.19	583.72	
	502.5	1.96	537.88	-74.78
	532.5	1.79	536.17	-74.31
	562.5	1.58	555.40	-74.55
	592.5	1.50	547.38	-74.03
	617.5	1.53	567.77	-73.96

## Appendix 6

### 6a. Gulf of Mexico brine sites sediment core concentrations and stable isotope ratios.

Site	Dive #	Core #	Depth (cmbsf)	porosity	sample volume (mL)	SO <sub>4</sub> (mM)	Cl (mM)	[CH <sub>4</sub> ] (uM)	δ <sup>13</sup> C-CH <sub>4</sub> (‰)	Std dev	δ <sup>13</sup> C-DIC (‰)	Std dev	%TOC	δ <sup>13</sup> C-TOC (‰)	H <sub>2</sub> S (mM)	
GC 233	4222	8	over brine			2.45	572.37									
			1.5			15.01	570.59				-6.38		2.04	-30.70	-0.01	
			8.0			12.18	578.06				-10.35				0.4	
			16.0			7.54	573.27							1.07	-28.15	5.02
			24.0			2.14	613.7					-31.53	0.39	1.09	-27.66	6.37
GB 425	4562	2	1.5	0.78		29.08	571.72	0.00	-35.03		na		na			
			4.5	0.66		29.75	570.80	19.45	-19.04							
			4.5						0.00	-19.05						
			7.5	0.59		30.23	692.86	42.81	-34.26							
			10.5	0.62		29.18	542.84	50.42	-35.70							
GC 205	4566	5	13.5	0.55		29.93	557.63	54.74	-45.45							
			1.5	0.9		27.57	693.61	0.69	-41.99		Na		2.34	-24.16		
			4.5	0.9		26.10	892.52	17.13	-45.55				2.01	-23.68		
			7.5	0.9		22.68	1345.38	25.55	-46.26				1.93	-23.48		
			10.5	0.8		16.26	1736.00	71.56	-50.09				1.86	-23.87		
			13.5	0.8		11.73	1995.53	107.13	-53.52				2.89	-25.82		
MC 709	4412	3	16.5	0.9		7.42	2201.89	233.28	-58.49				2.34	-25.17		
			18.5										4.16	-26.15		
			0.0			30.02	942.05					1.65				
			1.5			27.06	1199.30					-18.81		3.46	-26.38	
			4.5		23.0	12.38	1881.36	39.54	-42.53		-30.51		3.17	-31.66		
			7.5		18.0	3.29	2715.25	961.06	-51.82		-24.03		2.72	-26.62		
			10.5		16.9	1.84	3503.47	227.88	-50.88		-11.30					
			13.5		4.2	2.27	3673.03	320.98	-50.25		-4.45	0.25				



MC 709	4413	6	0.0		30.83	694.36					-0.10			
			1.5										1.61	-30.70
			4.5	12.4	2.38	2915.35	58.01	-55.49	-4.96				1.34	-33.01
			7.5											
			10.5	9.5	2.02	3758.00	2.10	-50.86	-0.26				2.92	-29.09
			13.5		1.83	3758.00	0.00		-0.30					
			16.5	11.8	1.69	3828.25	5.94		-0.26				1.04	-29.32
			19.5	3.5	1.28	3726.55	397.32		1.03				1.50	-27.67
			22.5	6.3	1.31	4031.88	78.52	-51.84	0.56					
			25.5	6.4	1.96	4205.02	39.07		-0.49					
			28.5	7.0		5813.54	31.43	-52.19	-0.73					
			31.5											
			34.5	5.2	1.71	4131.69	22.60		-1.81					
			37.5	7.7	1.35	4450.83	20.47	-49.95	-2.23					
			40.5	6.1	1.61	4212.06	41.46		-1.63					
43.5	10.1	1.45	4308.85	177.09	-50.14	-2.18								
GC 205	4566	2	1.5	0.8	12.87	2278.86	2424.06	-53.78	0.18	Na	na			
			4.5	0.8	8.63	3369.65	3171.17	-54.08						
			7.5	0.7	2.59	4460.12	1772.65	-53.74	0.33					
			10.5	0.7			798.17	-53.82						

---

6b. Gulf of Mexico brine sites HYDRA concentrations and stable carbon isotopes.

Site	Dive #	Port #	Depth (cm)	Sample volume (mL)	SO <sub>4</sub> (mM)	Cl (mM)	[CH <sub>4</sub> ] (uM)	δ <sup>13</sup> C-CH <sub>4</sub> (‰)	δ <sup>13</sup> C-CH <sub>4</sub> (‰)	Ethane (uM)	Propane (uM)	δ <sup>13</sup> C-DIC (‰)	Std dev	NH <sub>4</sub> (uM)	PO <sub>4</sub> (uM)	NO <sub>3</sub> /NO <sub>2</sub> (uM)
GC 205	4566	F10	0	7	15.97	325.69	0.57	-55.10				-3.2	0.03			
		F9	0	7	11.9	227.94	2.84	-57.14	-57.19			-4.66		0.45	0.2	1.85
		F8	0	7	8.13	154.3	3.33	-58.95				-5.61		0.27	0.22	1.95
		F7	5	7	7.33	235.22	5.01	-56.05				-5.19		0.28	0.18	1.48
		F6	10	7	11.66	246.4	3.56	-55.25				-5.17				
		F5	15	7	12.75	271.72	7.03	-53.69				-5.45				
		F4	20	7	9.28	352.96	15.07	-51.91				-13.62		14.76	0.18	2.17
		F3	25	7	9.19	735.99	143.31	-52.44				-12.49				
		F2	30	5	6.86	520.82	48.16	-49.25	-49.16			-17.99				
		F1	35	5	3.61	548.89	45.89	-52.58	-52.78			-16.6				
		S10	0	7	22.69	444.6	0.77	-53.81				-2.04				
		S9	0	7	17.43	323.95	5.77	-56.4				-2.86	0.06	0.22	0.33	2.23
		S8	0	7	16.49	321.96	5.18	-59.15				-4.53		0.39	0.17	1.36
		S7	5	7	15.62	307.79	7.11	-56.66				-3.54		0.4	0.18	1.17
		S6	10	7	18.83	388.26	4.76	-53.62				-5.33		0.34	0.23	1.63
		S5	15	7	18.70	545.06	9.51	-53.3				-14.86				
		S4	20	3	11.01	529.19	21.55	-51.34				-19.33		8.34	0.82	1.82
		S3	25	7	13.80	1241.54	232.20	-52.81								
		S2	30	3	5.69	607.85	63.67	-48.9				-19.32				
		S1	35	4	5.57	682.35	98.37	-49.34				-17.70	0.15	21.19	230.64	1.39
GC 233	4222	S10	4.5	na	28.75	556.55	9.91	-45.36		0.13	0.16	-8.30				
		S9	7.5		29.76	553.91	11.68			0.03	0.03	-9.01	0.98			
		S8	12.5		27.96	512.54	6.47				0.16	-9.35				
		S7	17.5		30.21	587.91	13.70			0.37	0.21	-7.715	0.15			
		S6	22.5		29.49	558.46	10.42	-49.28		1.32	1.57	-8.30				
		S5	27.5		26.45	557.91	17.23			1.31	1.46	-18.93				
		S4	32.5				22.90			1.84	3.73					
		S3	37.5				45.16			0.71	0.30					
		S2	42.5		21.54	615.62	32.93	-46.13		0.39	0.16					

		S1	47.5		20.24	685.98	38.41		0.29	0.11	-29.09	
	4555	S10	4.5	7	24.05	497.63	1011.23	-64.3	-64.57		-2.55	0.37
		S9	7.5	7	14.87	902.9	9900.09	-64.92			-9.39	
		S8	12.5	7	4.50	1380.96	11401.52	-65.16			-13.2	
		S7	17.5	7	3.84	1224.07	16055.62	-65.07			-12.87	
		S6	22.5	5	4.18	1236.51	14225.54	-65.04			-13.36	
		S5	27.5	3	4.87	1212.69	17763.93	-64.72			-12.88	
		S4	32.5	2	4.98	1131.45	18728.74	-64.04			-13.12	
		S3	37.5	2	6.18	840.26	22574.89	-64.76			-11.24	
		S2	42.5	0								
		S1	47.5	7	20.54	741.52	4025.50	-64.58			-4.99	
		F10	4.5	7	19	393.8	577.08	-64.68			-2.6	
		F9	7.5	6								
		F8	12.5	4	4.09	736.7	16488.70	-64.98			-12.85	
		F7	17.5	7	3.84	878.51	9047.59	-65.09			-12.34	
		F6	22.5	7	4.64	819.95	2957.64	-64.72			-11.84	
		F5	27.5	7	4.33	670.7	2286.42	-64.33	-64.65		-11.65	0.06
		F4	32.5	7	5.3	756.29	1991.35	-64.31			-12.5	
		F3	37.5	7								
		F2	42.5	4	7.94	367.46	2676.02	-64.03	-63.8		-8.29	0.08
		F1	47.5	0								
MC												
709	4413	S10	4.5	n/a	n/a	n/a						
		S9	7.5				57.88	-47.7		0.86		
		S8	12.5				2450.38	-54.28		36.89	0.57	
		S7	17.5				3952.85	-55.17		57.17		
		S6	22.5				3768.16	-54.24		20.85	0.28	
		S5	27.5				4061.30	-53.42		17.54	0.04	
		S4	32.5				5393.14	-52.88		66.99	0.12	
		S3	37.5					-52.68				
		S2	42.5				5372.57			99.30	0.37	
		S1	47.5				152.39	-52.32	-53.6	1.44		

4562	F10	4.5	7	19.67	386.49	3.036078	-44.78		-2.47
	F9	7.5	7	20.53	392.52	48.68409	-51.39	-52.27	-4.93
	F8	12.5	7	19.94	370.07	10.92026	-56.58		-2.51
	F7	17.5	7	20.24	388.53	22.81589	-57.03		-3
	F6	22.5	5	6.35	131.53	14.26266	-58.51		-7.27
	F5	27.5	5		191.91	18.88017	-57.17		-6.49
	F4	32.5	0						
	F3	37.5	2	2.56	50.01	44.62992	-54.14		-7.08
	F2	42.5	2	1.73	28.13	8.16787	-53.73	-53.51	-6.37
	F1	47.5	7	13.69	277.3	38.97922			-5.14
	S10	4.5	7	24.77	502.28	4.437286	-46.42	-46.43	-1.9
	S9	7.5	7	25.98	496.14	46.59158	-52.58		-2.51
	S8	12.5	4	21.41	436.92	14.55551	-54.12		-2.34
	S7	17.5	7	24.04	455.45	17.91641	-54.67		-2.65
	S6	22.5	0						
	S5	27.5	0						
	S4	32.5	2	4.44	95.98	26.07922	-57.43		-7.28
	S3	37.5	0						
	S2	42.5	0						
	S1	47.5	0						

---

## 6c. Description of modeling work in Chapter 6

1. open AFS
2. navigate to H:\Cl\_models
3. open document called “advection rates” in  
D:\lapham\Dissertation\ch6\_brine\advection (this document has all the Ds changes with depth)
4. Using an ‘equation of state’ thermodynamic model (Mao and Duan, 2007) which has been interfaced to a website: [http://www.geochem-model.org/models/h2o\\_nacl/index.htm](http://www.geochem-model.org/models/h2o_nacl/index.htm), calculate the generic viscosities and densities for each site, for different molalities. Convert these concentrations to molarities based on density (Table 1). Now, plot Cl (mM) vs viscosity or density. Fit the data to a linear line to calculate viscosities and densities per exact sample molarity (Table 2). This data is within the ‘generic viscosity and density’ worksheet.

**Table 1: Generic viscosities and densities for specific sites (ie P and T conditions)**

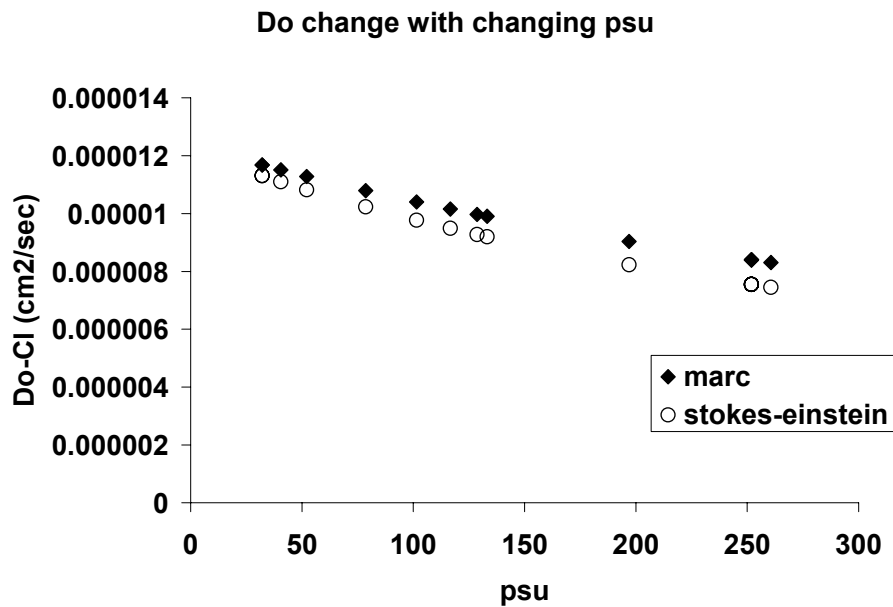
Site	T (K)	P (bar)	Cl (mol/kg)	viscosity (Pa.s)	density (g/mL)	Cl (mM)
GC 205	279 K	97 bar	0.55	0.001519	1.02772	565.246
			1	0.001572	1.0457	1045.7
			2	0.001721	1.08312	2166.24
			3	0.001915	1.11747	3352.41
			4	0.002159	1.14925	4597
			5	0.002458	1.17892	5894.6
			6	0.002817	1.20698	7241.88
MC 709	280	75	0.55	0.001477	1.02658	564.619
			1	0.001529	1.04454	1044.54
			2	0.001674	1.08193	2163.86
			3	0.001863	1.11627	3348.81
			4	0.002101	1.14805	4592.2
			5	0.002391	1.17773	5888.65
			6	0.002739	1.2058	7234.8

**Table 2: Equations of lines to Cl (mM) vs viscosity or density.**

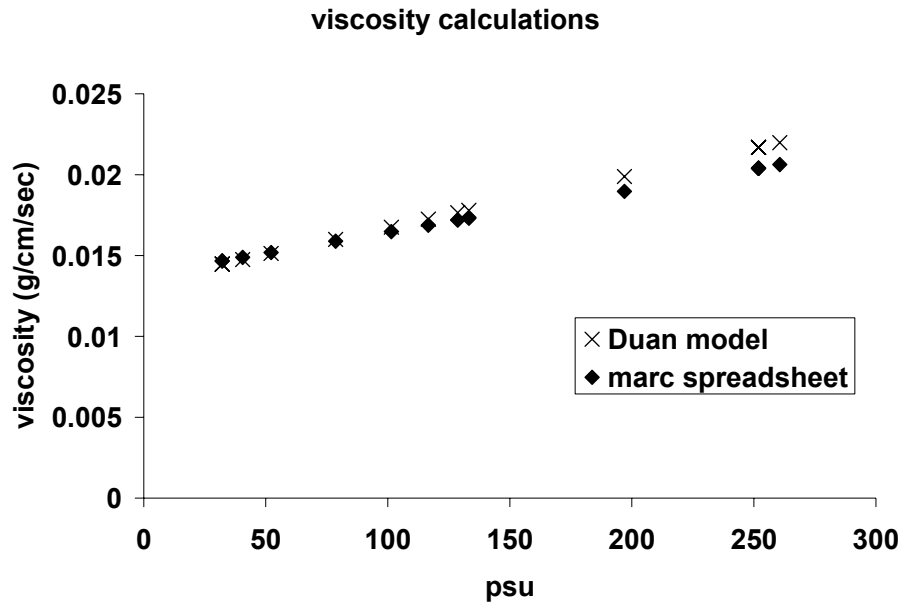
Site	parameter	Equation	R <sup>2</sup>
GC 205	viscosity	$y = 0.000000192x + 0.001341611$	0.983
	density	$y = 0.000026848x + 1.020232834$	0.991
MC 709	viscosity	$y = 0.00000019x + 0.00130506$	0.983
	density	$y = 0.00002687x + 1.01907745$	0.992

5. Get Do for SO4 and Cl using Marc’s “diff\_coeff” spreadsheet. Found in:  
D:\lapham\Studentness\Classes\Modeling class

6. Now, using the Stokes-Einstein Relationship,  $\left(\frac{D^o \eta^o}{T}\right)_{T_1} = \left(\frac{D^o \eta^o}{T}\right)_{T_2}$  where  $D^o$  is the diffusion coefficient,  $\eta^o$  is viscosity, and  $T$  is temperature, calculate new  $D_o$  for change in viscosity.
7. Incidentally, I compared  $D_o$  calculated from Marc's spreadsheet with changing  $\rho_{su}$  and  $D_o$  calculated in #6 and found that the  $D_o$  calculated from Marc's spreadsheet was systematically higher than that calculated with Stokes-Einstein equation (Figure 1). On second look, this deviation stems from the difference in viscosities calculated from Marc's spreadsheet and from the Mao and Duan model (Figure 2).



**Figure 1: Salinity (psu) versus  $D_o$  for chloride.**



**Figure 2: Salinity (psu) versus viscosity for the Duan and Mao model and Marc's spreadsheet.**

8. While it seemed there were deviations with the viscosity and  $D_o$  calculations between two different models, I decided to use the Duan model.
9. OK, back on track now. I have new  $D_o$  values with depth, setting the 100 and 200 cmbsf depth at 4500 mM chloride:

**Table 3: Calculated Do values for chloride and sulfate with depth.**

Site	core #	Depth (cmbsf)	Cl (mM)	Do-Cl (cm2/yr)	Do- so <sub>4</sub> (cm2/yr)
GC 205	c5	0	550.00	356.67	188.02
		1.5	693.61	350.00	184.50
		4.5	892.52	341.17	179.84
		7.5	1345.38	322.63	170.07
		10.5	1736.00	308.18	162.45
		13.5	1995.53	299.28	157.76
		16.5	2201.89	292.55	154.22
		100	4500.00	234.03	123.37
		200	4500.00	234.03	123.37
GC 205	c2	0	550.00	356.67	188.02
		1.5	2278.86	290.12	152.94
		4.5	3369.65	259.57	136.83
		7.5	4460.12	234.84	123.80
		100	4500.00	234.03	123.37
		200	4500.00	234.03	123.37
MC 709	c3 (4412)	0	942.05	359.19	189.35
		1.5	1199.30	347.74	183.31
		4.5	1881.36	320.64	169.02
		7.5	2715.25	292.74	154.31
		10.5	3503.47	270.49	142.59
		13.5	3673.03	266.14	140.29
		100	4500.00	246.78	130.09
		200	4500.00	246.78	130.09
MC 709	c6 (4413)	0	694.36	370.96	195.55
		4.5	2915.35	286.75	151.16
		10.5	3758.00	264.01	139.17
		13.5	3758.00	264.01	139.17
		16.5	3828.25	262.28	138.26
		19.5	3726.55	264.80	139.58
		22.5	4031.88	257.38	135.67
		25.5	4205.02	253.35	133.55
		34.5	4131.69	255.04	134.44
		37.5	4450.83	247.85	130.65
		40.5	4212.06	253.19	133.47
		43.5	4308.85	251.00	132.31
		100	4500.00	246.78	130.09
200	4500.00	246.78	130.09		

10. Make text files of depth vs Do-Cl for each core.

11. Now, open “crimson editor” to check out the model ‘curve\_fits.f’ (found in H:\Cl\_models\curve\_fits). This model will fit an exponential curve to each of the Do change with depth. Nothing needs to be changed within the code, you input the file name and give the output its own name.



12. Save and compile curve\_fit.f and run model. Get constants for exponential curve (Table 4). These are the values that will be used in the odeCl.f model to define the change of Do with depth. Also, plot output as depth vs Do (Figure 3).

**Table 4: Constants C1, C2, and C3 calculated from curve\_fit.f to define exponential curve:  $y=(C1-C2)\exp(C3*x) +C2$**

Site	core	C1	C2	C3	R2
GC 205	5	359.03	233.34	-0.046	0.997
	2	354.82	234.66	-0.450	0.989
MC 709	3	364.29	245.51	-0.124	0.989
	6	369.78	253.84	-0.247	0.973

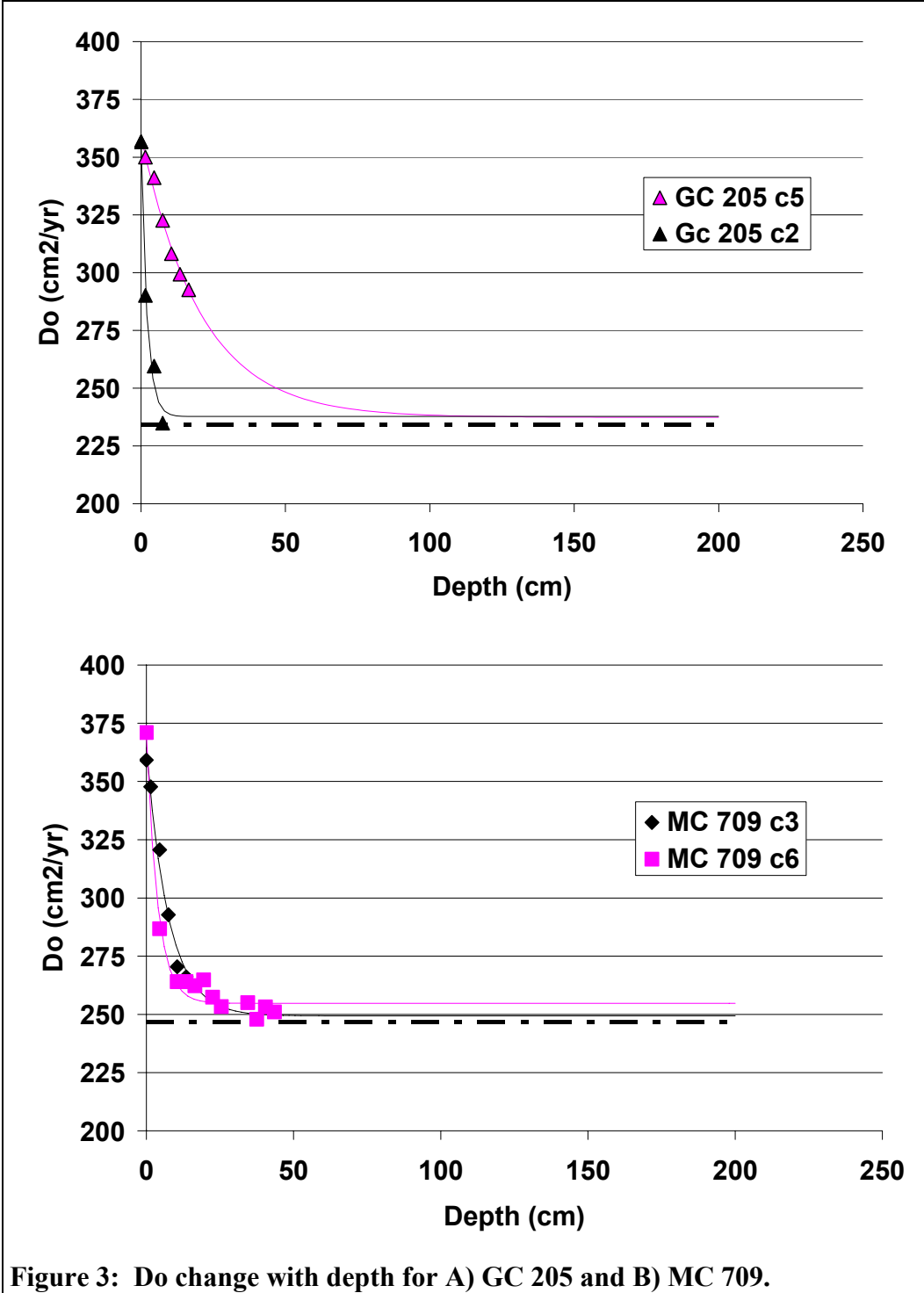


Figure 3: Do change with depth for A) GC 205 and B) MC 709.

- 13. Open odeCl\_expDo.f
- 14. Figure out what sedinf is for each site. I estimated that  $sedinf = SAR * porinf$  (Table 5)

**Table 5:**

<b>Site</b>	<b>SAR (cm/yr)</b>	<b>SAR-inf (cm/yr)</b>
GC 205	0.02	0.014
MC 709	0.07	0.049

15. For each core, input exponential coefficients, sedinf, and output file name. Run model.
16. Use Matlab to plot data next to modeled output.

## Appendix 7

### 7a. Stable carbon isotope ratios for carbonates collected in the Gulf of Mexico.

Sample ID	$\delta^{13}\text{C-CO}_3$ (‰)
Bucket 3, 709, Miss. Canyon, 4413 3 june 2002	-23.8
Lapham, 4405, 5/30/02, Rock	-20.5
4401, 5/29/02, Carbonate	-22.0
4413, Core 6 Rocks from 6-9 cm 6/3/02	-26.8
4403, #6, 27 cm carbonate, 5/29/02	-18.0
GC 232, 4403, core #4, carbonate at 21 cm	-14.6
4401, Core #2, 5/29/02, carbonate	-18.0
Lapham, 4405, 5/30/02	-22.0
Chanton, 4408, 6/1/02 Offshore 65-1	-49.7
4413, 118 Miss. Canyon 6/3/02	-28.6
Chanton, Gc 234, 4407, 5/31/02 smaller of 2 rocks	-20.4
4413, Miss Canyon, Block 3/6/02, 709, Bucket 9	-28.2

**7b. MC 118 core locations and descriptions.**

<b>Core #78y676y</b>	<b>Water depth (m)</b>	<b>Core depth (cm)</b>	<b>Latitude</b>	<b>Longitude</b>	<b>Core description</b>
PC4414	966	25	28°51.132	88°29.550	
1	903	211	28°51.264	88°29.952	
3	908	301	28°51.305	88°29.653	
4	894.6	154	28°51.461	88°29.490	
5	887	191	28°51.482	88°29.470	
6	892.6	131	28°51.432	88°29.490	
10	894	351	28°51.488	88°29.503	
23	894.4	140	28°51.2567	88°29.6133	
27	902	136	28°51.0215	88°29.5468	
32	897	132	28°51.1448	88°29.6905	Boring mud.
33	897	103	28°51.0420	88°29.4290	
34	895	120	28°51.0402	88°29.2963	
35	893	144	28°51.0388	88°29.3641	
36	889	136	28°51.1494	88°29.2240	
38	899	86	28°51.0431	88°29.5633	
39	898	71	28°51.0335	88°29.5116	
2	895	151	28°51.337	88°29.634	
7	895.3	205	28°51.342	88°29.574	
8	894	121	28°51.353	88°29.586	
21	894	122	28°51.2498	88°29.5907	
22	897	66	28°51.2400	88°29.5920	
28	903	113	28°51.3469	88°29.4898	
29	889	105	28°51.3293	88°29.4996	
30	892	131	28°51.1402	88°29.1340	Sulfide smell
9	877	450	28°51.448	88°29.503	
26	889	46	28°51.1551	88°29.4879	
31	891	103	28°51.1438	88°29.3996	Oily core. Shell hash at bottom
24	893	22	28°51.1388	88°29.5399	Short core. Oily, CO3 at bottom
		-			No core. CO3 rocks bent
25	889		28°51.1381	88°29.5492	catcher
37	889	-	28°51.1393	88°29.5498	No core. Too short, dark mud.

**7c. MC 118 May 2005 cores 1-10 without 9.**

Core #	Depth (cm)	NH <sub>4</sub> (uM)	PO <sub>4</sub> (uM)	NO <sub>3</sub> (uM)	CH <sub>4</sub> (uM)	SO <sub>4</sub> (mM)
1	1.5	94.88	3.40		0.76	26.43
	31.5	129.57	4.23		0.65	28.58
	61.5	106.25	3.40		0.77	25.99
	91.5	166.08	2.89		0.76	28.00
	121.5	187.11	2.59		0.79	26.74
	151.5	235.36	3.90		0.76	28.06
	181.5	292.95	2.32		0.82	24.70
	211.5	377.89	1.95		0.86	23.75
2	1.5	127.74	0.02		0.97	27.94
	26.5	118.63	1.25		2.48	26.05
	51.5	108.24	0.89		5.17	25.70
	76.5	110.25	0.73		7.68	24.17
	101.5	103.69	0.90		8.98	22.62
	126.5	151.43	0.56		10.96	22.62
	151.5	119.60	0.70		11.98	22.14
	176.5					19.85
3	1.5	123.95	1.55	12.62	1.48	27.30
	26.5	69.41	0.59	8.50	3.45	27.39
	51.5	85.16	1.87	9.85	3.52	27.08
	101.5	86.05	0.90	8.14	3.15	25.39
	151.5	125.96	1.22	16.05	4.04	25.16
	201.5	96.75	0.65	11.34	4.56	25.42
	251.5	126.66	0.43	13.49	6.08	26.85
	301.5	168.42	0.63	15.99	8.94	22.59
4	6.5	104.19	2.77	4.01	0.67	27.10
	17.5	116.96	2.77	10.23	0.70	26.85
	29.5	123.63	2.48	8.43	0.73	26.73
	54.5	145.21	2.41	6.15	0.81	26.00
	84.5	158.60	2.33	7.74	0.85	26.00
	114.5	165.37	1.45	7.50	0.83	25.82
	154.5	182.76	1.84	2.49	0.83	24.85
5	1.5	55.29	0.69	9.69	0.68	27.87
	11.5	35.56	0.98	9.90	0.89	27.87
	21.5	38.67	0.23	5.00	0.73	27.46
	41.5	50.86	0.66	10.34	0.73	27.11
	71.5	123.49	2.22	5.80	0.78	26.30
	111.5		0.80	5.30	0.85	26.98
	151.5	256.16	0.81	4.40	0.84	25.52

	191.5	282.79	0.71	10.10	0.83	23.88
6	1.5	26.05	0.41	3.48	0.75	27.20
	11.5	36.92	1.00	5.17	0.68	26.87
	21.5	31.45	1.10	3.68	0.69	26.67
	41.5	96.06	1.79	5.48	0.73	26.70
	81.5	142.32	1.82	1.64	0.80	25.56
	101.5	169.20	0.78	6.60	0.81	26.08
	131.5	209.94	0.61	12.02	0.78	24.49
7	1.5	89.09	4.30	1.32	0.88	
	11.5	71.33	2.80	1.33	0.93	
	21.5	70.88	2.32	2.05	1.30	
	61.5	66.63	3.40	9.87	2.61	
	81.5	32.26	1.98	3.50	4.11	
	101.5	42.37	1.57	3.35	5.00	
	151.5	32.57	1.62	1.54	7.22	
	201.5	43.16	2.26	0.40	8.55	
8	2	51.87	2.80	3.66	3.67	
	16.5	41.23	3.19	5.21	3.68	
	31.5	38.44	2.04	7.65	6.19	
	46.5	26.09	2.42	7.02	8.66	
	76.5	24.55	1.99	7.47	12.08	
	101.5	36.28	1.48	3.76	20.04	
	121.5	33.13	1.66	3.06	22.27	
10	1.5	110.46	7.35	8.15	1.35	
	16.5	60.19	8.57	7.69	0.83	
	41.5	76.89	9.41	8.78	1.11	
	81.5	91.03	8.02	7.81	0.94	
	116.5	118.76	8.05	6.89	1.02	
	150.5	180.32	9.36	7.06	1.01	
	201.5	208.08	7.55	7.18	1.02	
	251.5	207.76	7.57	6.94	1.02	
	301.5	298.80	9.16	7.85	1.05	
	351.5	344.37	9.08	8.66	1.13	

**7d. MC 118 May 2005 core 9.**

Core #	Depth (cm)	NH <sub>4</sub> (uM)	PO <sub>4</sub> (uM)	NO <sub>3</sub> (uM)	CH <sub>4</sub> (uM)	δ <sup>13</sup> C-CH <sub>4</sub> (‰)	stdev	SO <sub>4</sub> (mM)
9	1.5	49.43	9.08	7.80	186.18	-60.66	0.20	8.04
	13.5	47.44	8.35	7.31	450.40	-67.12	1.39	7.05
	41.5	67.37	15.03	13.52	2660.60	-68.96	0.32	1.55
	81.5	40.27	9.72	7.78	3518.84	-56.86	0.31	
	121.5	45.09	10.80	8.19	3162.89	-50.73	0.11	
	154.5	34.12	15.60	5.61	4285.04	-47.36	0.04	
	174.5	52.37	14.69					
	194.5	60.49	15.02		2009.46	-48.47	0.06	
	234.5	51.60	13.39		1907.97	-49.90	0.23	
	266.5	56.89	13.56		1766.80	-49.55	0.54	
	279.5	84.97	20.88	29.65	2298.15	-49.70	0.31	
	329.5	114.76	26.50	5.82	2156.68	-50.31	0.23	
	359.5	199.06	14.92	8.67	2421.03	-51.14	0.06	
	399.5	322.00	20.10	6.98	2107.56	-49.69	0.41	
	429.5	363.59	21.30	6.87	1899.27	-50.41	0.71	

**7e. MC 118 Push core 4414**

Core #	Depth (cm)	δ <sup>13</sup> C-DIC (‰)	SO <sub>4</sub> (mM)
PC 4414	Overlying water	0.26	
	1.5	-9.93	26.3
	4.5	-14.12	21.09
	7.5	-13.3	20.75
	10.5	-23.46	18.2
	13.5	-21.87	11.09
	16.5	-13.84	10.55
	19.5	-3.39	11.39
	22.5	0.47	6.41
	25.5	3.31	3.91



## 7f. MC 118 Cores 21-39

Core #	Depth	Cl (mM)	SO <sub>4</sub> (mM)	CH <sub>4</sub> (uM)	δ <sup>13</sup> C-CH <sub>4</sub> (‰)	δ <sup>13</sup> C-DIC (‰)	stdev
c21	1.5	489.11	27.28	0.85			
	13.5	538.74	30.19	0.93	-61.00	-11.81	0.22
	31.5	471.46	28.20	1.14	-66.62		
	51.5	547.52	30.30	2.09	-70.54	-16.03	0.32
	68.5	540.99	29.98	1.91	-67.39		
	89.5	527.61	26.53	5.33	-72.80	-22.75	0.11
	111.5	556.33	23.54	13.57	-76.13		
c22	2.0	563.17	28.61	1.26	-68.26	-7.23	0.23
	11.5	544.20	27.48	1.55	-68.44	-6.96	0.57
	22.0	562.13	28.05	1.94	-70.03	-8.56	0.12
	38.5	550.64	27.50	2.82	-74.20	-10.66	0.59
	51.5	551.75	26.68	3.60	-71.59	-13.96	0.20
	61.5	575.90	28.32	4.51	-72.36	-15.39	0.05
c23	1.5	550.61	30.90	0.47			
	18.5	558.79	31.40	0.48			
	47.5	495.77	27.93	0.52			
	81.5	504.70	26.60	0.56			
	111.5	588.88	30.34	0.56			
	135.5	541.76	28.55	0.59			
c24	1.5	538.73	28.60	9.76	-51.28	-18.36	0.06
	7.5	533.61	23.94	17.18	-52.78	-26.14	0.18
	13.5	538.93	18.30	56.40	-56.41	-26.68	0.36
c26	2.0	542.71	27.88	2.15	-65.67	-10.94	0.13
	16.5	546.18	15.05	24.69	-67.92	-30.51	0.05
	27.5	557.81	8.87	110.10	-73.10	-32.70	0.03
	38.5	531.63	2.75	911.82	-41.14	-33.73	0.11
	46.5	530.81	1.95	2064.41	-39.20	-31.15	0.05
c27	1.5	577.43	26.83	0.61			
	18.5	501.26	27.95	0.79			
	38.5	546.66	26.90	0.72			
	58.5	541.67	27.26	0.74			
	78.5	536.81	28.14	0.71			
	98.5	546.80	27.42	0.64			
	118.5	545.55	27.86	0.67			
	132.5	540.23	27.84	0.68			
c28	2.0	548.43	31.09	0.57			
	18.5	545.57	31.28	0.70			
	38.5	549.06	30.29	0.94			
	61.5	560.71	32.26	1.34			
	81.5	534.46	30.25	1.90			
	101.5	533.64	28.30	5.06			
c29	1.5	553.10	28.63	0.69			
	21.5	560.26	25.67	2.92	-63.19	-9.61	0.11
	41.5	541.34	27.37	3.88	-64.54	-17.28	0.25
	61.5	559.22	26.27	6.42	-66.23	-17.03	0.19
	81.5	547.76	25.63	6.80	-66.12	-23.12	0.22
	101.5	548.87	22.40	11.29	-66.54	-25.08	0.07

c30	1.5	524.80	28.24	0.97			
	16.5	553.44	26.31	2.89	-37.71	-13.505	0.22
	31.5	562.73	26.70	4.35	-36.34	-18.25	0.06
	46.5	575.73	27.10	5.07	-36.61	-18.54	0.06
	61.5	570.06	26.36	5.71	-36.80	-19.96	0.09
	76.5	550.73	26.02	5.98	-37.28	-22.81	0.03
	96.5	551.04	26.10	6.10	-37.98	-22.81	0.03
	121.5	547.97	25.25	14.74	-43.07	-32.01	0.24
c31	1.5	508.35	8.66	10.76	-81.22	-26.18	0.11
	18.5	571.81	4.63	30.36	-78.57	-30.79	0.09
	41.5	545.63	3.58	58.62	-79.85	-23.96	0.01
	61.5	539.44	3.89	69.54	-85.29	-38.55	0.08
	81.5	520.28	2.36	215.31	-91.88	-41.93	0.31
	91.5	549.11	1.47	430.58	-95.63	-43.84	0.20
	101.5	594.28	0.50	2494.26	-88.79	-44.65	0.08
	111.5			4040.54	-86.19	-41.53	0.01
121.5	555.81	-0.04	4309.17	-81.35	-37.94	0.28	
c32	1.5	535.89	27.59	1.00	-67.88		
	16.5	530.78	29.43	0.73	-55.30		
	31.5	536.09	29.03	0.53	-51.29		
	51.5	486.39	28.73	0.64	-51.47		
	71.5	535.89	27.92	4.60	-52.05		
	91.5	468.79	27.76	0.69	-48.88		
	111.5	544.65	27.00	0.66	-53.01		
	128.5	538.14	26.62	0.78	-53.90		
c33	9.5	565.65	31.98	0.49			
	31.5	578.68	31.50	0.59			
	61.5	572.99	30.75	0.63			
	91.5	553.61	28.49	0.59			
	121.5	553.93	28.06	0.66			
	151.5	550.82	27.82	0.72			
c34	1.5	580.38	32.72	0.66			
	21.5	504.02	28.07	0.61			
	41.5	549.54	29.78	0.56			
	64.5	544.53	30.25	0.52			
	96.5	539.66	28.59	0.57			
	118.5	549.68	27.37	0.59			
c35	2.0	474.72	26.24	0.58			
	26.5	542.20	27.02	0.55			
	51.5	548.80	26.73	0.58			
	76.5	542.45	26.28	0.59			
	101.5	562.33	26.61	0.63			
	131.5	573.27		0.65			
c36	1.5	542.76	27.19	0.51			
	26.5	536.59	28.98	0.55			
	51.5	517.48	27.44	0.57			
	76.5	546.24	26.94	0.61			
	101.5	591.29	27.12	0.63			
121.5	552.92	27.24	0.68				
c38	1.5	572.96	16.52	0.75			

	16.5	472.04	24.95	0.55
	41.5	539.34	28.05	0.62
	61.5	545.93	27.13	0.62
	81.5	539.59	26.30	0.66
c39	1.5	559.42	24.58	0.53
	21.5	570.33	28.61	0.60
	41.5	505.59	28.35	0.70
	61.5	568.87	32.77	0.76